2015

A MEASUREMENT OF THE PROMPT FISSION NEUTRON ENERGY SPECTRUM FOR ^{235}U(n,f) AND THE NEUTRON-INDUCED FISSION CROSS SECTION FOR ^{238}U(n,f)

Zachariah W. Miller
University of Kentucky, zaglamir@gmail.com

STUDENT AGREEMENT:

I represent that my thesis or dissertation and abstract are my original work. Proper attribution has been given to all outside sources. I understand that I am solely responsible for obtaining any needed copyright permissions. I have obtained needed written permission statement(s) from the owner(s) of each third-party copyrighted matter to be included in my work, allowing electronic distribution (if such use is not permitted by the fair use doctrine) which will be submitted to UKnowledge as Additional File.

I hereby grant to The University of Kentucky and its agents the irrevocable, non-exclusive, and royalty-free license to archive and make accessible my work in whole or in part in all forms of media, now or hereafter known. I agree that the document mentioned above may be made available immediately for worldwide access unless an embargo applies.

I retain all other ownership rights to the copyright of my work. I also retain the right to use in future works (such as articles or books) all or part of my work. I understand that I am free to register the copyright to my work.

REVIEW, APPROVAL AND ACCEPTANCE

The document mentioned above has been reviewed and accepted by the student's advisor, on behalf of the advisory committee, and by the Director of Graduate Studies (DGS), on behalf of the program; we verify that this is the final, approved version of the student's thesis including all changes required by the advisory committee. The undersigned agree to abide by the statements above.

<div align="right">

Zachariah W. Miller, Student

Dr. Michael A. Kovash, Major Professor

Dr. Tim Gorringe, Director of Graduate Studies

</div>

A MEASUREMENT OF THE PROMPT FISSION NEUTRON ENERGY
SPECTRUM FOR ^{235}U(n,f) AND THE NEUTRON-INDUCED FISSION CROSS
SECTION FOR ^{238}U(n,f)

DISSERTATION

A dissertation submitted in partial
fulfillment of the requirements for
the degree of Doctor of Philosophy
in the College of Arts and Sciences
at the University of Kentucky

By
Zachariah W. Miller
Lexington, Kentucky

Director: Dr. Michael A. Kovash, Professor of Physics
Lexington, Kentucky

ABSTRACT OF DISSERTATION

A MEASUREMENT OF THE PROMPT FISSION NEUTRON ENERGY
SPECTRUM FOR ^{235}U(n,f) AND THE NEUTRON-INDUCED FISSION CROSS
SECTION FOR ^{238}U(n,f)

Two measurements have been made, addressing gaps in knowledge for ^{235}U(n,f) and ^{238}U(n,f). The energy distribution for prompt fission neutrons is not well-understood below 1 MeV in ^{235}U(n,f). To measure the ^{235}U(n,f) prompt fission neutron distribution, a pulsed neutron beam at the WNR facility in Los Alamos National Laboratory was directed onto a ^{235}U target with neutron detectors placed 1 m from the target. These neutron detectors were designed specifically for this experiment and employed a unique geometry of scintillating plastic material that was designed to reject backgrounds. Fission fragments were detected using an avalanche counter. Coincidences between fission fragment production and neutron detector events were analyzed, using a double time-of-flight technique to determine the energy of the prompt fission neutrons. A separate measurement was made, investigating the neutron-induced fission cross section for ^{238}U(n,f). This measurement also used the pulsed neutron beam at the WNR facility. The neutron flux was normalized to the well-known hydrogen standard and the fission rate was observed for beam neutrons in the energy range of 130-300 MeV. Using an extrapolation technique, the energy dependence of the cross section was determined. These new data filled a sparsely populated energy region that was not well-studied and were measured relative to the hydrogen standard, unlike the majority of available data. These data can be used to constrain the fission cross section, which is considered a nuclear reaction standard.

KEYWORDS: Uranium Fission Cross Section, Prompt Fission Neutron Spectrum,
Fast Neutron Detectors, Plastic Scintillator, Particle Identification

Author's signature: Zachariah W. Miller

Date: April 24, 2015

A MEASUREMENT OF THE PROMPT FISSION NEUTRON ENERGY
SPECTRUM FOR ^{235}U(n,f) AND THE NEUTRON-INDUCED FISSION CROSS
SECTION FOR ^{238}U(n,f)

By
Zachariah W. Miller

Director of Dissertation: <u>Michael A. Kovash</u>

Director of Graduate Studies: <u>Tim Gorringe</u>

Date: <u>April 24, 2015</u>

iii

For Julie

ACKNOWLEDGMENTS

The completion of this document, and the work that it describes, would not have been possible without contributions from a great many folks. I've been lucky to be surrounded by knowledgable and talented people who have generously granted me their guidance and opinions. Without their input, the work would have never gotten off the ground... let alone come to frution.

Michael Kovash: Thank you for pointing me in a direction and having faith I would get there eventually. I've learned a great deal about research in the last few years, and 90+% has been due to your patience and guidance.

Hongwei Yang: Thanks for sticking with me as we learned how *not* to program DAQ systems, and for the friendship and discussion along the way.

My committee members: Thank you for helpful discussions on my progression and for helping me refine my presentations until they looked 'somewhat' professional. Your guidance along the way was not taken lightly and was greatly appreciated.

Steve Maynard: Thank you for constructing the detectors and rolling with the punches as I was learning how to blueprint.

Bob Haight: Thank you for letting us use the experimental area and for the many discussions about fission, detectors, and where to find the spiciest burrito in Los Alamos.

My fellow graduate students: Thanks for occasionally reminding me to come up for air and malted beverages... and that there is more to a man than his work.

Finally, I want to thank my wife Julie for putting up with me during this process. Neither one of us knew what we were in for when I signed on here, but her patience and support has allowed me to pursue my dream. I hope to repay the favor soon.

TABLE OF CONTENTS

LIST OF FIGURES

LIST OF TABLES

Chapter 1: Introduction

1.1   Introduction to Fission

Nuclear fission research has a long and storied history reaching back to 1938 and its tale contains many of the famous names in physics such as Ernest Rutherford, Lise Meitner, and Enrico Fermi. Otto Hahn is credited with discovering fission and Lise Meitner with developing the first theory of how the splitting of the atom could occur. Hahn's discovery was achieved by bombarding nuclei with neutrons, a type of fission known as 'neutron-induced fission,' based on the necessity of an incoming neutron to catalyze the reaction. This technique is widely used to generate fission events, especially with the elements commonly associated with fission such as uranium and plutonium. Much research has been done regarding fission in isotopes of these elements, bombarding them with neutrons of many different energies and studying the rate of reaction, the amount of energy released in the fission, and the number of outgoing neutrons. These outgoing neutrons are released by the nuclei after fissioning and can be used to create chain reactions, which is why fission has become 'famous' as an energy source. Due to this fame and practical application, a great deal of effort has been invested in determining the quantities related to energy production. Both the rate of reaction and the number of neutrons released per fission are of particular interest, since ejected neutrons can catalyze new reactions.

The research over the last eighty years has led to a concise theory of how fission occurs as well as correctly accounting for the fission rates given a certain bombardment energy. However, not every energy region has been well studied and there are still a few regions where there have been no measurements at all. In particular, this work will focus on two energy regions where there is little experimental data: fission with a low-energy outgoing neutron for ^{235}U(n,f) and fission with a high-energy

incoming neutron for ^{238}U(n,f).

Nuclei fission due to nucleon binding energy. The binding energy is a measure of how much energy it takes to remove a nucleon from the nucleus. For heavy nuclei, as the nucleus grows the binding energy per nucleon decreases. Nuclei 'want' to be stable, so it is energetically favorable to be in a tightly bound state. Since decreasing the number of particles in the nucleus will raise the binding energy, splitting the nucleus is a possible decay channel. As an over-simplified example*, the binding energy per nucleon for ^{238}U is $\sim$ 7.6 MeV. However, if it is split into two ^{119}Pd nuclei, the binding energy per nucleon increases to $\sim$ 8.5 MeV. This is an increase of 0.9 MeV per nucleon, or $\sim$ 214 MeV for ^{238}U.

Given this statement, it is natural to ask, ''why don't all nuclei split freely until they are in the most tightly bound state?'' This is answered by considering the nuclear potential. A nucleus can be treated as being bound within a potential well. A simple well potential is created by considering a combination of two forces, the nuclear (strong) force and Coulomb repulsion. The strong force only acts at short distances and holds the nucleons together. If the nucleus is 'pulled' far enough apart, this force will no longer apply and Coulomb repulsion will become the dominant force, pushing the nucleus apart. In the most simplified form, the nuclear well potential can be considered as an infinite well for a radius between 0 and some radius r_0 which indicates the distances at which the nuclear force no longer applies. At this point, the potential takes the value of the well-known Coulomb potential.

$$V = \frac{e^2}{4\,\pi\,\epsilon_0} \cdot \frac{Z_1\,Z_2}{r_0} \tag{1.1}$$

In the simplified example of splitting a single ^{238}U nucleus into two ^{119}Pd fragments with touching surfaces, r_0 would be two times the radius of ^{119}Pd and $Z_1 = Z_2 = 46$. This gives a Coulomb potential of $\sim$ 250 MeV at r_0. Since the energy gained by splitting into two ^{119}Pd is 214 MeV, the nucleus is still 36 MeV shy of overcoming the

---

*Example from [1].

2
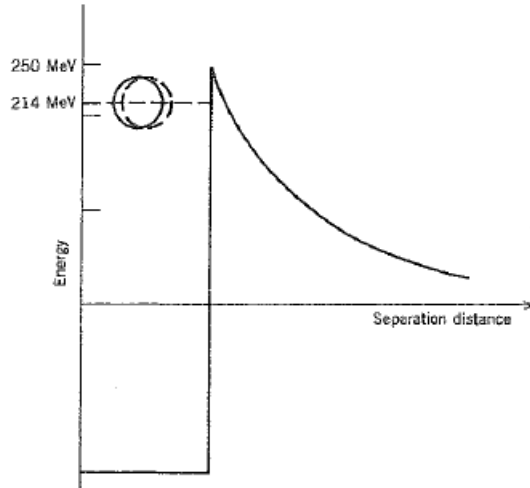
Figure 1.1: Example diagram of the idealized nuclear well potential. The well on the left is caused by the strong nuclear force which binds the nucleus together. The decay on the right is from the Coulomb potential, which goes as the inverse of the separation distance. Image from [1].

Coulomb barrier. **Figure 1.1** demonstrates the simplified nuclear well potential for this example. Choosing the example of splitting directly in half is a bit misleading, as this is not the state which gives the largest gain in binding energy per nucleon, nor is it a common fragment pair. However, it is easily calculable and demonstrates the same point as the more likely fission fragment pairs. The measured distribution of fission fragment mass is shown in **Figure 1.2** for thermal neutron induced fission. This shape changes slightly for fast neutrons, but shows the same two-peaked distribution of fragment masses. More common ^{238}U(n,f) fission fragment pairs will be even closer to the 'escape' energy. In both ^{238}U and ^{235}U, the nucleus almost never fissions without outside intervention. The spontaneous fission half-life for both is on the order of 10^9 years. Simply put, the difference between the energy gained by splitting and barrier energy is too great to overcome, even when allowing for quantum tunneling. This difference is known as the 'activation energy'. The activation energy varies based on the nuclear composition, with a dependence on both total number of nucleons and the number of protons. In this example, if the nucleus were to gain 36 MeV, splitting into two ^{119}Pd nuclei would become a possible decay.

3
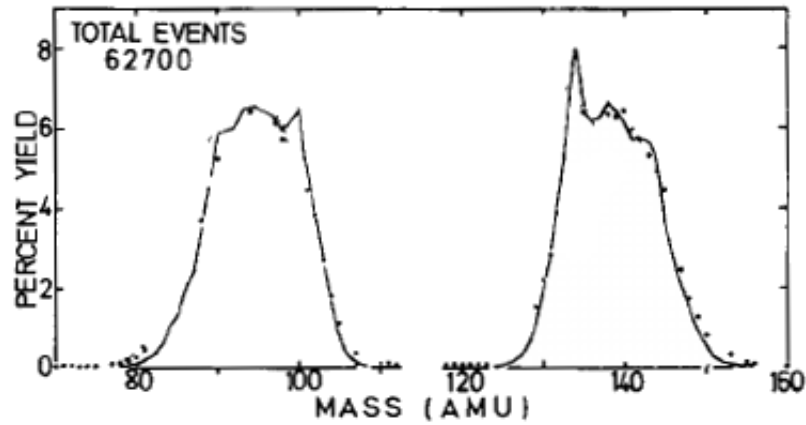
Figure 1.2: Fission fragment mass distribution for thermal neutron induced fission in ^{235}U. Image from [2].

A less idealized diagram of the fission barrier is shown in **Figure 1.3** with the activation energy highlighted. The need for an outside source of energy to overcome the fission barrier is where neutron bombardment comes into play. A uranium nucleus that captures a neutron can overcome this activation barrier. If a neutron is captured, changing the nucleus from ^{238}U to an excited state ^{239}U* (or ^{235}U to ^{236}U*), the binding energy per nucleon changes, which changes the shape of the barrier. Along with this change, the nucleus is disturbed by the captured neutron, which can cause the nucleus to fission. As an example, the activation energy for ^{236}U, which is formed via (^{235}U + n), is 6.2 MeV. The energy gained by capturing a neutron is calculated by looking at the mass difference between (^{235}U + n) and ^{236}U. This determines the excitation energy for the newly formed ^{236}U nucleus. Any kinetic energy from the neutron also

4
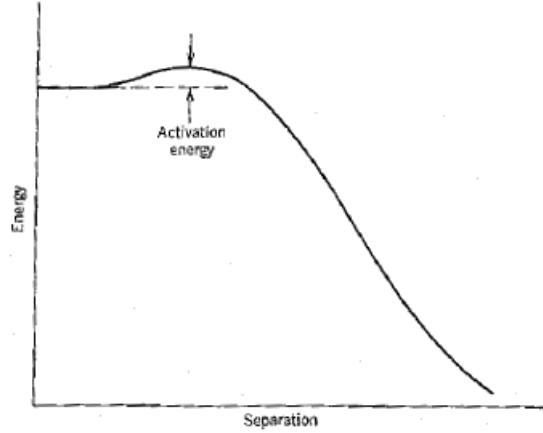
Figure 1.3: Example diagram of the Coulomb Barrier with the activation energy highlighted. Image from [1].

contributes to the excitation energy, but is not shown in this calculation.[†]

$$E_{ex} = [m(^{236}U^*) - m(^{236}U)] \cdot c^2 \tag{1.2}$$

$$m(^{236}U^*) = m(^{235}U) + m_n \tag{1.3}$$

$$m(^{236}U^*) = 236.052589 \, u$$

$$E_{ex} = (236.052589 \, u - 236.045563 \, u) \cdot 931.502 \, MeV/u$$

$$= 6.5 MeV$$

The energy gained by absorbing the neutron (E_{ex}) is greater than the fission barrier energy for ^{236}U by 0.3 MeV. Since the energy of the nucleus is greater than the binding potential, nuclear fission opens as a competitive decay channel. This is the essence of neutron-induced fission. By bombarding the nucleus with neutrons, the activation energy can be overcome by capture, even if the captured neutron energy is substantially lower than the initial activation energy.

1.1.1 Fission Models

One of the first and simplest models for describing how a nuclear fission occurs is known as the 'Liquid Drop Model'[3] and was proposed by Bohr and Wheeler in 1939

[†]This example is taken from [1].

as a model of the fission process. This model uses the same two forces described in the idealized well potential described in the previous section. The liquid drop model treats the nucleus like a charged droplet of fluid, with the charge causing the drop to spread apart and the fluid surface tensions holding the drop together as an analog for the strong nuclear force[‡]. The entirety of the model is based around the interplay of these two forces as they compete with one another. If the nucleus is modeled as a sphere, then any small distortions can be modeled as:

$$R(\theta) = R_0 \cdot (1 \ + \ \alpha_2 \, P_2(cos\,\theta)) \tag{1.4}$$

where R_0 is the radius of the spherical nucleus and $\alpha_2 \, P_2$ is a quadruple distortion term. **Figure 1.4** demonstrates the type of distortions being examined. With this formalism for the distortion of the drop, we can determine how the surface tension energy and the Coulomb repulsion energy are changed by distortions.

$$E_c = E_c^0 \, (1 \ - \ \frac{1}{5} \, \alpha_2^2) \tag{1.5}$$

$$E_s = E_s^0 \, (1 \ + \ \frac{2}{5} \, \alpha_2^2) \tag{1.6}$$

where the superscript 0 denotes the energy for the spherical nucleus model. Since the drop will become unstable when the Coulomb energy is greater than the surface energy, the nucleus will be stable against distortions as long as:

$$\chi = \frac{E_c^0}{2 \, E_s^0} \ \approx \ \frac{Z^2}{50.13 \cdot A} < 1 \tag{1.7}$$

χ is called the fissility parameter and is a model for whether a nucleus will readily undergo fission without outside energy. Z is the number of protons in the nucleus and A is the total number of nucleons in the nucleus. The approximation comes from writing E_c^0 and E_s^0 in terms of the nuclear composition. For $\chi \ \geq \ 1$, the nucleus will immediately fission, which determines the upper limit of observed nuclear size.

[‡]This discussion will be limited in scope for the sake of brevity. The full discussion is found in [4]. The present discussion and formalism have been borrowed from Vandenbosch's discussion[4].
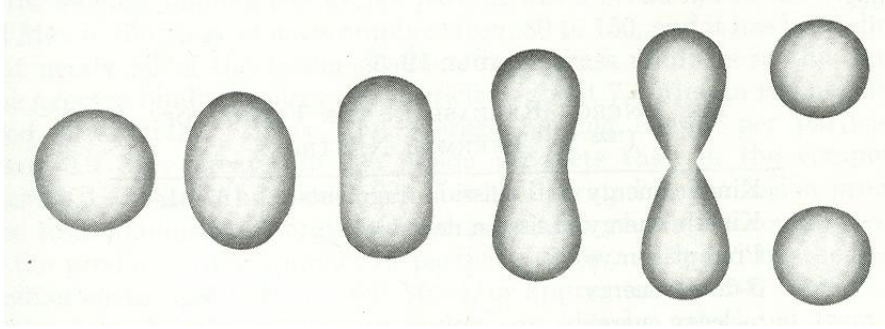
Figure 1.4: Liquid drop model fission diagram. Image from [5].

This analysis can be expanded to include higher orders of $\alpha_n P_n(cos\,\theta)$ Legendre polynomial expansion, which will more accurately determine the fissility parameter and the response to deformation. However, that will not be discussed in this paper and can be found in [4].

The distortion of a spherical nucleus may seem like an odd way to model a splitting nucleus; however, this is precisely what occurs when a neutron is captured. As the neutron is captured, the existing nucleons 'wobble about' like a drop of fluid that has been disturbed. This causes fluctuations that look very much like the 'pinched middle' diagram shown in **Figure 1.4**. With higher order terms in the polynomial expansion, more complicated distortions of the drop can be considered. Since this model allows a determination of the two opposing forces, a full theory of how and when nuclei will fission can be developed. This simple model predicts the macroscopic features of fission for heavy nuclei quite well. However, it misses many of the details that are related to more subtle effects like nuclear orbitals and spin-orbit effects.

The nuclear shell model builds upon the work of the liquid drop model, modeling these more subtle effects by treating them as deviations from the liquid drop model. The nuclear shell model is akin to the more famous electron orbital model from atomic physics. In both of these models, as more constituents are added to the system they arrange themselves in certain patterns. In particular, no two members of a single system can have the same quantum state. This is known as the Pauli exclusion
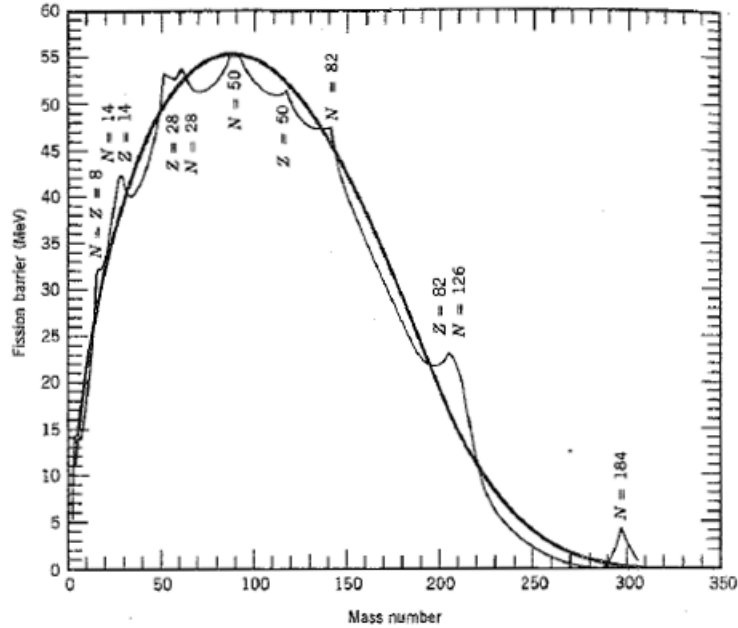
Figure 1.5: Predictions for the fission barrier in the nuclear shell model (light line) and the liquid drop model (heavy line). Image from [1].

principle. Due to this, there are various sets of possible quantum numbers, which are known as orbitals. These 'Pauli-exclusion orbitals' can be further split into finer orbitals by spin-orbit interactions. Orbitals are the vanguard to the appearance of 'magic numbers'. When an orbital is exactly filled, the nucleus will be more stable than if the orbital is incomplete. To fill an orbital takes a precise integer number of nucleons, so when the number of nucleons is equal to one of the so-called magic numbers nuclear stability increases. **Figure 1.5** shows the consequences of the shell model, with the lighter line being the shell model predictions for the fission barrier height shown next to the thick line of the liquid drop model. For magic numbers, the binding energy per nucleon spikes, making any decay channels that remove a nucleon less likely. The first seven numbers most commonly referred to as magic numbers are: 2, 8, 20, 28, 50, 82, and 126. In **Figure 1.5**, we see that when the nucleon value (N) is equal to one of these magic numbers, the fission barrier increases beyond the prediction of the liquid drop model. This makes fission much less likely for nuclei with these nucleon numbers.

The shell model also modifies the shape of the fission barrier. In the liquid drop model, the fission barrier is a single 'hump' in potential when viewed in terms of either deformation or nuclear separation. When including the shell effects, the fission barrier may have multiple 'humps' when viewed as a function of deformation. An example of this is shown in **Figure 1.6**. For uranium, there are two 'humps' in the nuclear potential. The shell model also introduces a few other interesting points.

- The stable point for uranium is not spherical in shape. In **Figure 1.6**, the ground-state well is at some appreciable deformation marked as ϵ_1.

- In order to undergo a normal neutron induced fission, the energy gained by absorbing a neutron must be taller than the first fission barrier, which is usually the higher barrier.

- There are also other types of fission which become possible with these effects included. Sub-barrier fission occurs when the energy gained by neutron capture is high enough to make penetrating the first barrier through quantum tunneling possible, and is also high enough to overcome the second barrier.

- Fission isomers are nuclei that are 'trapped' in the second well and cannot decay to the ground state via gamma emission due to the barrier at ϵ_1. These are nuclei that are distorted into an elongated shape finding a semi-stable configuration.

- Isomer fission occurs due to quantum tunneling through the barrier at ϵ_{11}, or through excitation of the nucleus.

- Spontaneous fission is still possible from the first well, but is quite suppressed due to the wide nature of the barrier at the ground state energy level.

The diagrams of the nuclear shape in **Figure 1.6** show the approximate nuclear shape at each feature in the potential spectrum. The saddle point occurs at the
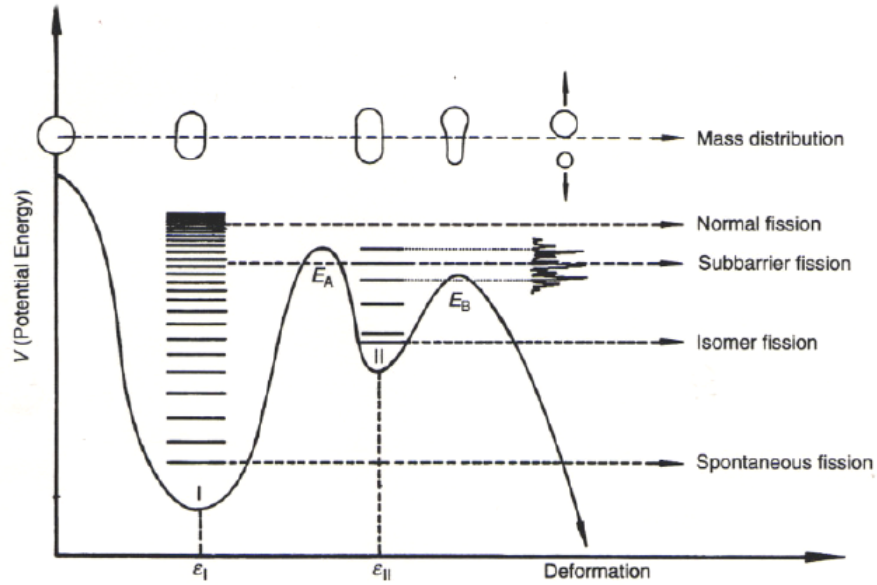
Figure 1.6: Fission barrier shape with shell model corrections. Note the change in x-axis to nuclear deformation. Image from [6].

second maxima, with scission occurring once the deformation is large enough that the nucleus has escaped the whole barrier.

1.1.2 Experimental Goals

This work will not have much direct connection to the models described in the previous section. However, the calculations that this work does connect with are built upon the results of the shell model. Since this work is concerned with the more practical values associated with neutron-induced fission, a practical guide to fission warrants some discussion. Neutron-induced fission can be thought of in a three step process.

1. A neutron is captured by the target nucleus. Though capturing thermal neutrons is more likely, captures can occur for fast neutrons as well. This causes the nucleus to become one atomic unit heavier, and to become unstable.

2. The nucleus splits into two fragments. These do not have to be of equal mass,

10

and in general are not. These fragments are, in general, not in a stable state.

3. The new fission fragments attempt to reach a stable state by shedding neutrons. These neutrons are released within a few femtoseconds of the fission event and are known as prompt fission neutrons.

There is a possible fourth step, in which neutrons are released after one of the fragments decays in a manner that is not releasing neutrons, such as β-decay. These are known as delayed neutrons, and do not factor into this work.

Steps 1 and 2 are mostly determined by the models discussed above, as the fission rate and the instability associated with the capture are questions of the nucleus itself. However, the prompt fission neutrons are a separate entity that require their own model. The prompt fission neutrons are produced by the newly formed fragment as it attempts to reach the smallest amount of deformation. Since the fragment will be distorted upon production, the nucleons will rearrange themselves into a less deformed state. This produces excess energy, which opens the removal of neutrons as a decay channel. This occurs 10^{-15} seconds after scission.

There are three values of particular interest for these neutrons: how they're distributed in the solid angle, the energy of the prompt neutrons, and the number of neutrons released per fission (multiplicity). B. C. Diven, H. C. Martin, R. F. Taschek, and J. Terrell measured the neutron multiplicity in 1956 [7]. **Figure 1.7** shows the characteristic distribution for prompt fission neutrons. The distribution about the mean is the same for nearly all fissile isotopes, however the mean value is isotope dependent. The angular distribution of these neutron events is also fairly well measured in the center of mass frame, with angle relative-to-fragment data being collected since 1952 [8].

The energy distribution is of interest for this work. A model for the prompt fission neutron spectrum has been developed by Madland and Nix and is known as
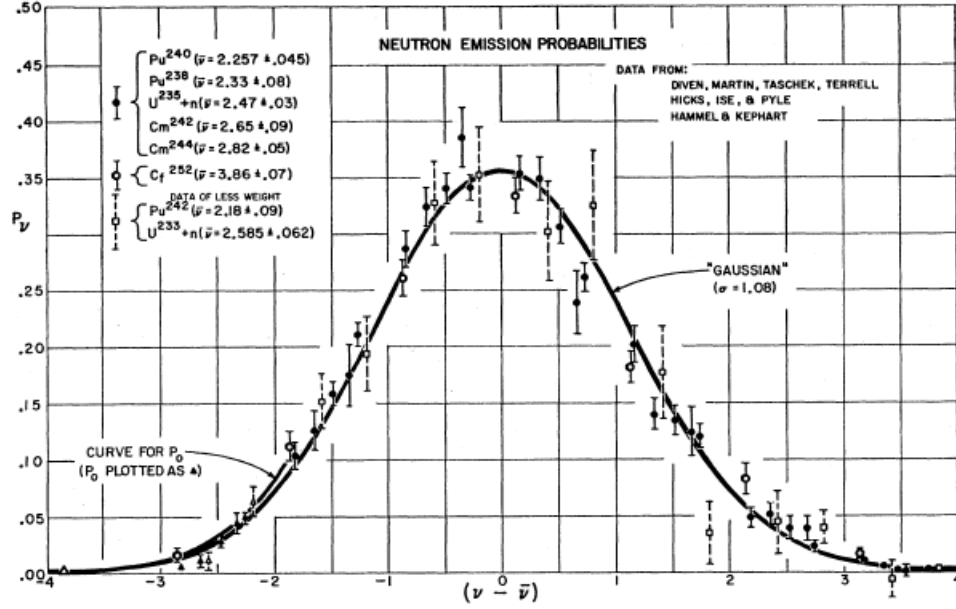
Figure 1.7: Prompt fission neutron multiplicity for various isotopes. Image from [7].

the 'Los Alamos model'[9]. This model starts with the basis of standard nuclear evap-
oration theory. In evaporation theory, the newly formed fission fragment is treated
as a compound nucleus. The compound nucleus has some associated energy, which
is treated as a temperature. Particles ejected from the nucleus are modeled as 'evap-
orating' from a hot surface. Using the Los Alamos model to predict prompt fission
neutron energy starts with a nucleus that has a temperature (T) sampled from a prob-
ability distribution $P(T)$[§]. This distribution varies depending on the nucleus type but
is generally defined relative to some maximum temperature (T_m), such that:

$$P(T) = \frac{2T}{T_m^2}; \quad 0 \leq T \leq T_m \tag{1.8}$$

With this temperature sampled, a center-of-mass distribution for neutron energy can
be constructed for the evaporated, or outgoing, neutron.

$$\Gamma(\epsilon, T) = q(T) \cdot \sigma_c(\epsilon) \cdot \epsilon \cdot exp[-\frac{\epsilon}{T}] \tag{1.9}$$

In this equation, T is the residual fragment temperature, σ_c is the compound nuclear
cross section, q(T) is a normalization factor, and ϵ is the energy of the neutron.

[§]The formalism for this discussion is borrowed from [10].

12

The compound nuclear cross section is the cross section for forming the nucleus in question via any nuclear reaction. $\Gamma(\epsilon, T)$ needs to be converted to the laboratory frame to determine the visible prompt fission neutron spectrum. In order to determine the distribution for all neutron energies, center of mass neutron energy and residual fragment temperatures must be integrated over.

$$N(E, E_f, \sigma_c) = \frac{1}{2\sqrt{E_f} \cdot T_m^2} \int_{(\sqrt{E}-\sqrt{E_f})^2}^{(\sqrt{E}+\sqrt{E_f})^2} \sigma_c(\epsilon) \cdot \sqrt{\epsilon} \cdot d\epsilon \cdot$$

$$\int_0^{T_m} q(T) \cdot T \cdot exp[-\frac{\epsilon}{T}] \cdot dT \qquad (1.10)$$

This formulation includes an implied average over the light (L) and heavy (H) fragment neutron yields, such that:

$$N(E) = \frac{1}{2}[N(E, E_f^L, \sigma_c^L) + N(E, E_f^H, \sigma_c^H)] \qquad (1.11)$$

All values in this equation are the same as their former definitions with the addition of E_f which is the average kinetic energy per nucleon and E which is the laboratory frame prompt neutron energy. The two main inputs that determine the prompt neutron spectrum are the maximum fragment temperature, which determines the center of mass energy of the nucleon, and the average kinetic energy per nucleon. The parameters are adjustable to match available data. Trends within available data can be used to make predictions for similar isotopes with no data. This model has been verified with a great deal of data since its inception and is still used today in most evaluations, including ENDF[11]. ENDF stands for 'Evaluated Nuclear Data Files', and contains evaluations of data to create 'standardized values' for nuclear information.

This work focused on studying steps 1 and 3 of the neutron-induced fission process. For ^{235}U(n,f), we measured the prompt fission neutron spectrum below 1 MeV for fast incident neutrons. Though there is a great deal of data about the fission neutron spectrum for thermal beam neutrons, there is almost no prompt neutron data

below 1 MeV for fast-neutron induced fission. At present, the Los Alamos model is used for evaluations of the prompt fission neutron spectrum, and though it agrees well with data collected above 1 MeV, there are no data to compare with below 1 MeV. This is due to the challenge of detecting $\sim 0.5\text{-}1$ MeV neutrons. These neutrons are difficult to distinguish from gamma rays and other background events, which makes a direct measurement a technical challenge. In order to make this measurement, we designed a new type of neutron detector which has the ability to separate the prompt fission neutrons from backgrounds.

For ^{238}U we focused on the neutron-induced fission interaction rate, as the cross section is not well-known for incident neutrons above 100 MeV. The goal of this measurement was to add data to this sparsely populated region, further constraining the neutron interaction standard. Since ^{238}U(n,f) is often used as flux monitor for fast neutron beams, it should be well-measured across all energy regions in order to produce an accurate measurement of the beam flux.

Chapter 2: Detector Design and Construction

2.1 Low Energy Neutron Detection

2.1.1 Scintillation and Pulse Shape Discrimination

The problem of detecting fast neutrons was solved decades ago by using materials doped with a fluorescing additive. Neutrons, due to their lack of charge, do not interact with materials via the Coulomb force. Thus, it is required that the neutrons scatter against other particles in order to be detected. This recoil particle can be detected if it excites the material via ionization, which produces light. This requirement implies that, in order to be detected, the neutron must scatter against a charged particle. The light produced by ionization can then be collected using a photomultiplier tube (PMT), which is a device that creates analogue electrical pulses when light is incident upon it. This technique, known as scintillation, was pioneered in 1903 by Sir William Crookes[12], and extended to plastic based materials by John Birks in 1964[13].

Detecting neutrons below 1 MeV is a unique challenge, as these traditional detectors fail as energies decrease below 1 MeV. This failure is not directly related to neutron detection, but rather that scintillation detectors are also adept at detecting gamma rays. At energies above 1 MeV, it is possible to discriminate between gamma rays and neutrons using a technique known as 'pulse shape discrimination.' Pulse shape discrimination relies on the fact that the pulses formed by gamma rays in the material have a different shape than those created by neutron interactions. In general, gamma rays create pulses that have a sharp leading edge and decay on the scale of a few nanoseconds in many materials. Neutron-induced pulses also have a sharp leading edge, but have a longer decay time. By comparing the total charge within
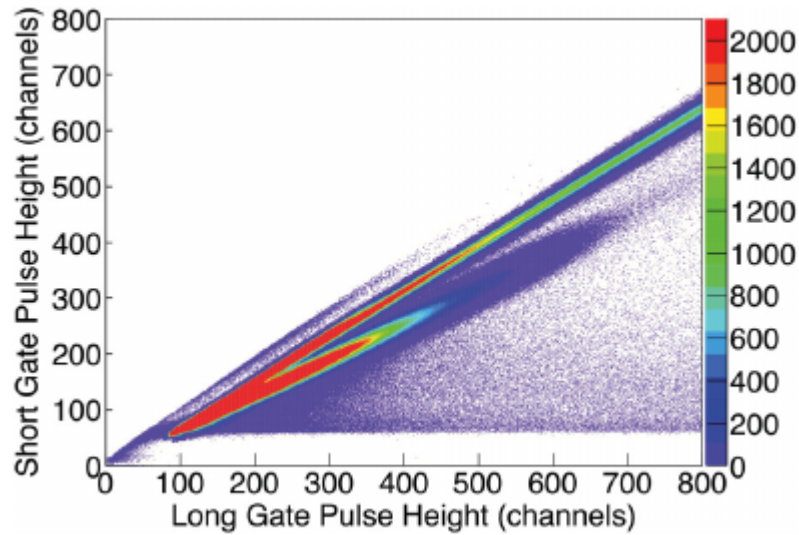
Figure 2.1: Pulse shape discrimination at low energies. On the horizontal axis is the total charge contained within the pulse, on the vertical axis is the charge contained within the first few nanoseconds of the pulse. The gamma rays (top band) have a slope of ~ 1. The neutrons (bottom band) have a smaller portion of their total charge in the leading edge. Image from [14].

the pulse to the charge contained within the decaying portion of the pulse (or, in an alternative method, the leading edge), different charge distribution ratios occur for neutrons and gamma rays. **Figure 2.1** demonstrates how pulse shape discrimination can separate gamma rays and neutrons.

As seen in **Figure 2.1**, this technique works well at higher energies. However, eventually the two 'bands' of particles merge together as the energy decreases. At these energies, it is no longer possible to distinguish neutron from gamma ray. Gamma rays are common particles and are also often byproducts of producing free neutrons, so the detectors are essentially awash in both neutrons and gamma rays, making neutron measurements no longer feasible.

It should also be noted that not all scintillating materials allow for pulse shape discrimination, just as not all scintillating materials have the same light production properties. The majority of this work will be concerned with plastic scintillators which do not allow for pulse shape discrimination due to the overall 'fastness' of the material in regards to light decays. Another common type of scintillator is a

liquid scintillator, which is quite similar to plastic scintillators. Liquid scintillators are created by dissolving an organic scintillator into a solvent, just like plastic scintillators, however in liquid scintillators this solvent cannot be polymerized. Though there is a wide variety of liquid scintillators, a particularly interesting type has a larger light output than plastic scintillators but a decay time that is $\sim 33\%$ longer. This allows for pulse shape discrimination, but has a slower overall reaction time than plastic. A liquid scinitillation detector of this type was used for **Figure 2.1**.

The primary interaction for neutrons in our energy region ($0.3 < T_n < 5$ MeV) is to scatter against protons elastically. Protons are an ionizing particle and can excite the fluorescing agent to produce light. Thus, a material with an abundance of ^{1}H is ideal for high efficiency detection of fast neutrons. Plastic scintillators fit this bill, as they are primarily made of ^{1}H and ^{12}C. **Figure 2.2** and **Figure 2.3** show the neutron cross sections for both ^{1}H (protons) and ^{12}C. These have cross sections on the order of barns, which makes the combination of these an excellent candidate for neutron interactions. As a quick example, we can look at a neutron attenuation calculation. Due to oversimplification for this calculation, the attenuation rate will be lower than the performance of an actual detector, but it should be a good first-order approximation. Assuming neutrons of energy 0.5 MeV are incident upon a 3 cm thick target of a typical plastic scintillator, we can look at the attenuation fraction of incoming neutrons.

$$f = 1 - e^{-\frac{A_0 \rho \sigma t}{M}} \sim 0.17 \tag{2.1}$$

where A_0 is Avogadro's constant, ρ is the density of the material, σ is the cross section for the reactions of interest (in this case, ^{12}C-total and n-p elastic), t is the thickness, and M is the molar mass of the material. While a 17% attenuation of incoming neutrons seems low at first glance, this efficiency is on par with other traditional neutron detectors such as liquid scintillators and organic crystal scintillators.
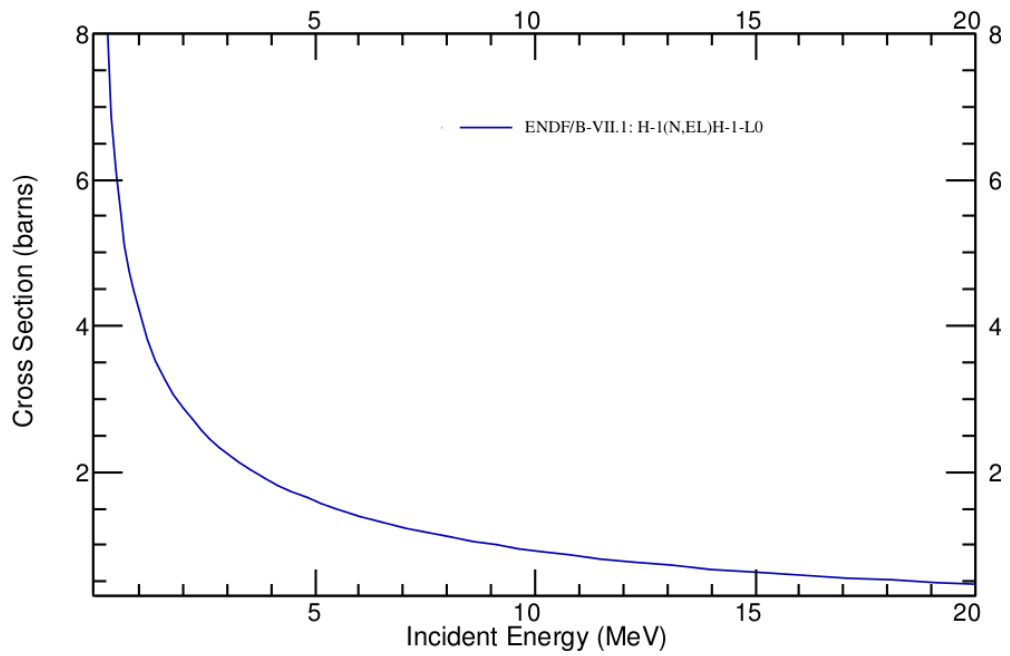
Figure 2.2: The cross section for n-p elastic scattering, as tabulated by the National Nuclear Data Center [15].
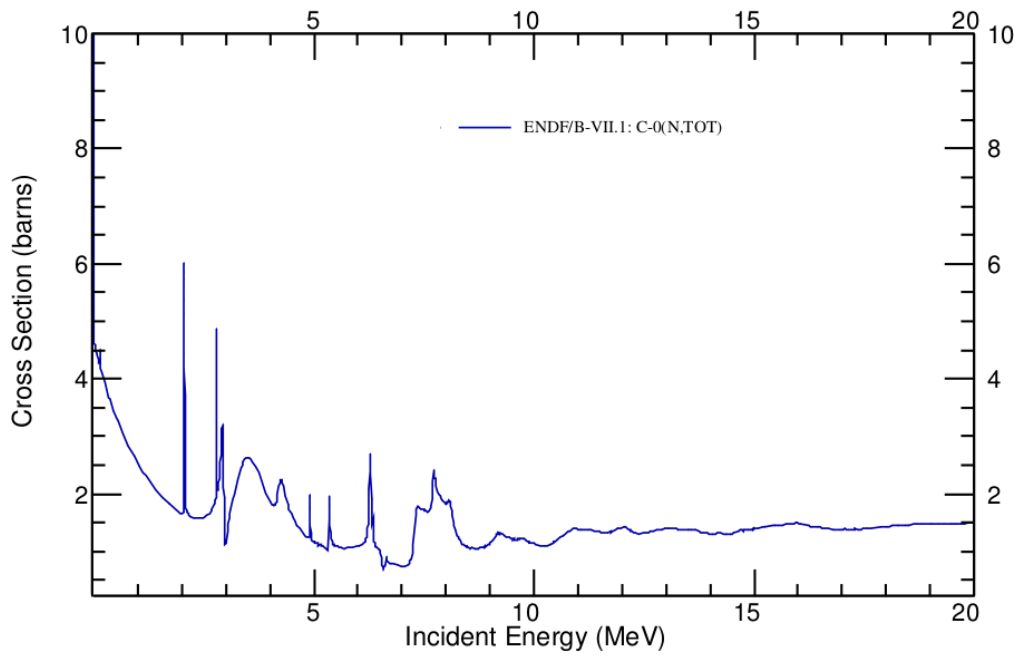
Figure 2.3: The total cross section for n-^{12}C scattering, as tabulated by the National Nuclear Data Center [15].

2.1.2 Detector Design

When constructing neutron detection systems, there are multiple factors to consider.

- What is the efficiency in the energy range of interest?

- What size solid angle must your detector subtend?

- How will I identify particles of interest?

- Is the decay time of the detector short enough for the experimental rate?

- What is the cost of building a detector?

The goal for this project was to create a detector that would be efficient in the region $0.3 < T_n < 5$ MeV while also maintaining a solid angle coverage area of ~ 100 msr at 1 m. The natural choice for this is plastic scintillator, because of the reasons discussed in **Section 2.1.1**, as well as its fast decay time and relatively low-cost.

By tweaking various properties of the scintillating plastic, such as polymer compositions or the fluorescing agent, scintillation properties can vary, even amongst similar plastics. This topic is covered in detail in [16], including a table that lists the details of many different common scintillating materials. In the end, we chose a plastic that has a fast response time, a high scintillation yield (light output), and a high hydrogen proportion in its chemical composition. This is a plastic produced by Saint-Gobain, called BC-408[17].

As part of this work, a unique detector design has been created that allows for a different method of discriminating between particles in this challenging energy region. The uniqueness in this design lies in the chosen geometry for the plastic. As can be seen in **Equation 2.1**, the thicker the plastic, the higher the chance of a neutron interaction. Instead of using the traditional method of one large layer of plastic, we use many thin layers of plastic. We then stack these thin sheets together to create a
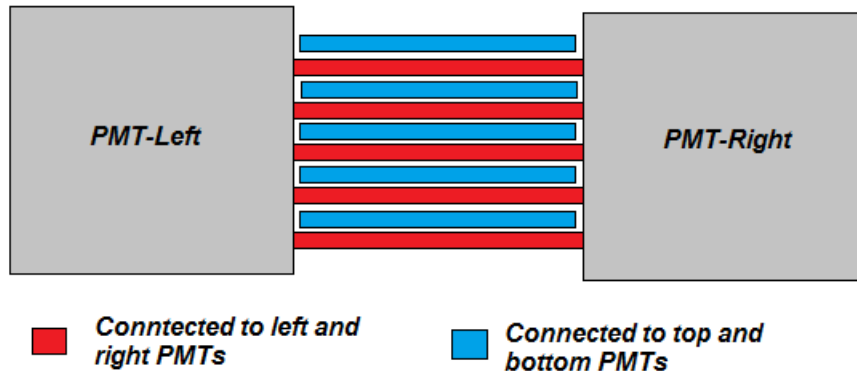
Figure 2.4: Sketch demonstrating the detector design. The red layers are connected to the horizontal pair of PMTs in the diagram, while the blue layers run to a second pair of PMTs (not shown). These adjacent layers are optically isolated from one another, such that an 'odd numbered' layer will never share light with an 'even numbered' layer.

single, thick active region. In the case of all prototypes discussed here, there are 10 total layers of plastic, giving a total thickness of 3 cm.

Each layer of plastic is 3 mm in thickness and is wrapped in Teflon tape to optically isolate it from adjacent layers in the stack. We then collect the light from every layer for analysis but separate the light collected by the even layers into one PMT and odd layers into another PMT, as shown in **Figure 2.4**. The basis for this design is the difference between the range of protons and electrons in the proton and carbon rich scintillator. We can calculate the range for these particles by first calculating the density of particles in our material. The atomic makeup of BC-408 is 52.5% hydrogen and 47.5% carbon.

$$M = .525 * 1.008 \, g \cdot mol^{-1} + .475 * 12.0107 \, g \cdot mol^{-1} \quad (2.2)$$

$$= 62.202 \, g \cdot mol^{-1}$$

This gives an overall density of 1.032 $g \cdot cm^{-3}$. With this density, we can calculate the mean range for each type of particle, given a known stopping power $\left(\frac{dE}{dx}\right)$ for the material. The stopping power is calculated using the Bethe formula, but is tabulated

for many materials. For 2 MeV protons in our scintillator:

$$R_p(T_p) = \int_0^{T_p} (-\frac{dE}{dx}\rho)^{-1}\, \mathrm{d}E \tag{2.3}$$

$$R_p(2\text{MeV}) = \int_0^2 (148.4*1.032)^{-1}\, \mathrm{d}E^*$$

$$R_p = 130.59\ \mu m$$

Similarly, for 1 MeV electrons:

$$R_e(1\text{MeV}) = \int_0^1 (2.64*1.032)^{-1}\, \mathrm{d}E^\dagger \tag{2.4}$$

$$R_e = 3.67\ \text{mm}$$

Since the layers in this detector are 3 mm in thickness, a typical neutron interaction event will only create light in a single layer, due to the dominance of n-p elastic interactions. In contrast, a typical gamma ray interaction will scatter from an electron, which will travel more than 3 mm, producing light in two adjacent layers. This acts as our particle identification method. In the analysis, we can tag which events had light in multiple PMTs (multi-layer), and which were single-layer events. Single-layer events are typically neutrons and multi-layer events are typically gamma rays. There is, of course, a limit to the accuracy of this identification method, however with proper simulation this can be corrected for. By combining this method with the excellent timing resolution of plastic scintillator, we are able to select out events of interest from the 'sea' of background particles in our energy region. The beauty of this method is that, as the neutron kinetic energy decreases, the method becomes more reliable since the mean distance traveled by the proton becomes smaller.

2.2 Proof of Concept Prototype

The concept of sorting based on layered interactions was simulated in 2009 by Khayrullo Shoniyozov (University of Kentucky). This simulation was completed via Monte Carlo

---

*Value for proton stopping power found in [18]

†Value for electron stopping power found in ESTAR database[19]
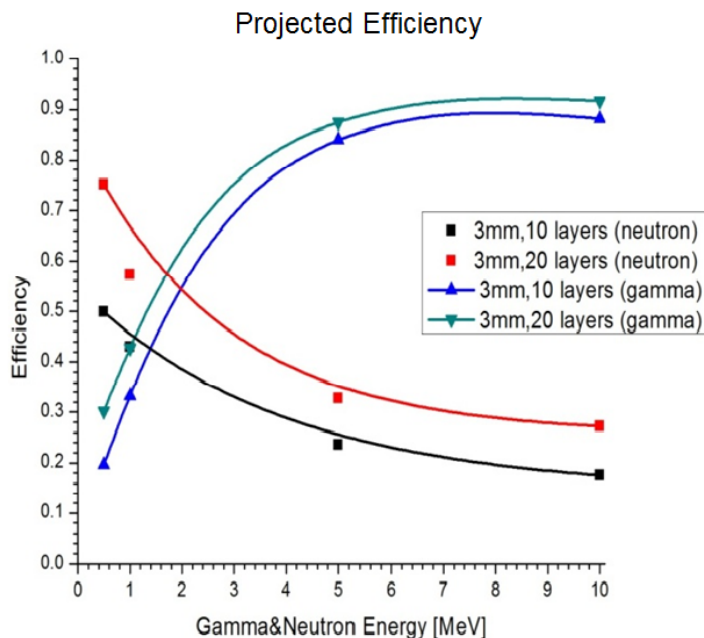
Figure 2.5: A plot of projected detection efficiency for various arrangements of plastic scintillator. Each curve is marked by the type of particle and the number of 3 mm layers of plastic scintillator. In the energy region of interest, neutrons have a higher detection efficiency. Further discussion of this work can be found in **Section 2.2**. Image from [20].

in the GEANT4 toolkit, by 'building' a calorimeter made of two materials: layers of plastic scintillator and layers of air. Neutrons and gamma rays of various energies were fired into the calorimeter where information regarding the amount of energy deposited in each layer was recorded. Shoniyozov was able to create efficiency curves from this simulation with free variables of plastic layer thickness, total number of layers, and spacing between layers. These efficiency curves predict a gamma rejection ability on the order of $\sim 20\%$ at 0.5 MeV using just the layer technique, as seen in **Figures 2.5** and **2.6**. Combined with traditional techniques such as time of flight (ToF) identification, our particle identification is sufficient to make measurements in previously unmeasured regions of neutron kinetic energy, as we can correctly remove $\sim 20\%$ of the gamma ray background that halted previous measurements.

Due to the results of the simulations, a small prototype detector was constructed in 2010. This detector was designed by Michael Kovash and though not used directly in this experiment, it laid the groundwork for the detectors that were. This detector

22
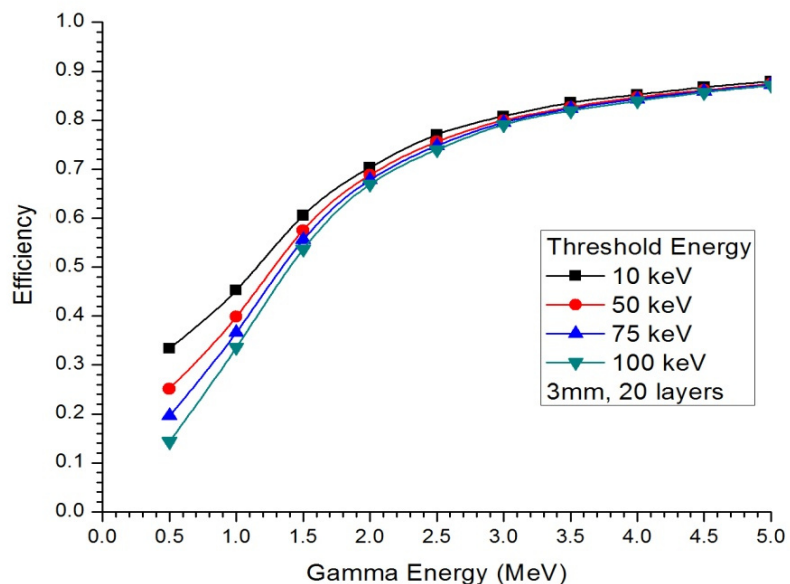
Figure 2.6: The results of the simulation by Shoniyozov. This shows that the layered geometry does have the ability to identify particle types, which allows removal of gamma ray backgrounds. As the gamma ray energy goes higher, there is a higher chance to reject it. Even below 1 MeV the rejection rate is high enough to make neutron measurements possible. Image from [20].

was made of 10 thin layers of scintillator. Each of these layers was 12 cm × 10 cm × 3 mm. However, due to the construction, the effective active area of each was 10 cm × 10 cm. As shown in the sketch in **Figure 2.4**, these layers were arranged such that half of the layers were read by one pair of PMTs, while the other half were read by a separate pair.

This introduces another concept that should be considered. The quantity of light generated in plastic scintillator has a strong positive correlation to incoming particle energy. For this scintillator, there are ∼ 10000 photons/MeV and the collection efficiency per photoelectron is lower than 25%, due to the quantum efficiency of the PMT. Given the overall efficiency of collection, detecting these events requires a threshold on the order of a single photoelectron. One of the benefits of attaching two PMTs to each active layer is that it allows us to overcome detector noise and set the thresholds at this level. If each PMT is seeing a small random dark current, we can
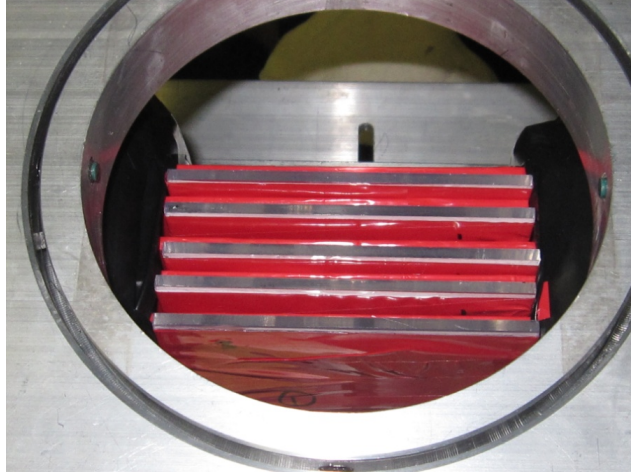
Figure 2.7: The interior of the small-cube prototype constructed in 2010. Each of the 'red' sheets is a piece of plastic scintillator. 5 run horizontally, connecting to the access points via the cylindrical light guides. The other 5 run vertically into an identical setup (removed for picture).

link the two in the analysis and only analyze events where both PMTs have a response within the same ~ 100 ns window. This allows us to set the analysis threshold at the dark current level (single photoelectron), but by only analyzing events where both PMTs have light at the same time, we reject the dark current itself. This method lowers the thresholds to a level that matches the smallest possible response of the PMT, so we do not miss any events that create only a small amount of light in the plastic.

The thin layered plastic, and pair of PMTs per layer are the two major elements that make this detector design unique. These requirements introduce an engineering challenge: how does one collect light from every other layer, and at two different points on the scintillator? In the detector designed by Kovash, he created a cubic aluminum frame with four access points, creating essentially a horizontal read-out plane and a vertical read-out plane. This interior geometry can be seen in **Figure 2.7** and the the exterior frame in **Figure 2.8**.

This prototype was used at WNR-LANSCE at the Los Alamos National Laboratory in an experiment to measure n-p elastic cross section with high precision[14]. This allowed us to essentially bench test the detection capabilities and particle identi-

24
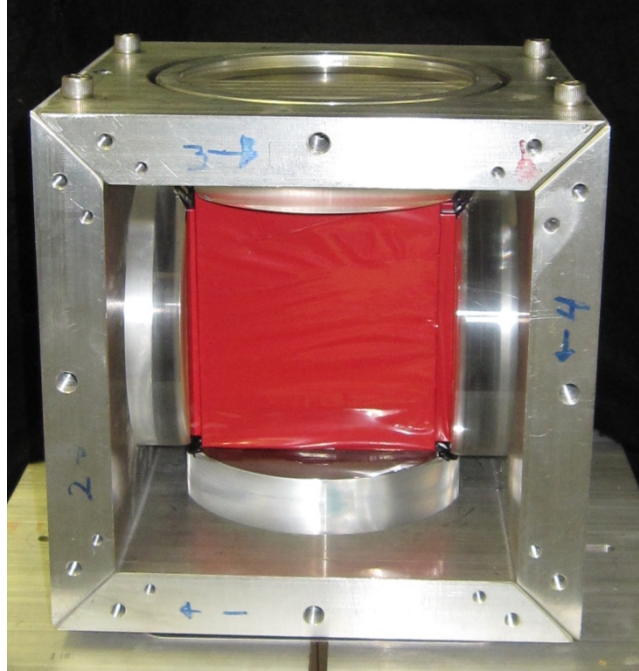
Figure 2.8: The exterior of the 2010 prototype as setup at the Weapons Neutron Research Facility in Los Alamos Neutron Science Center.

fication abilities of the detector. **Figure 2.9** shows one of these plots, which demonstrates the gamma rejection capabilities of the detector.

2.3 Large Solid Angle Prototype Design and Construction

2.3.1 GEANT4 Light Guide Simulations

The initial prototype demonstrated that this method of particle identification is viable. The next step was to increase the solid angle of the detector, as the goal of this project was to produce a detector with a solid angle on the order of ~ 100 msr at 1 m from the neutron source. To achieve this goal, we designed a detector with 1 m long plastic scintillator layers that are 10 cm wide. In the detector, there are 10 of these layers stacked directly upon one another. The largest engineering challenge is designing a method to extract the light from alternating layers with high efficiency, while maintaining a small geometric footprint for the detector and its enclosure. To investigate possible solutions, we used GEANT4 to simulate the optical properties of
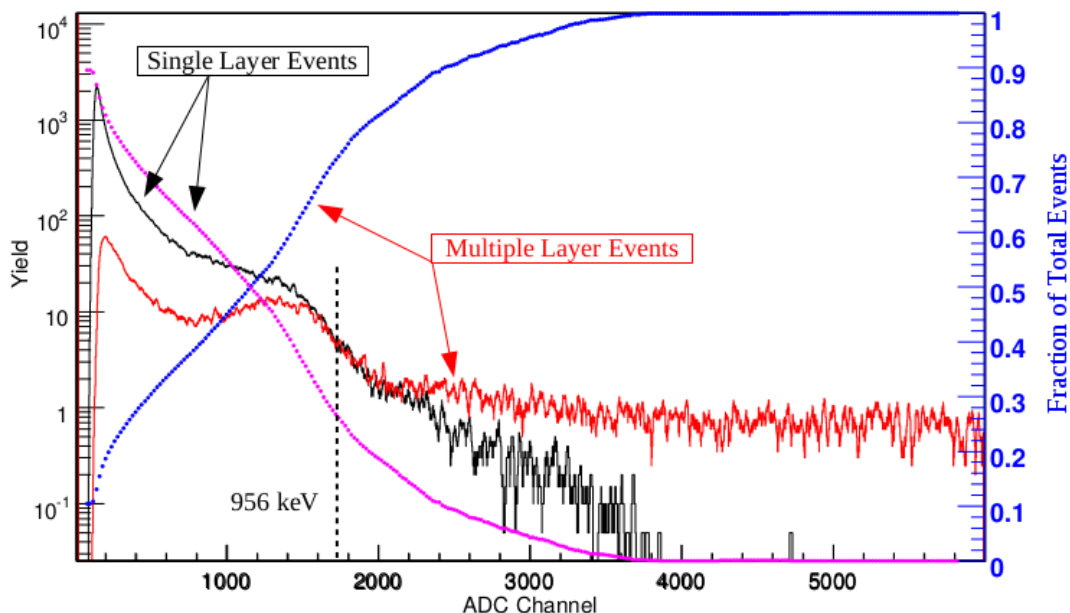
Figure 2.9: All lines show data from a single calibration run with a ^{60}Co source, without background subtraction. In red are those events that interact in multiple layers, which are most likely to be gamma ray events. In black are events that only interacted in one layer. In blue is the multiple layer curve, scaled to percentage of total events seen at that energy (right axis). Magenta is the same, but for single layers. Comparing the black line to the red, we see that the characteristic 'bump' from the source is still visible, but has been reduced in relative size. The blue line shows the upper limit for percentage of events properly identified as multiple layer events, and is in rough agreement with **Figure 2.5**.

various light extraction techniques.

We built a series of different shapes in the GEANT 'optical physics' framework, all made from the same material. This material was an acrylic light guide that is also made by Saint-Gobain, known as BC800[17]. The two shapes that were submitted to extensive testing are demonstrated in **Figures 2.10** and **2.11**. The guides needed to separate from the center line of the scintillator by 3 inches to allow for the PMTs to sit beside one another. Optical photons were generated at one end of the guide, with random initial conditions, such as position on the input plane and direction. These input values were biased to only allow events that could realistically occur, given the geometry of the detector. The ratio of the number 'shot' versus the number 'collected' at the other end determined the efficiency for each shape. As part of the
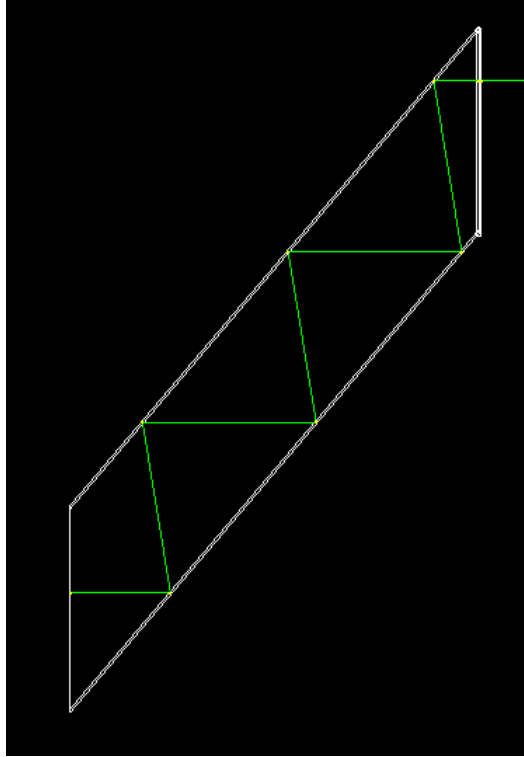
Figure 2.10: An angled light guide as designed in GEANT4. Three versions of this shape were tested, with $\theta = (22.39°, 30.53°, 49.64°)$ and an associated length of l=(20 cm, 15 cm, 10 cm), respectively. The green line is an example photon trajectory within the material.

simulation, each light guide was given surface optical properties that matched the properties of a polished surface wrapped in white Teflon tape.

The results for this simulation can be found in **Table 2.1**. The title 'Slant short' refers to the slanted light guide design 10 cm in length, the middle to the 15 cm piece, and so on. These light guides work almost exclusively on the principle of total internal reflection. Thus, this result is a balancing act between having a shallow enough angle to maintain total internal reflection for the majority of optical photons and having a light guide short enough that the bulk absorption properties of the plastic do not attenuate the light to an unusable level. In this result, the middle length slanted design outperforms all other designs. However, the difference between the slanted designs is on the 1% level, so any of these designs is viable. Due to our desire to keep the footprint of the detector frame as small as possible, a shorter guide is desirable
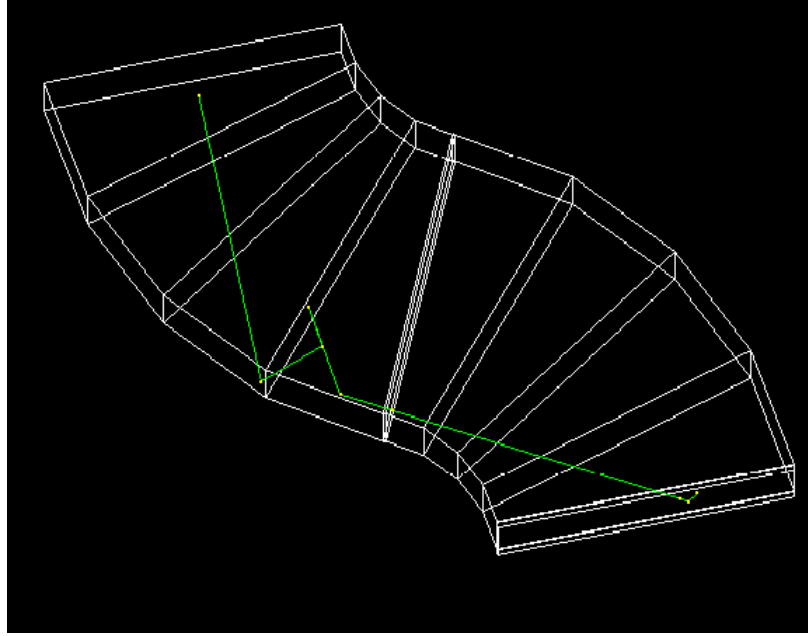
Figure 2.11: An 'S' shaped light guide as designed in GEANT4. The green line is an example photon trajectory within the material.

Table 2.1: The efficiency of each tested light guide shape.

Shape	Efficiency (%)
Slant Short	60
Slant Middle	61
Slant Long	58
'S' Shape	25

and also practical.

The 'S' shaped guide did not perform well at all. This was a bit unexpected, as this type of shape has been used before in large-scale scintillation detectors. The failure of this design can be linked to the geometry of the scintillation plane. In this design, the bend in the light guide is in the plane of the scintillator, instead of bending along the thinnest dimension of the guide. Thomas Massam [21] did a calculation that explains this, where he linked the width of the guide in the plane of the bend, as well as the radius of the bend, to the overall efficiency of the guide. His result can be seen in **Figure 2.12**. For the 'S' design, W/R = 1 which is far from ideal and
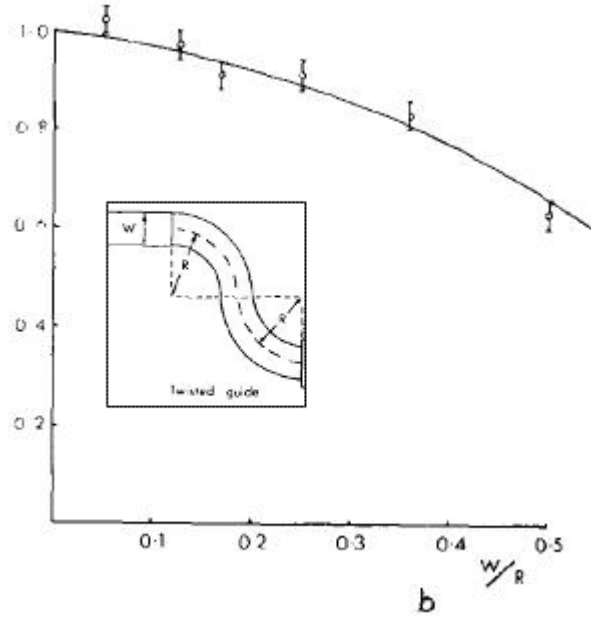
Figure 2.12: This plot demonstrates the link between a bend in a light guide and its overall efficiency. W is the thickness of the light guide in the plane of the bend radius. R is the radius of the bend.[21]

accounts for the low collection efficiency.

Massam's work also became important as we designed another light guide to make the footprint of the detector smaller. The PMT model we used is the Hamamatsu R1250[22], which is 18 inches in length once fully assembled. We chose to build a light guide 'arc' that would bend the light into a direction 90° from the plane of the detector, such that the 18 inches of extra length would not be added to the already >1 m long direction of the bar. To do this, we used Massam's result as a guide and designed a light guide piece that is 38 mm in thickness and has a 3 inch radius to its bend. This piece takes the light from the five slanted light guide pieces connecting to the same PMT and bends it 90° out of plane. The piece's geometry is demonstrated in **Figure 2.13**. It has $W/R = 0.39$, which means it will be $\sim 80\%$ efficient, before being wrapped in Teflon. The full GEANT simulation shows an efficiency of 98%, as seen in **Figure 2.14**. This difference is fully explained by the addition of Teflon and the difference in geometry: Massam's work has two curves, our guide only has one
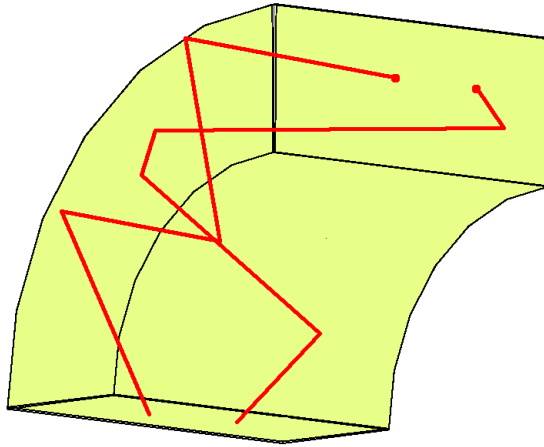
Figure 2.13: A demonstration of the light guide 'arc' piece that turns the light out of plane. This is the geometry as it was built in GEANT4. The red lines are two sample photon trajectories.

curve.

This completes the full geometry of the design. When the pieces are placed together in full, we have a design that looks like **Figure 2.15**. The cylindrical pieces on the end of the arc guides have not been discussed previously, but act as light mixers to converter the light guide shape to match with our chosen PMT, which has a circular input face. These are nearly perfectly efficient.

2.3.2 Bench Testing a Single Layer

Before building a full detector, we constructed an experiment to test the characteristics of the plastic. For this setup, we connected a single layer of scintillator to two of the slanted light guides; one on each end. To these light guides, we attached PMTs directly which bypassed the light guide arc for this bench test. The elongated nature of the scintillation detector presents two challenges:

- Is the pulse height constant across the whole length of the bar?
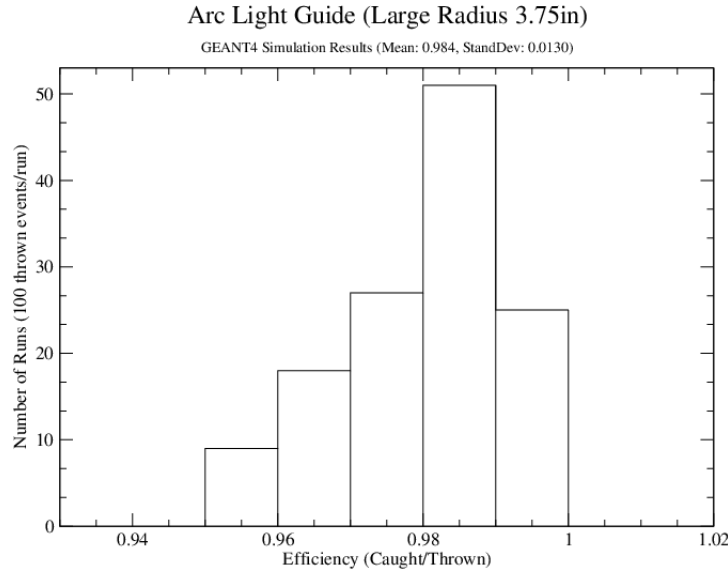
Figure 2.14: The result of a GEANT4 simulation to determine the efficiency of the light guide 'arc.' Optical photons were generated with random initial conditions at one end of the guide and the percentage that reached the other end is considered the efficiency. Each batch of 100 has a calculated efficiency. The number of runs with a given efficiency is on the y-axis.
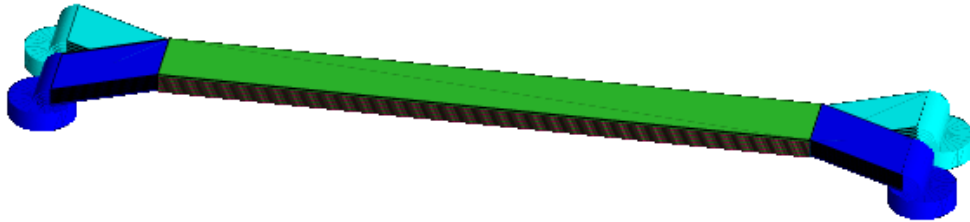
Figure 2.15: A GEANT mock-up of the full detector geometry. The 1 m long portion is the active scintillation region. The slanted pieces and the arcs on the end are made of BC800 and act as light guides. The dark blue connects to the green (or odd) scintillation layers. The light blue to the pink (or even) scintillation layers. The cylindrical pieces are also made of BC800 and act as a converter to match the PMT input face.

- Can we locate where in the bar the particle interaction occurred?

The single layer test is sufficient to test both of these questions. To do this, we used a gamma source placed in a 4 inch long lead collimator at different locations along the scintillator bar, which was sealed against outside light. We collected pulse-height (ADC) and timing (TDC) data for pulses at each end of the scintillator.

31
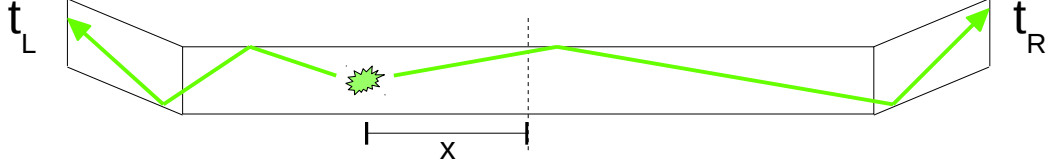
Figure 2.16: A cartoon demonstrating the macroscopic anatomy of an interaction. 'X' is the displacement from the center of the bar, t_L is the time of arrival for the photons at the left end, and t_R is the time of arrival at the right end. The variables labeled here are used in **Equation 2.5** to determine the location of the interaction in the bar.

With the timing information from each end of the bar, we can construct a time difference between the two tubes. **Figure 2.16** demonstrates why there is a time difference. This time difference can be used to reconstruct the position where the interaction occurred. This does rely on the bar being symmetric across the length mid-point (dashed line in the figure). The diagonal end pieces must be of equal length and angle, such that the light has the same path one each end once it leaves the scintillator. Even with a perfectly symmetric detector, adding diagonal pieces raises the minimum time resolution, as the path to the PMT is elongated and the path length variation is increased. The increase in possible path lengths makes the shortest possible path length less likely, and broadens the distribution of arrival times.

$$\frac{c}{n}\, t_L + x = \frac{c}{n}\, t_R - x$$
$$x = \frac{c}{2n}(t_R - t_L) \tag{2.5}$$

We use the idea that if we convert t_L and t_R into centimeters by using the speed of light in the material, we can use the difference of those distances to extract x. We see that the x-position and the time difference are linearly linked. So, as we move the source along the bar, we should see a linear regression between time difference and source position. The result for this test is found in the left half of **Figure 2.17**.

Similarly, we expect that the location of the interaction along the bar should determine how many photoelectrons are produced in each PMT. The absorption length of the plastic material (which attenuates the light based on flight path length in the plastic) will diminish the pulse-height for events far from the PMT. However,

we can construct a geometric mean pulse-height spectrum from two PMTs viewing the same scintillation layer.

$$\overline{ADC} \;\; = \;\; \sqrt{(ADC_L - Pedestal_L) * (ADC_R - Pedestal_R)^{\ddagger}} \qquad (2.6)$$

We expect that this geometric mean spectrum should remain constant across the length of the bar. This result can be seen on the right side of **Figure 2.17**. Due to the large attenuation of light for events interacting far from one PMT, the threshold for detecting event is set by the PMT furthest from the interaction point. This further necessitates a single photoelectron level threshold in each PMT, which can be acheived with proper hardware calibration. We also see that we are less likely to detect events that occur on the 'edge' of the scintillator, as the light from these events it heavily attenuated. A low energy interaction near the 'edge' of the scintillator may not have light reach the far PMT, which is required to mark the event for analysis. Despite this added complexity, both of the results in **Figure 2.17** demonstrate the expected and desired capabilities of the detector. The asymmetry seen in the right plot of **Figure 2.17** is due to the geometry of this prototype. In this prototype, differently shaped light guides were placed on the opposite ends of the bar to test the relative efficiency of the light guide shapes.

2.3.3 Constructing the Detectors

The BC408 is shipped in large thin sheets of a given thickness. This thickness is accurate to a few percent, as the plastic is cast between two large sheets of glass. From these sheets, we used a computerized milling machine with a high helix bit to cut the plastic to desired specifications. The high helix bit is very important, as the ability to collect the light hinges on total internal reflection. If the surface is not polished, total internal reflection becomes significantly less effective. The high helix

---

‡The pedestal is the value recorded by the ADC when there is no input. Since there is noise in the signal, the ADC never records exactly zero. The pedestal acts as the zero point for each ADC spectrum.
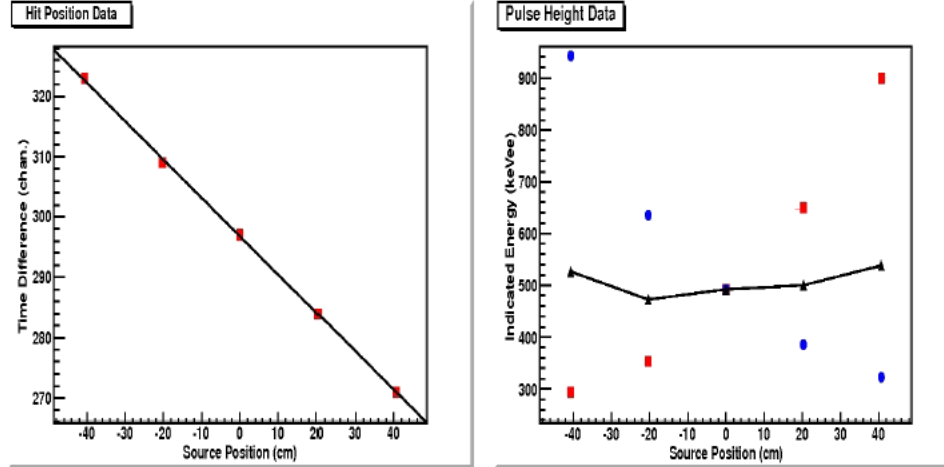
Figure 2.17: *Left:* A plot of end-to-end time difference versus source position. The linear regression shows that we can locate interaction positions using the time difference. *Right:* The ADC spectra recorded at both ends of the bar (blue and red) as well as the geometric mean (black) of these values. The geometric mean is relatively constant across the length of the bar, and demonstrates that a single gain may be used for the entire width of the bar when using the geometric mean.

bit, when sharp and used at a high rotational speed, does very little damage to the remaining edge and minimizes surface crazing, which cannot be removed by polishing the scintillator. Each of these layers, after cut from the sheet, must have all edges re-polished. To do this, we used a rotary hand tool with cotton buffing wheels and two stages of polishing. In the first stage, a small amount of water was placed upon the edge of the plastic and the buffing wheel was passed over it applying light pressure to help smooth out any large abrasions in the surface. For the second stage, we used an aluminum-oxide powder (2 μm particle size) that is made into a paste with water, and applied that to the plastic. We allowed the paste to dry onto the surface of the plastic. Then, using a clean polishing wheel, we buffed the surface with the now dry paste, working back and forth and visually inspecting the plastic to make sure that it achieves a mirror like finish. The final dimensions for the scintillator sheets are 1 m × 10 cm × 3 mm, and there are 10 in the detector.

The same process is applied to the thin, slanted light guides. These are also shipped in a single large, flat sheet. Using the same milling and polishing process, we cut out 20 of these (10 on each end of the scintillator). After the simulations
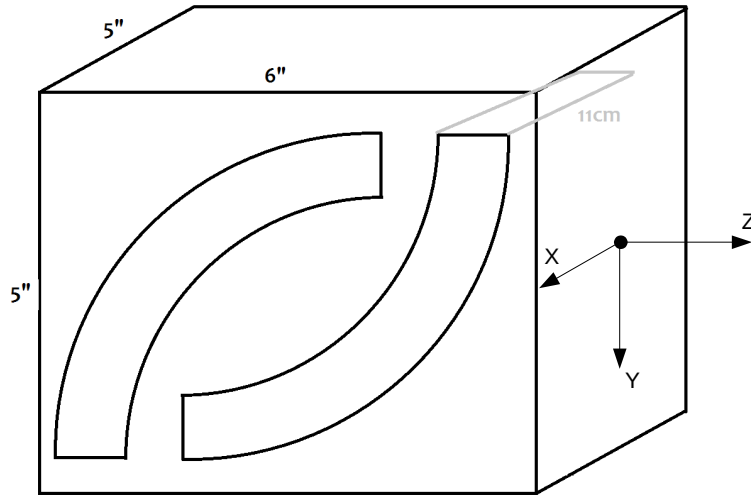
Figure 2.18: A cartoon demonstrating how two light guide arcs were cut out of a single block of plastic.

described in the previous section, it was decided to use a light guide with an angle of 24.2°, which has a corresponding length of 7.606 inches.

The light guide arcs were not so simply created. The design is cut out of a 5 in × 5 in block of BC800, as demonstrated in **Figure 2.18**. However, the milling machine bits were not long enough to cut the 'arc' from the side (x-axis in **Figure 2.18**). The solution was to have the mill do the cut using a vertical stepping technique that allows it to cut down into the plastic and trace the arc out in the 'z' direction. Once the main shape was produced in this manner, we needed to add receptacles to allow the arc to mate with the slanted light guides. On one end of the arc, we cut five pockets (one for each layer) with dimensions 10.3 cm × 4 mm × 3 mm depth.

The downside to the requirement to cut the arc with the 'vertical' technique is that even the high helix bit could not cut it without significantly damaging the surface. To fix this, a sanding and buffing technique was developed. It is outlined below:

35

- Using water as a lubricant, sand out machine marks with 120 grit paper.

- Repeat the above step, using finer and finer sandpaper, until reaching 1000 grit.

- Using the polishing wheel and water, buff the entire surface area. This is like using a super-fine sandpaper to remove sanding scratches.

- Make a paste using water and aluminum-oxide polishing compound (2 μm), apply using the buffing wheel.

- Once the paste dries, use a clean buffing wheel to polish the face.

- Using a microfiber cloth and water, clean the face.

Figure 2.19 shows one of the arc pieces. On the left is the guide before any polishing. On the right is after only running a buffing wheel over the surface. The abrasions and cuts in the surface are less than 1 mm deep and are removed by the sandpaper and water. **Figure 2.20** shows the same arc after the full polishing regimen. The cylindrical guides that attach the arcs to the PMT also go through the polishing regimen. There are a total of 4 of this combination made for each detector.

In principle, the entirety of the detector is made of plastic. However, the whole system must be sealed such that no light that is not from a scintillation effect can enter the PMT. To accomplish this, we designed and constructed a frame made of aluminum that houses the entire setup. An image of the frame can be found in **Figure 2.21**. The frame pieces are all solid aluminum of various sizes, which are categorized in **Table 2.2**. The original drawings for designing the pieces of the frame are found in **Appendix C**, alongside CAD diagrams of some of the pieces that were milled.

Figure 2.19: A light guide arc after manufacture. On the left is the raw surface, on the right is the surface after a buffing wheel has been passed over. On the left, the surface is extremely cloudy and there are cuts and abrasions in the surface that must be removed. On the right, the abrasions remain after light surface treatment, necessitating a more rigorous treatment.

Figure 2.20: The same arc as in **Figure 2.19**, but after undergoing the full polishing process we developed. The mirror finish and overall transparency are in the final, acceptable state.

Figure 2.21: The aluminum frame which will house the detector. The detector pieces are sitting inside, loosely fitted to check sizing. The cylindrical gaps on the end caps are pass-throughs that allows the cylindrical light guides to reach the PMTs which will be mounted on the outside of the frame.

Table 2.2: Material sizes for aluminum frame.

Piece	Size and Material
Braces	0.25 inch Al strut
End Caps	0.5 inch thick Al sheet
Skin	0.0321 inch Al sheet
Mounting Bracket	1 inch Al block

Once the frame was assembled, the next step was to attach all of the plastic pieces into one continuous detector. There are 3 major joints for each layer:

- Scintillator to slanted light guide.

- Slanted light guide to arc light guide.

- Arc light guide to cylindrical light mixer.

To attach each scintillator to its associated slanted light guide, a jig was developed that clamps both the scintillator and the light guide in place with an even offset from a flat wall. We used an optical cement sold by Saint-Gobain (BC-600[17]) as our glue. This cement comes in two parts: a thick resin and a liquid hardener. The correct ratio for mixing these is 100-to-28 by weight, resin to hardener. The angled guides were glued to the scintillator ends, connecting the angled side of the guide to the scintillator. At each joint, the guide has a longer edge than the scintillator due to the angled cut. To standardize how the scintillators will overlap, an 'overhang' of 9 mm was maintained. An image of the gluing jig can be found in **Figure 2.22**, alongside a closeup of the joint. In this image, the joint does not look very clean after the gluing, however we used a buffing wheel to clean up the opacity. To achieve a solid bond, the optical cement is mixed and allowed to sit for a few minutes, such that it reaches a more viscous state, as it is initially very difficult to handle. The cement is applied to the ends of both pieces, and then they are pressed together and

Figure 2.22: *Left:* The full light guide gluing jig. The plastic 'L' pieces are used to clamp the scintillator and light guide pieces in place. By using the same 'L' pieces at all clamping points, we maintained an even spacing between the plastic and the back wall, which is necessary to achieve a solid glue joint. *Right:* A close up of a single glue joint. The overhang is 9 mm for all joints on the interior angle side of the joint. This joint is both structural and for the light transmission, as the optical cement matches the index of refraction of the light guides.

clamped in place. These joints were rested for five days, the length of time necessary to fully harden. Each layer was then individually wrapped with two full layers of Teflon tape. Each pass is wrapped with a roughly maintained 2 mm overlap.

Attaching the arc guides to the cylinder guides was a much simpler process. Using the same BC-600, we fit the arc ends into the slots of the cylindrical guides after applying the optical cement to both surfaces. These are also rested for 5 days and the binding is complete.

Finally, the slanted light guides are connected to the arcs without optical cement. Each pocket in the arc guide is filled with optical grease. This grease is injected into the pockets using a syringe with a wide-mouthed 'needle' that allows for precision application. Once the grease is in place, the plastic is seated into the pockets. This
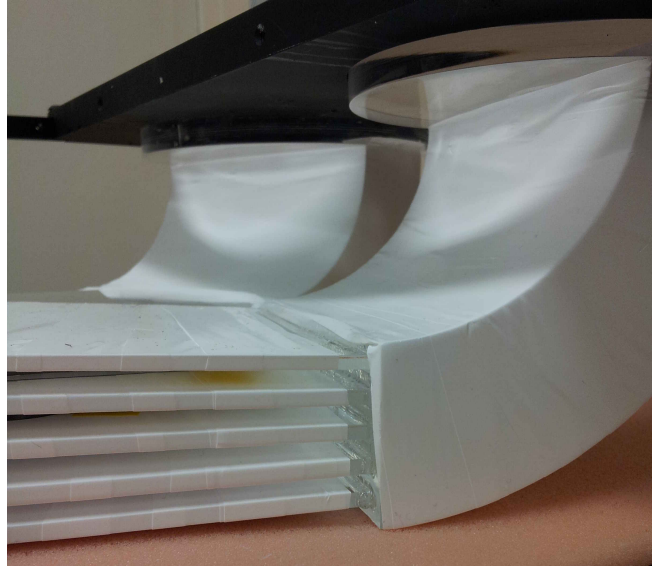
Figure 2.23: A close up view of the connection of the slanted light guides to the arc guides. The slanted guides fit into the pockets of the arc, after the pockets are filled with an optically transmitting grease to insure a solid optical junction.

can be seen in **Figure 2.23**.

Now that the detector is together, we can enclose the entire piece within the frame. To begin, 0.3 mm thick pieces of aluminized mylar are placed between each scintillation layer. This is to optically isolate the layers as well as add a 'last chance' reflection barrier to attempt to retain as much light as possible in the layers. Then dental floss is used to tie the 10 layer bundle together at 3 points along the length. Flexing in single layers is a major problem, as it can lead to breaking the cement junction with the light guide. By tying the layers together, they do not bend as much when compressed. Then foam is layered into the enclosure to help absorb shock and hold the plastic pieces in place. The 0.034 inch aluminum skin is screwed into place around the entire detector. The PMTs are placed against the cylindrical guides, using optical grease to maintain solid optical contact. The PMTs are seated inside of mu-metal shields which are held to the frame by an aluminum collar. This collar fits over three threaded rods which are screwed into the end cap. The shield also seats into a ring which is cut into the end cap as seen in the figures at the end of
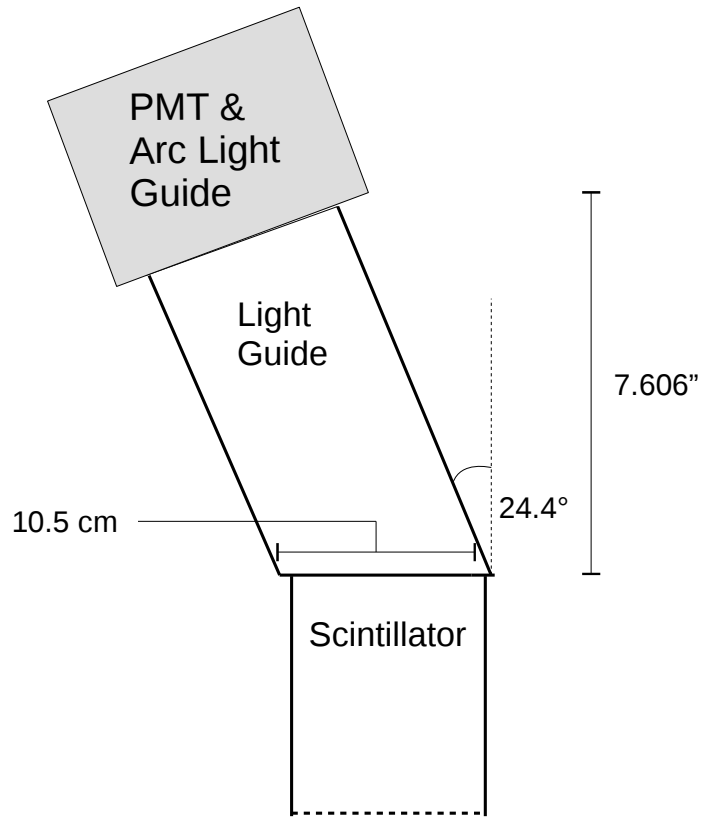
Figure 2.24: A schematic showing the connection of the scintillators to the arc light guides, demonstrating the exact specifications of the slanted light guides. Each slanted guide is 3 mm thick.

the chapter, which helps achieve a light tight seal. One-inch black electrical tape is then used to seal all edges and gaps against light. **Figures 2.24** and **2.25** show schematic diagrams of the light guide connections. **Figures 2.26** through **2.31** show the various stages of assembly.

Voltage
Divider

Photomultiplier
Tube

Mu-Metal
Shield

1.04"

Aluminum
Frame

Cylindrical
Light Guide

3.75"

2.254"

Arc
Light Guide

Slanted
Light Guides
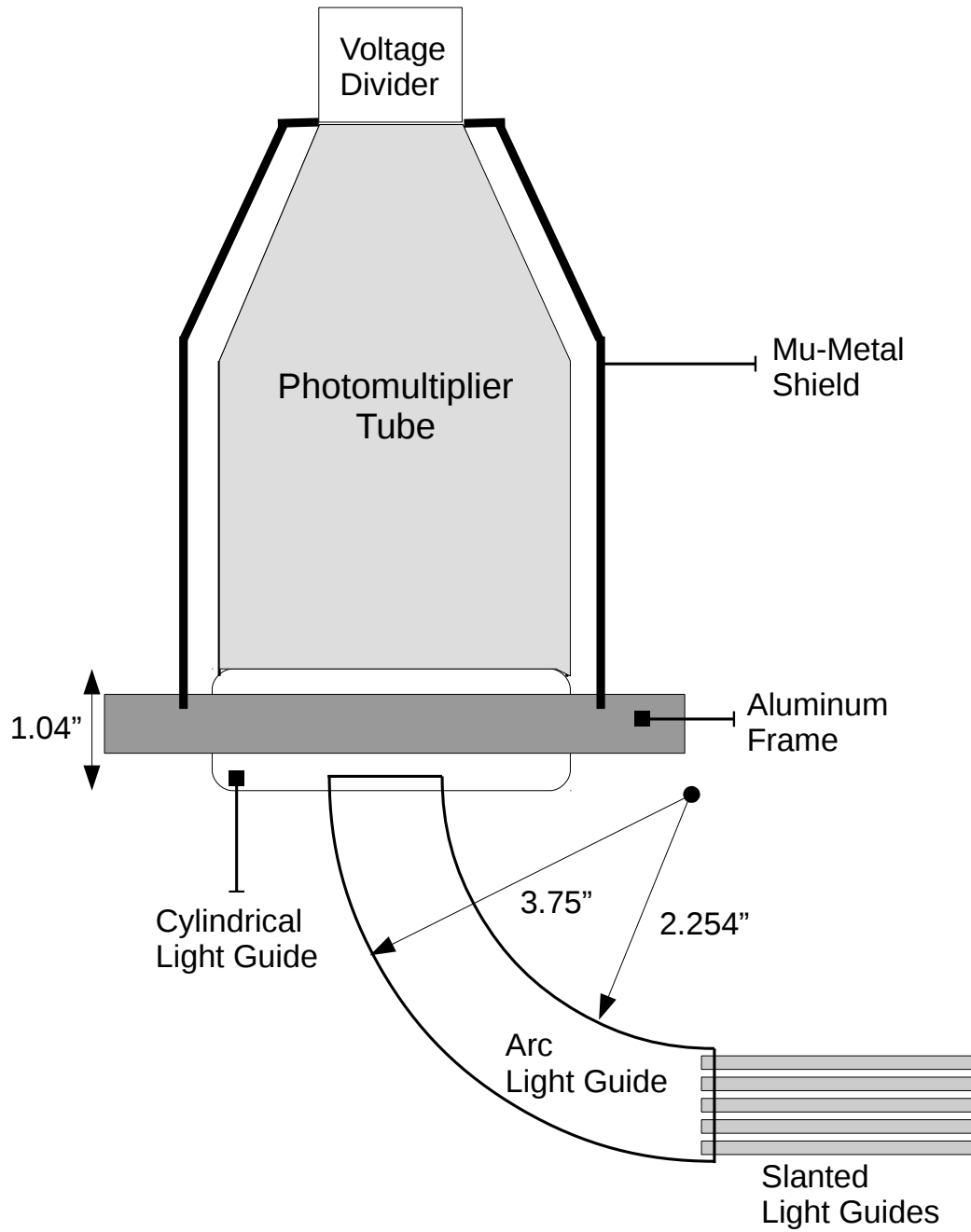
Figure 2.25: A schematic for connecting the light from the slanted light guides to the PMT. The incoming light first goes through the arc light guide, which is 11 cm in width. Then, in the cylindrical mixer, the light passes through the aluminum and into the PMT. The PMT shielding is shown, as it is mounted into the aluminum end cap. The PMT is a Hamamatsu R1250[22]. It has a circular face with 4.84 inch diameter.

Figure 2.26: Photograph of detector during final assembly, without foam. The reflective sheets are aluminized Mylar, meant to optically isolate the scintillation layers.

Figure 2.27: Photograph of detector during final assembly, end cap. The pass-through allows light from the layers to interface with the PMTs (not attached yet). The unique 'Y' design to separate light from adjacent layers is demonstrated.

Figure 2.28: Photograph of detector during final assembly, after inserting foam. The foam acts as a shock absorber for the entire system, as well as to help hold the plastic in place.

Figure 2.29: Photograph of detector during final assembly, after attaching outer aluminum skin. The skin seals out light as well as adding rigidity to the entire design. By fastening the skin in place at many locations, the skin is rigid against flexing in it's wide dimensions.

Figure 2.30: Photograph of detector during final assembly, PMT mounting system. The black pieces are mu-metal shields designed to stop magnetic effects from interfering with the PMT function. The aluminum collars are designed to seat onto necks of the mu-metal shields and clamp them in place. The PMTs are seated tightly into the mu-metal shields using foam. This whole assembly holds the PMTs tightly against the cylindrical light guides to obtain a solid optical connection.
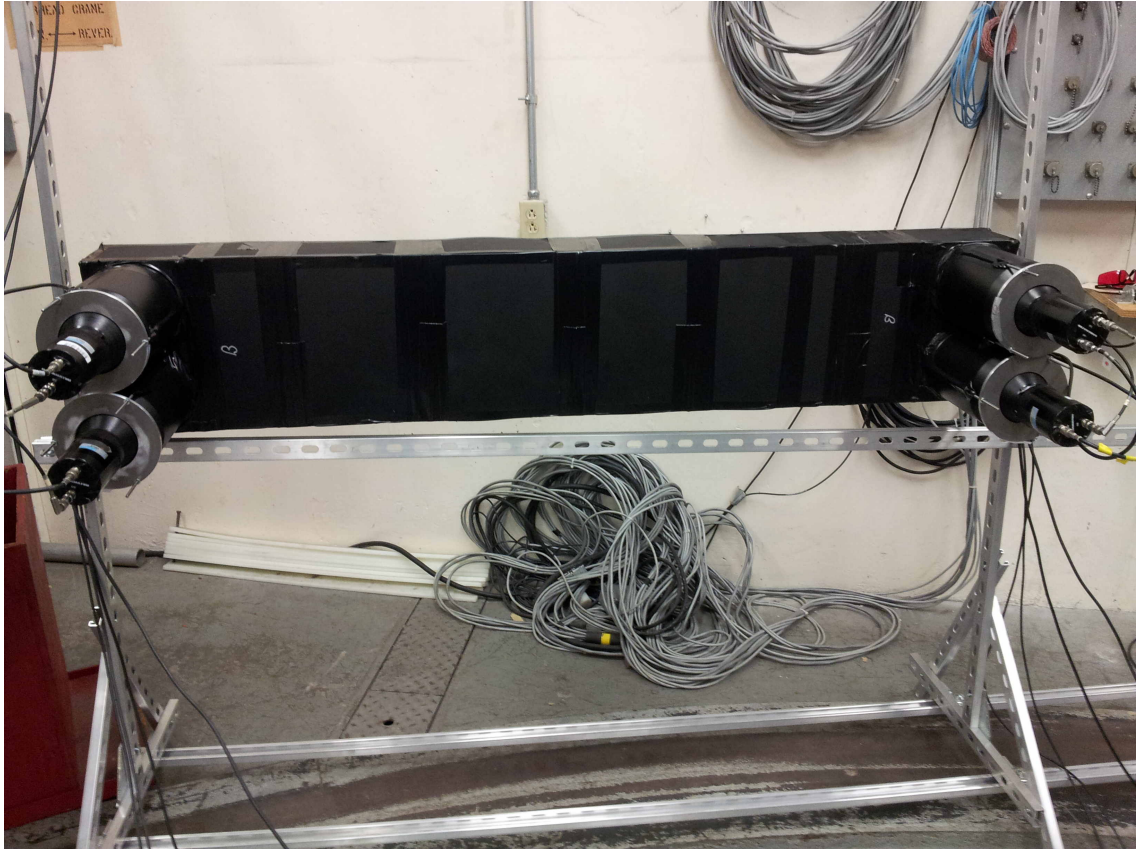
Figure 2.31: A photograph of the completed detector at its initial test run. The mounting system for the detector is made of aluminum strut, and was designed by Hongwei Yang. The detector is fully sealed using black tape around the edges, and is light tight. It has 4 channels of data readout, one for each PMT.

Chapter 3: Prompt Fission Neutron Yields in ^{235}U(n,f)

3.1 Introduction to the Measurement

The detectors described in **Chapter 2** were built with the intention of measuring the neutrons ejected by fission fragments. In particular, these detectors were designed to look at the prompt fission neutrons that have an energy of less than 1 MeV. The multiplicity of neutrons in fission reactions is well-studied, however the energy dependence of prompt fission neutrons is unmeasured below 1 MeV for ^{235}U (as a convention, ^{235}U will be used as a shorthand for ^{235}U(n,f) when referring to the prompt fission neutrons from ^{235}U). **Figure 3.1** shows the measurements of the prompt fission neutron energy spectrum. It is widely believed that 30% of the prompt neutrons have an energy that is below 1 MeV. One of the most recent experiments to measure this quantity was carried out by S. Noda, et al[23]. This experiment also used the the double time-of-flight method used in this work, with a different fission counter and different neutron detectors. This experiment measured the spectrum in the range above 1 MeV, but due to backgrounds could not measure below 1 MeV. Results from this experiment are shown in **Figure 3.2**. Note that this is a semi-log plot, so the error bars, despite appearing small near 1 MeV, are actually spanning nearly 1/2 an order of magnitude.

This measurement relied upon a double time-of-flight (ToF) technique to determine the energy of the detected fission neutrons. This technique is based on knowing the flight path of each particle with precision and measuring the amount of time for the particle to traverse the path length. In the case of this experiment, there were two flight paths of interest. These are demonstrated in **Figure 3.3**. The flight path for the particle labeled n was the distance from the neutron spallation source to the ^{235}U target. Using this distance, and the associated time of flight, allowed a determination
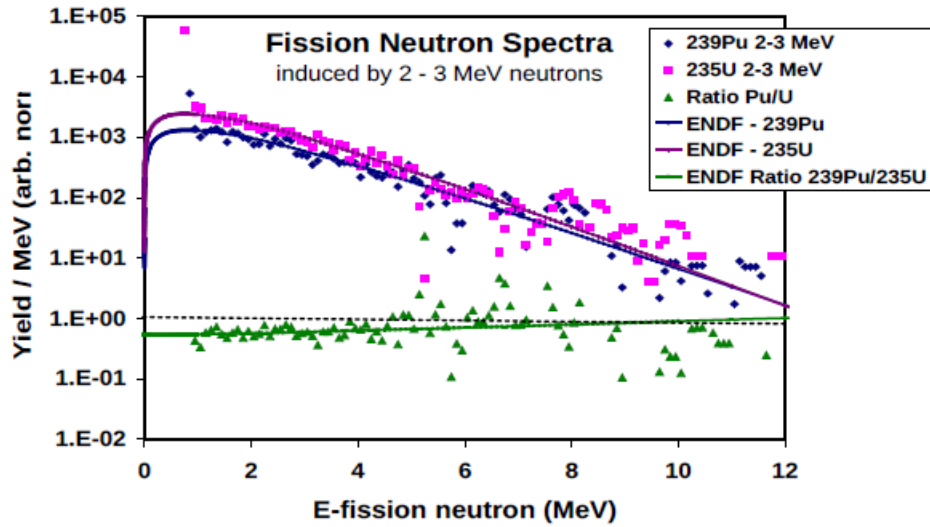
Figure 3.1: Existing data for ^{235}U prompt fission neutron energy. The data currently stops at 1 MeV. Image from [24].
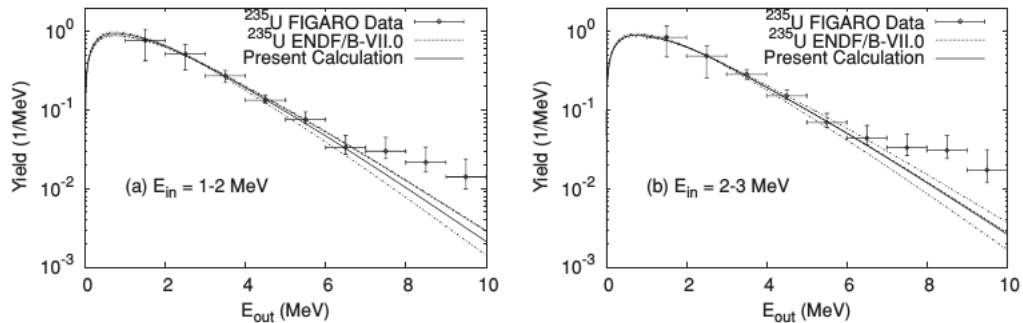
Figure 3.2: Recent measurement of the ^{235}U prompt fission neutron spectrum by Noda, et al. Image from [23].

of the energy of the neutron that caused the fission event. This is not the energy we attempted to measure, but plays a vital roll in the analysis. The flight path for the particle n' was measured from the center of the fission target to the neutron bar detector. This flight path was used to determine the energy of the prompt fission neutron; it is the energy of interest. For this method, we were particularly interested in recording two time differences: the time between neutron generation at the spallation target and the time of the fission fragment occuring, and the time between fission fragment creation and fission neutron detection.
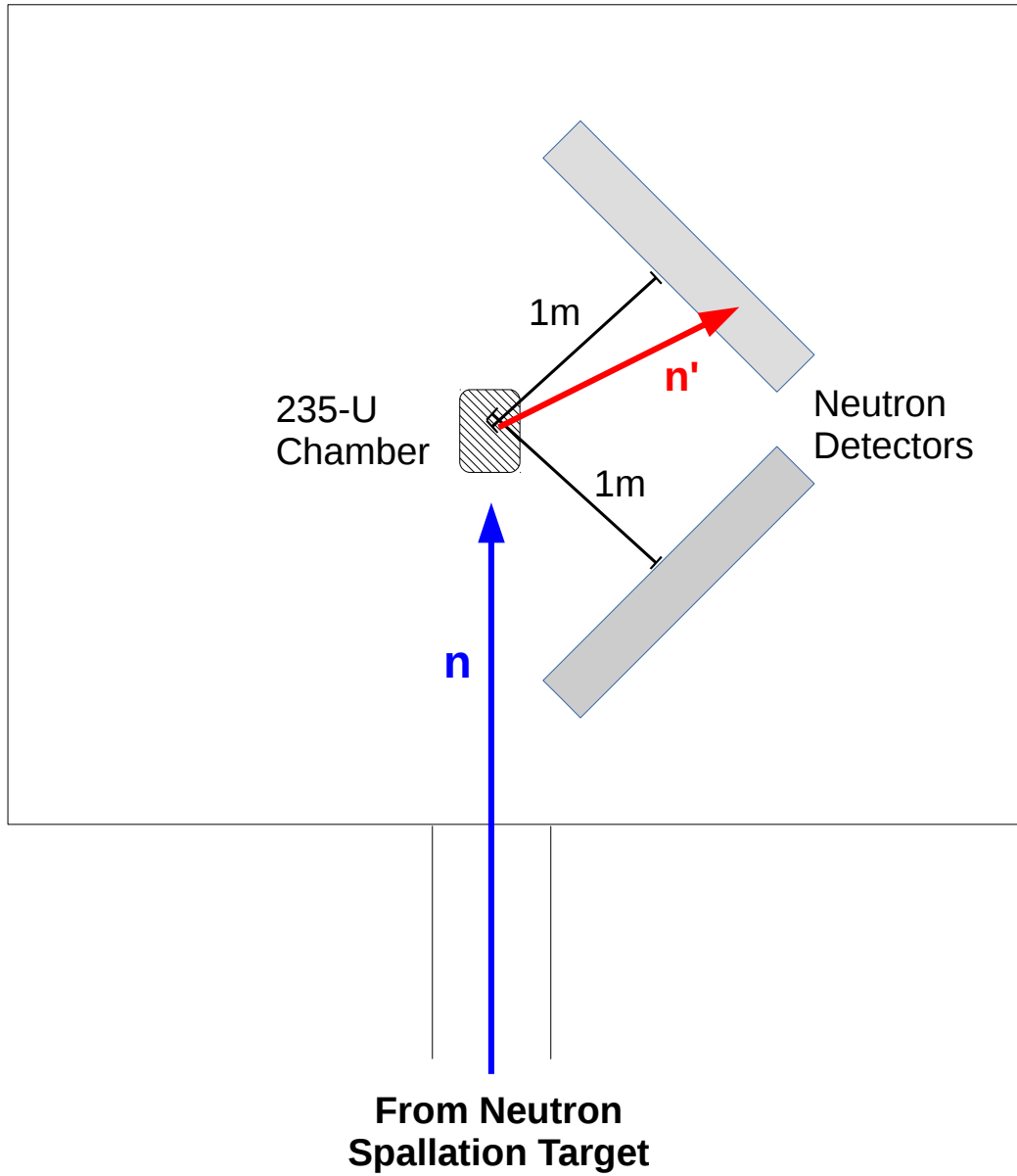
Figure 3.3: Top down diagram of experimental setup for prompt fission neutron spectrum experiment.

3.2   Experimental Setup

3.2.1   Experimental Apparatus

Chapter 2 is dedicated to describing the design and construction of the neutron detectors in detail. There are a few major aspects of the detector design that are worth reiterating:

1. The layered geometry of plastic scintillator allows a partial separation of neutron events and gamma-ray events in the analysis. This method of particle identification increases in efficiency as the energy of the neutron decreases.

2. The neutron detectors are designed to be efficient at detecting low-energy fast neutrons (energy near and below 1 MeV).

3. Each scintillating layer is viewed by a pair of PMTs. Requiring a coincident reaction in the linked PMTs allows the threshold for event analysis to be set near the single photoelecton level despite detector noise.

4. The plastic scintillator used in the detector has a decay time of $\sim$ 2 ns[17]. This allows for instantaneous events rates on the scale of kHz, without causing pileup in the detector. This also gives an excellent time resolution for the time of flight for each event.

Two neutron detectors were placed roughly 1 m from a fissile target, in the horizontal plane of the target's center. They were also placed such that the normal to the scintillator plane was approximately 45° from the line made by the neutron beam. A full diagram of the exact dimensions to each bar within the experimental area is shown in **Figure 3.5**. Throughout this report, the bars will be referred to as α (A) and β (B), with the Latin symbols being used wherever the Greek symbol is not available (e.g. diagrams). A photograph of the experimental area is shown in **Figure 3.4**.
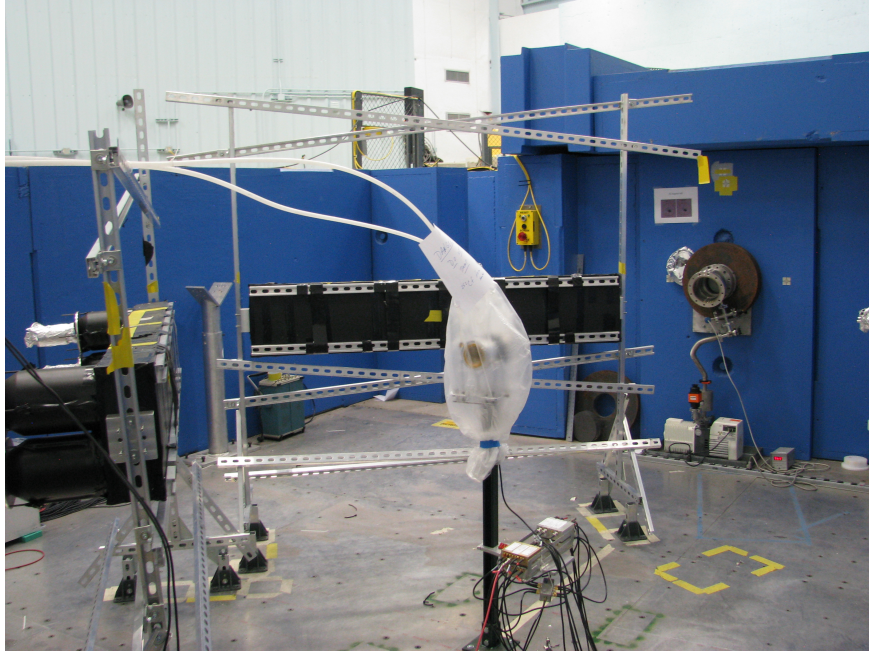
Figure 3.4: A photograph of the experimental area. Both neutron detectors are shown in the background, and the ^{235}U target/counter is in a plastic bag which lowers the alpha radiation exposure near the counter.

The ^{235}U target is a Parallel Plate Avalanche Counter (PPAC), and was designed by a collaboration between groups from Lawerence Livermore National Laboratory (LLNL) and Los Alamos National Laboratory (LANL) [25]. The lead designer and builder was Ching-Yen Wu at LLNL [26]. The PPAC contained 111.96 mg of ^{235}U, distributed over 10 foils [27]. The distribution of the uranium can be found in **Table 3.1**, noting that the measured isotopic composition was 99.912% ^{235}U, with the remaing percentage distributed between ^{238}U (0.0414%), ^{234}U (0.0298%), and ^{236}U (0.0165%). These masses were measured using a gamma counting technique, which was completed by C. Y. Wu[27] on 28 August, 2014. The uranium was electroplated onto both sides of a 3 μm titanium foil, with a deposit diameter of $\sim$ 4 cm. This gives a surface density of $\sim$ 400 μg/cm^2. An exploded diagram of one of these target cells is shown in **Figure 3.6**.

Each of the titanium foils containing the uranium was mounted between two aluminized mylar foils (1.4 μm) that act as cathodes for collecting ionization charge
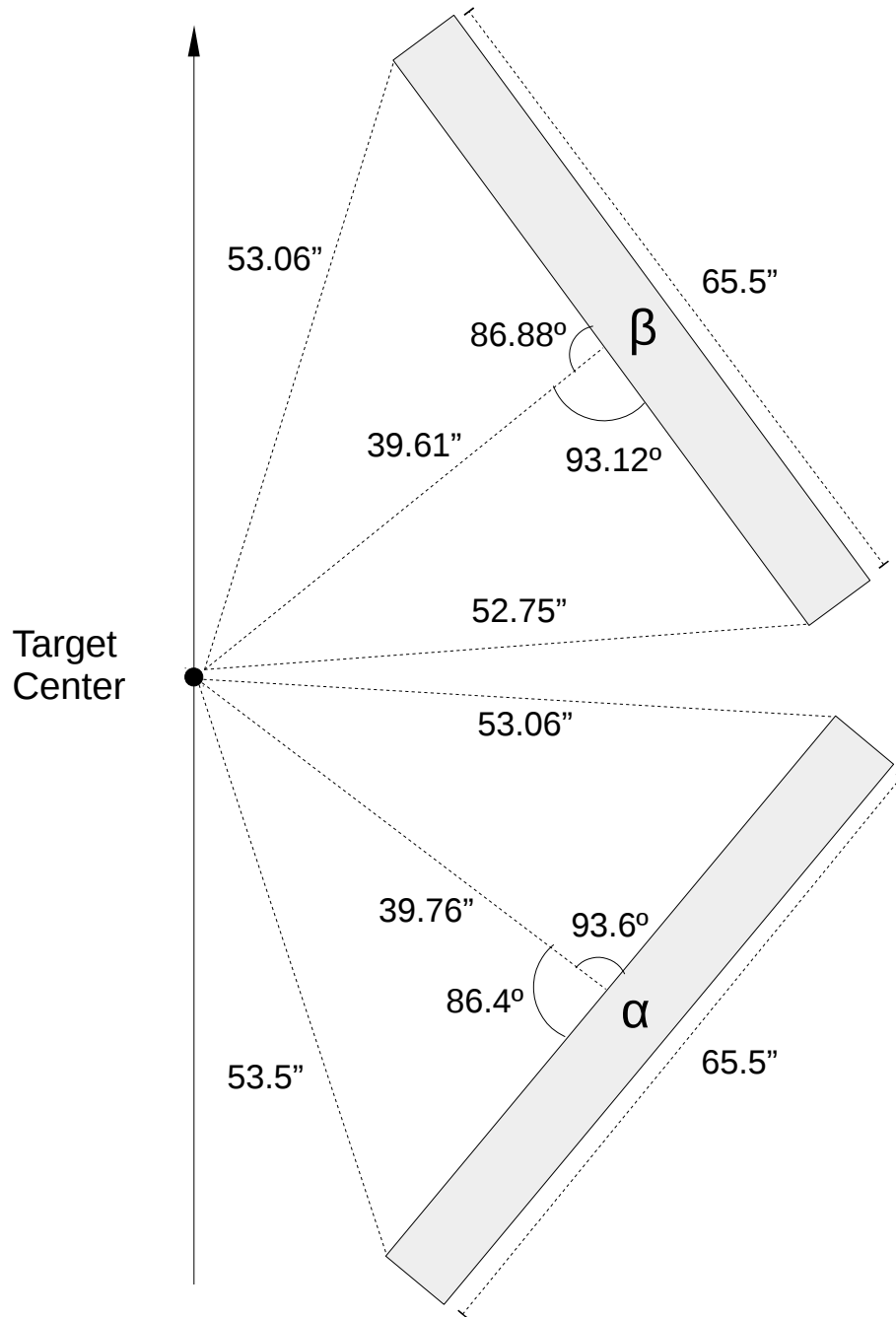
Figure 3.5: Diagram of neutron bar placement within experimental area (not to scale).

Table 3.1: Distribution of ^{235}U within the PPAC.

Foil Number	Uranium Mass (mg)
1	9.04
2	10.33
3	10.51
4	10.22
5	12.06
6	10.74
7	10.14
8	13.04
9	15.36
10	10.52
Total	111.96

5 μm Pt foil

3 μm Ti foils with ∼ 5 mg of target material on each side

The exploded view of one of the target assemblies in the current PPAC.

1.4 μm double-side aluminized mylar
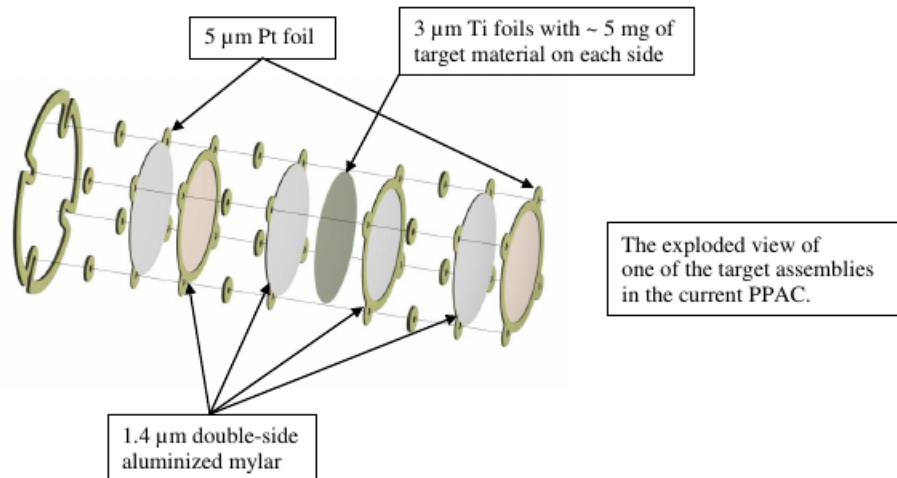
Figure 3.6: A diagram of a single (exploded) PPAC target cell. Image from [25].

from recoiling fission fragments. Two anodes, also made of aluminized mylar, were mounted 3.28 mm from each cathode (outward from the target foil). Each of these anodes had a 5 μm platinum foil mounted directly behind it to stop fission fragments from crossing between collection cells. The resulting series of foils was 21.6 μm in width and was mounted onto holding ring made of aluminum (0.82 mm in width), completing one cell. Ten of these cells were mounted together, using Teflon spacing rings. The total active region of the detector was 96.5 mm in length, with a circular cross section for each foil that was 2 cm in radius. These ten target cells were enclosed by a cylindrical aluminum tube that held the mounting assembly. This aluminum was 1.57 mm in thickness. The ends of the tube were enclosed with Kapton foil windows to allow neutron entrance and exit with a low interaction rate. The Kapton windows were 25.4 μm in thickness. This detector collects charge from ionization within each target cell, so an ionizing gas was pumped into the detector using aluminum feedthroughs that were mounted onto the aluminum tube. The PPAC used isobutane (at $\sim$ 4 torr) as its ionizing gas. To operate in a stable manner, the gas was constantly flowing. This was handled with a feedback loop and specialized equipment, which is described in [25]. An image of the complete assembly without the exterior aluminum frame is found in **Figure 3.7**. During operation, the voltage bias between cathode and anode was kept at $\sim$ +400 V. An image of the PPAC as it was mounted for the experiment (alongside the extended beam pipe, which was kept at vacuum) is shown in **Figure 3.8**.

The neutron beam for this experiment was produced at the Weapons Neutron Research (WNR) facility at Los Alamos Neutron Science Center (LANSCE). To produce the neutron beam, protons were accelerated, via a linear accelerator, up to 800 MeV. These protons were guided onto a cylindrical tungsten target, which acted as a neutron spallation source. Neutrons were produced into the full 4π solid angle by the spallation reaction, with a maximum energy of over 600 MeV. From the target
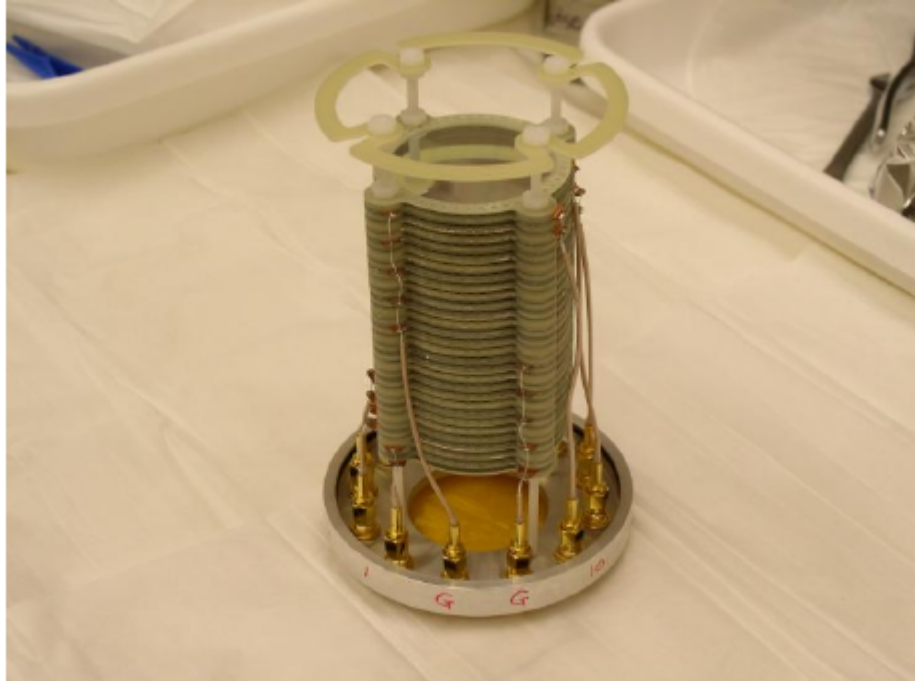
Figure 3.7: A photograph of the assembled PPAC detector. There were ten total cells. In this image, three foils form one cell, as the anode and cathode are separated by 3.28 mm. Image from [25].
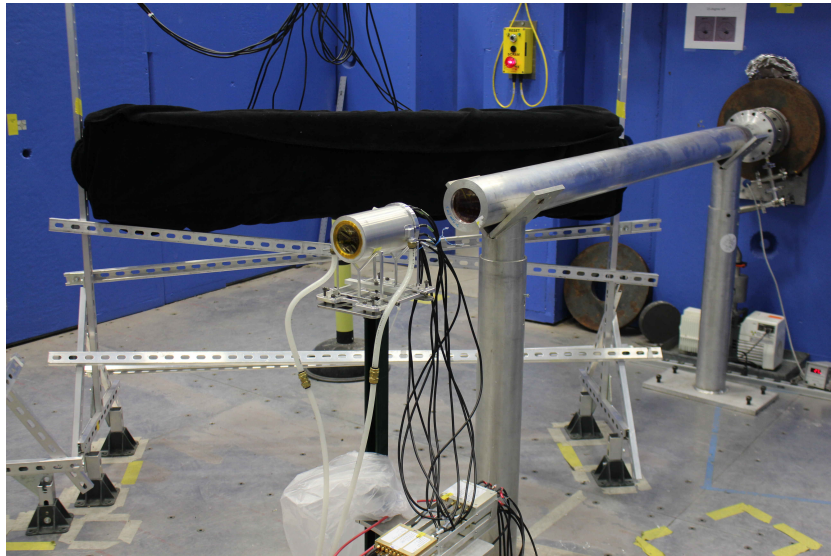
Figure 3.8: A photograph of the experimental area with PPAC mounted.

room there were numerous unimpeded beam pipes that allowed neutrons to travel to various experimental areas. For this data, the experimental area 15° left of the initial proton beam direction was used. **Figure 3.9** shows a calculation of the neutron flux for various laboratory angles, with the neutron flux for this experimental area being labeled as '15'. The beam pipe passed through twelve feet of magnetite shielding and concrete to stop all neutrons that are not directed through the beam pipe from entering the experimental area. Due to the pulsed nature of the proton beam, the neutron beam had a unique structure which is demonstrated in **Figure 3.10**. The beam was divided into 625 μs long macropulses, which were further subdivided into 1.8 μs micropulses. In between the macropulses there was 24.375 ms of dead time. This gave the beam a repetition rate of 40 Hz and a duty factor of ∼ 2.5%. Each flight path at WNR has the ability to stop or modify the shape of the neutron beam to the local experimental area with a pair of depleted uranium shutters. These shutters can be opened to various widths. For this experiment, the shutters were always opened to 2.37 inches in horizontal plane and 2.125 inches in the vertical plane. Along with these shutters, there was also traditional beam collimation to shape the beam spot. For this experiment, nine feet of stainless steel with a one inch bore was placed in the beam pipe to collimate the beam down to a one inch spot. During the collection of the ^{235}U data, the beam pipe was kept under vacuum. With the vacuum chamber, the beam pipe extended into the experimental area, until it was ∼ 8 inches from the the PPAC. The beam pipe also had a Kapton window to allow the beam neutrons to pass through with a low interaction rate. The pipe is shown in **Figure 3.8**. A low-energy neutron filter was also placed in the beam line. This filter is a piece of material with a high scattering cross section for low-energy neutrons. In this experiment the filter was very important, as there was signficant 'wrap-around' between beam pulses. As an example, when the 600 keV neutrons were arriving at the ^{238}U target from one beam pulse, the gamma rays from the next beam pulse were also arriving at
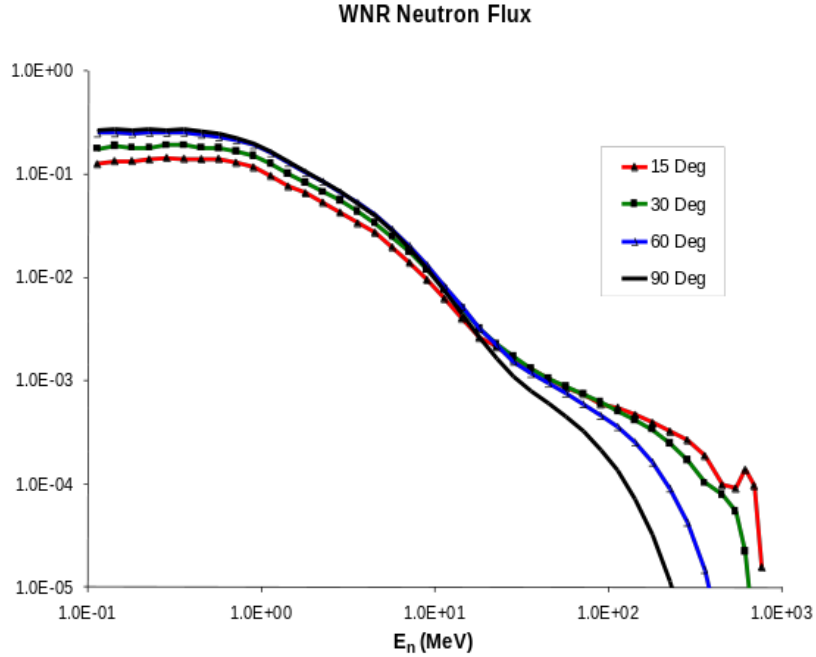
Figure 3.9: A calculation of the WNR neutron flux, in units of relative intensity. Image from [28].
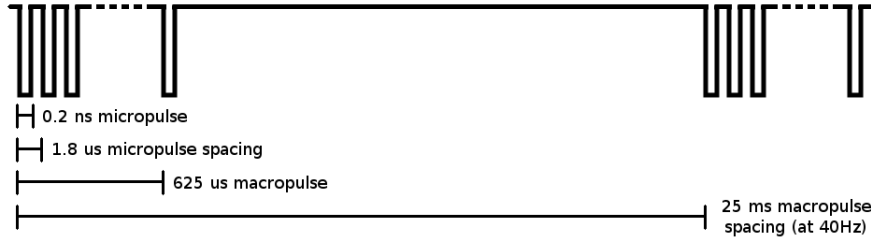
Figure 3.10: Beam structure during 2014 prompt fission neutron experiment at WNR.

the target. The low-energy filter removes a high-percentage of beam neutrons with energies below 0.5 MeV, meaning that the wrap-around is significantly reduced. This minimizes the possibility that a slow neutron from a pulse might be counted as a fast neutron from the subsequent pulse.

This experimental area was chosen for two main reasons. First, the LANSCE neutron beam is the most intense in the world for this region of neutron energy. ^{235}U has a neutron-induced fission cross section on the order of 1 barn, so the rate of reaction was not particularly high. Even smaller was the portion of fission events

that eject prompt neutrons into the solid angle of our detectors, since each covers a litle less than 1% of the total solid angle. Thus, we wanted a high intensity beam to increase the frequency of observed 'good' events. Secondly, this experimental area has a so-called 'pit'. As can be seen in the photographs of the experimental area, the floor in this area is made of aluminum. The floor is one inch thick (hollow) aluminum tubing, which is laid across a seven foot deep hole. All experimental apparatus were sitting upon, or bolted to, the aluminum flooring. This greatly reduced the number of background counts, since neutrons have a high rate of elastically scattering in concrete and are famously difficult to stop. By moving the concrete seven feet further from the apparatus, we lowered the chance of having a neutron 'bounce' off of the floor and enter our detectors as an accidental. Since aluminum is a relatively low mass material, it is ideal for spanning the pit.

3.2.2 Electronics

This experiment used a data acquisition system that was designed and built primarily for this experiment. The details of the data acquisition system construction can be found in **Appendix B**. This system is based on the FERA (Fast Encoding and Readout ADC) protocol developed by LeCroy. The system has 16 channels of 11-bit ADC, 16 channels of 11-bit TDC, and 12 channels of 24-bit scaler counters. To determine which events are recorded, all of the pulse analysis (finding coincidences, threshold checks, etc.) were done in real time, using assorted NIM and CAMAC modules. These electronic analysis chains are described below. The key to collecting the data was identifying fission events with a coincident neutron in our neutron detectors. Due to the 'white' nature of the beam (all energies from 600 MeV to a few hundred keV) and the large overall neutron flux, picking out the events of interest required looking for a coincidence between the PPAC and the neutron bars, with a window of only a few hundred nanoseconds.

The method we chose for collecting events was the common start mode on the TDCs. This start could be generated by three types of events:

1. Coincidence between a PPAC event and neutron bar event, or

2. Some fraction $(1/N_F)$ of PPAC events with no associated coincidence, or

3. Some fraction $(1/N_n)$ of neutron bar events with no associated coincidence.

Once the data acquisition was triggered by one of these events, each detector signal had both an ADC and TDC channel. The TDC channels were all delayed with cable delays such that they come after the trigger event. The 'trick' to this method was using the correct amount of delay, such that all neutrons of interest could properly trigger the coincidence. A sketch of the required timing is shown in **Figure 3.11**. In real time, the fission must occur before the neutron was produced and subsequently arrived at the neutron detector. The neutron time of arrival also varies depending on the neutron energy. To allow for this in the electronics, we created a gate when the fission fragment occured and then delayed that gate by a fixed amount of 400 ns. This gate was only 50 ns in width. When the neutron arrived at the neutron detector, we created a second gate. This gate was 450 ns in width. The reason for making this gate wide is demonstrated in **Figure 3.11**. For the fastest neutrons of interest, which take more than 30 ns to arrive at the detector, this gate was wide enough that it will overlap with the delayed PPAC gate. For the slowest neutrons, which take $\sim$ 150 ns to arrive at the detector, the delay in the PPAC gate was large enough that there was an overlapping region (the start of the overlapping region is marked by the dashed line in **Figure 3.11**). Given this choice of delays and gate widths, any prompt fission neutron that was in our energy region of interest could be seen as coincident with a fission.

In order to identify these coincidence events, we passed all detected signals through an analysis chain. Each detector had its own signal chain, with outputs
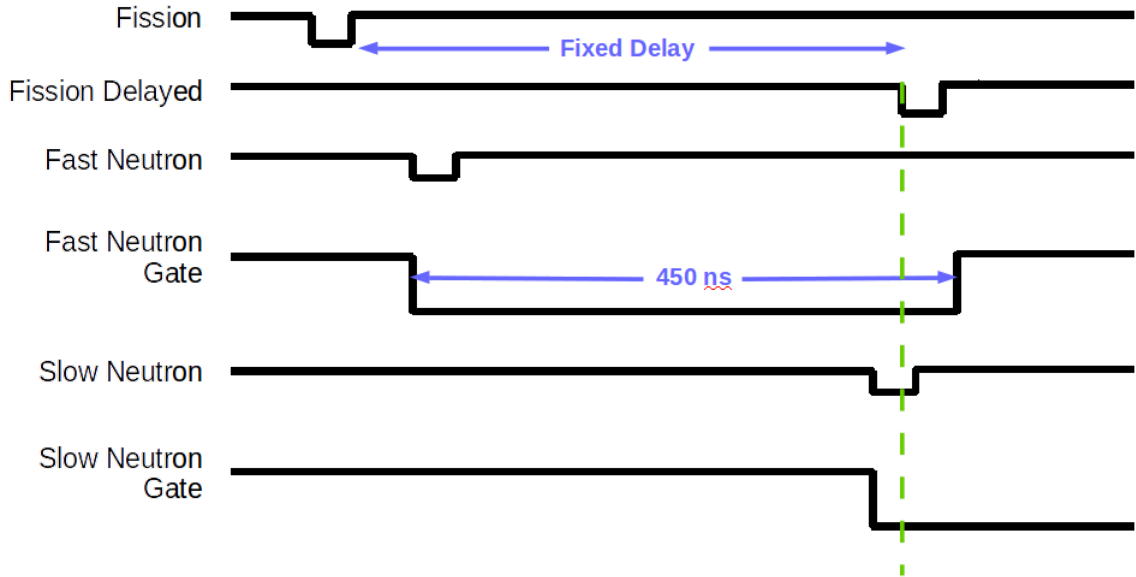
Figure 3.11: Diagram of the coincidence timing in the ^{235}U experiment.

that were merged together with other signals to make up the trigger electronics. In order to describe the whole system, each detector chain will be described on its own, with a separate discussion dedicated to the trigger electronics.

t_0: The signal known as t_0 was created when the proton burst struck the neutron spallation target. This acted as both a beam monitor and as a timing mechanism. The signal produced by the proton beam pickoff was immediately converted into a gate and then passed to our electronics system. Once in our system, the t_0 was split into multiple copies using a logic fan-out. One of these copies was sent to a gate generator, which was used to produce a gate that was 625 μs wide, the same width as a beam macro-pulse. Both this gate and its inverse were passed into the trigger electronics to inhibit trigger generation whenever the beam was not live. The rest of the gate copies were sent into a series of electronics we have called the 't_0 cascade.' In order to measure the time between neutron spallation and collection of events, we needed to know when the spallation occurred. Since trigger generation started the clock in the TDCs ('common-start mode'), we delayed the t_0 signal by a known amount and stopped the clock with the delayed signal to determine the time difference between

spallation and event collection. As an example, if the t_0 was delayed by 100 ns, and stopped a clock 20 ns after trigger generation, then the event must have occurred 80 ns after neutron spallation. A difficulty in using this method arose due to the TDC's limited time range. The TDC model we used has a maximum time range of 1 μs with an inverse relationship between time resolution and time range. To maintain an acceptable time resolution, we chose a 500 ns TDC width, which means each TDC bin is 0.286 ns in width. To cover the full range of beam energies, the t_0 signal needed to be observed for the full 1.8 μs of each micropulse. The 't_0 cascade' method split the t_0 gate into five identical copies. The first copy was sent directly to the TDC and monitored the first 500 ns of the micropulse. The second copy of the gate was delayed by 400 ns and then sent to a second TDC. This monitored from 400-900 ns after the spallation. The third copy was delayed by 800 ns and monitored from 800-1300 ns after the spallation, and so on until the full range of the micropulse was observed for each event. Each of these 500 ns windows overlapped with its 'neighbor' windows. By knowing where these overlaps occurred, we 'stitched' these windows together to have a single view of every recorded event's time relative to neutron spallation. A diagram of these electronics can be found in **Figure 3.12**.

Neutron Detectors: For the neutron detectors, we were only interested in events that trigger PMT pairs, as described in **Chapter 2**. As such, this discussion will look at a single pair of PMTs that view five layers of scintillating plastic. This setup was repeated for the three other paired PMT sets. The output of each PMT was patched into the electronics setup via a BNC-to-LEMO panel. After the patch panel, the signal was split into two lines. The first line went into a constant-fraction discriminator (CFD). The output gates from both PMTs were set to be 35 ns in width. The output of this discriminator was split again, with one line being delayed and going to the TDC stop. The level converter shown in **Figure 4.11** was neces-
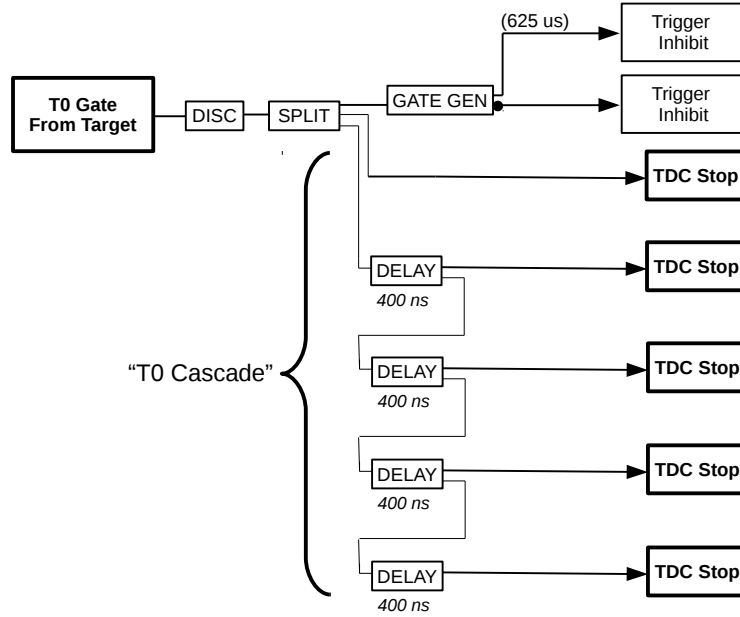
Figure 3.12: Diagram of the t_0 electronics for ^{235}U experiment.

sary, since the FERA system required a different voltage level than NIM modules provided. The other line went to a mean timer. The mean timer was the central piece to these electronics. The mean timer took a gate from each PMT as inputs and analyzed the overlap between them, outputting a new gate at the mean time of the input gates. This acted as a coincidence requirement and removed the position dependence of the gate generation. This dependence was due to the elongated nature of the detectors. The output of the mean timer was split in three, with two going to linear gates and one going to the trigger electronics after being discriminated to re-shape the gate to a proper width. Returning to the signal split after the patch panel, the other line remained an analog pulse. This signal was delayed and then passed to the linear gate input. The linear gate had two inputs: analog (IN) and gate. This module output only the portion of the IN signal that was within the range of the gate's active region. We used this module to remove background chatter and to only allow those analog signals that have a mean timer (coincidence) output to have access to the ADC. After the linear gate, the analog signal was delayed once

63
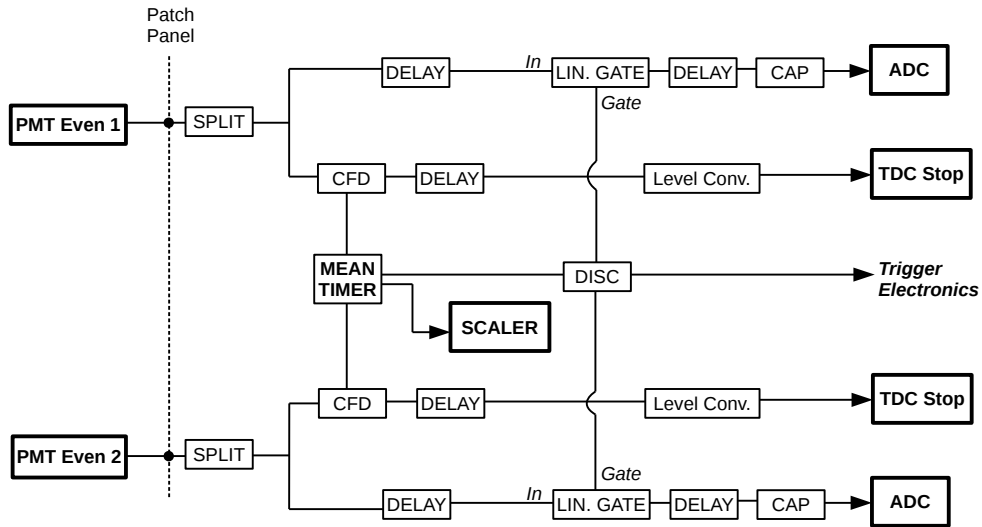
Figure 3.13: Diagram of the electronics for a PMT pair in the ^{235}U experiment. Each PMT pair has the same setup.

more and then passed to a capacitor to remove any DC-offset. This signal went to the ADC. A diagram of the electronics for a PMT pair can be found in **Figure 4.11**.

PPAC: The PPAC electronics were quite similar to the electronics for a single PMT, with the mean timer being replaced by a discriminator. To begin, all ten of the PPAC cells had their signals combined via an electronic OR. This was done to decrease the number of required DAQ channels. All ten cells were designed to be read individually, but we did not have the proper number of ADC or TDC channels. This signal was passed through a patch panel to the experimental electronics. This signal was split into two lines. The first line went into a CFD, where it was discriminated and then further split into three parts. One of these was delayed, discriminated again to shape the gate, and then sent to the TDC stop. The second went to the linear gate as the GATE input. The third was input into the trigger electronics. The second line out of the original signal splitter was the same as the analog path for a neutron bar PMT, with the minor change that instead of being gated by a mean timer at the linear gate,

64
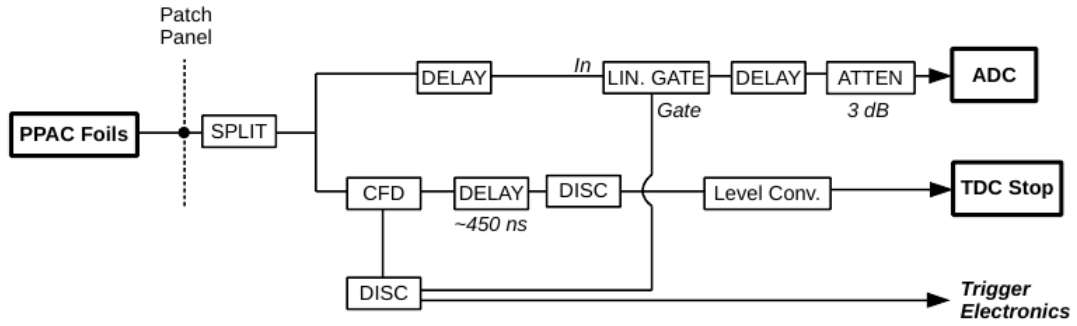
Figure 3.14: Diagram of the electronics for the PPAC in the ^{235}U experiment. Not shown is the combination of the ten PPAC cells into a single signal via electronic OR.

this pulse was self-gated. **Figure 3.14** demonstrates the electronics for the PPAC.

Each of the detectors (four PMT pairs and one PPAC signal) had an output gate that went into trigger generation. These gates were combined in various ways and then used to start the data acquisition system. **Figure 3.15** diagrams how these gates were combined. The four PMT pairs were combined into a single 'neutron bar trigger' via an n = 1 coincidence OR. This gate was split into two lines, one which is labeled as 'n-Singles' in **Figure 3.15** and one which went to the 'coincidence' trigger. The PPAC gate was also split into two lines. One became the 'PPAC-Singles' line in **Figure 3.15**, the other went to the 'coincidence' trigger. Both of the 'singles' trigger types were treated in the same manner. Each ran into a pre-scaling module, which is a module that only allows every Nth input gate to pass. For these modules, N was controlled by the user. This allowed us to record non-coincidence events at a low rate to characterize the detector responses to individual events. After the pre-scaler, each trigger was delayed. This delay was put in place to make sure that if an event was both a coincidence and the Nth 'singles' event, the coincidence would take precedence, as its gate arrived first. After this delay each 'singles' trigger was split in four. The first line went to the MASTER trigger, which was an OR module that passed triggers to the data acquisiton start. The other three lines went to three monitoring systems:

1. The scaler, which logged a count of the total number of this type of trigger have

65

been seen.

2. The counter, which displayed a 'counts/second' value and was used by the experimenters as an online feedback method.

3. The 'ADC-bit' or 'Trigger-Bit.' This was a dedicated ADC channel which received a gate whenever an event of its associated type was generated. Since the gates were always the same size (width and height), a spike in the spectrum was formed due to integrating the gate. This created a method for separating event types in post-experiment analysis.

The other type of trigger was the coincidence trigger. These are the events we were most interested in. The timing for making this trigger behave properly is shown in **Figure 3.11**. The gates from both the neutron bars and the PPAC were input into a coincidence module, and the output was the 'coincidence trigger'. This was treated the same as the 'singles' triggers, except it was not pre-scaled or delayed since we wanted to collect every coincidence event and we wanted coincidence events to take precedence. This trigger also had an associated scaler, counter, and trigger-bit.

The MASTER trigger connected directly to the FERA data acquisition system, and whenever a trigger was passed to the MASTER, the DAQ recorded data for all detector lines. However, we did not want data to be recorded when the beam was not live. A t_0 gate was generated every time a new burst of protons struck the tungsten target to expel neutrons. This gate was 625 ms long. Whenever this gate was not active, we vetoed the MASTER trigger, such that no new data could be recorded. Along with this, we also vetoed the MASTER trigger whenever the system was busy. To determine when the system was busy, we used an output from the data memory module, which was high whenever an event is being integrated and recorded. This veto was the system's only electronic dead time. To quantize the dead time, we used two methods, both of which used the systems scalers. In the first method, we

66
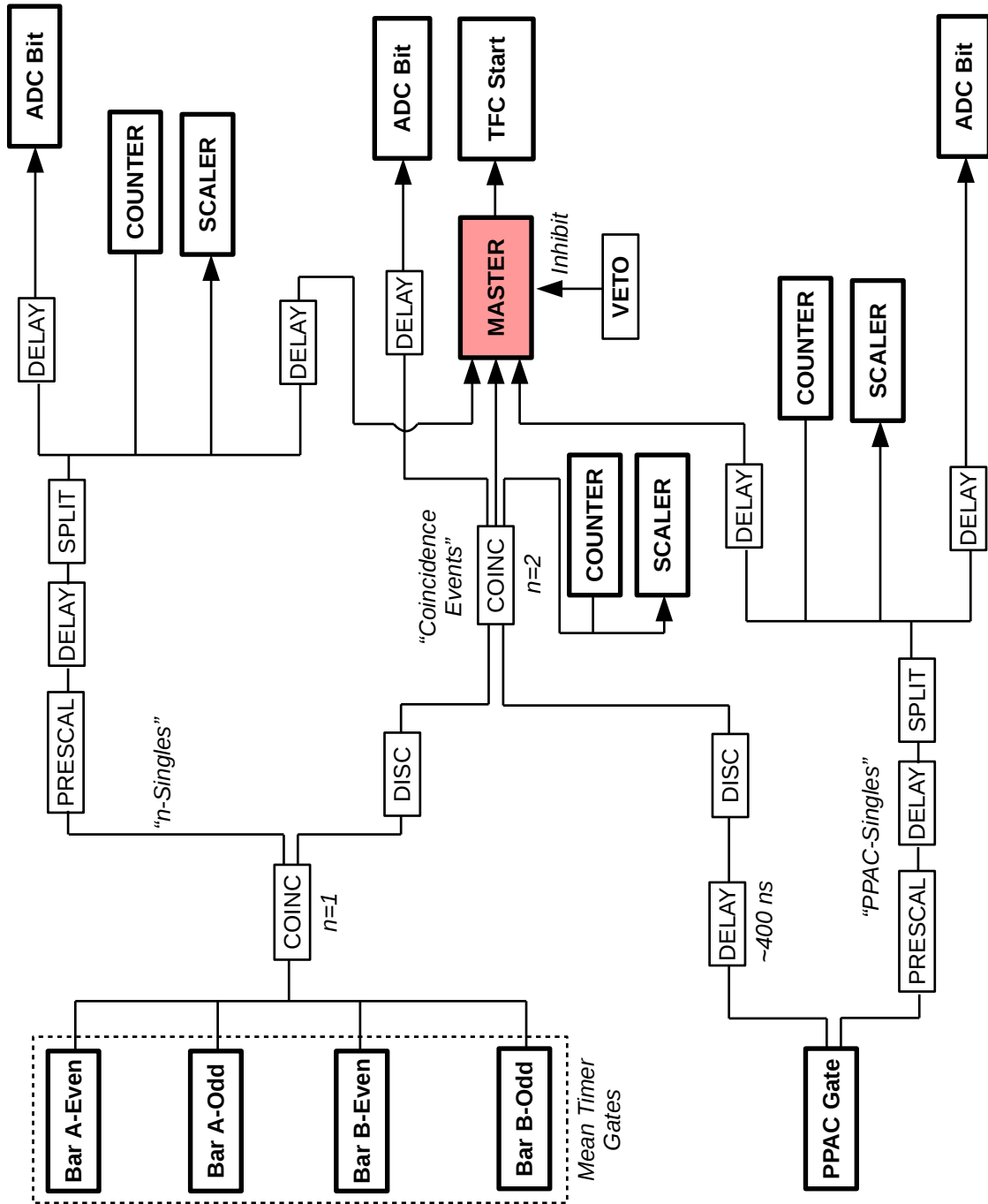
Figure 3.15: Diagram for trigger generation setup in the ^{235}U experiment.

used a clock which created pulses at 100 Hz. We split the output of this clock with one branch going into one scaler and the other branch going to a module that only recorded those clock pulses that occur when the veto is negated. By comparing these, we determined what percentage of our time was 'dead.' In a similar method, we used a scaler to count the MASTER trigger rate with and without the veto. Once again, a comparison of these two counting rates determined what percentage of the time our system was unable to record true events. Both methods agreed that our system was live 96.2% of the beam's active time. This agreed with a calculation of the expected live time.

This completes the discussion of the electronics. We recorded ADC and TDC information for each PMT, the PPAC, as well as using various ADC and TDC's to record trigger type information. **Table 3.2** lists all of the signals recorded for each event for reference.

3.3 Calibration

3.3.1 Collection of ^{252}Cf Data

During our initially scheduled beam time, the beam facility experienced an unexpected outage. This outage stopped all neutron beam production. One benefit of this outage was the ability to attempt to calibrate and study the response of our new detectors. To accomplish this, we needed a neutron source, preferrably similar in behavior to the uranium PPAC we would be using in the actual data analysis. Fortunately, this concern had already arisen for the other groups studying fission and a PPAC with a single cell of ^{252}Cf had been constructed. This PPAC was constructed and behaved in the same manner as the ^{235}U PPAC, save that the element that is electroplated onto the target cell is californium. ^{252}Cf is an actinide that has a spontaneous fission decay channel. Once fission occurs, prompt neutrons can be shed in spontaneous fission as well. The ^{252}Cf(0,f) prompt fission neutron spectrum has been

Table 3.2: List of all relevant data signals for ^{235}U measurement.

Signal	Number of Channels	Data Type
Data Signals		
Bar α	4 PMTs	ADC/TDC
Bar β	4 PMTs	ADC/TDC
PPAC	1	ADC/TDC
t_0	5	TDC
Trigger Bits		
Coincidence Triggers		ADC
n Singles Triggers		ADC
PPAC Singles Triggers		ADC
Scalers		
Coincidence Triggers		Counter
n Singles Triggers		Counter
PPAC Singles Triggers		Counter
α-Even Layer Events		Counter
α-Odd Layer Events		Counter
β-Even Layer Events		Counter
β-Odd Layer Events		Counter
Clock		Counter
Clock with Veto		Counter

well-measured in the range of 300 keV to 2 MeV, which is our region of interest. Since the PPAC behaved in the same manner for both the ^{252}Cf and the ^{235}U, this was an excellent chance to calibrate our experiment. There were a number of benefits to be gained by using this source:

1. Collect real, meaningful data with the experimental setup.

2. Debug electronics and data acquisition system.

3. Development of an anaysis method, since ^{252}Cf data mimicked the uranium

data (albeit with a different distribution).

4. Any algorithm developed for determining the prompt neutron energy spectrum would also work for ^{235}U, after properly accountig for the t_0 signal.

5. Given the well-known energy spectrum for ^{252}Cf, we could calibrate our detector response using this energy spectrum.

The beam failure, despite being a setback, provided an ideal way to characterize the expected response of the detectors. With this in mind, we collected data using the ^{252}Cf source using the same experimental setup as our final data.

We used the same electronics as described in the previous section. The main difference was that we removed the t_0 veto from the MASTER trigger requirements, and there were no t_0 stops. The same method of starting the data acquisition was used: a common start mode for the TDC which was triggered by the same three trigger types.

A second difference in the electronics was one of data acquisition speed. When this source data was recorded (March 2014), the CMC203 module that is the center-piece of the low dead time data acquisition system had not yet been integrated into the system. Due to this, we were using the original LeCroy 4301 and LeCroy 4302 combination to control the data acquisition. This combination has a significantly higher read-out time, which was further increased by a failure in the 'block-read' mode of the LeCroy 4302. Since we could not read blocks of data, a word-by-word method was required. Each word read required 0.5 ms due to USB latence. The dead time in this calibration data was $\sim 50\%$ due to this.

3.3.2 Neutron Bar Response Calibration

To begin the analysis of the ^{252}Cf calibration data, we first calibrated our detectors and data acquisition method. There were two systems to calibrate: the ADCs

and the TDCs. To calibrate the neutron bar ADCs, we used a gamma source with a known energy. We collected data with this source near the bar and then collected data with no source. This allowed us to subtract the background spectrum from the gamma collected spectrum, highlighting events due to the gamma source. Our plastic scintillator, along with not allowing pulse shape discrimination, does not show photopeaks. Instead, we relied on Compton scattering as the method of determining the ADC-to-energy calibration.

To do this calibration, we constructed the geometric mean ADC $(\overline{ADC})$, the definition of which is shown in **Equation 2.6**. This variable construction was required due to the elongated nature of the bars. We were looking for a 'sharp edge' in the spectrum, and the absorption of light along the bar broadens this edge until it is no longer visible in the spectrum. By forming the geometric mean, we removed this position dependence and the associated broadening of the spectrum. To form the mean, we first looked at one of the raw ADC spectra for the neutron bar in order to learn how to combine the two ADC spectra. A raw neutron bar ADC spectrum is shown in **Figure 3.16** for coincidence events. There are two features we must examine: the spike at the low end of the spectrum and the 'start' of the true spectrum, which appears around 100 channels in this plot. The spike at the low end of the spectrum is known as the pedestal and is the value recorded by the data acquisition system when there is no event in the channel. This value was not exactly zero due to noise in the system. In our system, the ADC signals were passed through a 100 nF capacitor, which removed DC offsets and a large portion of the low frequency noise in the signal. This resulted in a small width to the pedestal and localized it to a few channels. The pedestal's centroid will act as the zero point for our geometric mean combination, which is why it was subtracted from the ADC value in **Equation 2.6**. The other point of interest is the start of the 'true spectrum.' Since we wanted to create a single quantity out of two quantities, we had to make sure we
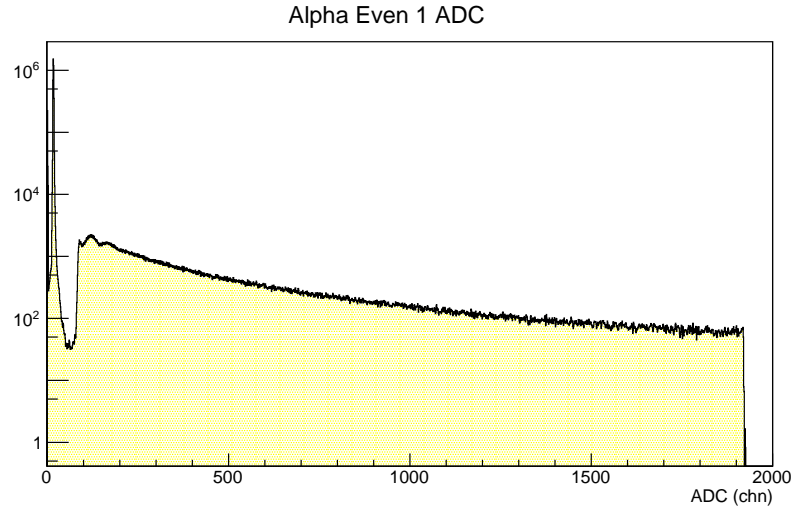
Figure 3.16: Example raw ADC spectrum from neutron bar.
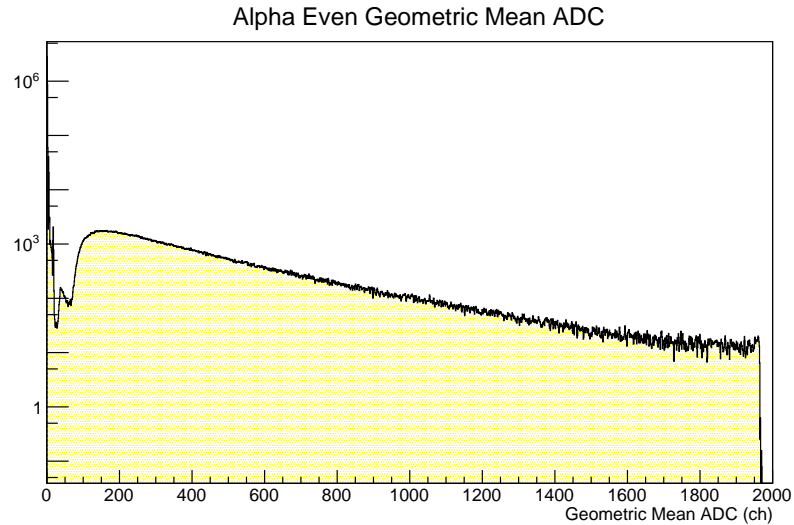
Figure 3.17: Example geometric mean ADC spectrum from neutron bar.

were comparing 'apples to apples.' This required that the threshold for true events was similar in the two spectra that are being combined into one. After subtracting the correct pedestal value and having similar thresholds for analysis, the geometric mean was computed on an event by event basis. $\overline{ADC}$ is shown for the same event set as the raw spectrum in **Figure 3.17**.

We used the gamma source data to find a 'channels/MeV' conversion for each pair of PMTs. For our calibrations, we used two gamma ray sources: ^{60}Co and
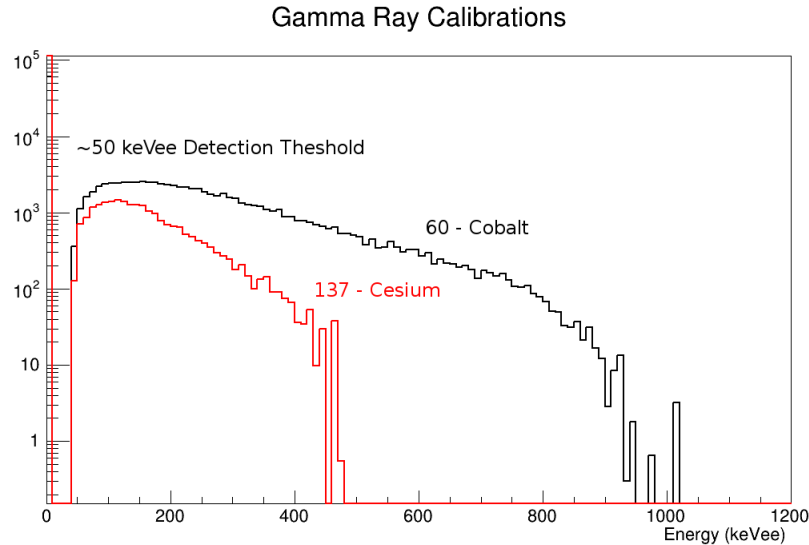
Figure 3.18: Gamma ray source calibration spectra. The calibration is made using the cobalt spectrum and checked against the cesium Compton edge.

^{137}Cs. The cobalt source has a Compton edge at 975 keV. The cesium source has a Compton edge at 477 keV. For our calibration runs, we collected one source per bar, then switched the sources. This allowed us to isolate each source in its individual run instead of collecting all of the gamma rays at once. We also collected room background for the same length of time as the gamma ray collection. During these runs, the ^{252}Cf source was still in the experimental area, so we also required that there be no coincidence between the PPAC and the neutron bar in those events which we analyzed for calibration. In the background subtracted spectrum for ^{60}Co, we found the Compton edge and then noted the channel where it occured. The value of the Compton edge is determined by the center point of the edge. Since we knew this value must be 975 keV, this set the 'channels/MeV' calibration. We double checked this calibration by plotting the ^{137}Cs spectrum with this calibration and making sure that the Compton edge falls at 477 keV. A figure showing both gamma ray source spectra after calibration is shown in **Figure 3.18**.

This calibration also presented another important piece of information, which is marked in the figure: the value of the threshold for event detection. One of the

questions regarding this detector design was, "what is the lowest energy neutron that it can detect?" To answer this question, we must discuss the difference between keV and keVee. Electrons and protons produce different amounts of light as they pass through an ionizing material. Electrons produce much more light per keV lost in the material. Due to this, keVee (kilo-electronVolt electron equivalent) is often used to discuss energy measurements. A threshold of 50 keVee means we can see 50 keV gamma ray events since they scatter from electrons in our detector. Protons produce less light, so we can only see neutrons that have an energy that would produce the same amount of light (via n-p scattering) as a 50 keV gamma ray. The mapping between keVee and keV is not linear in energy and changes based on the material, so there is no quick way to know the exact value of keV given the keVee value. However, in the low energy region for plastic scintillator the rule of thumb is a little less than 6 keV per keVee, meaning that our neutron threshold energy will be roughly 300 keV. This was the first quantitative proof that our detectors were able to measure the energy region lower than 1 MeV.

The second calibration required for the neutron bars was a TDC calibration. The double time-of-flight technique is based on measuring the time of flight with high precision. Given this requirement, an accurate 'ns/channel' was a pre-requisite for this measurement. The manual for the TDC (LeCroy 4303 TFC) offers a method of calculating the calibration point, however this method is less than ideal, as it doesn't test the actual response of the system, but predicts what the system should do. In order to actually test this, we used a time calibrator module. The time calibrator module had two outputs: a START signal and a STOP signal. Both of these were 20 ns wide gates with sharp leading edges. The module had two settings: range and period. The range set the time range to calibrate. Since our TDC had an active window of 500 ns, we set the range to be slightly longer than 500 ns. The period setting adjusted how long after the START gate a STOP gate was generated. For

example, if the period is set to 10 ns, the module will create a START gate, wait N·10 ns, then create the STOP gate (where N is an integer that, when multiplied by the period setting, is smaller than the range setting). Since the range of the integer N spanned the whole width of TDC range by design, the TDC spectrum consisted of a series of peaks that were exatly 10 ns apart. Since we knew the time spread of the peaks and measured the channel spread of the peaks by examining the spectrum, we calculated a 'ns/channel' for each TDC. Multiplying the recorded TDC value for each event by this calibration allowed us to know the time, in ns, that each event occured.

Once the channels for each TDC were converted to real time, we wanted to construct two quantities for the neutron bar: the time difference and the time mean. The first step was to align the time of flight spectra, as the offset for time of arrival was set by many cable delays which were not necessarily evenly applied to each channel. To do this, we relied on the gamma rays created in the fission event. When looking at events that are in coincidence with a fission event, we get a spectrum that looks like **Figure 3.19**. There are two features in this spectrum, the left peak is the gamma flash. These are gamma rays released during the fission event. Gamma rays move at the speed of light and arrive earlier than the neutrons. The neutrons are the right 'bump.' Since we know that the flght path was 1 m, we know that the gamma rays should arrive after 3.3 ns. Before corrections, the gamma rays appear at a shifted point in the spectrum. For each PMT, we used this gamma flash to align the time of flight spectrum. **Figure 3.19** is an example time of flight spectrum after adjustment.

The mean time spectrum was made by combining the adjusted time of flight spectrum for pairs of PMTs. These were combined as a pure average.

$$\overline{ToF} = \frac{1}{2}(ToF_R + ToF_L) \tag{3.1}$$

Since this value is position independent, it was an ideal quantity for calculating the
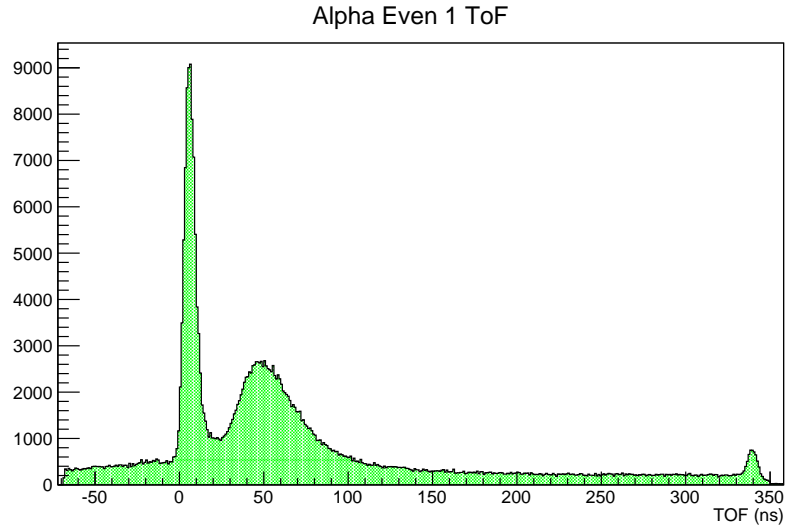
Figure 3.19: Example neutron bar time of flight spectrum.

energy of the prompt fission neutrons. The mean time of flight spectrum looks similar **Figure 3.19**, since it is just an average of times seen by two tubes seeing roughly the same time. While the mean time of flight and the 'raw time of flight' for an event may have a different value, the overall structure of the two spectra is the same.

The time difference was constructed by doing a simple subtraction of the two ToFs. **Figure 2.16** and **Equation 2.5** demonstrate the reason why we want to construct the time difference. As a brief reminder, if we have the time difference between the two ends of the detector, we can use the speed of light within the material to determine the location of the interaction within the bar. A general time difference spectrum is shown in **Figure 3.20** for neutron bar events with a coincident fission event. After converting the time difference to centimeters, we get **Figure 3.21**. For the duration of this chapter, this measurement of position will be called 'x-position'. We see that in the x-position spectrum, the edges of the 'main block' are at ± 50 cm, precisely the width we expect to see since the bar is 100 cm, with 0 cm at the center point in this parameterization. The long tails hint that the position resolution may be larger than expected

In order to determine the resolution of the x-position method, we used a col-
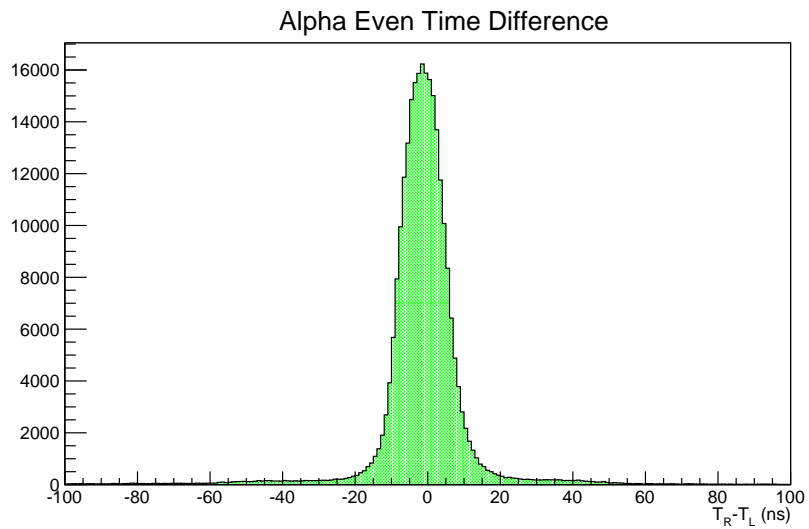
Figure 3.20: Example neutron bar time difference spectrum.
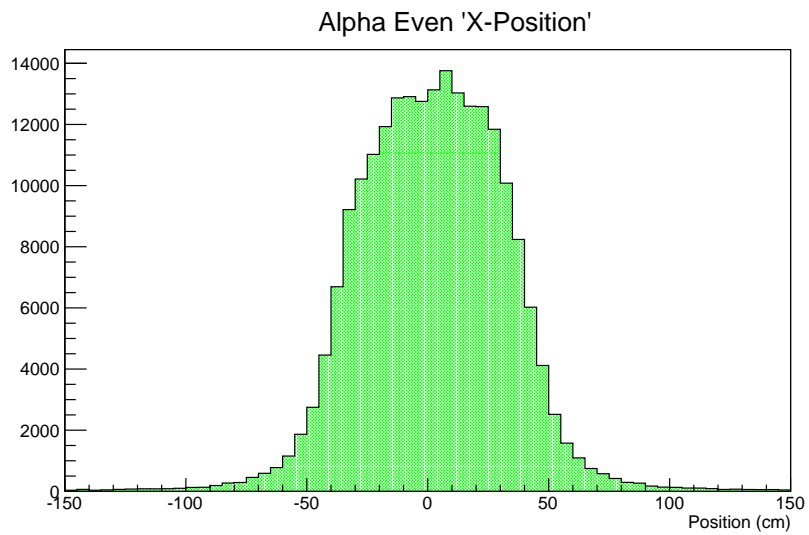
Figure 3.21: Example neutron bar 'x-position' spectrum.
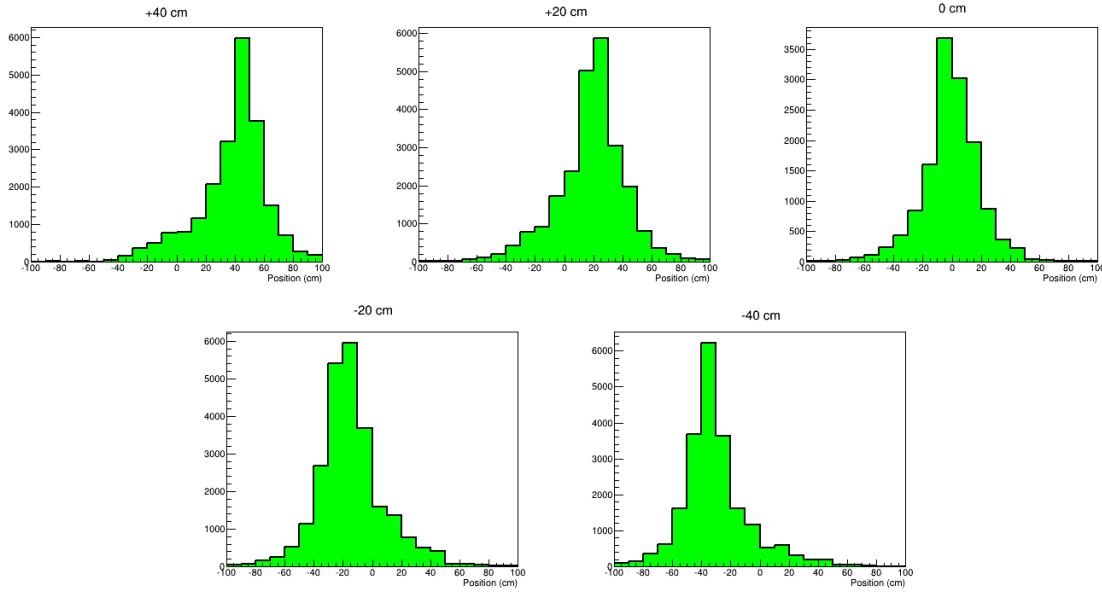
Figure 3.22: Gamma ray x-position calibration data. Using a collimated gamma ray source, we place the source at known points along the bar. We then look at the resulting x-position spectra to test the resolution and accuracy of the x-position reconstruction algorithm.

limated gamma source. We moved this source along the length of the bar, using a 1.5 inch long, 0.25 inch bore lead collimator to localize the interaction point of the gamma rays. We recorded data for each position, as well as a background run in order to subtract the room background from the data. Data was collected at x = (-40, -20, 0, 20, 40) cm. The x-position data from these runs is presented in **Figure 3.22**. We see that the centroid is properly shifted within the spectrum, and that we locate the centroid reliably. However, the width of the peaks is wider than what we desired. For all five peaks, $\sigma \approx 13$ cm. This is approaching the best case scenario for this design (as will be discussed in **Section 3.4.2**). A 13 cm spread in distance, when calculating with the speed of light in the plastic, is only a 0.68 ns time difference spread. Given the width of the bar, the various paths that the light can take to arrive at the PMT, and the time resolution of the detector, a 0.68 ns FWHM is not unreasonable. Simulations predict that the resolution is dependent on the layer thickness.

78

3.3.3 Analysis of ^{252}Cf Data

Once the neutron bar signals were calibrated, we examined the ^{252}Cf data. The events that we wanted to analyze were those events which have a fission fragment in the PPAC as well as a neutron in the neutron detectors. In the electronics, these were labeled as 'coincidence' events. However, the requirements made in the electronics were not stringent enough to truly identify events of interest. To further restrain which events were analyzed, we used the trigger bits and the PPAC timing spectrum.

As discussed in the electronics section, every trigger sent to the data acquisition system also sent a gate to an ADC. The ADC integrated the gate, determining how much charge was contained within the gate. Since the gate was always the same size, we see a spike in the ADC that corresponds to events when the gate was present during data collection. Any events where the gate was not collected should show up in the pedestal. These are events from a different type of trigger. **Figure 3.23** shows the trigger bit spectrum for coincidence events. For the ^{252}Cf data, this spectrum is a bit strange. We expect there to be two features in this spectrum, the pedestal and the coincidence event peak. However, for this data, no pedestal is shown. Also, instead of seeing a single peak, we see three peaks near one another. These oddities are linked to an electronic issue which was found after the data was collected. A connector linking two different cable types was causing distortions to the coincidence gate, including reflections. The ^{252}Cf data was collected in March 2014 and the broken connector was not found or corrected until October 2014. To select true events, we selected the first peak. The second and third peaks correspond to events that have a secondary, reflected gate which was also integrated, and the timing for these events is suspect. A loose cut around this first peak selects those events which had a true coincidence gate. The small percentage of events that have a trigger bit value lower than the peak are events in which the coincidence was the second event type registered in the same event, such that the gate was only partially integrated (e.g. a neutron single event
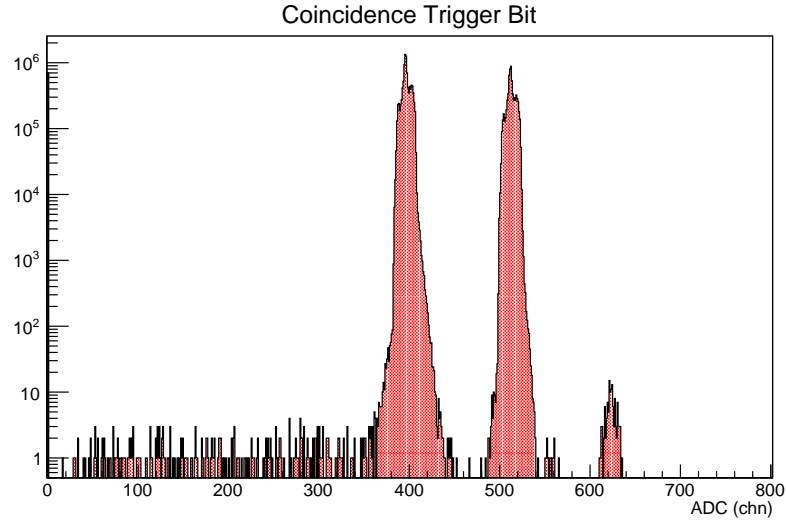
Figure 3.23: Trigger Bit Spectrum for Coincidence Events. The multiple peaking is due to an electronics failure.

happened 40 ns before a coincidence, so the neutron single event set the timing for the data acquisition). Since these events are 'tainted,' we ignore these in our analysis and plan to correct for them later.

One of the complications which the trigger bits do not address is identifying the type of reaction which occurred in the PPAC. Though fission is the event type of interest, it is not the only decay channel available to ^{252}Cf. **Figure 3.24** shows a sample ADC spectrum for the PPAC, this plot is from the ^{235}U data run but the spectrum is similar for ^{252}Cf. The full spectrum was taken with the beam on, the 'alphas only' spectrum with the beam off. This shows that the full spectrum is a sum of alpha decays and fission fragments, which is the right bump in the full spectrum. We are only interested in those coincidence events which had a corresponding fission fragment. To select these events, we set a threshold at the minimum value of the valley between the alpha events and the fragment events, analyzing only those events which had an ADC value larger than the threshold. Adding this requirement in tandem with the coincidence requirement, we see a PPAC ADC spectrum that looks like **Figure 3.25**. The threshold causes the truncation of small pulse-height events.

80

A small portion of true fission events are lost by applying the threshold, cutting off the tail of the distribution which sits underneath the alpha decay events. This can be corrected for by fitting the peak and determining how many events are lost by using this technique. Similarly, we allow some alpha style events to make it into our analysis, since the tail on the alpha events extends into the allowed range. This must also be accounted for.

The strange shape on the right-hand side of the distribution in **Figure 3.25** was due to over-saturating the pre-amplifier for the PPAC. This was adjusted mid-way through the data collection when the problem was diagnosed, however this is simply a gain problem, and those events that are in the peak and subsequent decay are valid fragment events. The analysis for this data accounted for the gain shift associated with adjusting the pre-amplifier, though this plot does not show the adjustment.

The PPAC timing spectrum was also used to identify event types. Due to the delays applied to the triggering gates (see **Figure 3.11**), the PPAC always set the absolute timing of the trigger if it saw the event. Thus, we expected to see a self-timing peak for coincidence style events. We also expected a peak at the maxiumum allowable TDC value, which corresponds to n-Single events, so there was no PPAC response . Finally, we expected to see a second self-timing peak that corresponds to the PPAC-Single events, which had a later trigger time than the coincidence events by construction. **Figure 3.26** shows the PPAC TDC for all event types. The left peak corresponds to coincidence trigger events, the center peak contains the PPAC-Singles events, and the right peak is the 'time-out' peak for the TDC and contains those events that have no PPAC response (n-Singles).

When we looked for events to analyze we made the following requirements:

- The event was labeled as a coincidence in the electronics (coincidence trigger bit).
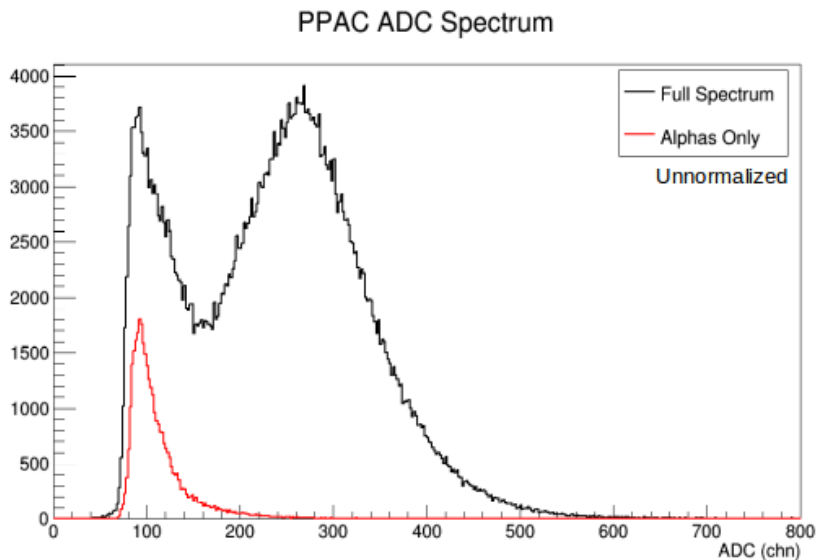
Figure 3.24: An example PPAC ADC spectrum. This data was taken with the ^{235}U PPAC. The full spectrum was taken with the beam on, the 'alphas only' spectrum with the beam off. This shows that the full spectrum is a sum of alpha decays and fission fragments, the right bump in the full spectrum.
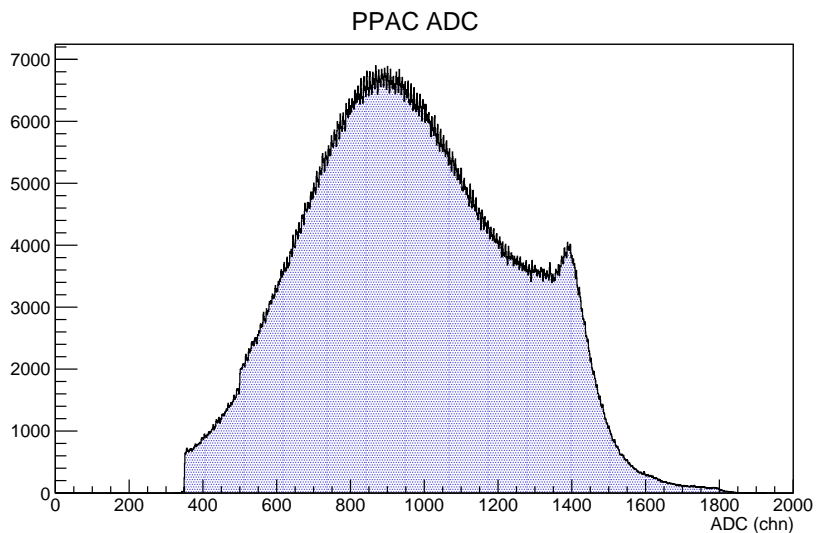
Figure 3.25: The PPAC ADC spectrum, selecting out those events in the the PPAC which are analyzed in the ^{252}Cf calibration data. The hard cut on the left side of the spectrum is due to applying a threshold. The odd shape on the right is due to saturation in the pre-amplifier and was corrected for in later runs.
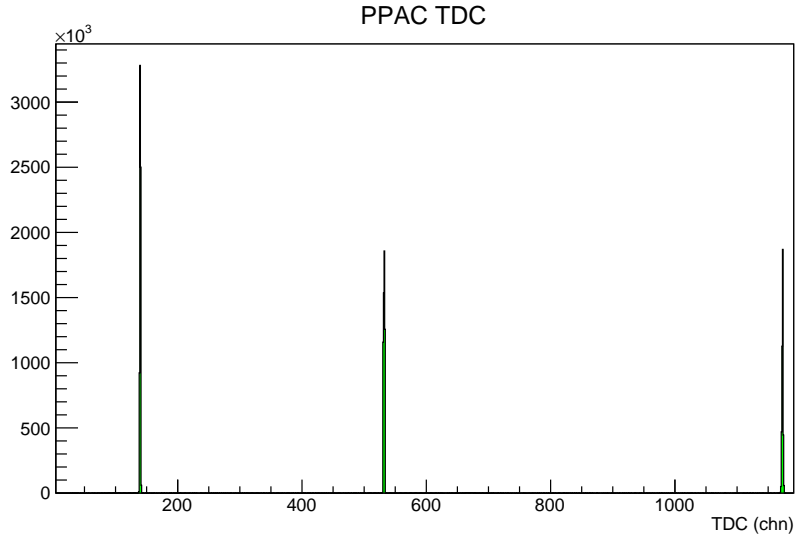
Figure 3.26: The PPAC TDC spectrum for all event types in ^{252}Cf analysis. The three peaks correspond to the three types of triggers being used in the experiment.

- The event had a corresponding fission fragment (PPAC ADC cut).

- The event was in the 'coincidence self-timing peak' in the PPAC TDC.

For these events, we expect to see a response in the neutron bar that is time correlated with the fission fragment. This limits us to two types of events: gamma rays and neutrons emitted by the fission fragments while decaying into a stable state.

Figure 3.27 shows a neutron bar mean time of flight spectrum for events that pass the cuts described above. The gamma ray events start at 3.3 ns (as discussed in **Section 3.3.2**). The structure starting around 30 ns are the prompt neutrons from the fission fragments. We are interested in these events, and want to find a way to select these events from the background.

We used a technique for separating interesting neutron events from those that are accidentals that involved the geometric mean ADC. The ADC value is essentially a measurement of how much light is produced by an interaction in the plastic. This value is scaled by losses during photon transport, but should be energy independent in the range of wavelengths produced by our scintillator. A high energy neutron
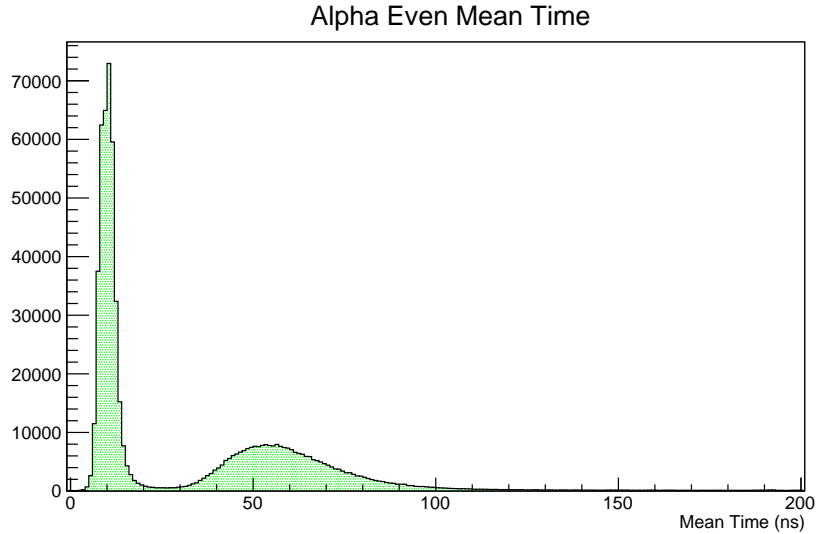
Figure 3.27: Neutron bar mean time spectrum for coincidence events.

produces more light than a lower energy neutron, so we expect that those neutrons with a lower time of flight would have a larger maximum ADC value (maximum because the neutron does not necessarily impart all of its energy to the proton). To investigate this, we looked at a two-dimensional plot of geometric mean ADC versus mean time of flight. A plot of this type is shown in **Figure 3.28**. We see two main features, and they again correspond to gamma rays and neutrons. Near 3.3 ns, we see that the gamma rays span the full range of the ADC while being narrow in time of flight. More of interest, we see that the neutrons do follow the expected behavior, with high ADC correlating with short time of flight. This 'wedge' shape can be used to select events of interest. A two-dimensional cut is shown in **Figure 3.29**. When combined with all the previous cuts, this selects only properly time correlated neutrons with a corresponding fission fragment and a small, but appreciable, background which will be discussed later.

One of the reasons for designing our detectors with multiple layers of thin plastic was to help reject backgrounds. The thin plastic has excellent time resolution ($\leq$ 2 ns) which we used to make the time of flight part of the two-dimensional cut. However, the thin layers were also used to discriminate event types based on whether the light
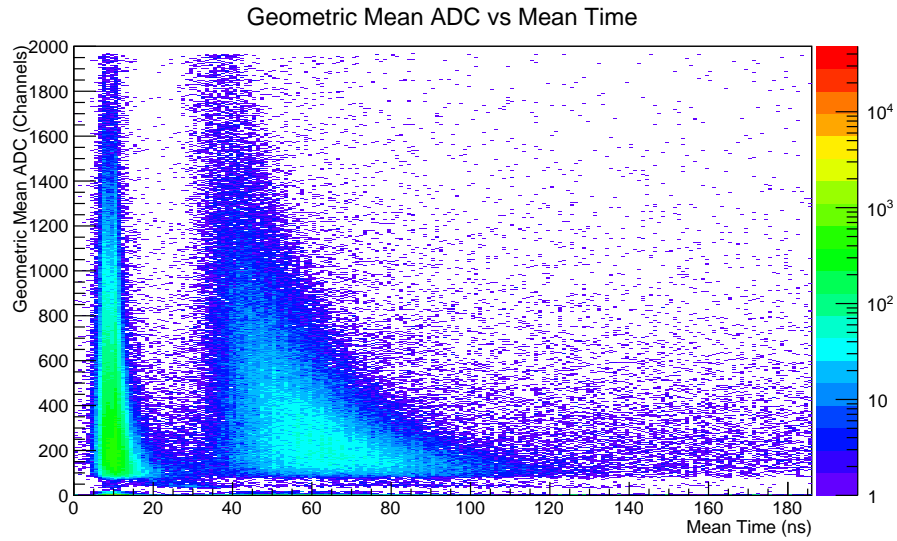
Figure 3.28: Geometric mean ADC versus time of flight for fission correlated events.
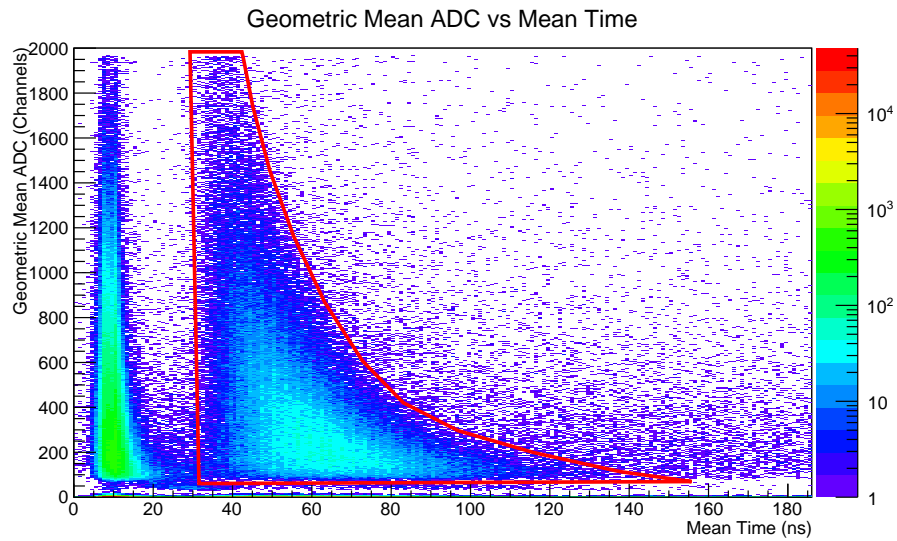
Figure 3.29: Geometric mean ADC versus time of flight for fission correlated events with the applied two-dimensional cut shown in red. This cut selects the events which are at the appropriate time to be neutrons, and have the appropriate ADC response.

is seen in adjacent layers or not (as described in **Chapter 2**). We are interested in those events which have light in only one layer of plastic, since these are most likely to be neutron events. To apply this requirement, we designed an algorithm to sort data based on the responses of the PMTs, checking for responses in multiple layers. For each PMT, we look at the TDC spectrum. An example raw TDC spectrum is shown in **Figure 3.30** for all events and event types (showing all event types creates the structure seen in the plot). For this TDC, all events that have no response time out near channel 1180. We are interested in knowing which PMTs had a response for each event. So, for each PMT we can select the region between ~ 50 - 1180 channels and have a variable for each PMT that is set as true for an event in that region and false for an event outside. This 'response' variable can be used in the data replay to determine which layers saw the event and which did not. Let's examine an example event, with each PMT response labeled as either true or false.

α-Even 1: True

α-Even 2: True

α-Odd 1: True

All others: False

We first compare each PMT with its mate (the PMT viewing the same layer), since we are only interested in those events seen by both ends of the bar. In this example, only one PMT in the α-odd pair is active, so those layers are considered inactive. With both PMTs responding, the even layers in bar α would be marked as a valid event for this example. The algorithm then checks if there was a valid event in bar β. If so, this event is disregarded as the timing is suspect when both bars are activated, and the energy conversion cannot be trusted. These 'multiple neutron bar' events will be an appreciable portion of the data, as the neutron multiplicity for ^{252}Cf(0,f) is ~ 3 and the gamma multiplicity is ~ 7. The percentage of events that are rejected in this manner will be estimated and corrected for. Finally, the algorithm checks if there was
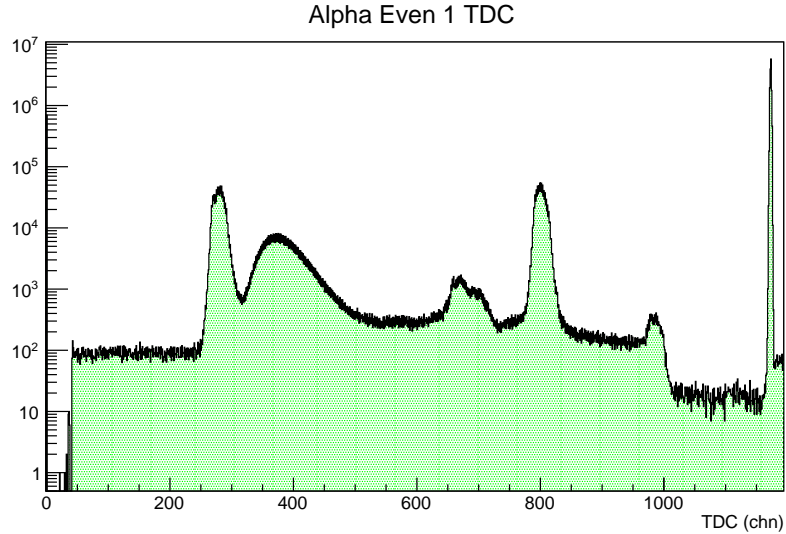
Figure 3.30: Raw neutron bar TDC for all event types.

a response in multiple layers (even and odd). If so, this event is most likely to be a gamma ray and will be rejected. This will reject a portion of those backgrounds that cannot be separated using timing methods, such as time-uncorrelated backgrounds. For each event, we use this method to decide if it is a single-layer or multi-layer reaction. We make a final cut to those events which pass the two-dimensional cut, only allowing events which are both in the two-dimensional cut and only seen in a single layer to be treated as prompt fission neutrons. In this example, the event would be labeled as single layer and allowed into the analysis.

With this algorithm developed, we had an ideal method for determining the background rejection capability of the detector design. To examine this, we looked at the neutron bar time of flight spectrum for all coincidence events and for only 'single-layer' coincidence events. **Figure 3.31** demonstrates the rejection capability. We expected that the rejection capability would be between 30% and 40% for gamma ray events since the gamma rays are ~ 1 MeV for ^{252}Cf fission events. This is based on Shoniyozov's simulations shown in **Figure 2.6**. When we investigated the integrated efficiency, the region from 0-30 ns (the gamma ray region) shows a rejection rate of 31.24%. We expect to also see some of the neutron bump rejected, both since we

are throwing out background and because some portion of the neutrons, especially at higher energies, will be seen in multiple layers. If we integrate the entire 'neutron region', we see a rejection rate of 18.75%. This was a bit higher than expected. However, we are mostly interested in events that are below 1 MeV, so we integrated the region between 72-150 ns (1 - 0.232 MeV). This region sees a 15% rejection rate, which is inline with the Monte Carlo prediction.

Using the cuts discussed, we are selecting those events which we wish to further analyze to determine the energy of the neutron. This can be done using a relativistic calculation which converts time of flight into energy.

$$L_c = \sqrt{L_0^2 + x_{bar}^2 - 2\, L_0\, x_{bar}\, cos(\theta)} \tag{3.2}$$

$$v = \frac{L_c}{t_n}$$

$$\gamma = \frac{1}{\sqrt{1 - \frac{v^2}{c^2}}}$$

$$E_n = (\gamma - 1) \cdot M_n \cdot c^2 \tag{3.3}$$

In this conversion, L_c is the total flight path length, L_0 is the distance from the target to the center of the bar, x_{bar} is the position of the interaction along the plane of the bar which is calculated for each event with the time difference, θ is the angle between L_0 and the plane of the bar, t_n is time of flight for the neutron, and M_n is the neutron mass in MeV. The time of flight used in this calculation will be the mean time of flight (the same value used in the two-dimensional $\overline{ADC}$ vs time of flight plots).

By projecting the two-dimensional plot into a one-dimensional plot of energy, we also afford ourselves a simple method for subtracting the time-independent background. **Figure 3.32** shows our method for selecting the background events. In this method, we artificially subtract time from the mean time for each event. This forces the entire two-dimensional plot to 'shift left'. By doing this, we are now applying the graphical cut to the time region beyond the region of interest. At this later time in the spectrum, the only events recorded are beam-independent backgrounds, as seen
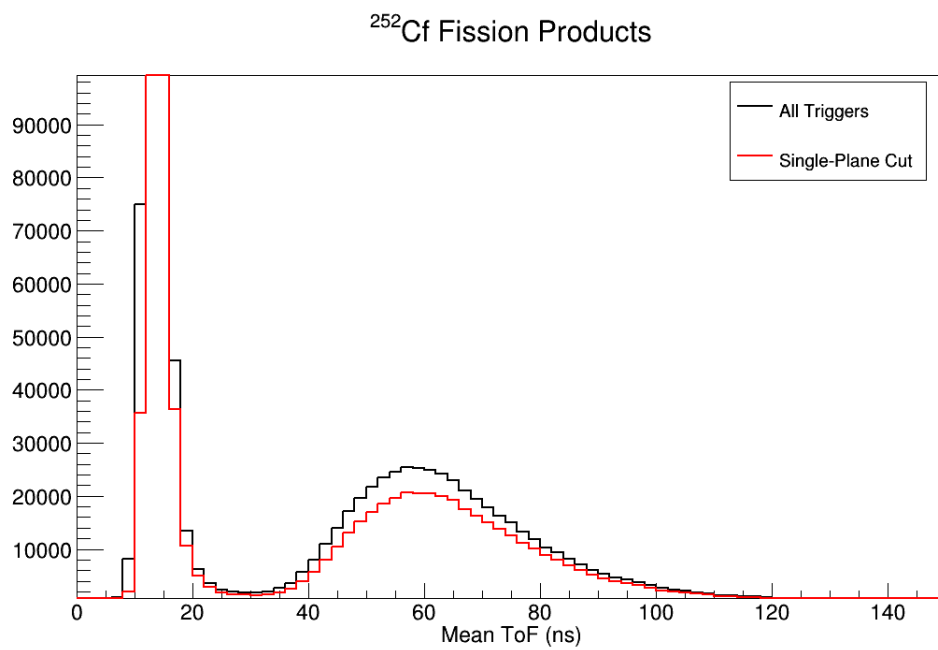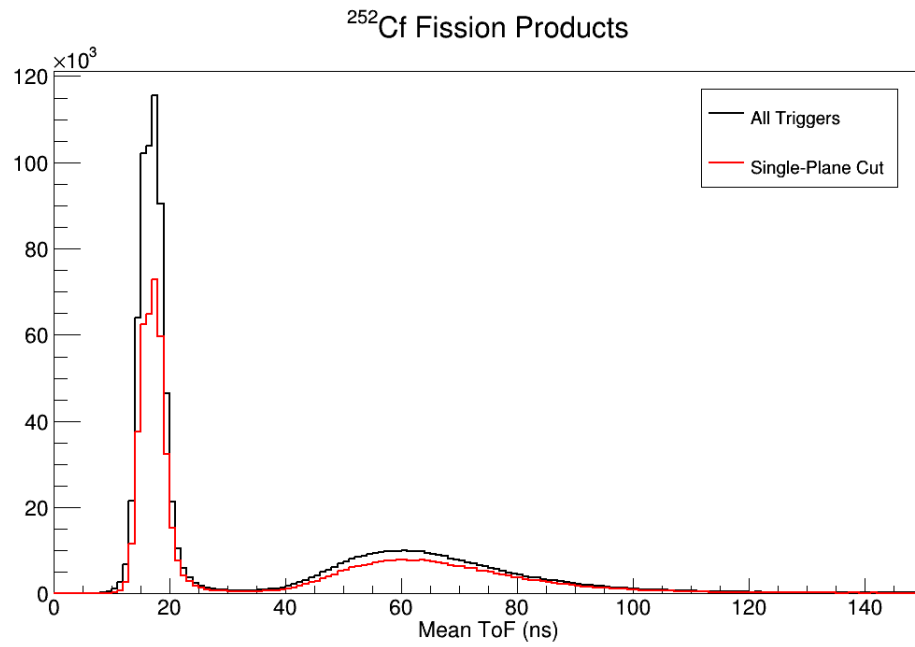
Figure 3.31: Neutron bar time of flight spectrum demonstrating the gamma rejection ability of using the 'single-layer' event cut. *Top*: Full Spectrum. *Bottom*: Zoomed in on the neutron events.
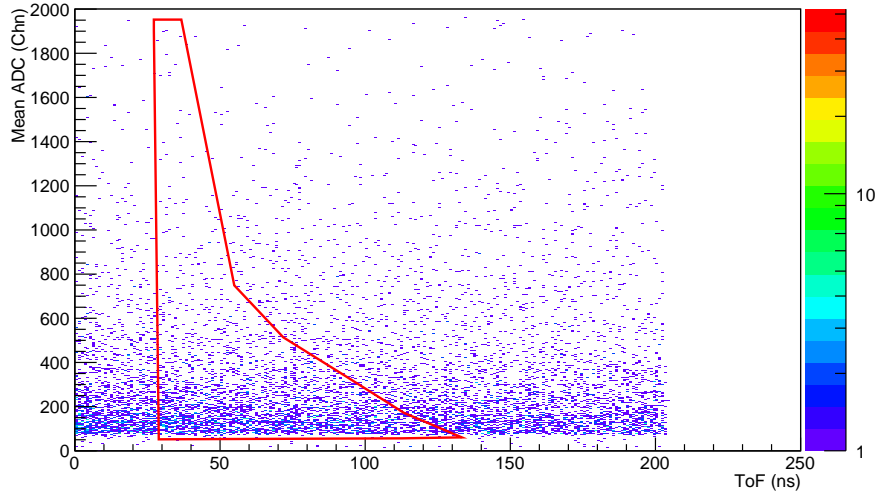
Figure 3.32: Geometric mean ADC versus neutron time of flight, with the time adjusted such that we select the time-independent background.

by the constant-in-time nature of event distribution. By using the same cut on the background events, and using the same time of flight to energy conversion, we can see how many background events fall within each energy bin.

With prompt neutron events and background events properly selected, we constructed an energy distribution. Using **Equation 3.3**, we calculated the energy for each neutron event. **Figure 3.33** shows the energy distribution for neutron events with a coincident fission fragment, the energy distribution of the time-independent background, and the corresponding two-dimensional cuts to select the events in each energy spectrum. In the energy spectrum for the prompt fission neutron events, the backgroud has already been subtracted. The background spectrum does have a peak in the lower energy region despite the background being constant in time. This is due to the nature of the time to energy conversion. As the energy decreases, the range of time that falls within each energy bin increases. This comes from the time dependence of the time to energy conversion being $(1 - \frac{1}{t_n^2})^{-0.5}$ (from γ in **Equation 3.3**).

The energy spectrum in **Figure 3.33** shows a number of positive results for
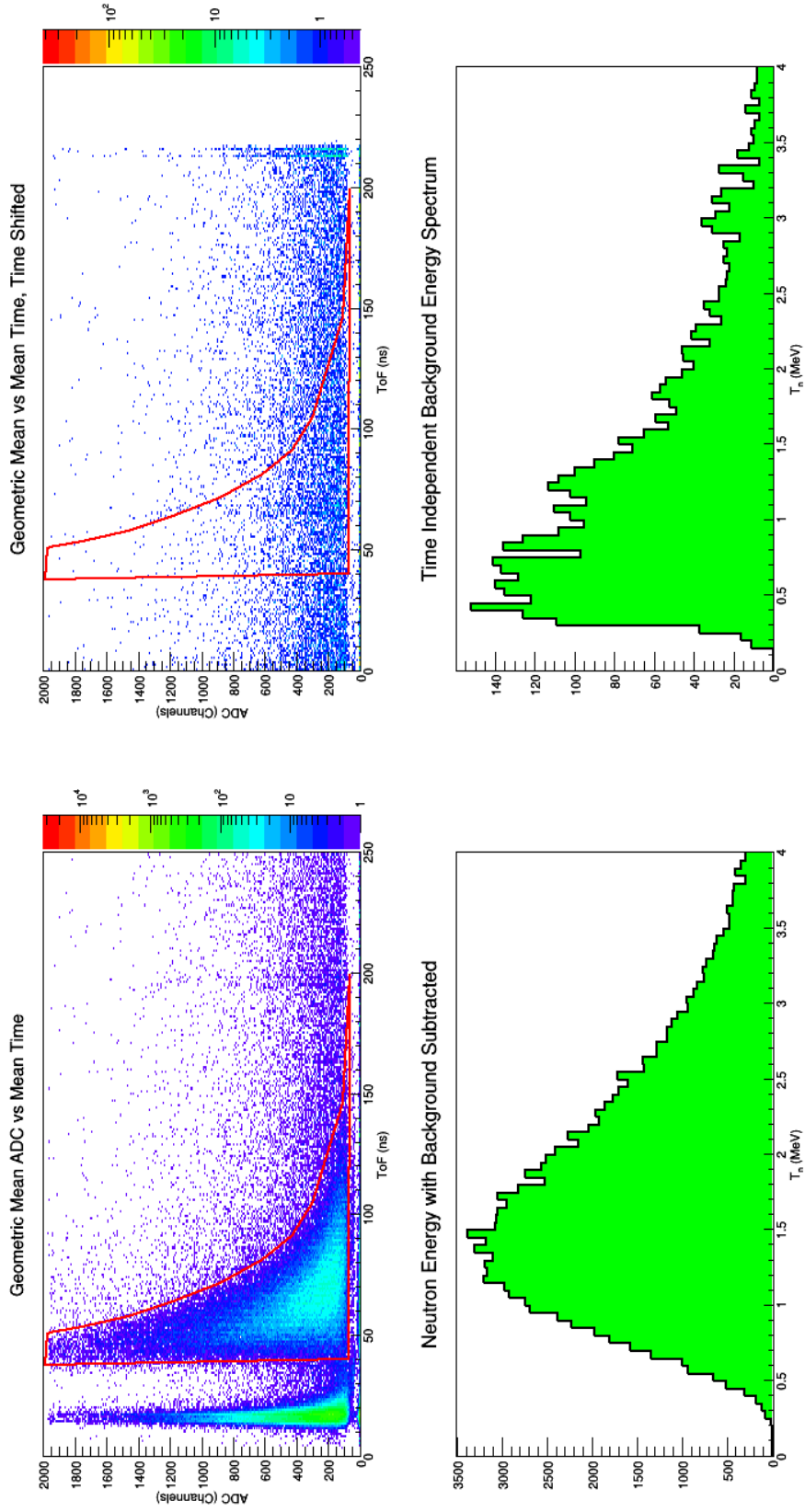
Figure 3.33: *Top left:* The two-dimensional cut that selects prompt fission neutron events. *Top right:* The two-dimensional cut that selects background events from the time-shifted spectrum. *Bottom Left:* Measured prompt fission neutron energy spectrum for ^{252}Cf with backgrounds subtracted. *Bottom Right:* The energy spectrum for background events.

the experiment. First, this demonstrates that our detectors are capable of selecting out fission correlated neutrons and determining their energy. Second, it shows that we are measuring neutrons with energies as low as 300 keV, as expected from the calibrations. The target for this measurement was to measure below 1 MeV with an ultimate goal of measuring below 500 keV. This data is the first direct confirmation of the ability to make this measurement.

The shape of this spectrum is incorrect. The prompt fission neutron energy spectrum for ^{252}Cf has been well-measured in previous years and is known to peak around 0.7 MeV. Our spectrum clearly peaks at more than 1 MeV. However, this is just the raw data and does not take into account the detector efficiency, which will have a very strong energy depedence. To correct for this, we used a Monte Carlo simulation. This is discussed in **Section 3.4.2**.

After correcting for efficiency, we must also use the correct units for the comparison. The standard units for presenting an absolute measurement of the prompt fission neutron spectrum is yield/MeV/fission/steradian. To achieve these units, we divided our yield by the bin width and then divide by the total number of fission events. To determine the total number of fission events, we added the number of coincidence events with the total number of PPAC single events. The total number of PPAC events is found by multiplying the recorded number of PPAC single events by the pre-scaler setting. The resulting corrected spectrum is shown in **Figure 3.34**, for the center of neutron bar α. In the shown plot, we have not made an absolute measurement and are only comparing the shape of the spectrum as a diagnostic, which is why the axis is labeled as 'arbitrary units / MeV'. Both the data and evaluation shown are arbitrarily normalized.

We see that the spectrum, does not agree well with the shape of evaluation or the previous data. A great deal of effort was invested in attempting to correct this by investigating the Monte Carlo inputs, the cuts applied to the data, and the exper-
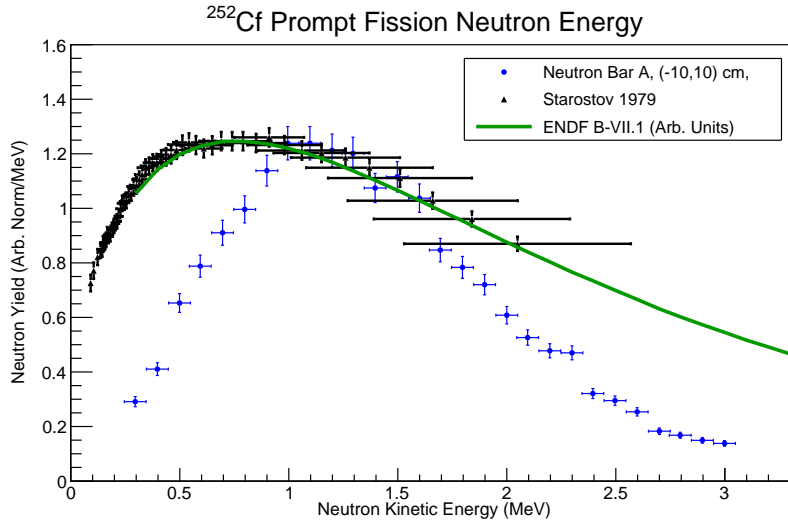
Figure 3.34: The efficiency corrected prompt fission neutron spectrum for ^{252}Cf.

imental method. The Monte Carlo inputs are well understood for plastic scintillator as shown in **Appendix A**, so the output of the Monte Carlo was trusted. To address the possibility of poor of analysis, an independent analysis of the ^{252}Cf data was undertaken by Michael Kovash. His analysis resulted in the same energy spectrum for the prompt fission neutrons. This left only the possibility of problems in the experimental setup.

This ^{252}Cf data was taken in March 2014 and was the first real data collected with this experimental setup. A number of changes were made to the setup after the collection of the ^{252}Cf data as we became better acquainted with the experiment, which resulted in more accurate spectra for later data. Given this retrospective view, there are a number of possible causes for the discrepancy between our data and the previous measurements.

- Improperly tagging coincidence events. One of the main cuts that we use is selecting those events which are coincidences by recording the hardware triggers in the trigger bits. In the ^{252}Cf data, the coincidence trigger bit had an odd structure in the data. Instead of showing a single, non-zero peak, it showed

93

three non-zero peaks which were right beside one another. There are two likely causes. Pile-up events, due to an extremely high counting rate (perhaps due to light leaks), or the bad connector which was replaced in October after the data was taken.

- Time of flight measurement error. In October, when investigating the electronics, a number of questionable connectors were replaced. In particular, the coincidence gate generation had a signal reflection due to a broken LEMO-to-BNC converter. This reflection makes all timing measured relative to this gate suspicious. Since our energy conversion is based on this timing, this broken connector could partially explain the incorrect energy spectrum.

- Light leaks. Great care was taken to stop light leaks, including wrapping the detector frame in black tape. However, during the next use of the detector in October 2014, light leaks were observed. These leaks could have formed during the downtime between experiments, however we cannot rule out that they existed during the ^{252}Cf data run. For data taken after the ^{252}Cf run, a black blanket was wrapped around the detector frame, which lowered the counting rate appreciably. Any high rate caused by light leaks would add fake coinicidences, which could contribute to the incorrect coincidence trigger bit spectrum.

- Data acquisition difficulties. For the ^{252}Cf data, the new data acquisition system (see **Appendix B**), was not yet fully operational. Instead, we were using a hybrid of the system that used the FERA ADC modules, but the memory read required a great deal of time (~ 1 s) due to a failure of the 'block read' mode. This should have no energy depedence, but is an added factor that complicates this analysis.

- Master trigger veto method. For the original data acquisition method, the mas-

ter trigger veto was created using fixed length gates that were generated each time a trigger was sent to the data acquisition. This method, while effective, is not as clean as it could be. With the new data acquisition model, a busy signal is generated by the data acquisition system itself and is of variable length. This veto is only active when the system is busy, and produces a shorter and more reliable dead time. Once again, this artificially elongated dead time should not have an energy dependence. However, by generating the gates externally from the data acquisition system, we increase the likelihood that we are rejecting true events. If we are rejecting true events, there is a possibility of an energy bias.

With all of these complications, the failure to match the previously measured ^{252}Cf prompt fission neutron spectrum is not necessarily fatal to the measurement of the ^{235}U prompt fission neutron measurement. By analyzing this ^{252}Cf data, a method for the analysis has been developed. We have also been able to correct most of the difficulties experienced in the ^{252}Cf measurement, such that the ^{235}U measurement has a higher chance of being accurate.

3.4   Analysis

3.4.1   Analysis of ^{235}U Data

The analysis of the ^{235}U data follows a similar method to the method described for the ^{252}Cf data. We are interested in finding those detected neutrons which have a corresponding fission fragment. After identifying these events, we used the time of flight to determine the neutron energy. One of the complications for this data is that we must now account for the neutron beam which is incident upon the uranium target. To do this, we rely upon the t_0 signal described in **Section 3.2.2**. Since each TDC channel for the t_0 cascade covers 500 ns, each channel overlaps with the

TDCs covering the neighboring ranges. We use the overlapping regions to stitch together all five TDC channels for t_0 into one complete view of the 1.8 μs micropulse from the beam. **Figure 3.35** shows our method for deciding on the 'stitch points' between neighboring TDC channels in the t_0 cascade. In this plot, we have the timing response of two t_0 TDCs. Since they overlap in a small time region, we expect that there should be some region where both TDCs have a response. At all other times, we expect that one of the two TDCs would time-out. In **Figure 3.35**, the region on the left where both TDC's see the same event has a slope of ~ 1. The other regions show at least one of the TDCs registering no response. By knowing which regions overlap, we can then reconstruct the whole time range. **Figure 3.36** shows an entire micropulse of events (1.8 μs) after conversion from TDC to time of flight. The gamma flash is adjusted to occur at 70 ns, which is the time it takes light to traverse the 21 m flight path. The plot is visually subdivided to show the region each TDC section subtends. The sharp drop on the right occurs at the point where the next gamma flash would arrive (1.8 μs + 70 ns). This wrap around limits us to only investigating those events caused by beam neutrons of an energy ~ 600 keV or above, since they arrive before the next gamma flash. The conversion from TDC to time of flight is done by using the time calibrator as described in **Section 3.3.2**.

With the time of flight recorded for each beam neutron, we can then convert this to energy using the same formulation as in **Equation 3.3**, but with the time of flight changed to the time of flight for the beam neutron and the the flight path length changed to the distance between the neutron spallation target and the PPAC. With this information, we can investigate the prompt fission neutron spectrum for fission induced by beam neutrons of a certain energy. This is known as a double time of flight method, since the time of flight from the neutron production target to the PPAC determines the beam energy and the time of flight from the PPAC to the neutron bar determines the prompt fission neutron energy.
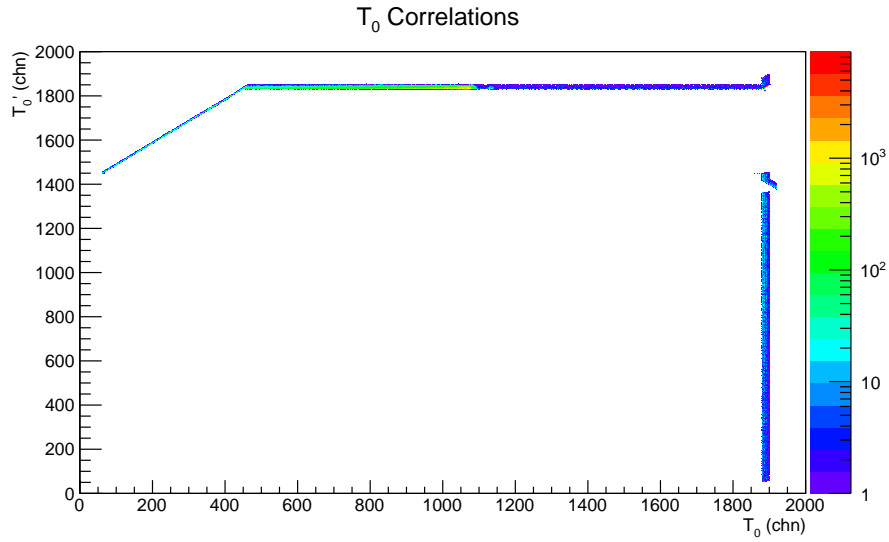
Figure 3.35: Correlations between adjacent t_0 windows in the t_0 cascade. By determining the overlap between adjacent t_0 TDCs, we can construct a single TDC for the entire micropulse. This allows a determination of beam neutron energy for each event.
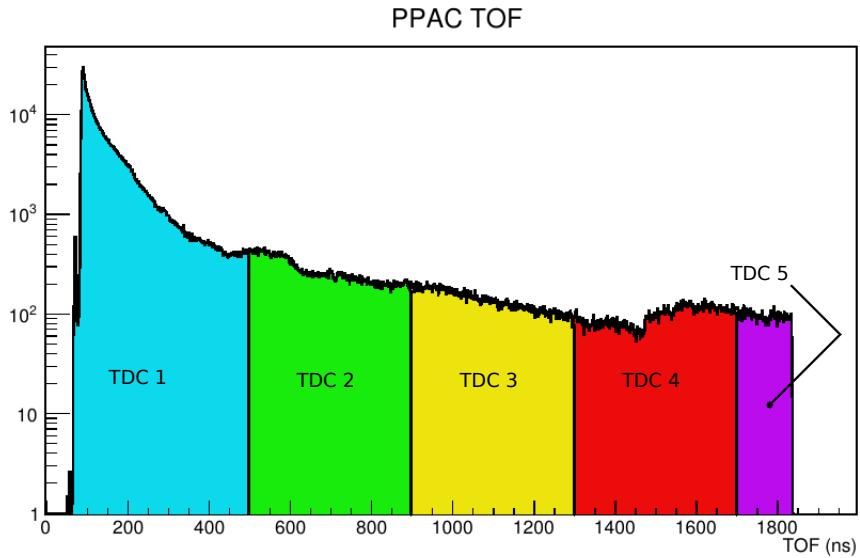
Figure 3.36: Time of flight for beam neutrons. This histogram shows the time of flight for coincidence events, with the full time range available in each micropulse.
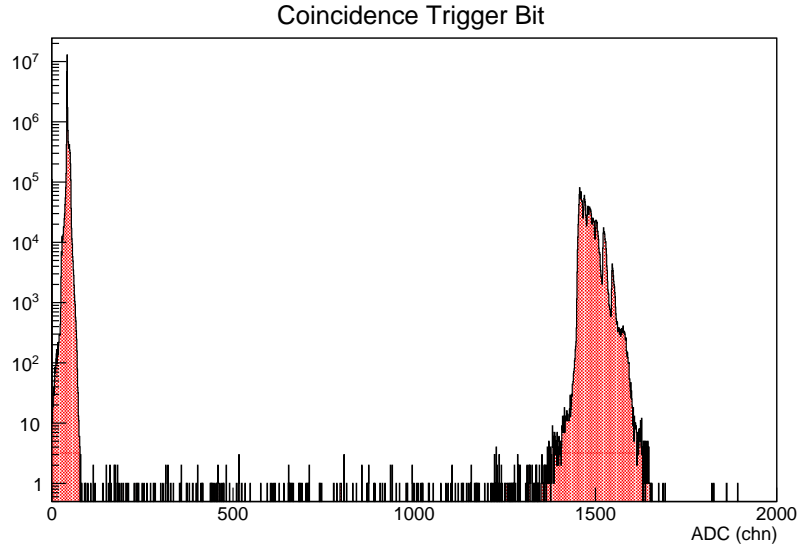
Figure 3.37: The coincidence trigger bit spectrum for all ^{235}U data.

In the ^{252}Cf data there was no beam, so by accounting for the beam in the ^{235}U data and determining the energy of the neutron that caused the fission event, we have reduced the analysis back to analyzing the outgoing neutrons. In the following paragraphs, I will quickly revisit the method for analysis, showing the relevant plots from the ^{235}U data. For a more in-depth discussion of the analysis method, see **Section 3.3.3**. Unless otherwise noted, all following plots of neutron bar response in this section are showing data for bar α's middle region (-10 to 10 cm), for events with a coincident fission fragment induced by a neutron with a beam energy between 1 and 7 MeV. The region of the bar is determined by using the time difference to x-position calculation. The requirement of a beam neutron with the energy of interest is applied to all data in the following discussion.

First, we select those events which are coincidence events. To do this, we use the coincidence trigger bit. Due to replacing a bad connector (compared to ^{252}Cf electronics), this trigger bit spectrum is well-behaved, and features a single active peak and a pedestal which corresponds to non-coincidence events. This is shown in **Figure 3.37**.
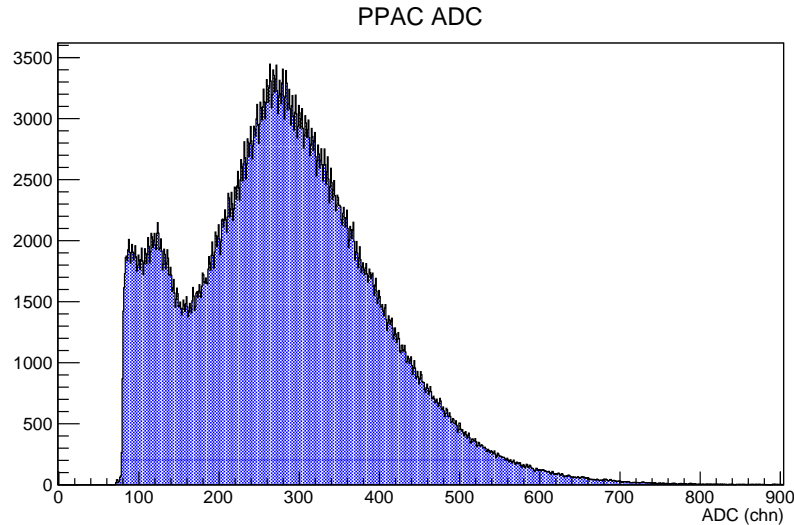
Figure 3.38: PPAC ADC spectrum for ^{235}U data. The structure on the right contains fission fragment events.

We then narrow the selection to only include coincidence events with associated fission fragments. **Figure 3.38** shows the PPAC ADC spectrum. Fission fragments are the right feature in this spectrum, with the left feature corresponding to alpha particle events (these are suppressed due to the beam energy cut, causing the odd shape seen here) and fission fragment events with a small pulse height. By selecting only those events above 150 channels in this spectrum, we can look only at those event which have a fission fragment. This introduces a small systematic error due to not counting those fission fragments 'under' the alpha peak, however all of our results are reported as yield/fission, so this cut only effects our final result as a ratio which makes this cut acceptable without a correction.

Using only coincidence events with a fission fragment, we examine the neutron bar response. Example mean time of flight and geometric mean ADC spectra are shown in **Figure 3.39**. These values are constructed from individual tube data as discussed in **Section 3.3.2**. The gamma flash in the mean time spectrum is used to calibrate the time of flight since we know it arrives 3.3 ns after the fission event. These two signals can be combined into a single two-dimensional plot. Since higher energy
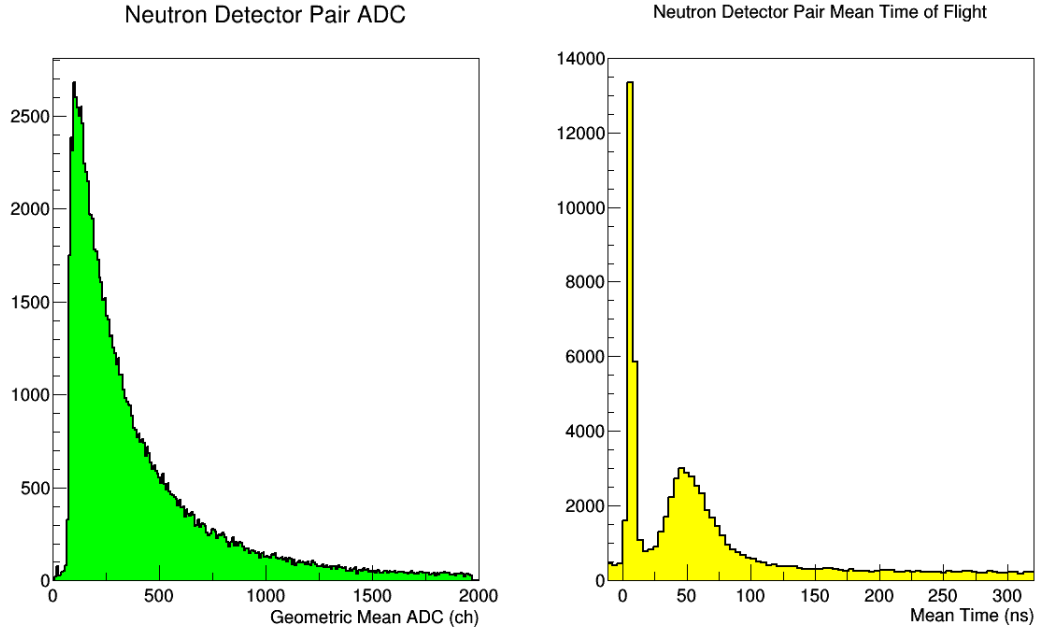
Figure 3.39: *Left*: Geometric mean ADC for bar α-Even layers. *Right*: Mean time of flight for bar α-Even layers.

neutrons create more light via proton ionization in the material, we expect that those events with a shorter time of flight should have a larger ADC response. This two-dimensional plot allows us to select those events which have a proper, neutron-like response as our events of interest. **Figure 3.40** and **Figure 3.41** show this plot both without and with the applied graphical cut to select neutron events.

With these events selected, **Equation 3.3** allows us to convert the time of flight for these events into energy. **Figure 3.42** shows the raw event yields by energy bin for prompt fission neutrons. This data, once corrected for energy-dependent detector efficiency, will show the prompt fission neutron spectrum for ^{235}U(n,f).

3.4.2 Monte Carlo Simulation

To make the correction to the prompt fission neutron yields, we must determine the detector efficiency as a function of energy. A Monte Carlo simulation was completed to help characterize the detectors, both by determining the efficiency and

100
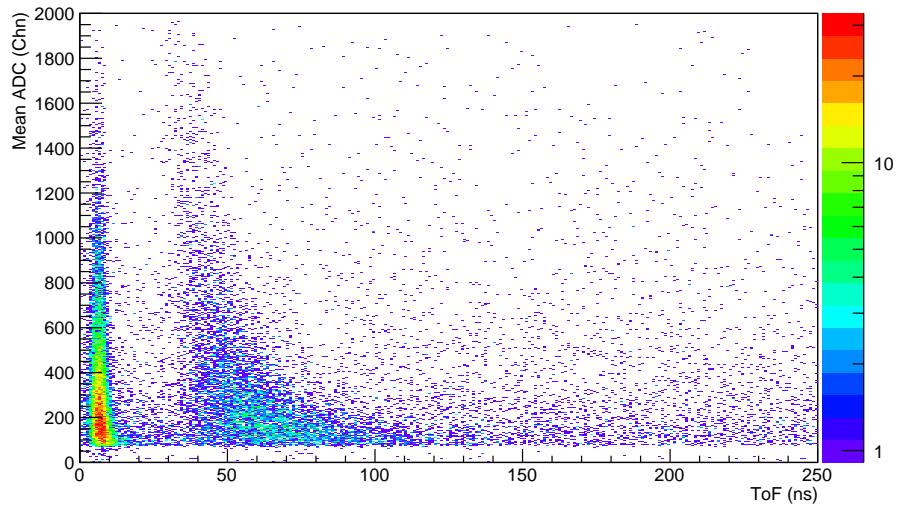
Figure 3.40: Geometric mean ADC versus time of flight for fission correlated events. Beam energies between 1 and 20 MeV are shown in this plot.
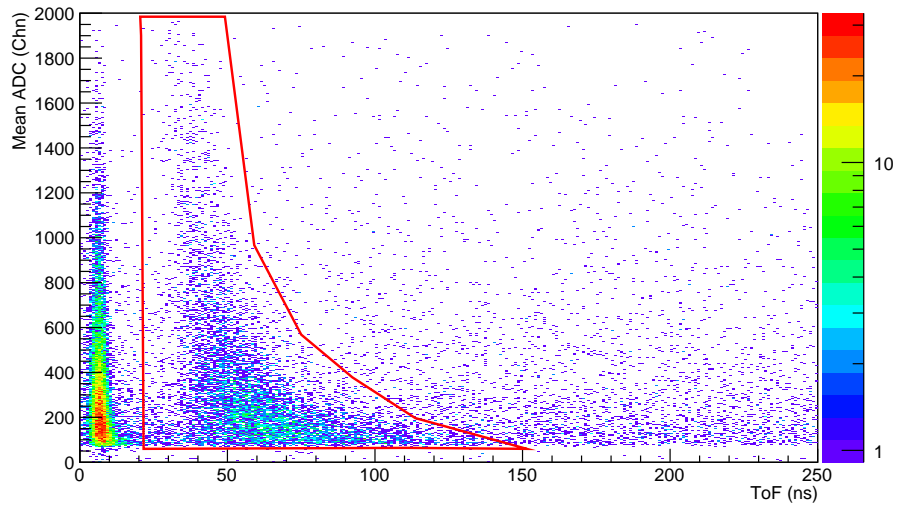
Figure 3.41: Geometric mean ADC versus time of flight for fission correlated events with the applied two-dimensional cut shown in red. Beam energies between 1 and 20 MeV are shown in this plot. This cut selects the events which are at the appropriate time to be neutrons, and have the appropriate ADC response.
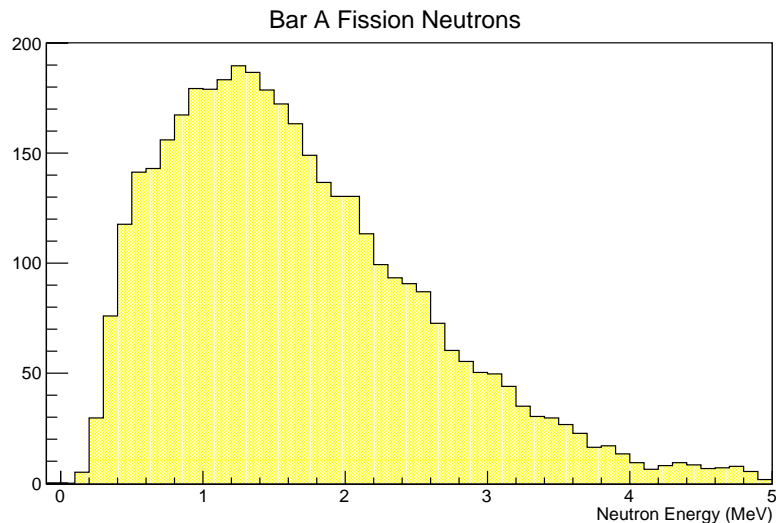
Figure 3.42: Prompt fission neutron yields for ^{235}U. This data is not yet corrected for detector efficiency.

investigating the expected detector response. To complete this investigation, we used the Monte Carlo toolkit GEANT4. To create an accurate Monte Carlo result using GEANT, the input cross sections must be accurate. **Appendix B** discusses the input cross sections and the corrections made to them for this simulation. For neutron interactions below 20 MeV, GEANT has a special class known as the 'high precision data' that uses ENDF cross sections[11].

Using this toolkit, the experimental geometry was recreated. To accomplish this reconstruction, the first step was to build the neutron detectors. Since we wished to test the full response of the detectors, the layered geometry of the detectors was built into the simulation, including the ability to read the light response of even layers in one pair of PMTs and the odd layers in another pair. **Figure 3.43** shows the detector geometry as recreated in the GEANT framework. The whole detector was wrapped in a 1/32 inch aluminum frame, with the 0.5 inch endplate caps shown with holes punched through for the PMTs. The right side of the image has the aluminum stripped away to show the interior of the detector. The 'Y' light guide design is included as are the light guide arcs. At the top of the arc is a thin strip of plastic
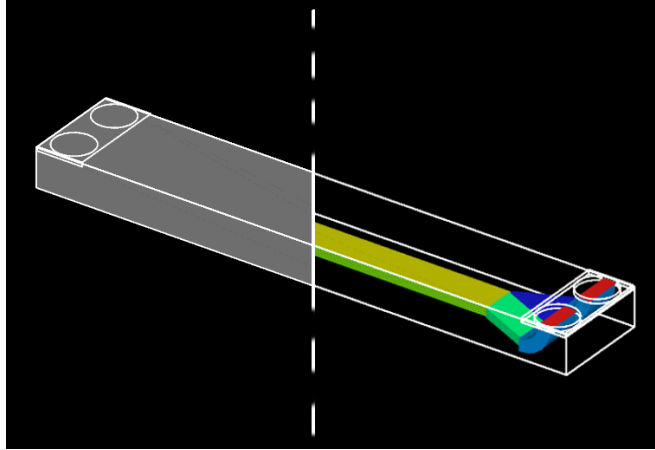
Figure 3.43: A demonstration of the detector geometry in GEANT4. The whole detector is wrapped in an aluminum frame, with the 0.5 inch plate shown with holes punched through for the PMT. The right side of the image has the aluminum stripped away to show the interior of the detector. The 'Y' light guide design is included as are the light guide arcs. At the top of the arc is a thin strip of plastic that acts as the light collector (PMT) within the simulation.

that acts as the light collector (PMT) within the simulation.

In the simulation, each material is defined by its density and chemical composition. In this case, the scintillator and light guide materials are uniquely defined, such that neutron interactions within the material via hadronic interactions will be accurate to the material composition. Similarly, we used the optical physics package within GEANT4 by defining the light response of those materials which will create light. For our scintillator, the light response is measured relative to anthracene, which is a well-studied fluorescing material. BC408[17] has a scintillation yield that is 64% of anthracene, or 11,200 photons/MeV. BC408 has a refractive index of 1.58 and a bulk attenuation length of 380.0 cm [16]. By defining a refractive index for all materials (including air and vacuum), GEANT is able to propagate light within materials, calculating at each surface whether the light will reflect or transmit. The material's absorption length is the average length which light will travel in the material before being attenuated by *1/e*. The final required definition is the Birk's constant for the scintillation material. The Birk's constant is used to simulate quenching effects. Quenching causes the recoiling proton to not produce as much light due to a higher

ionization density along the track of the particle. This 'quenches' some of the energy from the proton causing it to not produce as much light. The Birk's constant is used in calculating light production per unit length, $\frac{dL}{dx}$, for the particle passing through the material, via the empirical Birk's Law.

$$\frac{dL}{dx} = L_0 \frac{\frac{dE}{dx}}{1 + k_B \frac{dE}{dx}} \tag{3.4}$$

In this formula, L_0 is a normalization factor, $\frac{dE}{dx}^*$ is the energy lost per length, and k_B is the Birk's constant. Energy loss is converted to light, save for when quenching occurs. For BC408 the Birk's constant is 0.126 mm $\cdot$ MeV^{-1}. By defining all of the materials and the associated geometry carefully, GEANT is able to recreate interacting events and track the particles as they move through materials.

In order to track the response of the detectors in a physically accurate manner, we measure the light at the point where the PMTs are mounted. GEANT4 handles light physics by creating 'optical photons', which are low-energy photons ($\sim$ 3 eV/photon) with an assigned polarization. Each optical photon is handled as an individual particle with the behavior of light at surface interfaces such at total internal reflection modeled by probablities. During a neutron scintillation event a number of optical photons, N, is produced. N is correlated with the energy of the recoil proton. Each of these optical photons is tracked individually, moving through the material with some probability of transmission at each surface interface and some probability of being absorbed due to bulk absorption in the material. This means that, if the material is well-defined such that all the processes that cause light loss are accurate, the number of optical photons to reach the PMT is an accurate substitute for the ADC value in the experiment, since the ADC is just a measure of the light produced in the material. Shown in **Figure 3.43**, the red strips on the end of the arc light guides act as the PMTs. These red strips are just thin layers of the light guide material that are defined in a special manner within the simulation. When an optical photon enters these strips

---

$^*\frac{dE}{dx}$ for heavy particles such as the proton is determined by the Bethe formula[29].

from the arc guides, information about that photon is logged to a file. In particular, we log the time of arrival for first the optical photon (the TDC value) and the number of optical photons to reach the PMT area (the ADC value). By logging a proxy for both the experimental TDC and ADC value for each event, we were able to use the same method of analysis on the Monte Carlo data as we did on the real data.

To properly model our detector, we assigned the proper surface properties to each volume within the geometry. For the scintillators, we treated the surface as a polished surface. This matches the actual construction, as every surface was polished. We also increased the reflectivity of the surface by defining the surface to be wrapped in Teflon. Similar definitions were made for the light guides, which have a different index of refraction but the same surface style. For the aluminum frame, we defined the surface as coarse such that the reflectivity of the surface is greatly reduced.

An aluminum tube with the same dimensions as the PPAC frame was also created in GEANT. Inside the tube, ten aluminum holding rings were placed. Kapton windows are also placed on the ends of the tube. T. Taddeucci has also simulated neutron multiple scattering within the PPAC[30] and the effect that it has on the prompt neutron spectrum. In our energy range, the effect is small but appreciable. By including the PPAC in the Monte Carlo, our efficiency curve corrects for neutron scattering within the PPAC.

An aluminum floor was placed in the simulation geometry. This was built to match the dimensions of the floor covering the pit in the actual experimental area. **Figure 3.44** shows the final setup of the experiment (note that the aluminum frame wrapping the neutron detectors is transparent for diagnostic purposes).

In this simulation, we are interested in determining the neutron bar response. The PPAC has been well studied and simulated by its creators[25], so no further work is needed to characterize this detector. To study the neutron bar response, we do not need to simulate the fission events, but instead can simply create neutron events
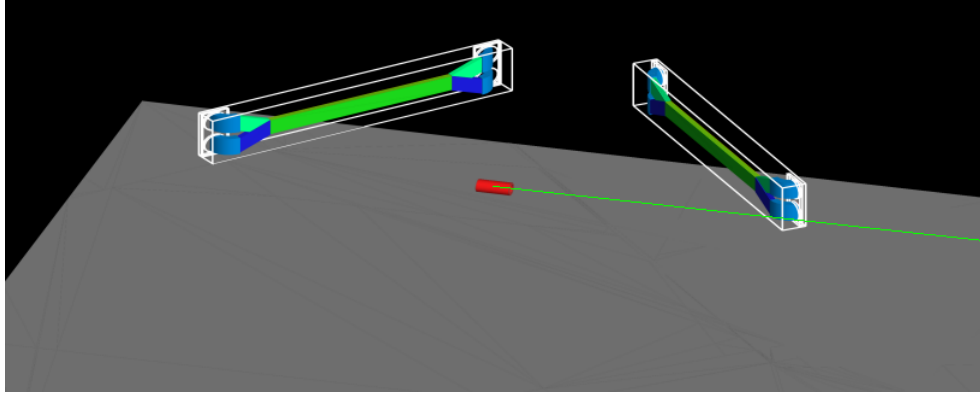
Figure 3.44: The full GEANT4 geometry for the ^{235}U Monte Carlo simulation. The green line shows the path of the neutron beam for reference.

at a point where a fission event would happen. We generated neutron events within the PPAC's active region, randomly selecting the starting position and direction of the neutron. To expedite the simulation, only those neutrons with a direction within the solid angle of the neutron detector frames are allowed to progress beyond generation. The neutrons are generated such that every unit solid angle of the neutron detector will have an equal probability of seeing each neutron event. The energy of each neutron is selected from a uniform distribution betwen 0.1 and 3.25 MeV. This does not match the expected ^{235}U prompt fission neutron energy spectrum. However, we were not interested in simulating the exact result. We were attempting to determing the detector response to neutrons of various eneries. A uniform distribution allowed the response at each energy to have roughly the same statistical accuracy in the simulation. For each event, a log of data is created for the intial conditions of the generated neutron. We record the initial energy, position, and direction of the generated neutron.

By logging all of the data for the generated neturons and the response at each PMT position, we can replay this data using the same analysis technique developed for the measured data. To test that the simulated detector response is behaving properly, we first checked for consistency between the simulated spectra and the real data. To test this, we examined the 'raw' ADC and TDC spectra for the simulation.
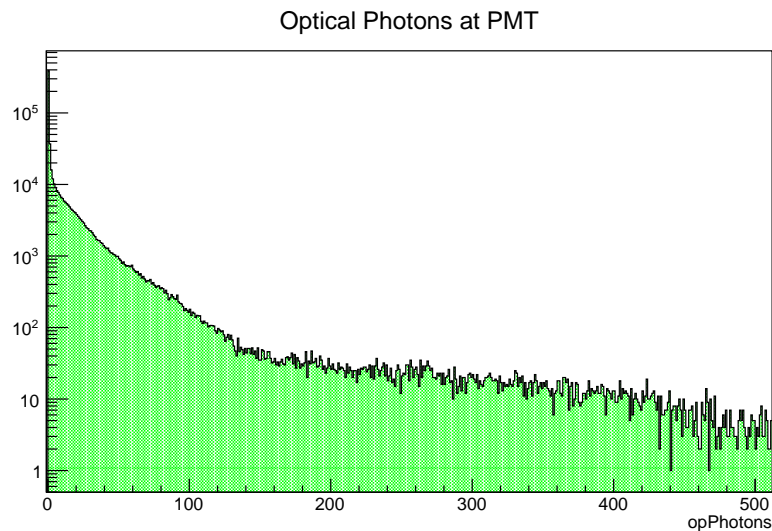
Figure 3.45: The observed light response for the neutron bar simulation at a single PMT position. The number of optical photons seen at the PMT position is a proxy for ADC value.

Figure 3.45 shows the number of optical photons observed at a single PMT per event. This is not yet converted to the geometric mean, so we expect to see a great deal of low-to-medium responses, with a long tail of events that look to produce high results, due to interacting at the near end of the bar. This also matches with the observed spectrum in the collected data.

Similarly, we can investigate the time of flight response of the simulation and compare it to what we physically expect and what the data shows. **Figure 3.46** shows the mean time of flight spectrum for the generated neutrons, using a pair of 'PMTs'. We expect that this spectrum should occur around 50 ns, since the time of flight for a 1 MeV neutron is 72 ns and neutrons were generated with an energy up to 3.25 MeV. Also, the spectrum should be a 'bump' of neutrons with nothing surrounding it since no backgrounds or gamma rays have been generated. Once again, the simulation proved consistent with the data and the expected behavior.

We also want to investigate the correlation between the time of flight and the number of optical photons seen. For the analysis, we have assumed that higher energy neutrons will produce more light in the material. This seems to be true,

107
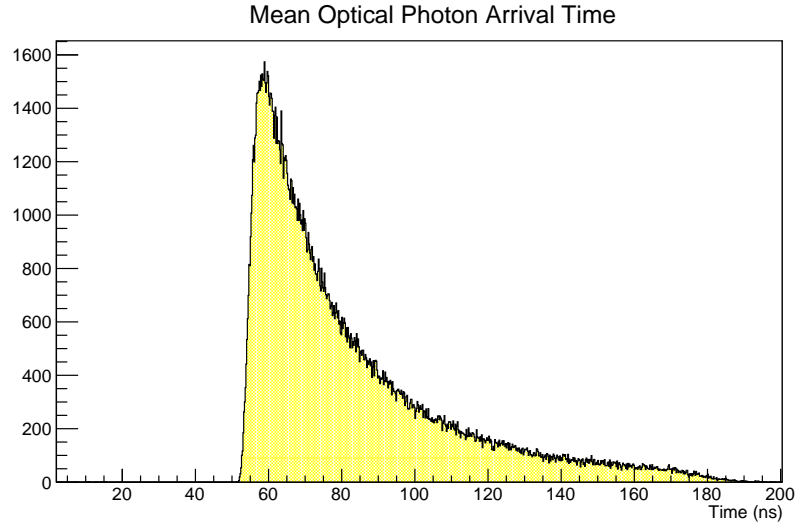
Figure 3.46: The observed mean time of flight spectrum for the neutron bar simulation using a single pair of 'PMTs'.

but the Monte Carlo allows us to map this directly, since we know the energy of the generated neutron. **Figure 3.47** shows the mean number of optical photons collected by a PMT pair versus the energy of the generated neutron. We see that the assumption that the higher energy neutron will produce more light is well-founded.

A two-dimensional plot of geometric mean optical photons versus neutron time of flight was also created, and is shown in **Figure 3.48**. We see the same characteristic shape in the Monte Carlo result as we do in the experimental data. Events with the events with a shorter time of flight have a larger value for the observed light response. The main difference between this plot and the data plot is the width of the 'bottom band.' However, this is explained by threshold effects. In the Monte Carlo, no threshold is applied while in the real data a threshold of ~ 300 keV is observed. If we apply a threshold of five optical photons to the geometric mean spectrum, we see that the width of this band is reduced and the spectrum begins to resemble the data spectrum. The figure is shown again in **Figure 3.49** with the threshold applied. The agreement between the Monte Carlo and the data is once again qualitatively excellent.
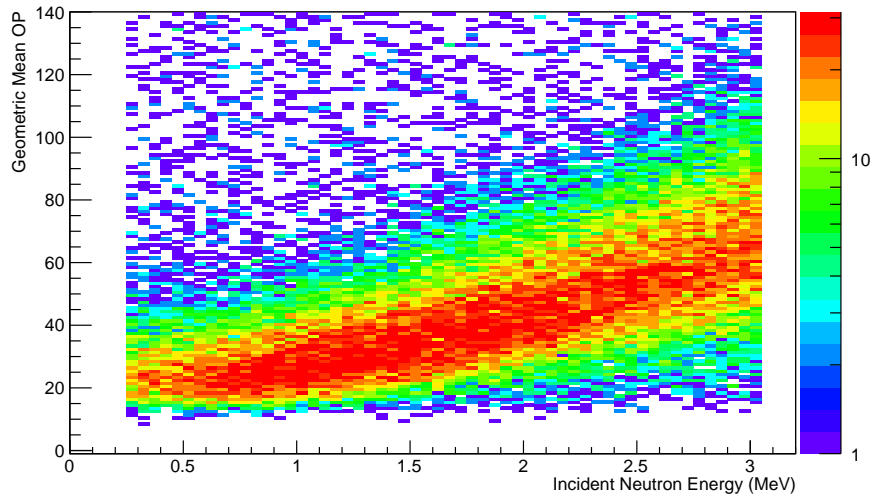
Figure 3.47: Optical photons collected versus generated neutron energy for the Monte Carlo data.
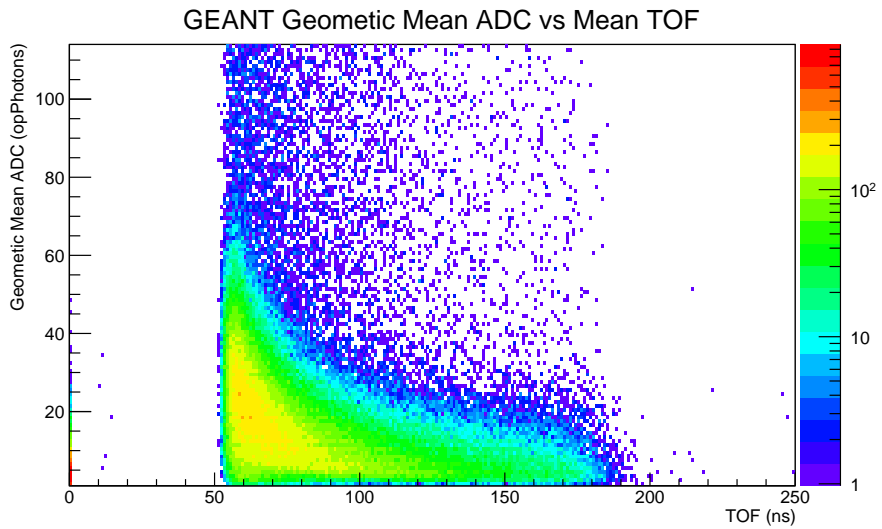
Figure 3.48: A plot of geometric mean optical photons observed versus mean neutron time of flight for a pair of 'PMTs' in the Monte Carlo simulation.
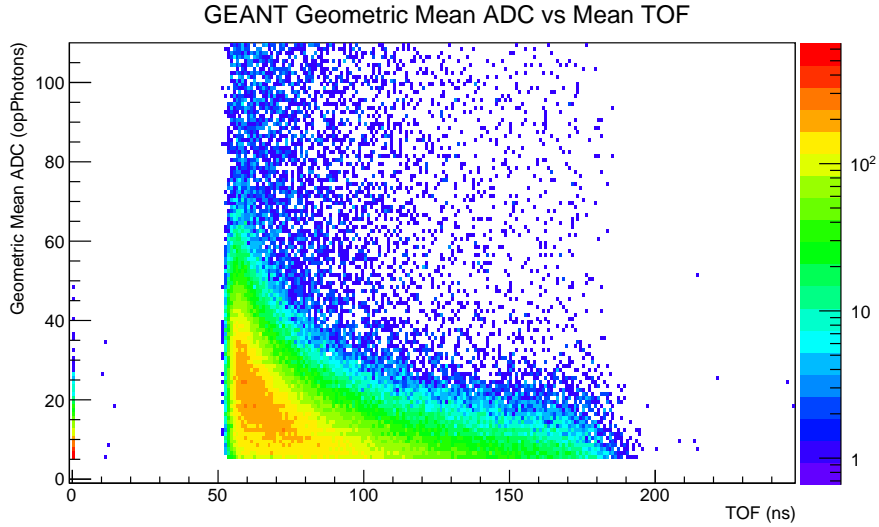
Figure 3.49: A plot of geometric mean optical photons observed versus mean neutron time of flight for a pair of 'PMTs' in the Monte Carlo simulation, with a threshold applied.

The agreement between the data and the simulation allows the Monte Carlo to also act a predictive tool. In particular, we are interested in the accuracy of the 'x-position' calculation and the absolute efficiency of the neutron bar using our cuts. First, we can investigate the accuracy of the time difference spectrum. In the Monte Carlo, we log the exact position of the interaction within the scintillator as well as the time of arrival of the light at each PMT. With this information, we can compare actual position with calculated position. **Figure 3.50** shows this comparison via a scatter plot of the Monte Carlo data. We see that calculation is very good at predicting the overall trend, with some dispersion about the actual value for x-position. This plot validates the choice to use the x-position in our calculation of flight path length. To further investigate this, we can project the distribution of events to the x-axis and look at the overall distribution of events. **Figure 3.50** shows the projection for those events at the center of the bar. This projection, when fit with a Gaussian, has $\sigma = 7.89$ cm. While this is smaller than the value measured with the collimated gamma ray source in the real data which predicted $\sigma = 13$ cm, this Monte Carlo represents the best case scenario where the first photon arriving at both
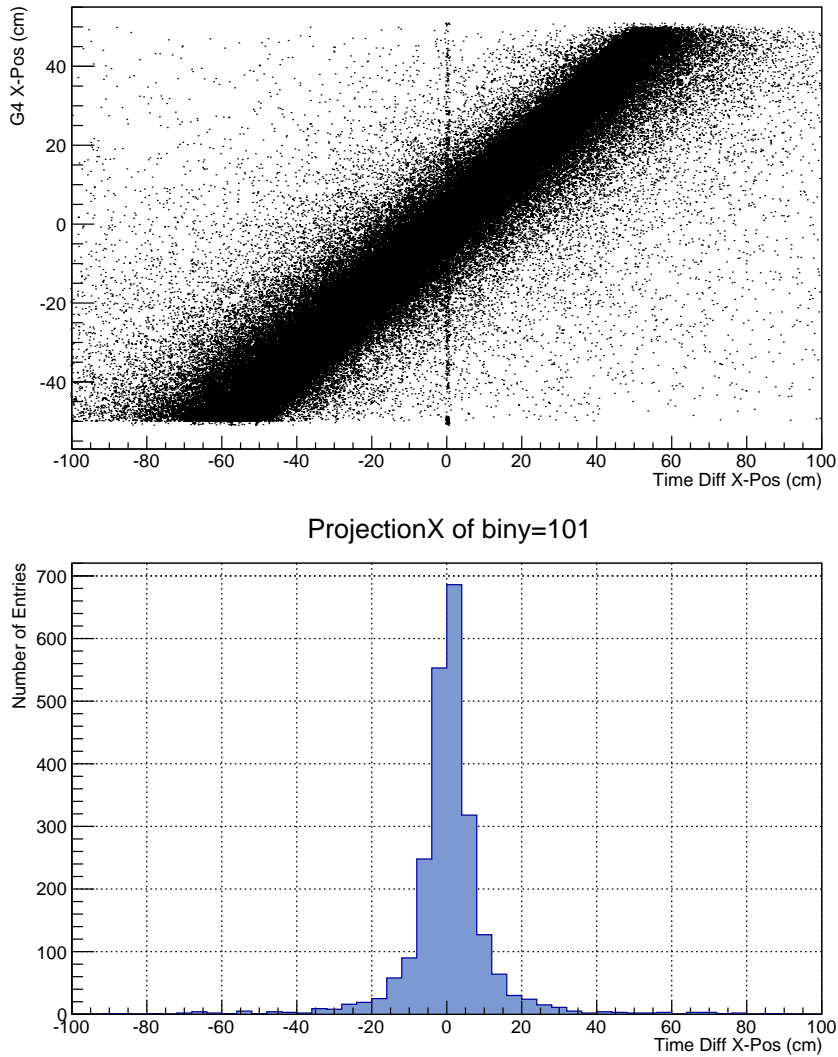
Figure 3.50: *Top*: GEANT4 actual 'x-position' versus calculated 'x-position'. *Bottom*: 'x-position' calculation using GEANT4 data for events at 0 cm. This is created by projecting the $y = 0$ bin to the x-axis in the top plot.

PMTs sets the time, there is no threshold effect, and there is no width to the input event distribution as there would be from a real collimated gamma source. Some discrepancy is expected. The discrepancy is larger than expected and a reanalysis of the collected source data returned the same results. However, the overall ability to predict the position of interaction based on the time difference is well-demonstrated by these plots, even if the standard deviation of that prediction is larger than desired.

111

The final information we extract from the Monte Carlo is the absolute efficiency for the neutron bar data. Beyond determining the percent of neutrons interacting in the scintillator, we need to know the percentage of neutrons that produce enough light that, once propagated to the PMTs, the light crosses the threshold for our analysis. We also need to adjust for how many of those events make it into our cuts. To measure this, we analyze the Monte Carlo data the same way we analyze the real data, making cuts for 'single plane', time of flight, and a graphical cut (shown in **Figure 3.51**). Since we know how many events are generated at each energy, we can see how many of those events pass all of the cuts and make it into the final prompt fission neutron energy spectrum via the analysis. This provides an answer to the question, "if a neutron of energy E is produced by a fission, what is the likelihood that it will interact and my analysis will place it in the energy spectrum?" This also corrects for those events which are above the graphical cut, which are true events. These events are visible in the real data, and were originally thought to be reflections of high energy neutron events off of the experimental area's walls. However, the Monte Carlo shows that these events are true events, and our cut misses them. By recreating the graphical cut within the Monte Carlo data, the correction for these 'missed true events' will be part of the efficiency correction.

However, this value is extremely sensitive to the threshold of the experiment, especially for lower energies. This is demonstrated in **Figure 3.52**, which shows the efficiency calculation for various threshold values. The shift in the low energy portion of the spectrum is due to fewer low energy events creating enough light to overcome the threshold. In order to create an efficiency curve that matches the experimental parameters, we recreated the threshold level within the program. To do this, we used the same method of determining the threshold level as with the real data, using gamma ray events of a known energy. Using a gamma ray with an energy of 662 keV (the same as ^{137}Cs), we expected a 477 keV Compton edge. GEANT4 has a
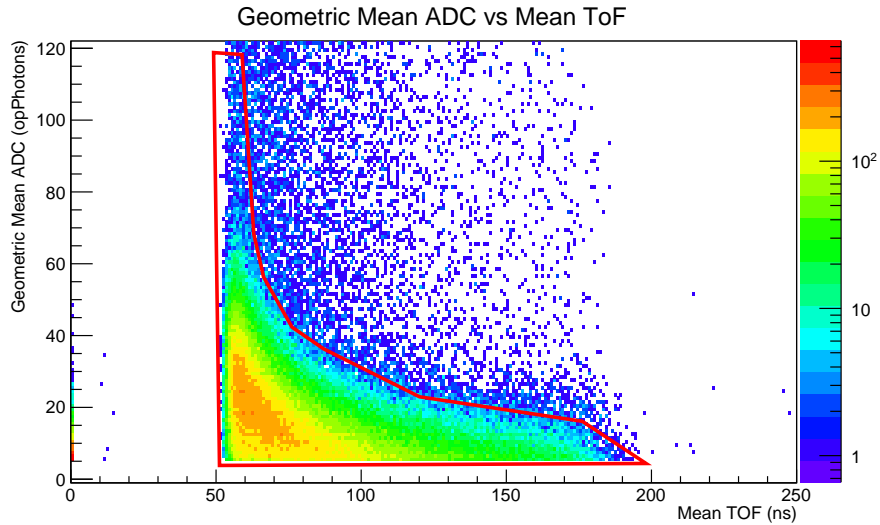
Figure 3.51: A plot of geometric mean optical photons observed versus mean neutron time of flight for a pair of 'PMTs' in the Monte Carlo simulation, with the graphical cut shown in red.
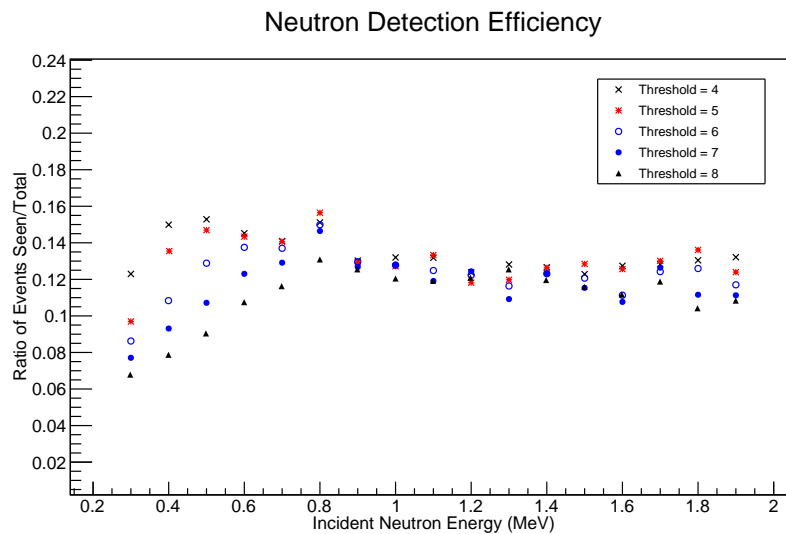
Figure 3.52: Absolute detector efficiency for various optical photon thresholds in the Monte Carlo.

fully functioning gamma ray scattering class that is able to reproduce the Compton edge. By using this gamma ray, we can determine a conversion factor with units of $\frac{optical\ photons}{\mathrm{MeV}}$. Using this conversion factor, we can calculate the number of optical photons that corresponds to our 50 keVee (~ 300 keV) threshold. **Figure 3.53** shows the efficiency in bins of 100 keV, for our threshold. In this calculation, a threshold of 10 optical photons was used at each PMT.
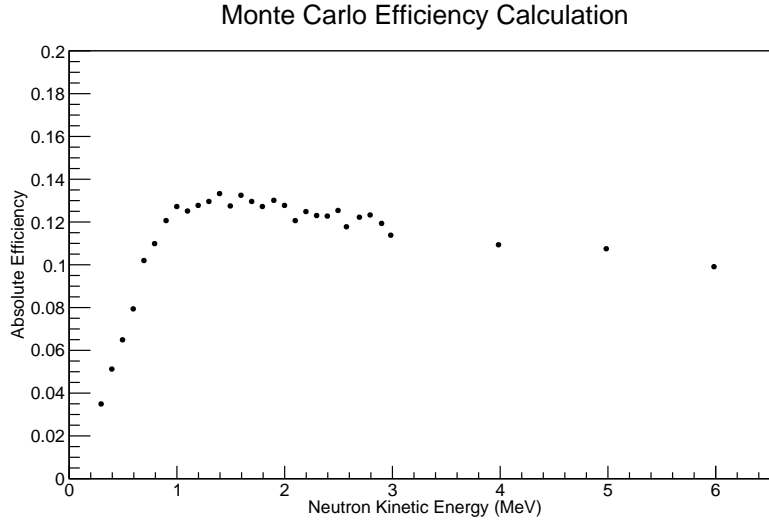
Figure 3.53: Energy-dependent absolute efficiency for layered neutron detectors.

The overall trend for the efficiency is clear, however there is fluctuation about that trend. This is mostly due to statistical uncertainty. Tracking optical photons is a labor intensive process for the machine, with >10,000 optical photons produced per MeV of neutron energy. This limits the amount of events a single machine can reasonably simulate. To overcome these fluctuations, a curve was fitted to the efficiency result. This fit is shown in **Figure 3.54**. To make the fit, the Monte Carlo was extended to collect data for neutrons of energies 4, 5, and 6 MeV, with these points used in the fit.

3.5 Experimental Results

In this chapter, the experimental results for the ^{235}U(n,f) prompt fission neutron measurement will be discussed. However, two issues need to be addressed before discussing the results.

First, the relative lack of data. For all of the results, the largest error is the statistical error. For this measurement, we were granted two weeks of neutron beam time with a beam repetition rate of 100 Hz. This rate is particularly important, as our detectors only cover 200 msr of solid angle, making the coincidence rate between
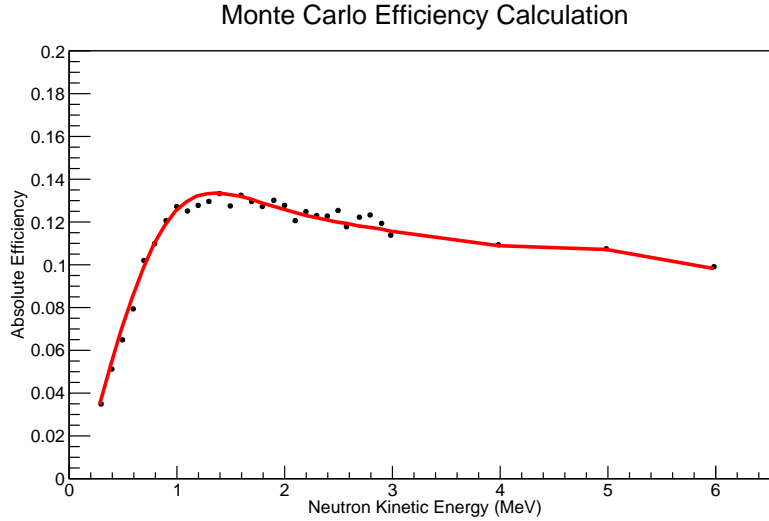
Figure 3.54: Energy-dependent absolute efficiency for layered neutron detectors with a fit applied to smooth the result for inclusion in energy calculations.

our detectors and the PPAC low. During our allotted beam time, the beam was only functioning at a 40 Hz repetition rate, meaning our statistics were reduced by 60% in an ideal case. During our time, the ideal case was not realized, as the beam was unstable for a large portion of our time. Roughly 40% of the allotted time had a beam current that was less than the expected 1 μA. Along with these unexpected complications, we also subdivide our data a number of times in order to make the measurements. There are the following subdivisions within the data: two bars, five angles per bar, and only a small portion of the beam energy is used in each data set. As an example, if we collected 10,000 coincidence events, only $\sim$ 100 of them would have a beam energy between 1 and 2 MeV. Of those, only half would enter bar α (assuming isotropy for simplification). Of those in bar α, only 20% would be in the middle region. That means only 10 events would be recorded in that detector region, and those would have a range of energies between 0.3 and 6.5 MeV. With all of these divisions, we needed to collect a great deal of overall data, such that the subdivided data would have reasonable statistics. With the beam-based difficulties, we simply did not collect enough data. To partially overcome this, the data shown will use larger

beam energy regions and bar region widths to improve the statistics, however this has the side effects of less angular resolution (not as important for spectrum shape measurement) and a less narrow investigation of the beam energy dependence of the spectrum. Even with these concessions to increase statistics, the statistical error is still on the order of 10-15% for the majority of our results.

Second, consider bar β's data problems. When constructing these prototypes many small errors were made, which is part of prototyping and not unexpected. As examples, some of the scintillators were handled without gloves and some of the plastic developed surface crazing during polishing. Both of these errors lower the likelihood of total internal reflection. Also, one of the light guide arcs was cut out of the only piece of plastic available at the time, which was too small, further decreasing efficiency for those layers. To maximize the chance of recording at least some high quality data, the best pieces and materials were all placed in bar α. This meant that bar β, while it should have been functional, had a higher likelihood of being incapable of measuring the region of interest, since low-energy neutrons produce less light than their higher energy counterparts and β did not have an optimal efficiency. This is best seen by comparing **Figure 3.55** to the two-dimensional plots in the previous section. The plots for β simply don't have the low-energy neutrons with a correlated low ADC value, as seen by the neutron distribution stopping below 90 ns. The relatively small amount of light seen in bar β causes the low energy neutrons to be cut off by the threshold as seen in this plot. Compounded with this, we placed bar β at the forward angle from the target. Neutrons and gamma rays can elastically scatter from uranium or the PPAC casing, and this elastic scattering is forward peaked. Due to this, bar β also received a much higher beam-correlated background rate of both gamma rays and high-energy scattered neutrons, which look very similar to true fission events. This is most easily seen by looking at the time difference spectrum for bar β, which is shown in **Figure 3.56**. The higher rate of multiplane events on one side of the
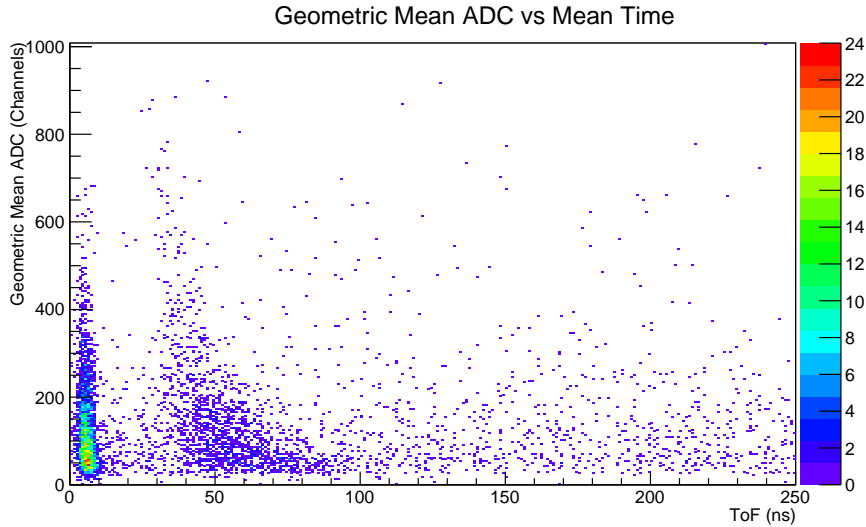
Figure 3.55: Geometric mean ADC versus mean time of flight for bar β. The neutron distribution does not extend as far in time for bar β as it does in bar α. This causes the low-energy data in bar β to be incorrect, since the threshold removes some of the low-energy neutrons from the result.

bar is indicative of the extra, high-energy backgrounds that are seen on the side of the bar closest to the beam. In this analysis, bar β was treated similarly to bar α however, it does not see the low-energy neutrons like bar α does. The data for bar β should be looked at with a healthy grain of salt, especially for lower energy results. In these results, the agreement with expected values at high energy is relatively good, however as the energy decreases the yields in β fall off so quickly that they are no longer viable data points. For completeness, all of the recorded data for bar β will be shown.

3.5.1 Systematic Errors

The traditional way of presenting prompt fission neutron energy data is to measure in yield/MeV/fission/steradian. The yield is determined by analyzing the data (an example is presented in **Figure 3.42**). The division by MeV is completed by dividing by the energy bin width. This removes any dependence on the bin widths. We also wish to scale by the total number of fissions. In this data, we collected both coincidence events and pre-scaled PPAC single events. The total number of fissions

BO Time Difference Spectrum
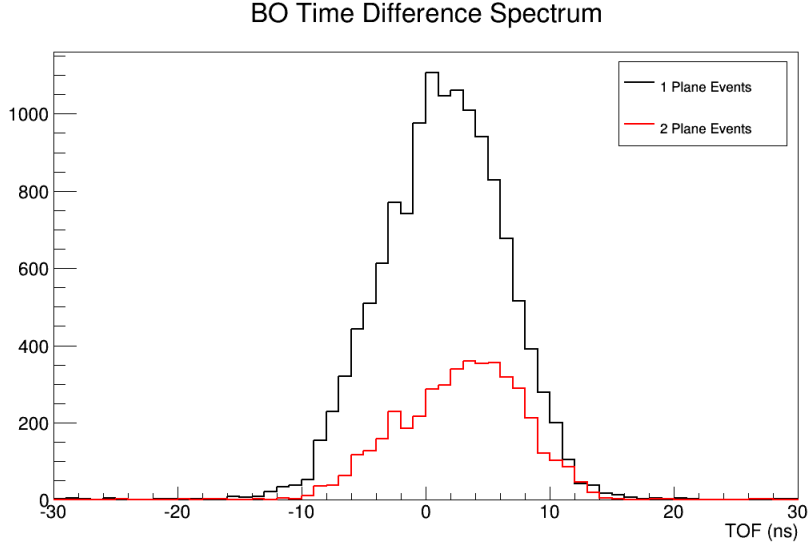
Figure 3.56: Time difference spectrum bar β for single and double plane events. The side with the higher rate was near the beam line.

is calculated by:

$$Total \; = \; Coincidence\, Counts \; + \; Prescaler\, Setting \cdot Single\, Counts \qquad (3.5)$$

With this data, we can calculate this value on a per one hour run basis. We also scale by the solid angle of the neutron detector, which can be calculated for each section of the bar, and is different depending on which portion of the bar is being analyzed. Each of these scaling factors contributes to the overall uncertainty of the measurement.

Due to the already large statistical error bars, presenting this data as an absolute measurement would make the error bars exceedingly large. This extra uncertainty would come from accounting for angular dependence of the neutron multiplicity, solid angle of the detector regions, neutron multiplicity causing multiple scattering, PPAC efficiency, PPAC alpha particle rejection, and other more subtle factors. However, this data can be useful when presented as 'shape of the spectrum' data. When presented as shape data, the only factors that matter are the yield and the bin width, as both the total number of fissions and the solid angle are absorbed into an 'overall normalization'

118

factor that is without error. If we were making an absolute measurement, the result would be very sensitive to treatment of the PPAC spectra, since we are losing some events which have an ADC value similar to an alpha particle. The spectrum would also have a strong dependence on the threshold for frament events in an absolute measurement, as the total yield of prompt neutrons would be correlated with how many fission events are counted. This would be partially removed by scaling by total number of fissions, but a perfect cancallation would require a totally energy independent response by the PPAC. By making only a shape measurement, this dependence is removed entirely.

Presenting our results as shape data also removes the angular dependence of the spectrum which is non-trivial, as the number of prompt neutrons ejected into some solid angle $d\Omega$ will vary depending on both θ and ϕ. This angular dependence would change the overall yield/fission, which would change the prompt fission neutron spectrum's overall normalization. Presenting this data as shape data, we can still say something useful about the prompt fission neutron spectrum, despite our limited statistics at each angle. Our final expression for the prompt fission neutron yield becomes:

$$Y(E) = A_0 \cdot \frac{Y_m(E)}{\eta(E) \cdot \delta E} \tag{3.6}$$

where Y(E) is the final yield for an energy E, A_0 is the normalization factor, Y_m is the measured yield, η is the absolute efficiency for the neutron detector, and δE is the bin width.

This method still has some associated systematic errors. Though the vast majority of the error for this measurement will come from the low statistics associated with Y_m in the above calculation, there are still other factors to consider. Each factor will be discussed below.

Neutron bar time resolution: Since the energy of the prompt fission neutrons is deter-

119

mined by the time of flight, any error in the time of flight will also be in the energy distribution. By fitting the gamma flash in the mean time of flight spectrum with a Gaussian fit, we can see that our time resolution is 1.7 ns. A 3 MeV neutron, which are the most time sensitive events in these results, has a time of flight of $\sim$ 59 ns, which gives a resolution of $\sim$ 3%. A 3% change in the time of flight for a 3 MeV neutron is a 5% change in the overall energy. This uncertainty applies to the energy axis.

Flight path length: The conversion from time of flight to neutron energy is also dependent on the flight path. With a specialized measuring apparatus available to us, the direct flight path is determined to the 1% level. A 1% change in the flight path leads to a 2% change in the fission neutron energy calculation. However, we must also account for the x-position calculation. The x-position resolution is on the order of 10 cm. This value is summed with the flight path to the center of the bar via the law of Cosines to determine the overall flight path. A 10 cm change in the x-position measurement leads to an overall change of 1.5 cm of the $\sim$ 1 m flight path. This 1.5% change leads to a 3% change in the energy measurement. Summing all of these uncertainties in quadrature leads to a total associated error of 3.6% in the energy.

Bin width: The bin widths are treated as 'sampling points' within the data. Any associated error is already included in the time resolution and flight path length.

Efficiency: The error associated with the Monte Carlo simulation has multiple contributors. First, we consider the validity of the input cross section data. As discussed in **Appendix A**, a great deal of care was put into selecting the correct cross sections. The final cross section input files are the standards currently produced by the NNDC [11]. These are accurate to 1% in the energy region of interest. The simulation is also

a product of the accuracy of the optical physics models. This was tested using the work of Massam[21] as a baseline, and found to be an exact match with his experimental results. The statistics of the simulation are also relevant. Each energy bin had more than 2000 events which interacted in the scintillator, and more than 20,000 generated events. Using the interaction event count as the baseline for determining the statistical accuracy of the efficiency since only interacting events tracked optical photons, there is a 2% error in each bin. Within the final efficiency calculation there was a fairly wide distribution of points around the overall trend. Subtracting the point value from the fit, we found a gaussian distribution centered around zero. This had a standard deviation of 4%. Combining these associated errors in quadrature, we have an overall error of 4.5% for the efficiency calculation.

Background subtraction: Hidden in the measured energy spectrum is a background subtraction. This background is time-independent and, when integrated across time of flight, constant. The statistical error is expressed as

$$\frac{\sigma_N}{Y_N} = \frac{\sqrt{Y_T + Y_B}}{Y_T - Y_B} \tag{3.7}$$

where N denotes net yield, T denotes measured total yield, and B denotes background yield. Thus, the background yield is accounted for within the statistical error for each measured point in the spectrum.

All other errors are scaled out by presenting the data as shape data. The efficiency calculation also corrects for data missed in the analysis. Summing all of these sources of error in quadrature, we see a total systematic uncertainty of 5% for the fission neutron yield. By using a 300 keV bin width for all measured results, the error in the energy is encompassed by the width of the bin and is not shown on the plots of the spectra.

3.5.2 Prompt Fission Neutron Energy Spectrum for ^{235}U(n,f)

Due to data volume constraints, we only subdivided the bar into three x-position 'regions' during analysis: -50 to -20 cm (negative region), -20 to 20 cm (center region), and 20 to 50 cm (positive region). The center region is the largest due to the more even ADC response and the flight path being more accurately determined for x-positions near zero. The results for these portions of bar α are shown in individual plots. All data were arbitrarily normalized, as was the associated ENDF calculation. The results are presented in units of 1/MeV such that results could be compared for different bin widths. For all results shown in this section, the bin width is 300 keV, both for increased statistics and due to the error associated with the time to energy conversion. The results are also presented for various incident beam energies, using three energy regions: 1 to 3 MeV, 3 to 5 MeV, and 5 to 7 MeV. The goal for the measurement was to use beam energy regions of less than 1 MeV, however the statistics weren't high enough when using small beam energy bins. As discussed in the introduction to this results section, bar β suffered from a number of problems, making its data unreliable at low energies. For completeness, the data for bar β has been combined into three plots, one for each bar segment. **Figures 3.57** through **3.65** show the measured prompt fission neutron spectrum in the region between 0.3 and 3 MeV for the three regions of bar α.

Bar β's data is shown in **Figures 3.66** through **3.68**. This data has not been subdivided by beam energy due to the known issues with the results. The down turn in the yield below $\sim$ 1.5 MeV is a real effect and is discussed in the introduction to this chapter. These data do portray some useful information. For these plots, the shown range of energy is larger than in the previous plots. The measured energy spectrum extends to 6 MeV. In the data, we see events with energies up to $\sim$ 6.5 MeV. These higher-energy events were observed with a very low frequency due to the declining n-p elastic cross section (which dictates the interaction rate). However, the plots of the
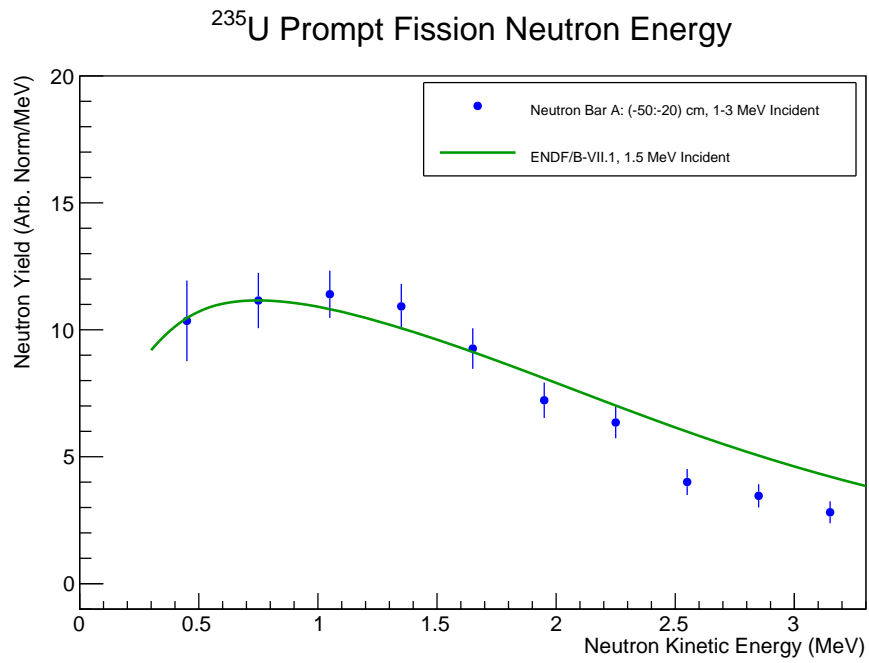
Figure 3.57: Prompt fission neutron spectrum result for bar α's negative x-position region for 1-3 MeV beam neutrons.
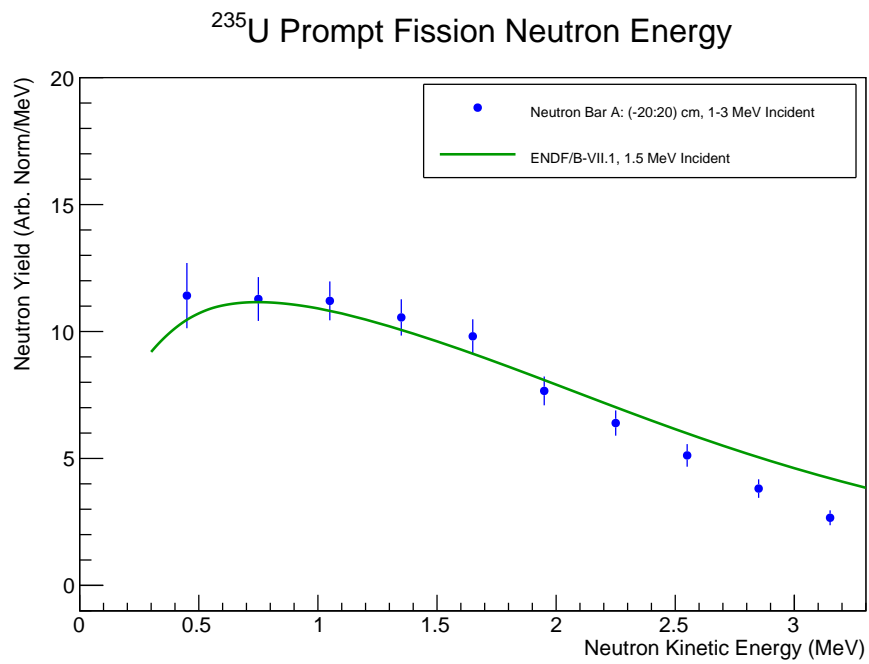
Figure 3.58: Prompt fission neutron spectrum result for bar α's center x-position region for 1-3 MeV beam neutrons.
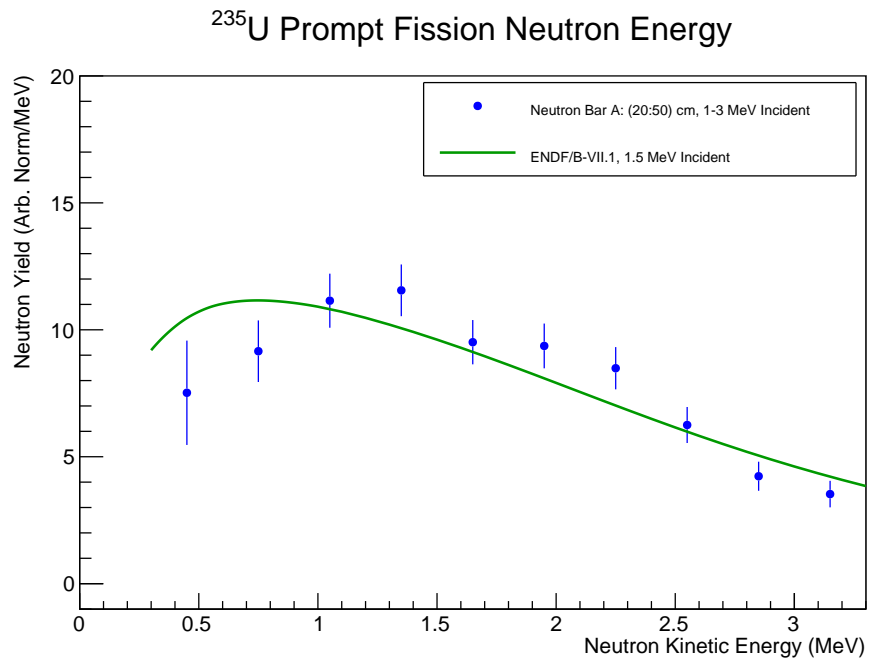
Figure 3.59: Prompt fission neutron spectrum result for bar α's positive x-position region for 1-3 MeV beam neutrons.
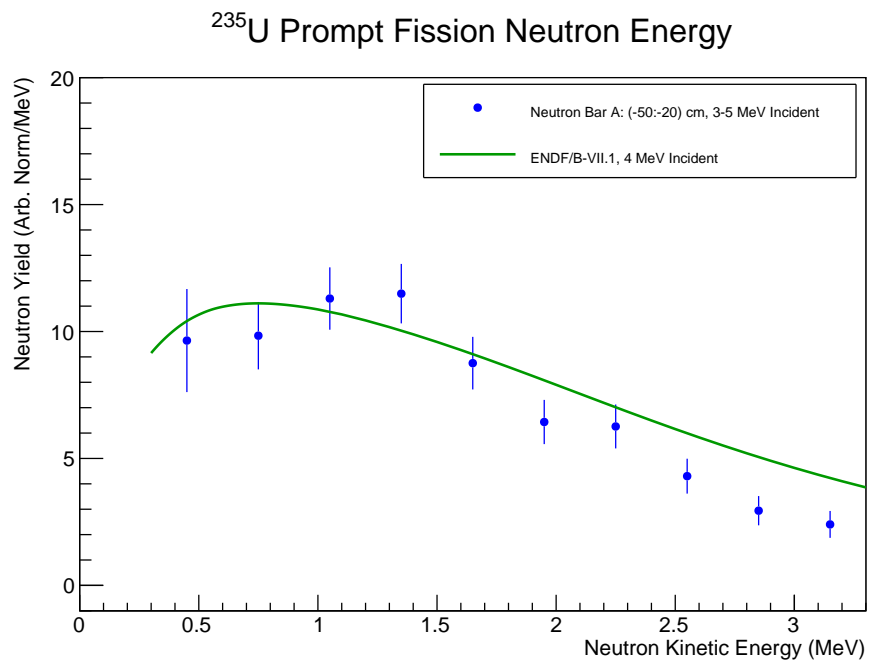
Figure 3.60: Prompt fission neutron spectrum result for bar α's negative x-position region for 3-5 MeV beam neutrons.
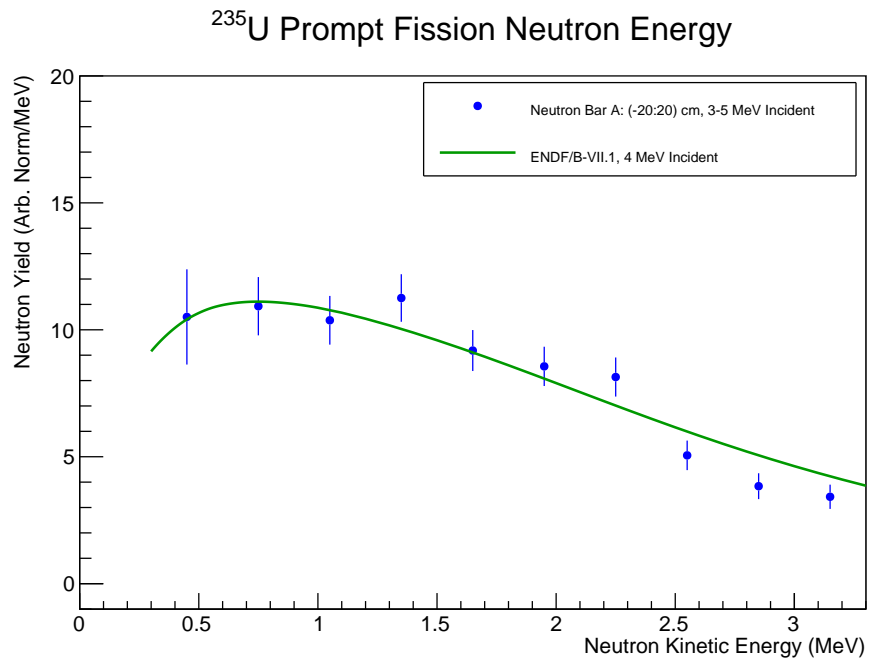
Figure 3.61: Prompt fission neutron spectrum result for bar α's center x-position region for 3-5 MeV beam neutrons.
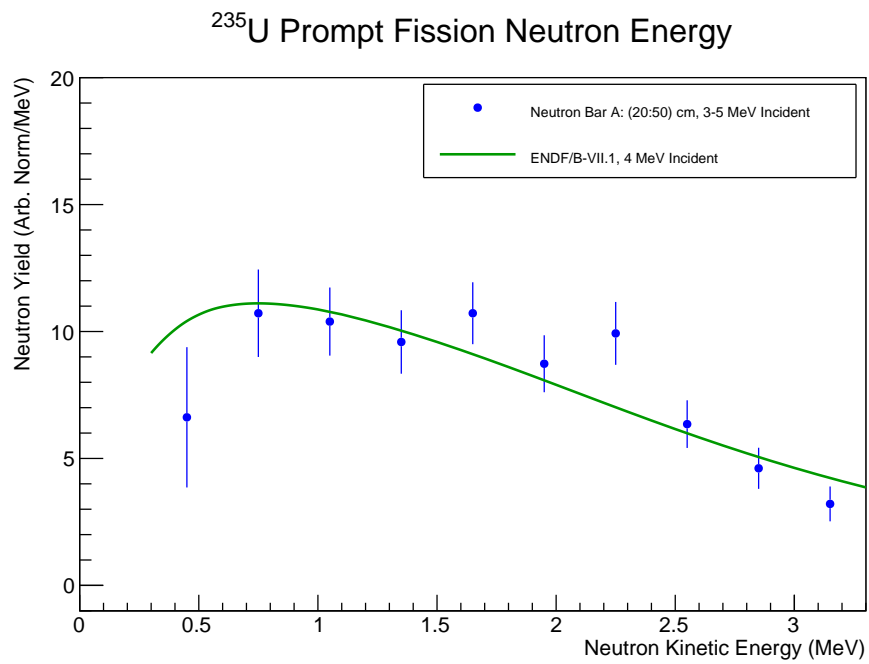
Figure 3.62: Prompt fission neutron spectrum result for bar α's positive x-position region for 3-5 MeV beam neutrons.
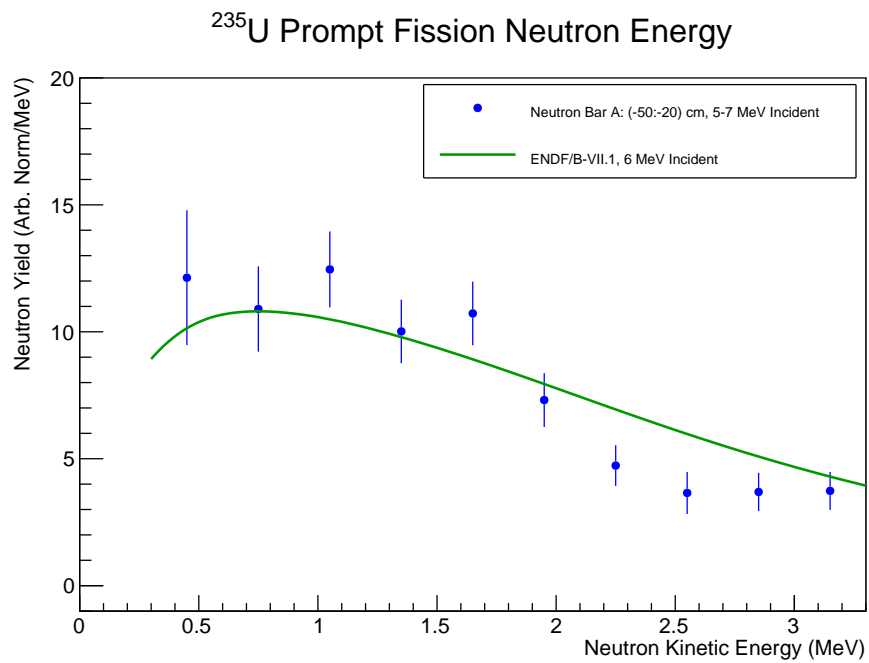
Figure 3.63: Prompt fission neutron spectrum result for bar α's negative x-position region for 5-7 MeV beam neutrons.
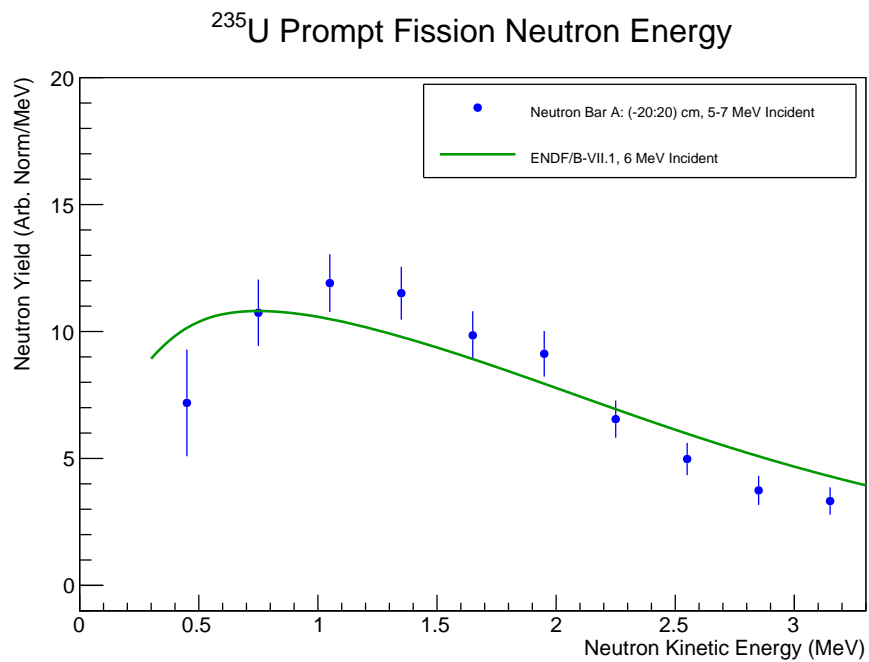
Figure 3.64: Prompt fission neutron spectrum result for bar α's center x-position region for 5-7 MeV beam neutrons.
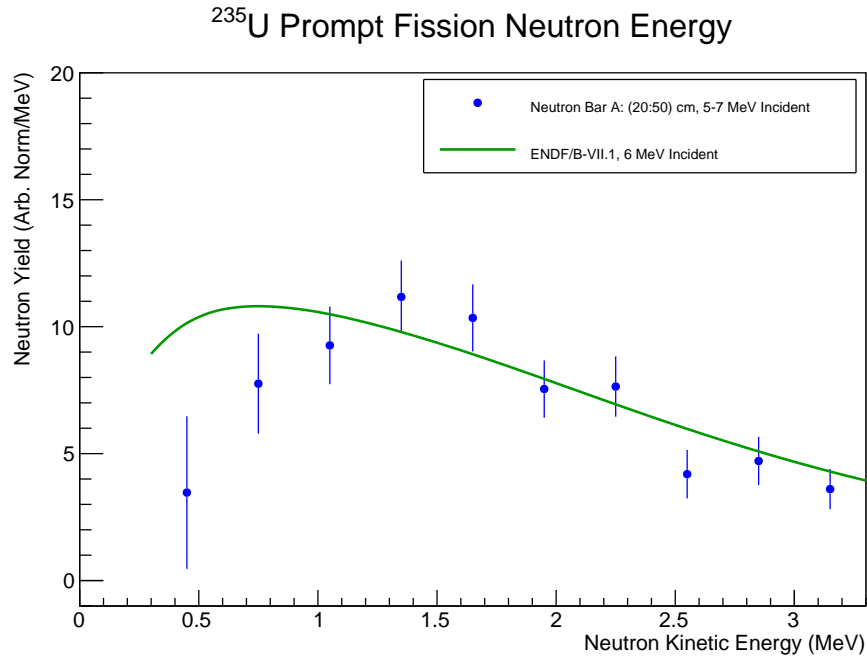
Figure 3.65: Prompt fission neutron spectrum result for bar α's positive x-position region for 5-7 MeV beam neutrons.

data recorded in bar β show that range of the measurement for these detectors could extend as high as 6 MeV. Bar α has a similar result to bar β for prompt neutron energies near 6 MeV, as shown in **Figure 3.69**. Both bars underpredict the yield for the spectrum as the energy increases beyond 3 MeV. However, with an optimized method for finding and recording the higher energy portion of the spectrum this same experimental setup could measure the prompt fission neutron spectrum from 0.3 to 6 MeV and perhaps higher.

These results demonstrate a number of important concepts and results that should be considered as the program of prompt fission neutron measurements continues:

- The detectors are able to measure the prompt fission neutron spectrum below 1 MeV.

- In general, the results match the expected curve shape for the low-energy prompt fission neutron spectrum within error, with moderately good agreement
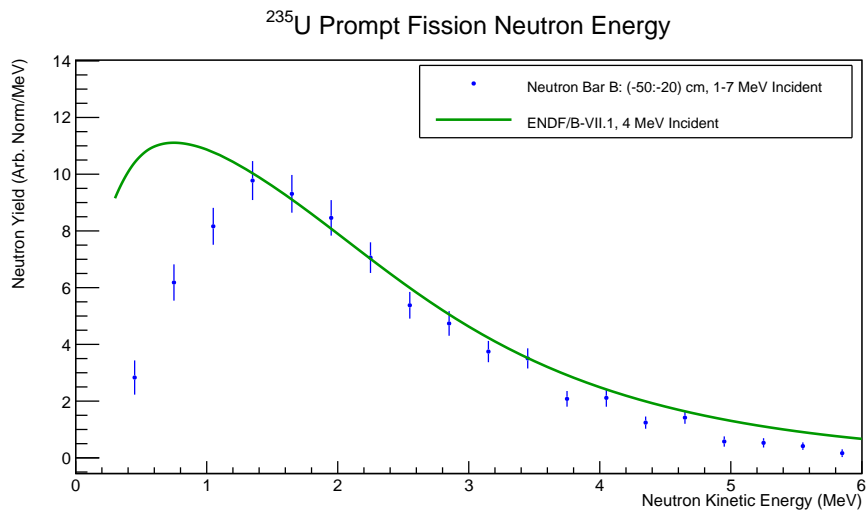
Figure 3.66: Prompt fission neutron spectrum result for bar β's negative x-position region for 1-7 MeV beam neutrons.
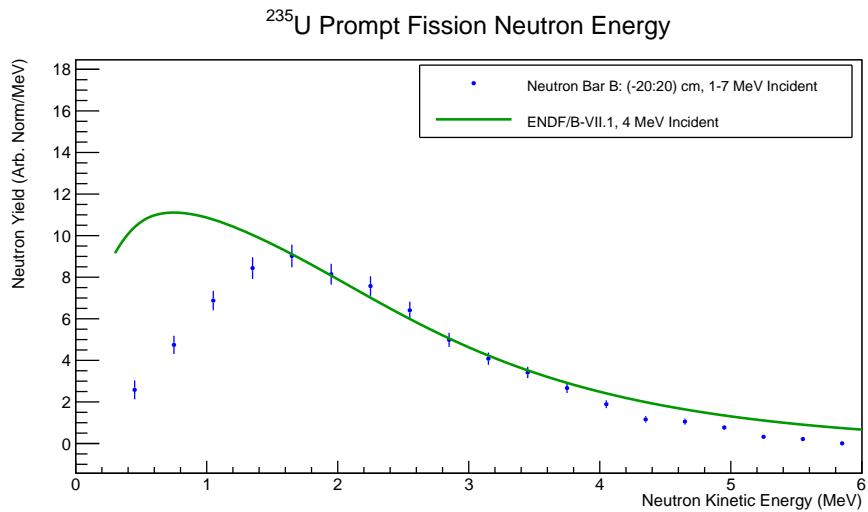
Figure 3.67: Prompt fission neutron spectrum result for bar β's center x-position region for 1-7 MeV beam neutrons.
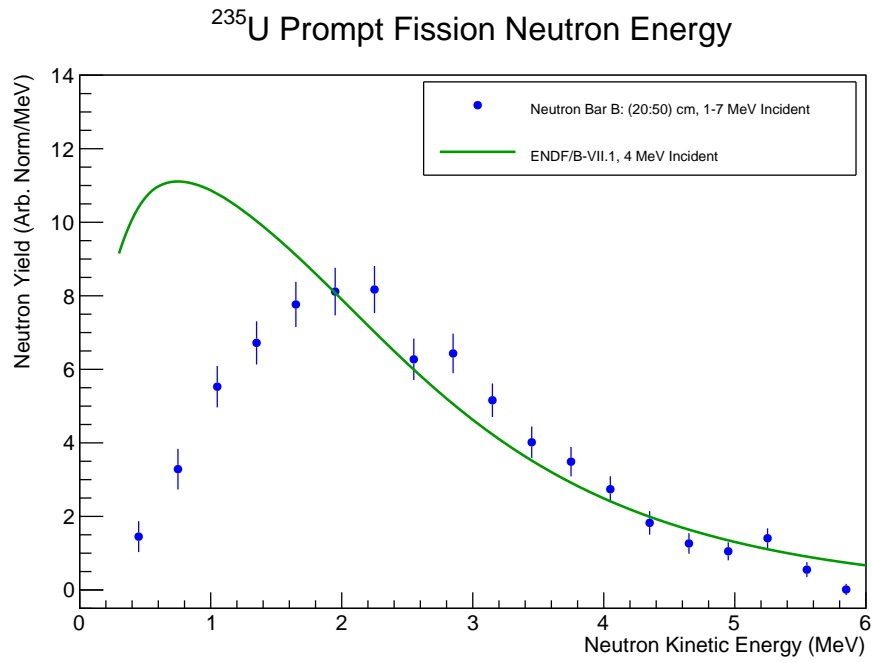
Figure 3.68: Prompt fission neutron spectrum result for bar β's positive x-position region for 1-7 MeV beam neutrons.
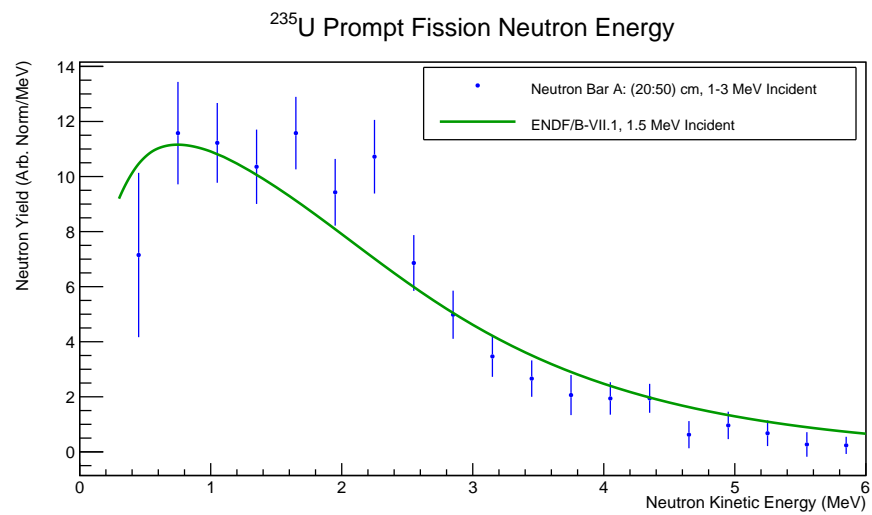
Figure 3.69: Prompt fission neutron spectrum result for bar α's positive x-position region for 3-5 MeV beam neutrons, show for the full recorded range of neutron events.

in the region below 1.5 MeV.

- The full range of the measured spectrum extends to 6 MeV. In this data the agreement of the measurement with the theory above 3 MeV is not good; however, the data hints that with some optimization a measurement could be made for the full range of 0.3 to 6 MeV.

- High overall statistics are vital to making the measurement with precision. By subdividing the data to make a measurement in a small angular region for a small region of beam energy, the statistics quickly become the dominant uncertainty.

- An absolute measurement should be possible with this measurement technique. The yields are measured in a manner that, with the proper scaling factors, lends itself to an absolute measurement. The traditional method of presenting an absolute measurement is in units of yield/MeV/Fission/sr/multiplicity. The multiplicity's angular dependence has been measured [8] and the current method provides all of the other scaling factors. The added complications of PPAC efficiency, threshold dependence in the PPAC, and angular acceptance as a function of bar region are all obstacles that could be overcome.

In the end, this measurement provides and excellent first step in the program of prompt fission neutron study. The measurements, though not precise due to the available statistics, show that the detectors have the ability to identify fission neutrons with energies as low as 0.3 MeV. The initial energy target for this project (≤ 0.5 MeV) has been met and exceeded. Improvements for this detector design are already being simulated, with the goal of producing a second set of bar prototypes to improve upon this measurement. To our knowledge, this measurement has also provided the first experimental look at the prompt fission neutron spectrum below 1 MeV for fast beam neutrons. The agreement with the Madland and Nix model [9] (labled ENDF/B-VII.1

in the plots) is expected, as the model is highly parameter driven and fits the prompt fission neutron spectrum for thermal beam neutrons well. The expected change for fast neutrons versus thermal neutrons, according to modern fission theory, is not in terms of shape but of multiplicity. However, this is the first experimental data to compare with to the shape of this curve below 1 MeV for fast beam neutrons.

Chapter 4: Neutron-Induced Fission Cross Sections in ^{238}U(n,f)

4.1 Experimental Setup

4.1.1 Introduction to the Measurement

In 2002, an experimental group comprised of members from both the University of Kentucky and Massachusettes Institute of Technology (MIT) collected data at the LANSCE facility in New Mexico[31][32]*. The goal of their measurement was to investigate the neutron-deuteron elastic scattering cross section as a probe of the three-nucleon force. As part of this measurement, an ionization fission chamber with ^{238}U foils was used to monitor the beam's neutron flux. Due to bubbling within with the liquid deuterium target, the group also collected data with a liquid hydrogen (LH$_2$) target to characterize the target thickness. In 2013, it was realized that a reanalysis of the LH$_2$ data could yield a measurement of the ^{238}U neutron-induced fission (^{238}U(n,f)) cross section.

The method of extracting the fission cross section is reliant upon the 'white' beam that was used in the original experiment. At the Weapons Neutron Research (WNR) facility, where this experimental data was collected, the beam contained neutrons of various energies, ranging from a few hundred keV up to 800 MeV. This is known as a 'white' beam due to the nature of having a full range of energies. Since data was simultaneously collected for all energies, we can make comparisons between the event rates for various energies. Essentially, we are investigating the phrase: if I saw N$_1$ fissions for energy E_1, how many fissions do I expect at E_2? With the right combinations of scaling variables, this allows an extraction of the energy dependence

---

*Many of the diagrams and descriptions found in this chapter come directly from [31][32][33], with minor edits made for this analysis. I have done my best to summarize the papers, such that this work is understandable on it's own accord. However, these papers have more detail regarding experimental setup and detector information.
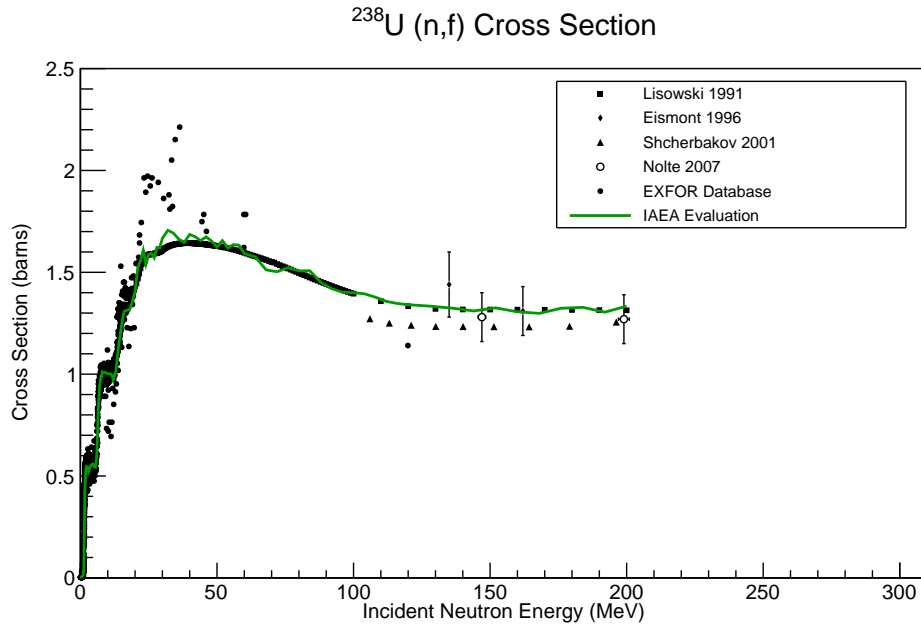
Figure 4.1: Current world data and standard evaluation for ^{238}U neutron induced fission cross section.

of the cross section in any energy region where we have reliable data.

The original experiment was designed to look for nd scattering in the range of 100-240 MeV. As such, the detectors have been optimized for this energy region. Coincidentally, this energy region is also not well-measured for the neutron induced fission cross section in ^{238}U. In **Figure 4.1**, we see a great deal of data constraining the cross section below 50 MeV. However, above 100 MeV, there is remarkably little data[†]. The evaluation shown is the ENDF/B-VII.1 standard and was created by the International Atomic Energy Agency (IAEA)[35]. Above 100 MeV, the plotted data is almost exclusively measured using another actinide, in particular ^{235}U, as a flux monitor. For the purposes of calculating a more accurate cross section standard, it is important to have multiple measurements using different monitor interactions. In the setup of the 2002 experiment, the LH$_2$ target acted as the flux monitor, such that we are measuring the fission cross section relative to a hydrogen cross section standard.

[†]This only shows publicly available data.[34] Many data points are submitted to evaluators without being submitted to databases. More data points are included in evaluations completed by the IAEA[35]. The Lisowski[36] data is the standard data source in the region.

Table 4.1: Symbol definition for yield to cross section calculation.

Symbol	Definition	Units
E & E*	Energy of beam neutron	MeV
Y_f	Fission fragment measured yield	
Y_e	np Elastic interaction measured yield	
$\frac{d\sigma_e}{d\Omega_e}$	np Elastic cross section	barns
η	Detection efficiency for flux monitor events	
t_f & t_e	Target thickness	cm
$\frac{N_0}{A}$	Target number density	
$\phi(E)$	Neutron flux at energy E	

The hydrogen cross section is well-measured.

In this measurement, we compare yields for fission events at the various interesting energies. This technique does not allow an absolute measurement, primarily due to a lack of knowledge of the target thickness. In 2002, the collaboration was having difficulty with the liquid deuterium target bubbling. To overcome this, they took data with LH_2, which has a well-known cross section and similar bubbling within the target chamber,to characterize the target thickness. Since we use the LH_2 as a flux monitor, we cannot rely on the data they recorded for target thickness. To remove the target information from our measurement method, we use ratios of the yields at various energies. **Table 4.1** has definitions for all relevant symbols in the following equations. The fission yield can be defined in terms of the uranium target information as follows:

$$Y_f(E) = \sigma_f(E)(\frac{t_f N_0}{A_f})\phi(E) \qquad (4.1)$$

For some special energy, E*, this can be rearranged as:

$$(\frac{t_f N_0}{A}) = \frac{Y_f(E^*)}{\sigma_f(E^*)\phi(E^*)}$$

which can be placed back into **4.1** to give:

$$Y_f(E) = \frac{\sigma_f(E)}{\sigma_f(E^*)} \frac{\phi(E)}{\phi(E^*)} Y_f(E^*) \tag{4.2}$$

This gives a method of linking the fission yields, and there by the cross sections, for different energies E and E*. It also requires no information regarding the target thickness (since we have assumed this value is constant across energies, which is true for a 'white' beam measurement). A complication for this method is that we are required to know the neutron flux at both energies. The LH$_2$ target and associated detectors allow us to determine the flux. The yield for n-p elastic events for a given energy E and scattering angle θ will be:

$$Y_e = \frac{d\sigma_e(E,\theta)}{d\Omega_e} \left(\frac{t_e N_0}{A_e}\right) \eta(E) \, \phi(E) \, d\Omega \tag{4.3}$$

Assuming the same special energy E^*, we can replace the target information with the rearranged equation. This gives a relation for neutron fluxes at different energies.

$$\frac{\phi(E^*)}{\phi(E)} = \frac{Y_e(E^*)}{Y_e(E)} \frac{\eta(E)}{\eta(E^*)} \frac{\frac{d\sigma_e(E,\theta)}{d\Omega_e}}{\frac{d\sigma_e(E^*,\theta)}{d\Omega_e}} \tag{4.4}$$

By rearranging **Equation 4.2** to solve for $\sigma_f(E)$ and inserting the result of **Equation 4.4**, we can get an expression for the cross section that is totally independent of any target information.

$$\sigma_f(E) = \sigma_f(E^*) \frac{Y_f(E)}{Y_f(E^*)} \frac{Y_e(E^*)}{Y_e(E)} \frac{\eta(E)}{\eta(E^*)} \frac{\frac{d\sigma_e(E,\theta)}{d\Omega_e}}{\frac{d\sigma_e(E^*,\theta)}{d\Omega_e}} \tag{4.5}$$

If E^* is chosen such that the cross section for neutron-induced fission is well-known at that energy, **Equation 4.5** gives a method to extrapolate the value of the cross section at another energy E. Since the IAEA calculation is considered the standard, it is logical to pick an energy for E^* and use the IAEA value as the normalization. More discussion will be dedicated to this in the analysis section of this report.

135
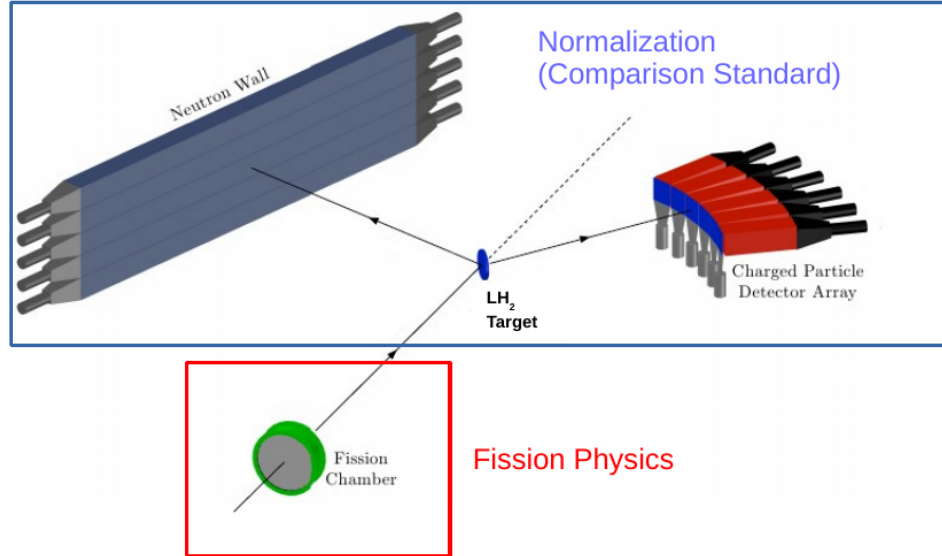
Figure 4.2: A diagram of the experimental geometry for the ^{238}U induced fission measurement. The block labeled 'Normalization' contains the detectors necessary for measuring n-p elastic events. The block labeled 'Fission' contains the detector for measuring fission events. Diagram from [31].

4.1.2 Experimental Apparatus

As previously discussed, there are two experimental goals for this measurement. First, we must measure the number of fission events for various beam energies. Second, we must measure the number of n-p elastic scattering events for various beam energies. To complete this, we use two separate detector sets. **Figure 4.2** demonstrates the geometry of the detectors for this experiment. There are a large number of relevant detectors, so each detector is described below. A schematic of the entire setup, with more details regarding detector placement can be found in **Figure 4.4**

Fission Chamber: This design was created by Wender, et al. in 1993.[37] This is an ionization chamber that houses up to 3 deposits of target material. In our experiment, the chamber contained ^{238}U deposited onto the foil of interest. Each foil is a 0.0013 inch thick steel piece and each uranium deposit is $\sim$ 55 mg. The active site for each foil is a 13.3 cm diameter circle. Each foil is sandwiched between stainless steel holding rings. The chamber is filled with a gas called P10 which is 90% argon
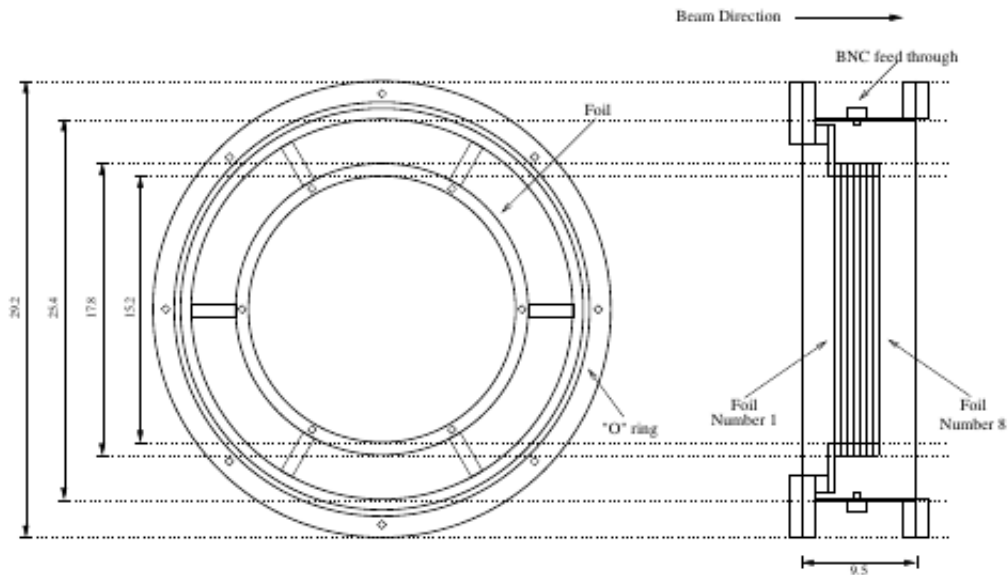
Figure 4.3: A schematic of the fission chamber designed by S.A. Wender, et al.[37] This chamber was used in our measurement to collect the fission event yield. Diagram from [32].

and 10% methane, and kept at a pressure of 68 kPa. When a fission event occurs, the fission fragments move through the gas, creating ion pairs. The chamber is kept at a biasing voltage of -300 V. The negative charge created in the gas is quickly collected on the anode, which produces a negative analog pulse. This signal passes through a pre-amplifier and can then be used in analysis. The time resolution of this detector is on the order of 1 ns. **Figure 4.3** is originally from [37], and is a diagram of the inner workings of the detector. The chamber is placed such that the foil backing is upstream of the uranium deposit.

Neutron Wall: These detectors were created by the University of Kentucky group and details of the device can be found in C. Jiang's thesis[38]. The wall is made of five scintillating 'bars.' Each of these detectors is a 2 m × 10 cm × 10 cm piece of scintillating plastic (BC-408[17])‡. The ends of each bar are attached to a light guide that is a 'half Winston Cone.' A Winston cone is a device that concentrates light

---

‡A discussion of this scintillator can be found in **Chapter 2**

from a large area onto a smaller area, minimizing the losses. A schematic for this light guide can be found on page 29 of [38]. The bars and light guides were wrapped in a reflective foil, then wrapped in black paper and tape to seal them against outside light. These 5 bars were placed horizontally, and stacked on top of one another. This results in a total 'detector area' of 200 cm $\times$ 50 cm. The wall was placed such that the center is 132 cm from the center of the LH_2 target and the bar normal formed a 71° angle with the direction of the beam. Vertically, the detectors were aligned such that the center bar was in the horizontal scattering plane of the beam.

Neutron Veto: This detector set is not shown in **Figure 4.2**. Between the neutron wall and the target were four thin scintillator paddles, which were arranged to fully shield the neutron wall. These were 100 cm $\times$ 25 cm in area. Each is connected to an individual PMT. The purpose of these detectors was to tag charged particles that enter the neutron wall. In this analysis, we require an anti-coincidence between events in the neutron wall and events in the veto detectors, which removes interactions due to charged particles.

Position Strip Detectors: These detectors were thin plastic scintillator strips. They are also not shown in **Figure 4.2**. Two of them were placed along the downstream face of the neutron wall, at 49.5 cm and 149.5 cm from the right hand light guide. Each detector is long enough to span the height of all five bars. These are used as calibration points in the analysis. By requiring a coincidence between the neturon wall and the position detectors, we have localize where the particle passed through the bars. We can then use time difference spectra to locate the event in the bar position spectrum.

CsI Detectors: These detectors comprise the majority of the charged-particle tele-

scope detectors. Each pure CsI crystal had dimensions 30 cm × 9.2 cm × 9.2 cm, with the longest dimension along the 'stopping' direction of the incoming protons. Each crystal had its own PMT, and was analyzed in coincidence with the ΔE detectors. There were six of these detectors in total, placed at angles of 16°, 24°, 30°, 36°, 42°, and 48° relative to the beam direction. Each detector was placed such that the face was 100 cm from the center of the LH$_2$ target.

ΔE Detectors: These detectors are thin sheets of scintillating plastic with a cross-sectional area of 9.2 cm × 9.2 cm. They fully covered the face of each CsI crystal by being placed between the target and the CsI. The scintillating plastic has a much better time resolution than the CsI crystal and was used to gather timing information about the charged particles. These detectors were used in coincidence with the CsI. Two-dimensional plots of energy deposited in both ΔE and the CsI crystal (ΔE-E plots) are a method of particle identification.

This experiment was conducted at the Weapons Neutron Research (WNR) facility on the campus of Los Alamos National Laboratory. **Figure 4.5** shows a top down view of the facility as it was in 2002 when this experiment was run. At WNR, neutron beams are generated by directing an accelerated proton beam onto a neutron spallation target. The protons are accelerated to 800 MeV before impinging upon the target. Neutrons generated by this interaction cover a full 4π solid angle. The spallation target is housed in a building (marked 'Target 4' on the diagram) that has multiple small, unimpeded outlets that act as beam pipes. This experiment used the 4-15R flight path. 4-15R is a reference to being 15° right of the incident proton beam onto Target 4. Each flight path had the ability to collimate the neutron beam[§], as well as stop it entirely by closing shutters made of depleted uranium. Of particular importance for this measurement is the beam structure. This measurement makes

---

[§]See [32] for a full discussion of the collimation in this experiment.
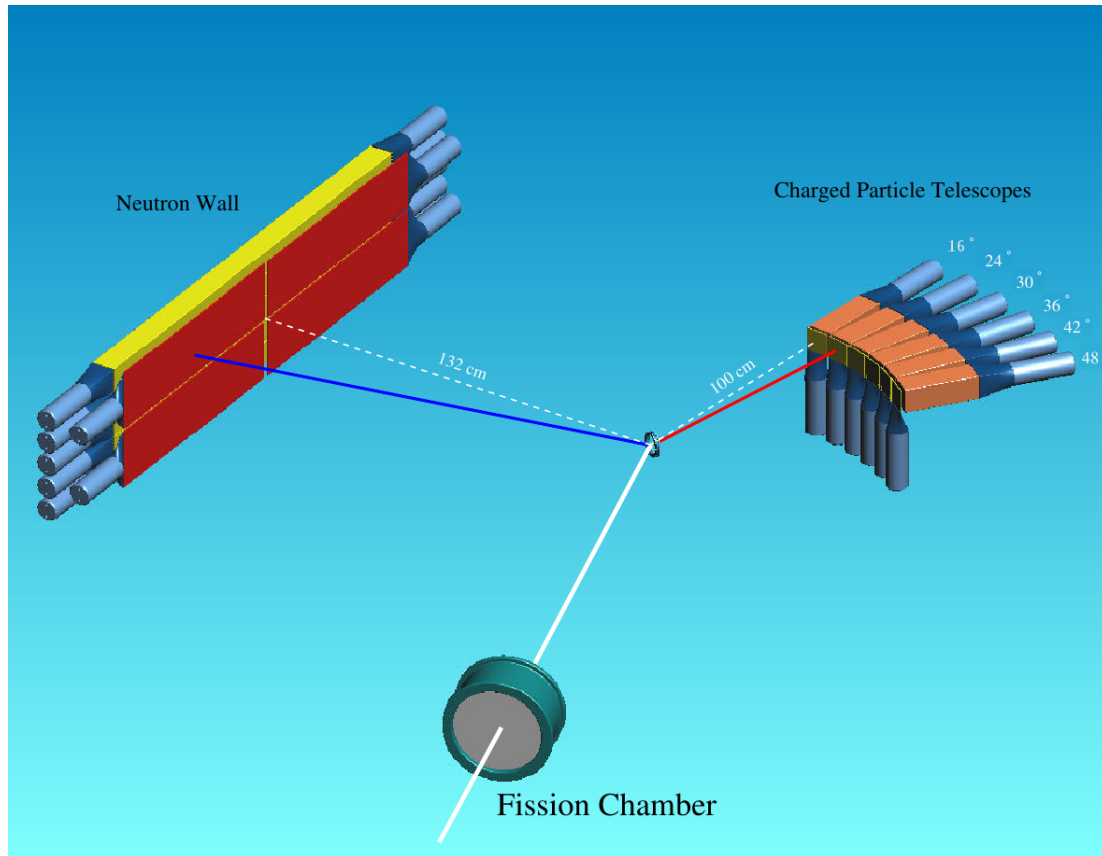
Figure 4.4: A schematic diagram of the experimental geometry for the ^{238}U induced fission measurement. The angles for the proton telescopes have been changed from the original to match this experiment. Diagram from [32].

use of a time of flight technique that is used to calculate the energies of all involved particles. Since the beam had a pulsed structure during the experiment, it is important to know if the pulses were far enough apart in time that the slowest neutrons of interest were no longer propogating through the experimental area when the fastest events from the next pulse arrived. The beam stucture is demonstrated in **Figure 4.6**. The 1.8 μs spacing between pulses is long enough that there was no overlap of pulses for our energy region.

The beam for this experiment was collimated to 0.5 inch diameter, using steel collimators. The depleted uranium shutters were opened to 1 inch $\times$ 1 inch. The result is the beam profile shown in **Figure 4.7**. This image was created by using a storage-phosphor image plate and a laser-based scanning device that determines the
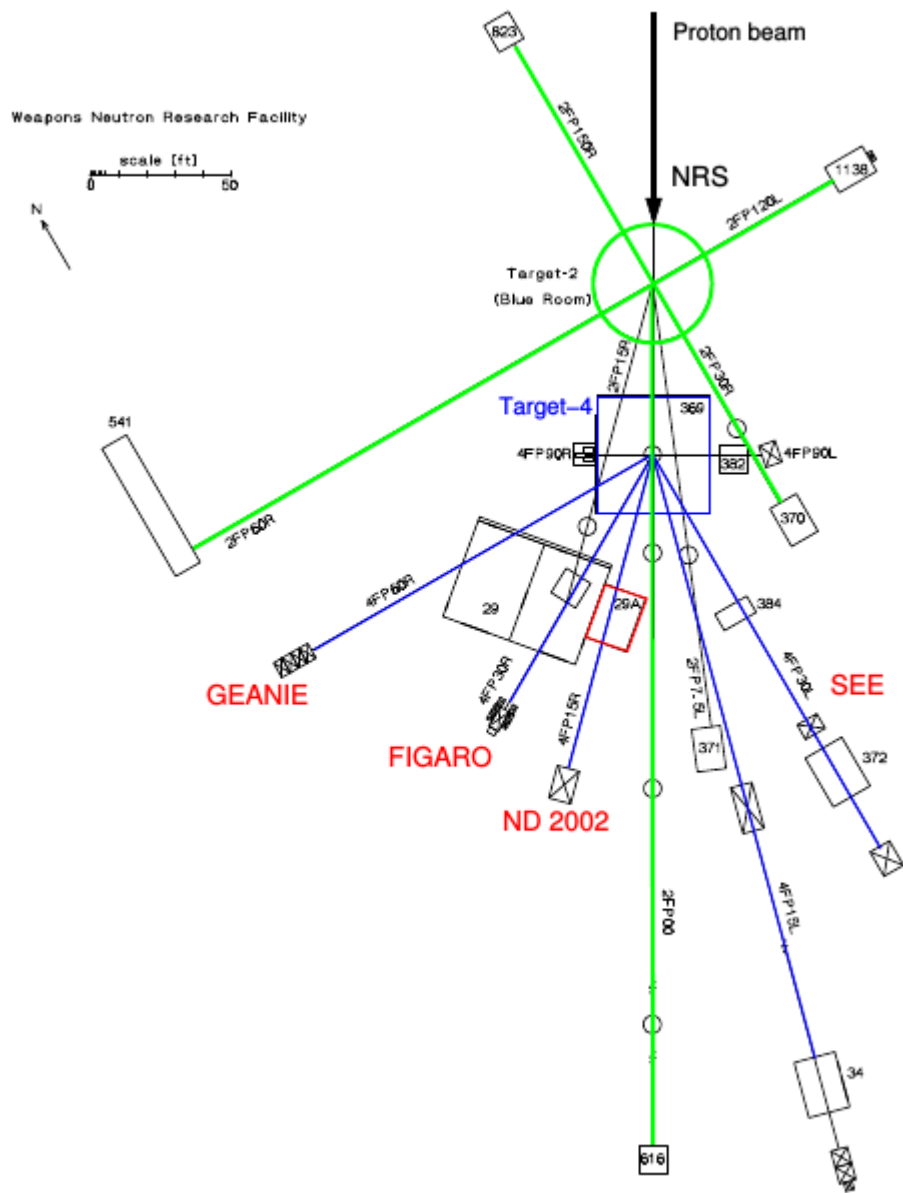
Figure 4.5: A schematic diagram of the WNR facility. This experiment occurred in 4-15R, marked as 'ND2002' on the diagram. Diagram from [32].
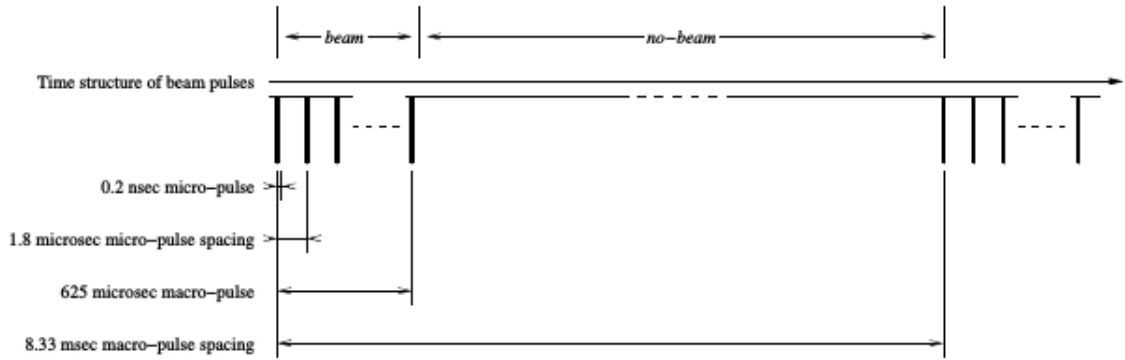
Figure 4.6: The beam structure at WNR. This was pulsed in two manners. On the macroscopic scale, there were 8.33 ms between whole pulses (120 Hz). In each 625 μs macro pulse, there were ~ 350 micropulses for a micropulse spacing of 1.8 μs. Diagram from [32].
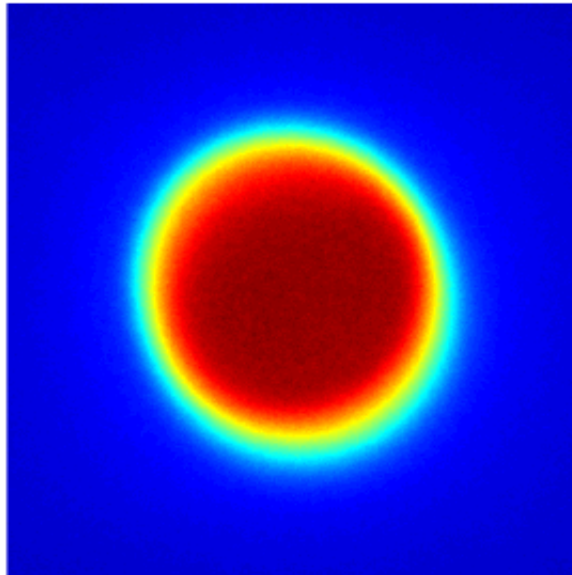
Figure 4.7: Incident beam profile from a positional dependent intensity measurement. Measured by a storage-phosphor image plate. This locates the beam within the room, as well as determining the effective beam width at the target position. Diagram from [32].

neutron flux across the beam profile. More details can be found in [33]. The intensity profile and beam width are important, as the LH$_2$ target did not have a large active site like the fission chamber. With this measurement, the beam position was known to 1 mm.

Table 4.2: List of all relevant data signals for ^{238}U measurement.

Detector Type	Number of Detectors	Channels/Detector	Data Type
Charged Particle Telescope	6	2 (ΔE/CsI)	ADC/TDC
Neutron Bar	5	2 (Left/Right)	ADC/TDC
Neutron Veto	4	1	ADC/TDC
Neutron Position Strip	2	1	ADC/TDC
Fission Chamber	1	1	ADC/TDC
t_0	1	1	TDC
PuBe (tagger)	1	1	ADC/TDC

4.1.3 Electronics

This experiment used a CAMAC-based FERA (Fast Encoding and Readout ADC) data acquisition system to record data. In order to record the correct data, each signal passed through a large array of modules to process it, generating various readout triggers. For the purposes of this analysis, 6 trigger types were of interest: fission, neutron single, proton single, np-coincidence, cosmic ray, and plutonium-beryillium (PuBe). With each trigger, the system accessed data values for all detectors. **Table 4.2** lists all data outputs. Each set of detectors had an associated signal processing chain. Each chain is described in brief below, noting that detectors with multiple copies will only be discussed once, as each instance of the detector had the same electronic setup.

t_0: The t_0 signal was generated by the proton beam as it struck the neutron spallation target. In this experiment, this signal was then delayed and acted as the stop for all of the timing devices, providing the time scale for all events. This signal was split upon creation, going to three different 'algorithms.' One segment was delayed and sent to the TDC stops. A second segment was fed into a gate generator, inverted, and then used as a veto to insure that only events with a valid neutron generation were
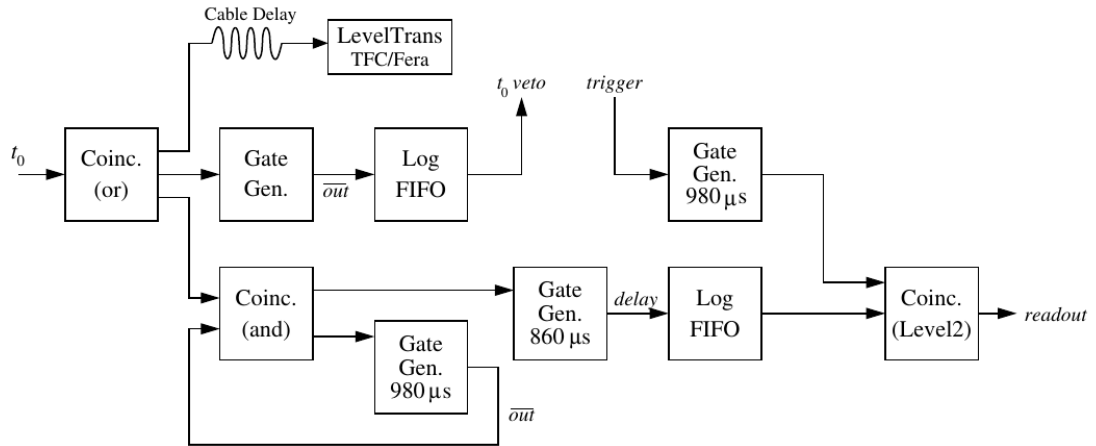
Figure 4.8: Block diagram of t$_0$ electronics. Diagram from [32].

collected as 'live events.' The final segment was used to improve data acquisition live time. Due to the low duty factor of the beam, it was ideal to read memory buffers during the existing dead time between macropulses. The FERA system had a large enough memory to store all of the data taken during a single macropulse, so the first t$_0$ of a new macropulse opened a gate, which controls the memory read timing. This gate was 625 μs in length. When this gate closed it would activate the memory read algorithm, such that the memory was only read while the beam was inactive. A block diagram for the t$_0$ system is found in **Figure 4.8**

Fission Chamber: The output signal from the fission chamber was divided into three segments by a linear fan-out after pre-amplification. Two of these signals went into discriminators, which were used alongside the t$_0$ veto to decide whether a fission event should be processed. The 'double discrimination' technique was used to get pulse-height independent timing. Both lines went through 'constant fraction timing discriminators (CFTD)' which minimized time dependence. The threshold was set at the single photoelectron level on the line used to determine the true timing. The 'actual' threshold was set on the other line, which was used to reject pulses that were

144
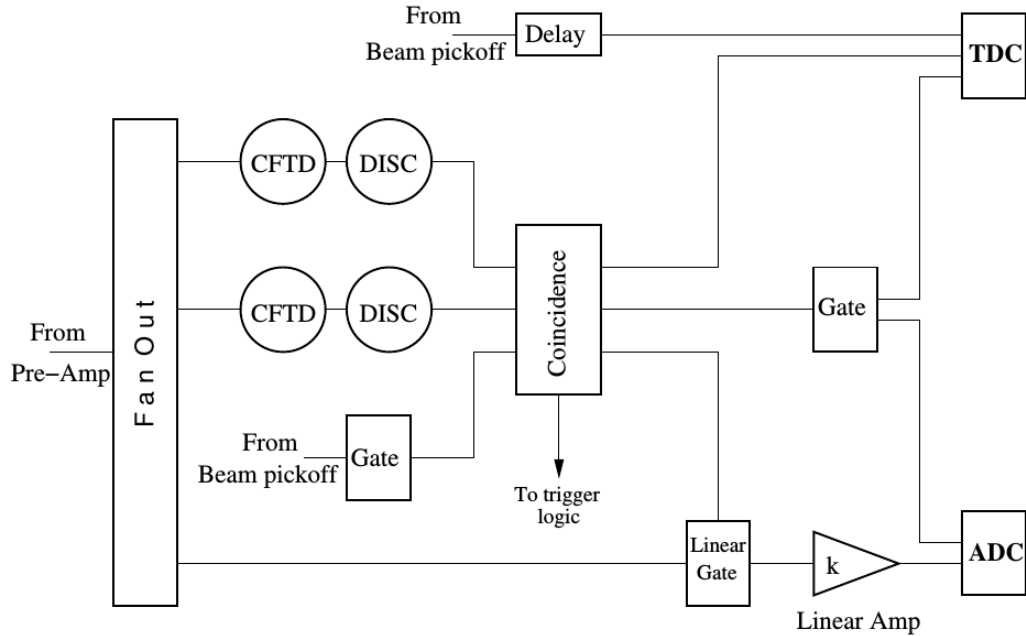
Figure 4.9: Block diagram of fission chamber electronics. The lines labeled 'Beam Pickoff' are referring to the t_0 signal. Diagram from [32].

not large enough to be true signals. The threshold for the discriminators was set below the smallest fission fragment pulse size. The other line from the fan-out was amplified again and passed through a linear gate to remove background noise and reject double pulsing. For those events that passed the discrimination threshold, the timing gate was used to start a TDC which was stopped by the t_0. The output of the discriminator was also sent to the trigger logic. **Figure 4.9** demonstrates the fission chamber electronics.

Charged Particle Detector: The CsI portion of the detector was split into two lines. One of these lines was delayed and then sent to a linear gate, which lead to the ADC. The second line entered a constant-fraction discriminator. From the discriminator, one line acted as the timing information by acting as the start for the TDC. The second line from the discriminator acted as the gate for the linear gate, self-timing the analog pulse to remove surrounding background noise. A third line went to a co-

145
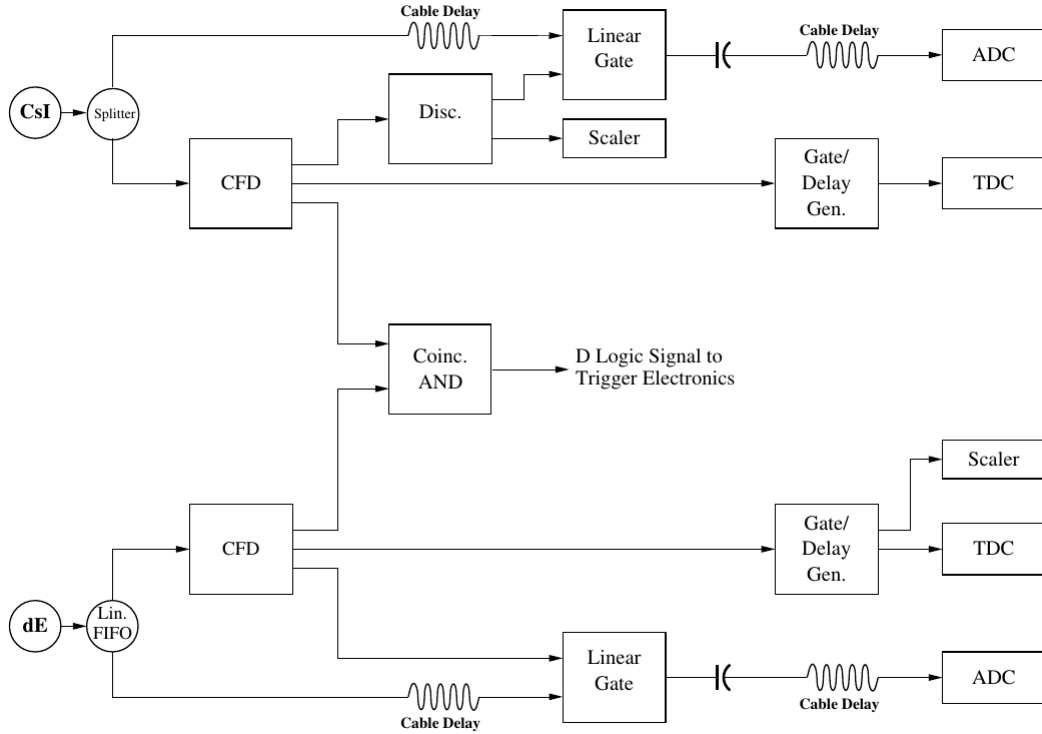
Figure 4.10: Block diagram of charged particle detector electronics. Diagram from [32].

incidence module, that allowed interaction with gates from the ΔE electronics. The ΔE detector had the same electronic setup as the CsI, save the addition of a scaler to monitor interaction rates. The shared coincidence module was used for trigger information from the charged particle detector. This coincidence requirement ensured that only particles that passed through both the ΔE and the CsI were analyzed, since only these events could have come from the target. **Figure 4.10** demonstrates the charged particle detector electronics.

Neutron Detector: Each PMT on the neutron bar was treated like the CsI portion of the proton detector. The main difference was that the coincidence requirement was not between itself and the ΔE detector, but between itself and the PMT on the other end of the bar. Additionally, each neutron PMT was used as part of a timing device, so a scaler was attached to each PMT to monitor count rates. The coinci-
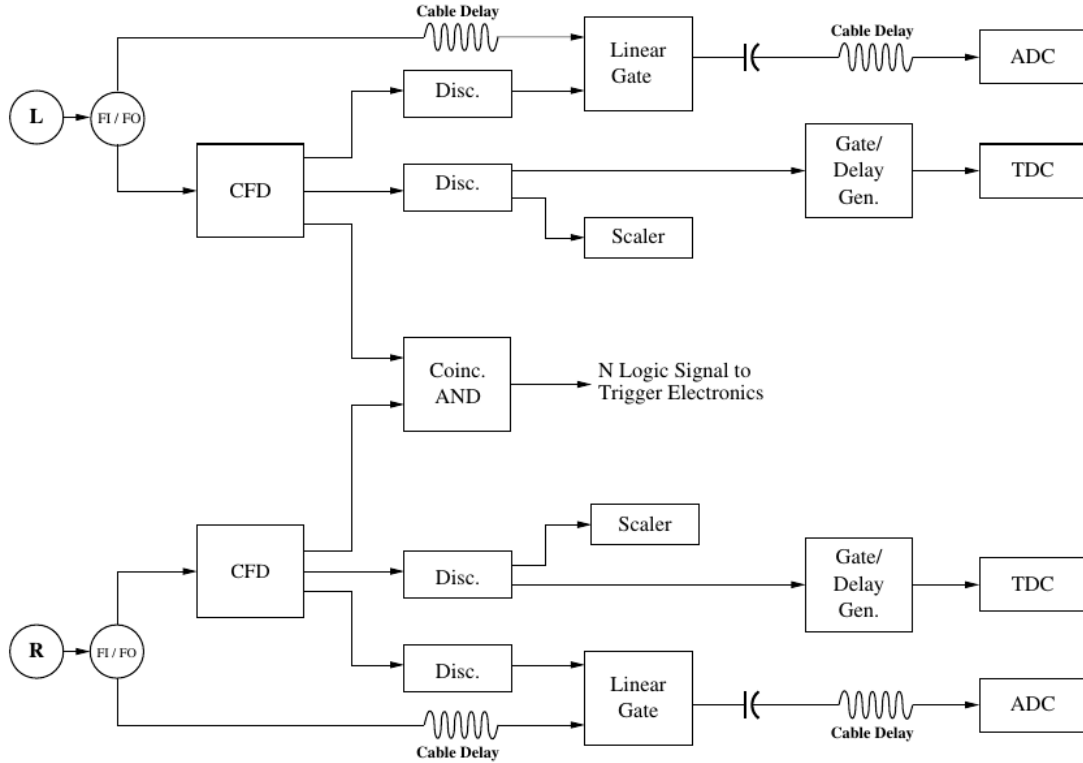
Figure 4.11: Block diagram of neutron bar electronics. Diagram from [32].

dence between the pair of PMTs was used in the trigger electronics. **Figure 4.11** demonstrates the neutron bar electronics.

Neutron Veto Detectors: The neutron veto detectors were stand-alone detectors, in the sense that their electronics were self-contained. Each signal was split in two. One line was delayed and sent through a self-timed linear gate. The second line was discriminated and then used as both the gate for the linear gate and as the TDC start. A scaler was attached to the discriminated line to monitor the event rate. These detectors did not interact with the trigger logic in any way, as the veto was applied in the software during replay.

Neutron Position: These detectors were like the neutron veto detectors, with the signal split to gather both ADC and TDC information. These detectors did not in-

147

teract with the trigger electronics. However, they are not used in every event during the analysis like the neutron vetos are. Instead, they are used to tag 'special events' that pass through a specific portion of the bar. By using replay processing, we can identify events that share a coincidence between a neutron bar and the position strip. This software coincidence allows calibration of the particle position calculation.

Plutonium-Beryllium Tagger: As a calibration mechanism, a PuBe source was placed behind the neutron bars. To tag events coming from the source, a liquid scintillator was placed 1.5 m behind the source. PuBe emits neutrons and gamma rays in coincidence whenever an alpha particle, which is emitted by ^{239}Pu at a high rate, is absorbed by ^{9}Be, to form ^{12}C in its first excited state. This combination of plutonium and beryllium is the reaction:

$$\ _2^4He + \ _4^9Be \ \rightarrow \ _6^{12}C^* + n \tag{4.6}$$

By detecting the emitted neutron in the PuBe tagger, the neutron bar may see the associated gamma ray in coincidence, which has a well-defined energy value of 4.4 MeV. To identify these events, the PuBe tagger was treated like the 'Neutron Veto' detectors, with the key difference that the discriminated line was linked into the trigger electronics. More detail about the generation of that trigger will be discussed in the section dedicated to trigger electronics.

The trigger electronics were the most complicated portion of the setup for this experiment. For this discussion of trigger generation, all signals are assumed to be from the discriminated line of their respective electronics. To begin, all of the outputs from the charged particle array were OR*ed* together in a logic unit.[¶] This was also done for the neutron bar outputs. These are the 'proton singles (pSing)' and

---

[¶]In Figure 4.12, the charged particle detectors are labeled as 'D##.' This is a reference to their initial purpose as deuterium detectors. Also, the ##'s correspond to the angle of the detector. In the proton data, the detector at 54° was moved to 16 °

'neutron singles (nSing)' triggers respectively. These were not the triggers of primary interest, thus each of these was passed through a $\frac{1}{N}$ pre-scaler, which only allowed every N^{th} trigger to pass. The outputs of these two ORs (before pre-scaling) were also connected to a coincidence module. This coincidence formed the 'neutron-proton coincidence (Coinc)' trigger. This is the trigger of primary interest, and was unscaled during data collection. To minimize background for these triggers, a t_0 veto was applied to each trigger generator. This veto was inactive if a proton pulse had struck the neutron target within the past 1.8 μs. This removed a large portion of those accidentals that occur uncorrelated with the beam. After this veto, all of the triggers were OR*ed* together by a single module that connected all triggers to the data acquisition START. This was known as the 'Master Trigger.' **Figure 4.12** shows this portion of the trigger generating electronics. The triggers labeled 'Laser' and 'Americium (Am)' are not used in this analysis and haven't been discussed.

The fission chamber trigger was independent of all the coincidence requirements between neutrons and protons, as this detector was a self-contained portion of the experiment. The trigger generated by the chamber was fed into the master trigger after being vetoed by the same 1.8 μs requirement discussed in the previous paragraph.

There were two calbration triggers, which were treated differently than the production triggers. Cosmic rays are used in this analysis as a calibration for the neutron bars due to being minimum ionizing particles. In order to identify cosmic rays we require that three or more neutron bars trigger in coincidence. This only occurred when an event entered the detectors from the top down. **Figure 4.13** shows an example track of a cosmic ray. The neutron bar triggers were multiplexed in a way that was only active when there was a signal in three sets of connected PMTs, since PMT pairs require a coincidence to mark the bar as active. This is also shown in **Figure 4.12**. The other calibration data came from the PuBe trigger. This trigger type was generated whenever there was a coincidence between an nSingle trigger and the PuBe
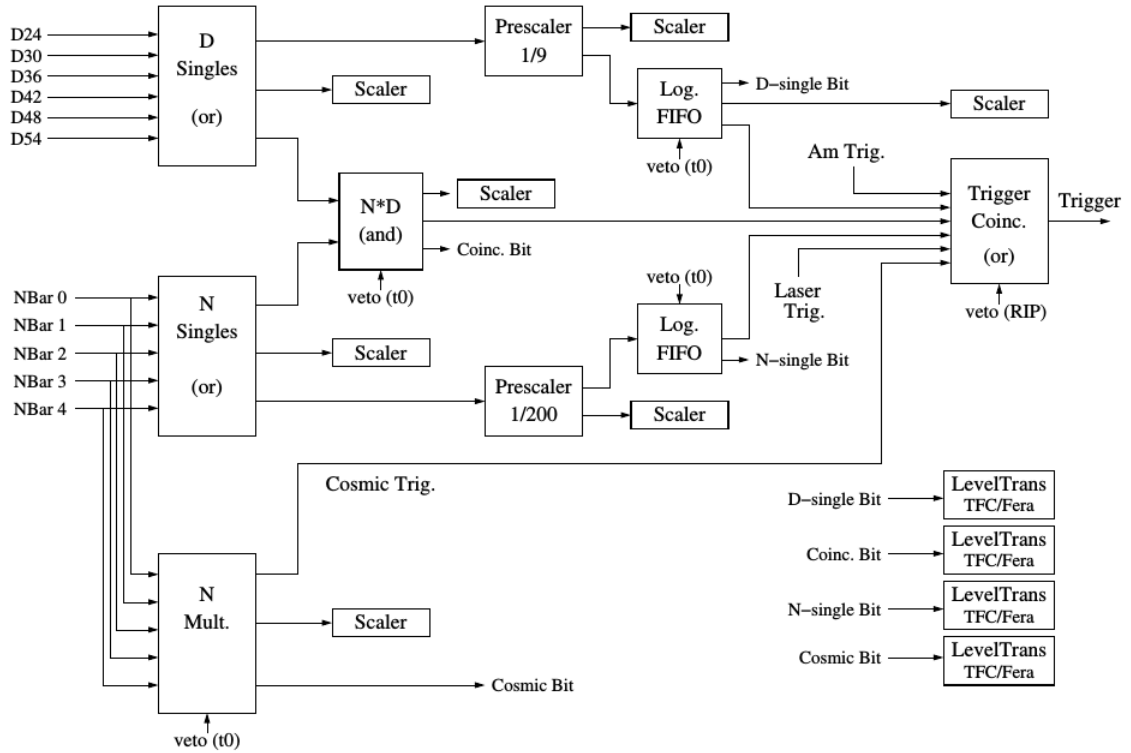
Figure 4.12: Block diagram of the trigger generation electronics. The charged particle detectors are labeled a 'D##.' This is a reference to their initial purpose as deuterium detectors. Also, the ##'s correspond to the angle of the detector. In the proton data, the detector at 54° was moved to 16 ° Diagram from [32].

tagger detector. Both of these calibration triggers required an anti-coincidence with the t_0 veto gate. This guaranteed that calibration data was only collected when beam events were not present in the experimental area.

For all trigger types, the output of the trigger generation was routed the master trigger, which connected each trigger to the DAQ. However, each trigger generator is also connected to a TDC. These TDCs acted as 'trigger tagging bits' that were 0 when there was no event of that type, and formed a self-timed peak when the associated trigger was generated for the event. Using cuts in the software replay, we are able to select event type based on the trigger bits.
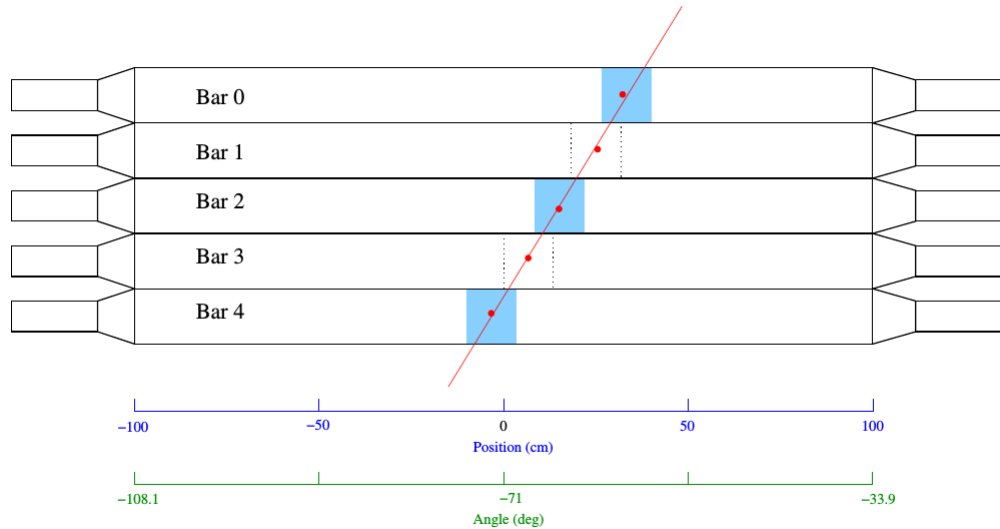
Figure 4.13: Cartoon of a cosmic ray interaction in the neutron wall. By selecting only events that are seen in 3 or more bars, we select out events that can only have come from above or below the wall. Diagram from [32].

4.2 Analysis

4.2.1 Calibration

For this measurement, the largest portion of the calibrations involved identifying the energy level of interactions in the neutron bar. Both the fission chamber and the charged particle telescopes are vital for the measurement, but the absolute scale of these responses is less important when we are only interested in the total number of interactions. For these two the time of flight calibration is important, but is not a complicated calibration. By design, this experiment had two tagged interaction types that were exclusively for calibrating the neutron detectors: cosmics ray triggers and PuBe triggers. In the neutron detector, the response (and efficiency) is strongly linked to the value of the threshold. As the detector efficiency is one of the main ingredients in the cross section calculation, we must know it precisely. In order to accomplish this, a low threshold was set in the hardware, such that we analyzed a very high percentage of all events. In the software replay of the data, a higher threshold is set. In this analysis, that threshold is set at 4.159 MeVee. MeVee (MeV electron

151

equivalent) is a unit sometimes used to compare the scintillation reactions of electrons and heavy particles (e.g. protons). This difference is due to quenching. Quenching is based on the assumption that high ionization density in a material will result in less light production for heavy ions. Due to quenching, a proton will produce less light in the scintillator than an electron with an equivalent energy. When determining the threshold for this analysis, we used a gamma ray source. This means our threshold is set in terms of electron light production, or MeVee. There is no quick mapping between MeVee and MeV, as it changes based on material.

The plutonium-beryllium (PuBe) source is the more exact of the two calibration methods. The liquid scintillator PuBe tagging detector was 1.5 m behind the neutron wall. In between these two, a PuBe source was placed. This source produces γ-n pairs. The gamma ray is 4.4 MeV, as it is created when ^{12}C* decays from it's first excited state. The trigger for this type of event was only active when both the PuBe tagger and the neutron wall saw an event in coincidence. By analyzing both time and pulse-height information for the PuBe tagging detector, it is possible to select events in which the tagging detector saw a neutron. If the tagger saw a neutron in coincidence with the neutron wall, the wall mot likely saw the associated 4.4 MeV gamma ray. A 4.4 MeV gamma ray has a 4.159 MeVee Compton edge. Due to light attenuation across the length of the bar, picking out a Compton edge is nearly impossible for a single PMT. The edge is simply too smeared by the attenuation of the signal over the length of the bar. Only events near the PMT will record the true maximum value, and these are a small portion of the total detected events. The solution is to form a position-independent quantity out of the two pulse height spectra, which is known as the geometric mean ADC, or $\overline{ADC}$.

$$\overline{ADC} = \sqrt{(ADC_L - Pedestal_L) \cdot (ADC_R - Pedestal_R)} \tag{4.7}$$

When analyzing this value, nearly all position dependence is removed and a correction factor can be applied, since this dependence has been measured[38]. The $\overline{ADC}$
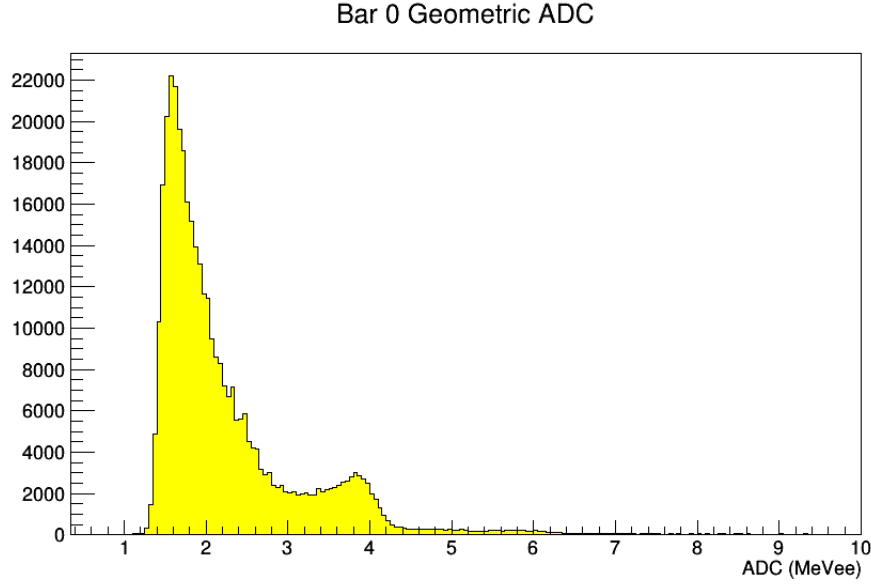
Figure 4.14: An example spectrum from a single neutron bar, for events tagged as gamma rays from the plutonium-beryllium source. The Compton edge at 4.159 MeVee acts as the energy calibration point for the detector.

spectra clearly shows a Compton edge. We use this point to convert ADC channels into a true energy value. **Figure 4.14** shows an example Compton edge spectrum. The downward slope at 4.159 MeVee acts as our calibration point to determine an MeV/channel conversion.

The cosmic ray calibration involves looking for events in which three or more of the neutron bars were activated while the beam is not active. This trigger generation has been described in the previous section and **Figure 4.13** shows an example of how this type of interaction would occur. Cosmics muons are a type of minimum ionizing radiation. Ths means we know precisely how much energy a cosmic ray should impart as long as we know the path length inside the scintillator.

$$E_{Dep} = \frac{dE}{dx}\bigg|_{CR} \cdot \rho_{BC408} \cdot \Delta x \tag{4.8}$$

$\frac{dE}{dx}$ for a cosmic ray is 2.1 MeV $\cdot cm^2 \cdot g^{-1}$ and the density of BC408 is 1.032 $g \cdot cm^{-3}$. Due to the design of the trigger, we know that the minimum distance that a cosmic can travel in the bar is 20 cm since it must interact in three total bars (and neglecting

153

the special case where it enters through the side of one bar). If the ADC to energy calibration from the PuBe source is correct, the energy distribution of cosmic ray events should have a peak at ~ 40 MeV. For an event that passes through three complete bars, and starts into the fourth, we expect a peak at ~ 60 MeV. If an event passes through four complete bars and into the fifth bar, we would expect a peak at ~ 80 MeV. We also expect the peaks to broaden as the energy rises. The larger the required path length, the lower the chance an event will have had *exactly* the correct angle to see the whole bar. **Figure 4.15** shows the neutron bar geometric mean energy spectrum for cosmic ray events. This distribution is precisely what we expect to see, and the leading edge of the distribution shows that our calibration with the PuBe source is correct. The long tail at the end is because of the various flight paths that the cosmic muons may take through the plastic. The largest possible path is 206 cm long, which corresponds to an energy of 433 MeV. In Chtangeev's [32] analysis of this same data, he completed a more involved method that used the position resolution of the bars to correct for the path length in the detector wall to determine the energy if the cosmic muon had arrived in an exactly vertical direction. This resulted in better definition to the peaks and removed the long tail. For the purposes of this work, the ability to confirm both the PuBe calibration and Chtangeev's result was sufficient to say that these detectors were properly calibrated.

The last calibration exclusively for the neutron bar is to calibrate the hit-position detection. The method described in **Equation 2.5** is still valid in this case. The bars have a different width and length, but the method is the same. We use the time difference from PMT pairs to locate the position of the interaction. The 'neutron position' detector output is also used as each detector is a thin strip that is lined up 50 cm from one end of the bar. By analyzing events that have interactions in both the bar and the position strip, we know that the hit must have occured within the solid angle formed by the union of these two. Using the time difference and
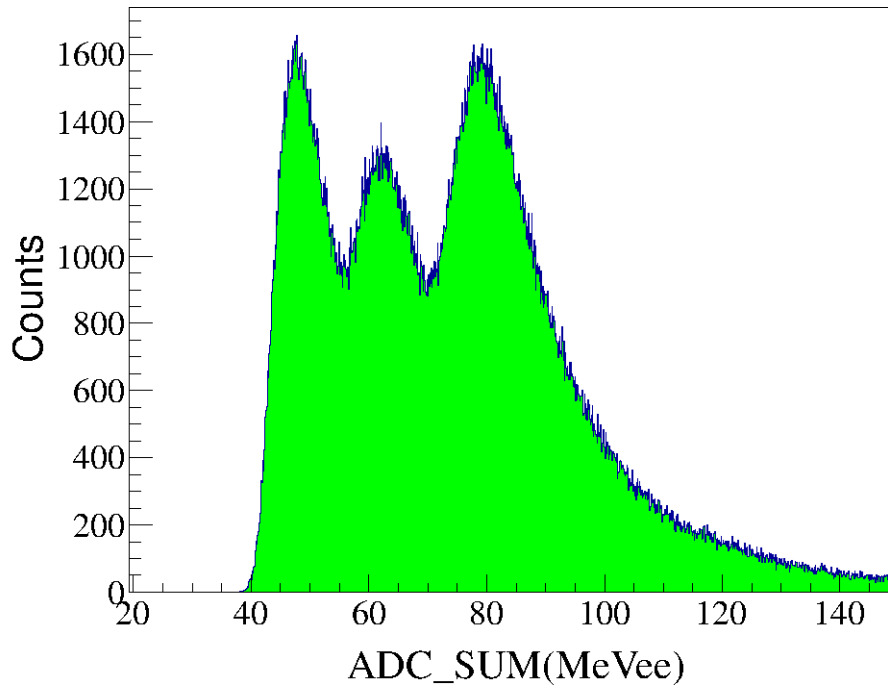
Figure 4.15: The energy distribution of the cosmic ray triggers. This distribution is precisely what we expect to see, and the leading edge of the distribution shows that our calibration with the PuBe source is correct. The long tail at the end is because of the various flight paths that the cosmic muons may take through the plastic. The largest possible path is 206 cm long, which corresponds to an energy of 433 MeV.

material information, we calculate the position of the interaction within the bar. This position is known for events that also have signals in the position strips. This can be convereted into a 'neutron scattering angle/time difference' conversion. The data points from the position bar provide a first-order fit to determine whether the conversion is accurate. A result similar to **Figure 2.17** is found. This result is improved by using conjugate n-p scattering pairs from the real data. Since we know the angle and energy of the proton from the charged particle detector data, we can calculate the angle of the neutron using kinematics. These four angles and the position detector data point form a quadratic fit, as shown in **Figure 4.16**. This maps the time difference spectrum into an angle spectrum. Since we also know the angle to the center of the bar, this can also be mapped to a 'position along bar' spectrum, which we call the 'x-position'.

155
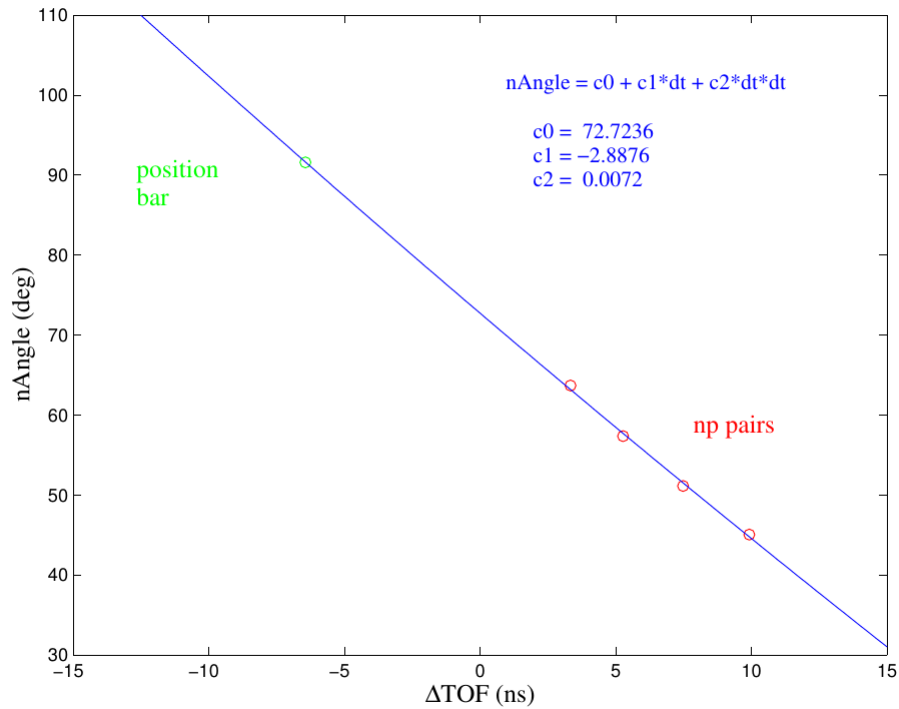
Figure 4.16: The neutron scattering angle as a function of time difference in the neutron bar. The angle directly determines the position in the bar. Both the position bar and the n-p conjugate pairs are used to make this fit. Image from [32].

All energy conversions in this measurement are based on time of flight. This method relies on knowing the time of arrival for each particle in an event to a high degree of accuracy. It also relies on successfully converting TDC channels into a true time. Converting between TDC channels and time is simple thanks to the time calibrator module. It produces periodic pulses, that can be fed into the start and stop portions of the TDC. With this known time difference between the pulses, a 'bins/ns' calibration can be constructed by finding spikes in the TDC spectrum.

All three detectors have reliable methods for determining the time of arrival as well due to excellent time resolution. In the fission chamber, the time resolution is on the order of 1 ns. In the charged particle detectors, we can use the ΔE detectors which are thin, fast scintillators. These scintillators have rise times of < 1 ns and have a total time resolution on the order of 2 ns. In the neutron wall, things aren't

so simple. The time delay between neutron arrival and photons arriving at the PMT is position dependent. However, we can construct a position independent quantity using the information we have.

$$\bar{t} = \frac{1}{2}(t_R + t_L) \tag{4.9}$$

This quantity is called the mean time and is independent of hit position within the bar, due to the constant speed of light in the material. Using the mean time, the neutron bars also have a time resolution on the order of 2 ns. To construct the mean time for the neutron bar, we must first calibrate each PMT individually to have a correct conversion between channels and time.

For all three detector types, we calibrate the time of flight by using the 'gamma flash.' When protons strike the neutron production target, they also produce gamma rays. These gamma rays move at the speed of light down the flight path, and can be seen in all three detectors. Gammas can be elastically scattered from the LH_2 then interact via electron scattering in scintillator and CsI. They also interact in the fission chamber via (γ,f). Since we know the flight path length with a high degree of accuracy, we know precisely how long it should take a particle traveling at the speed of light to reach the detector. We line up the earliest arriving true events (the gamma rays) with the correct amount of time for them to propagate to each detector. This sets the absolute time scale for all events, as all other events else can be measured relative to the gamma flash. An example time spectrum from the charged particle detectors is shown in **Figure 4.17**.

The gamma rays that elastically scatter from the LH_2 target are forward peaked. This is not a problem for the charge particle telescopes due to their small overall size. However, this caused the neutron bar to be nonuniformly illuminated. Given it's length and angle, the side of the wall farthest from the beam saw very few gamma rays near the PMT. 'Nearby' events are required to see a well defined gamma flash edge in a single PMT. However, by selecting a small central region of the bar's x-
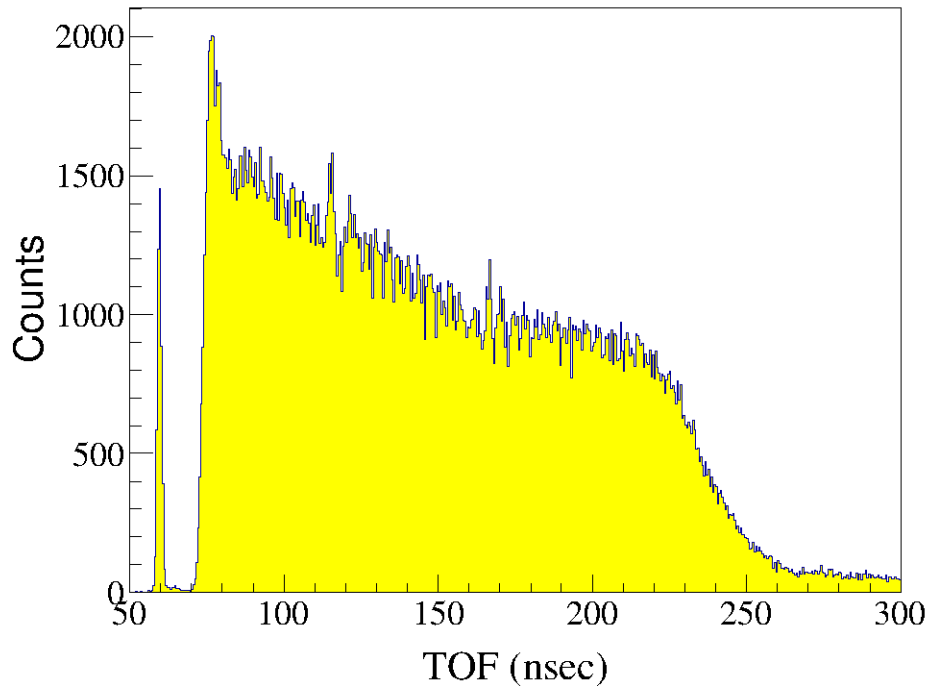
Figure 4.17: Time of flight for a single ΔE detector, for all beam energies. The leading peak is the gamma flash, which sets the overall time calibration. The following data is the time structure of the protons as they arrive from the target.

position as the 'hit region' and only analyzing events from that region, a large portion of the smearing associated with the bar length is removed. This allows identification of the gamma flash. This gamma flash is used to calibrate each individual tube, which is required for making the position independent quantities. The flight path to the central region is 132 cm from LH_2 to bar and 16.93 m from spallation target to the LH_2 target. This is an iterative process, as one must use the time difference to clean up the calibration of the time.

4.2.2 Fission Yield

Extracting the fission yield is actually the easiest part of this measurement. The TDC information is first converted into time of flight using the gamma flash technique described in the previous section. This time of flight is aligned such that the gamma

flash's leading edge is at 48 ns, which is determined by the flight path for the target. The flight path to the fission chamber was 1545.0 cm in length. This sets the time of flight for the neutrons of interest. This time can then be converted into energy using a relativistic calculation.

$$v = \frac{L}{t_n}$$

$$\gamma = \frac{1}{\sqrt{1 - \frac{v^2}{c^2}}}$$

$$E_n = (\gamma - 1) \cdot M_n \cdot c^2 \tag{4.10}$$

In this conversion, L is the flight path length, t_n is time of flight for the neutron, and M_n is the neutron mass in MeV. **Figure 4.18** shows a typical time of flight spectrum for all beam energies impinging on the fission chamber. Once the energy is determined, we can seperate events by incoming beam energy.

We also need to determine the number of fission type events for each beam energy. In the pulse height spectrum for the fission chamber, there are two types of events. A typical spectrum is shown in **Figure 4.19**. On the left side of this plot, at low pulse height, are alpha particle decays. For ^{238}U, the alpha particle rate is comparable to the fission rate for energies we are interested in. This peak can be fitted with a Gaussian to determine its distribution. On the right side, the 'bump' in the spectrum contains the fission events. To obtain the yield, we integrate the fission 'bump.' The key to this integration is deciding where to place the lower integration threshold. By fitting both of these peaks, we can find a point in the minimum where the number of alphas above the threshold is the same as the number of lost fission events below the threshold. With this threshold position there is no necessary correction to the total fission yield, as the correction is inherent in the threshold selection. The threshold was set at 317 channels in the analysis. In Chtangeev's analysis[32], he tracked the fluctuation of the gain in the fission chamber by monitoring where the true minimum between these peaks occurs for each run. He found that when calculated for every
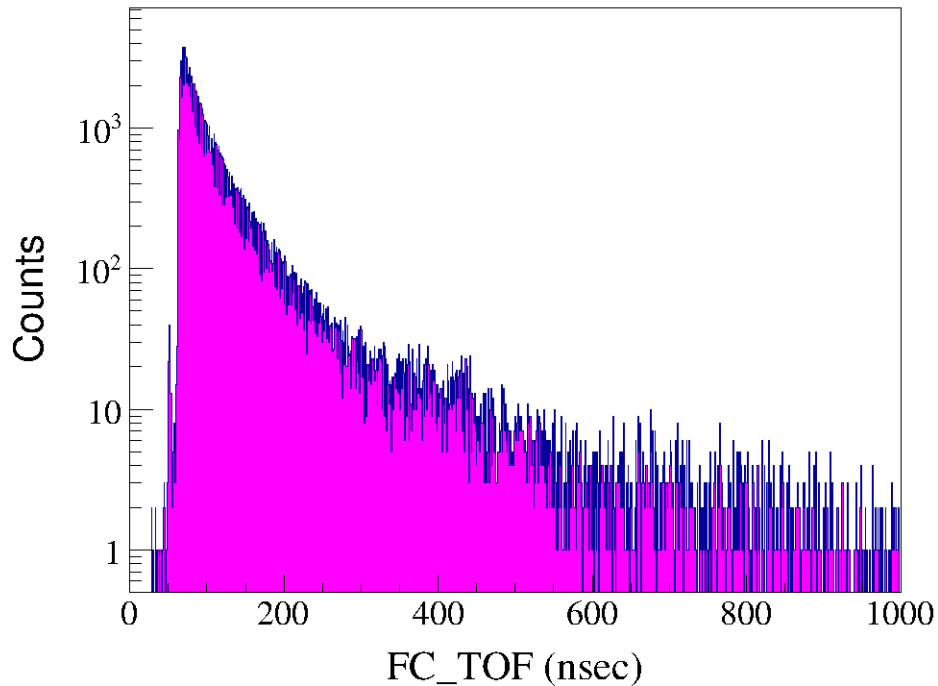
Figure 4.18: Time of flight for the fission chamber detector, for all beam energies. The leading peak is the gamma flash, which sets the overall time calibration. The following data is the time structure of the neutrons as they arrive.

two hour run, the location of the true minimum was stable within the fitting errors. Based on his analysis, only a single threshold was used in analyzing these data. For each beam energy bin of interest (10 MeV bin width), a histogram was compiled for all available fission chamber data. The integration from the low threshold to the top of the fission fragment range fully determined the yield for a given energy range.

The choice of using a 10 MeV bin width is neither arbitrary, nor based on needing higher statistics per bin. This limit is set by the resolution of the fission chamber. As discussed in the calibraton section, the fission chamber has a time resolution of ~ 1 ns. With an incoming neutron energy of 200 MeV, a 1 ns time resolution translates to roughly 5 MeV energy resolution. A 10 MeV beam energy bin width for the fission chamber data fully encloses the variation based on the timing resolution. Since we normalize the data on a bin to bin basis, this also sets the bin width for the
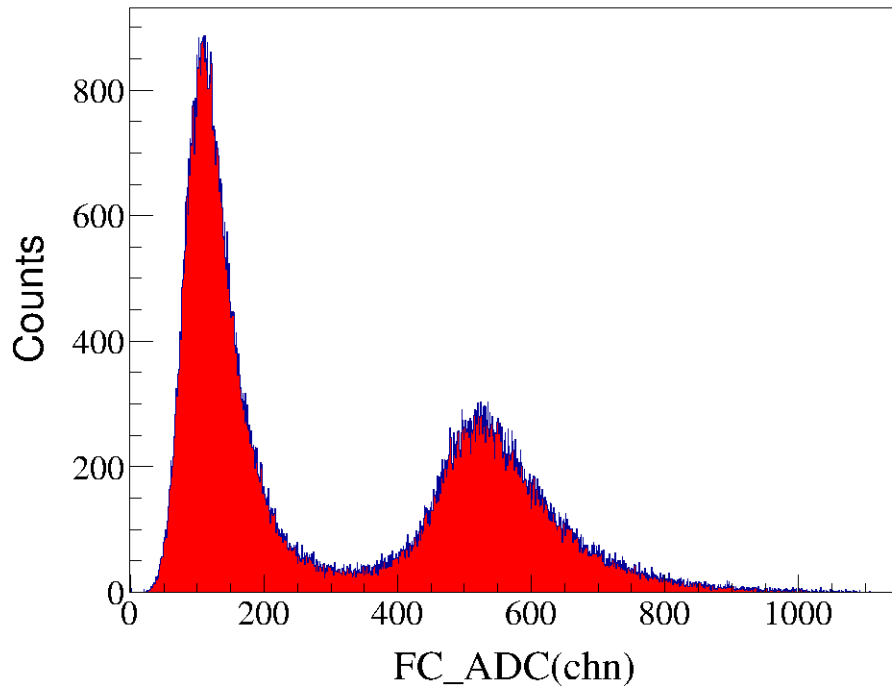
Figure 4.19: The pulse height spectrum for the fission chamber. The left peak is the alpha decay peak. The right 'bump' is made by fission fragments. The threshold for this analysis is set at 317 channels.

np-scattering portion of the data as well.

4.2.3   n-p Elastic Yield

With the experimental setup provided, it is possible to identify events that occur via elastic scattering process. Elastic scattering is by far the dominant contribution to np interactions in this energy range, comprising $\sim 99\%$ of the np-total cross section for these energies. Thus, if we identify conjugate np-pairs in the analysis, it is almost certainly from an elastic event. With the geometry of the 'normalization' part of the experiment, the proton detectors set the angular acceptance of our np-pairs due to their smaller solid angle. Since we know the proton angle (by geometry), if we identify the beam energy and proton energy, then the kinematics of the interaction are completely determined and the neutron angle is known. Based on the calibration of

161
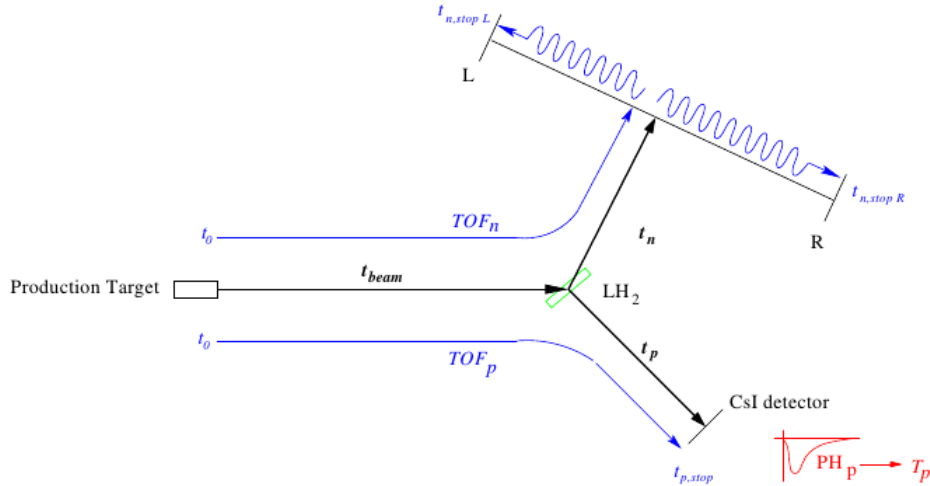
Figure 4.20: Diagram of the time of flight calculation variables and geometry of a typical n-p interaction. Image from [32].

time difference to angle for the neutron bars, if the angle is known, the time difference region of interest will also be known.

The first step is to determine the beam energy. For this setup it is not as simple as just looking at the time of flight, as the detectors themselves are not directly in the path of the beam. **Figure 4.20** shows a diagram of the data we record for each event (noting that we use $\overline{ADC}$ and $\bar{t}$ for the neutron bars). To first order, we can treat the arrival of protons as if they are on a single long flight path, the length of which is the sum of the flight path to the hydrogen target (1693 cm) and the flight path from target to detector (100 cm). We also treat the event as if a proton was travelling the whole path length to the proton detector. This does not account for the mass difference between neutrons and protons, interaction time within the target, or energy losses during transit). This is a rough version of the calculation but it is sufficient to predict the angle of the conjugate neutron. We can do the same type of calculation using the time of arrival for the neutron bar detectors to determine the scattered neutron energy. Knowing these two energies and the proton angle, we can use relativistic kinematics to calculate the incoming beam neutron energy.

To improve this calculation and obtain a more realistic answer, a full Monte Carlo

162

simulation was completed by T. Akdögan[33] and M. Chtangeev[32]. This simulation included interaction times, energy losses for protons in the target, and energy losses in air. This simulation is detailed in chapter 5.1 of [32]. For the purposes of this analysis, we used a table generated by this simulation that maps observed proton time of flight into a true proton energy. This, in effect, repairs all of the somewhat unreasonable assumptions of the calculation described above. For the scattered neutron time of flight to energy calculation, the above assumptions are much more reasonable as energy losses are minimized for a neutral particle, so we do not use a mapping. With these energies determined by time of flight, we can calculate the energy of the beam. To do so, we use the formulation presented in chapter 3 of Hagedorn's *Relativistic Kinematics*[39] on an event by event basis.

In order to identify events that are n-p elastic, we look at the time difference spectrum for the neutron bars. The spectrum for all events shows a roughly uniform distribution of events, as is expected. However, if we look at the same spectrum with the requirement that there be a coincident, beam correlated interaction in one of the proton detectors, we see a peak emerge. This peak is from the neutrons that have a conjugate proton, which are elastic neutrons. **Figure 4.21** shows the time difference spectrum for each of the five bars with no requirement on event type. **Figure 4.22** shows the time difference spectrum for a single neutron bar, with the coincidence requirement for each of the six proton detectors. As dictated by kinematics, we see that the angle for the neutron increases as the angle for the coincident proton increases. We place cuts around these peaks, selecting out elastic events. This technique is repeated for each of the five neutron bars. **Figure 4.22** also demonstrates why only the four forward angle detectors are used in this analysis, as the two widest angles have resultant neutrons that no longer scatter within the solid angle of the neutron wall. This seems like a design flaw in the experiment, but this experiment was originally designed for deuteron scattering. The angle placement is
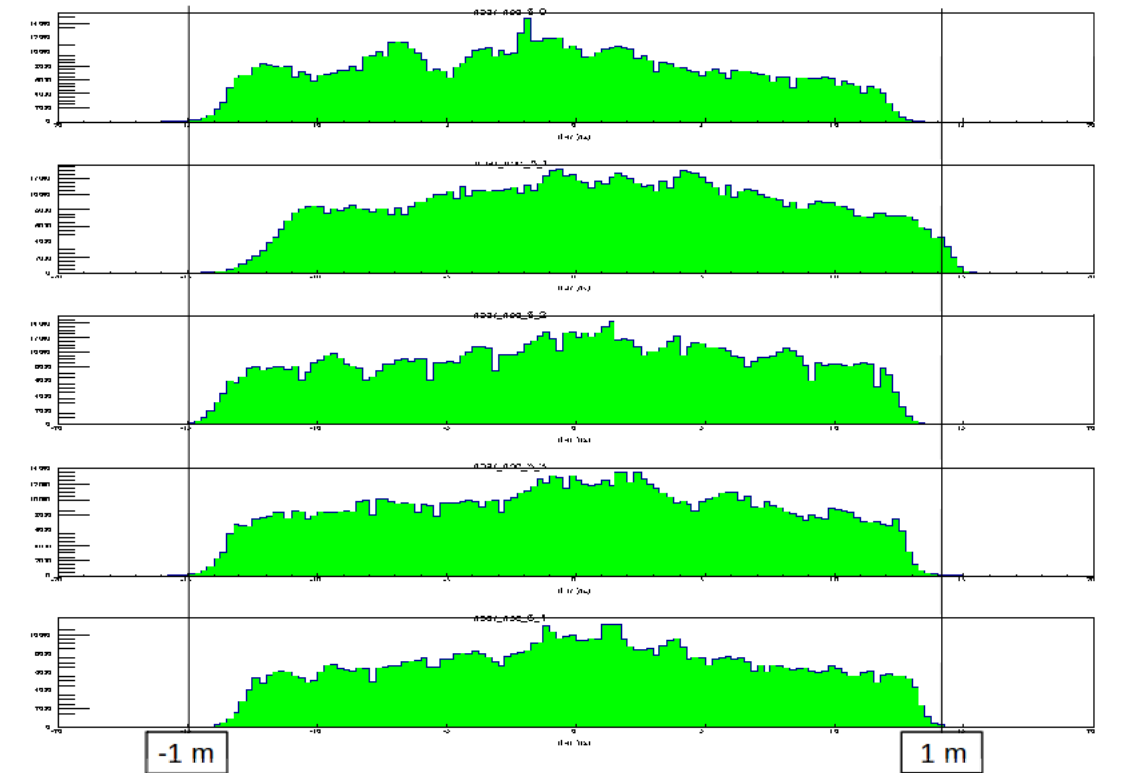
Figure 4.21: The time difference spectrum for all incoming neutron events, for all 5 neutron bars. The external markers show the effective end of the bar. This time difference does not exactly correspond to end of the bar, but rather to the point in the time difference spectrum where events are no longer included in analysis.

correct for the intended purpose of measuring nd scattering.

Once we select elastic events, we can further refine our method by investigating the charged particle telescope data. One of the benefits of having both the CsI telescope and the plastic ΔE detector data for each charged particle interaction is the ability to identify event types by plotting CsI ADC versus ΔE ADC. **Figure 4.23** shows a typical spectrum before any cuts are made. **Figure 4.24** shows a typical spectrum for all incoming beam energies, for events that have a corresponding elastic neutron. This 'banana' shape contains all of the elastic protons. In the uncut spectrum, we see a hint of this shape, but the data is drowned in other events. The shape is characteristic of the detector, as lower energy protons deposit the majority of their energy in the ΔE detector[29]. The higher energy protons will move through the plastic quickly, depositing little energy, and stop almost exclusively in the CsI.

164
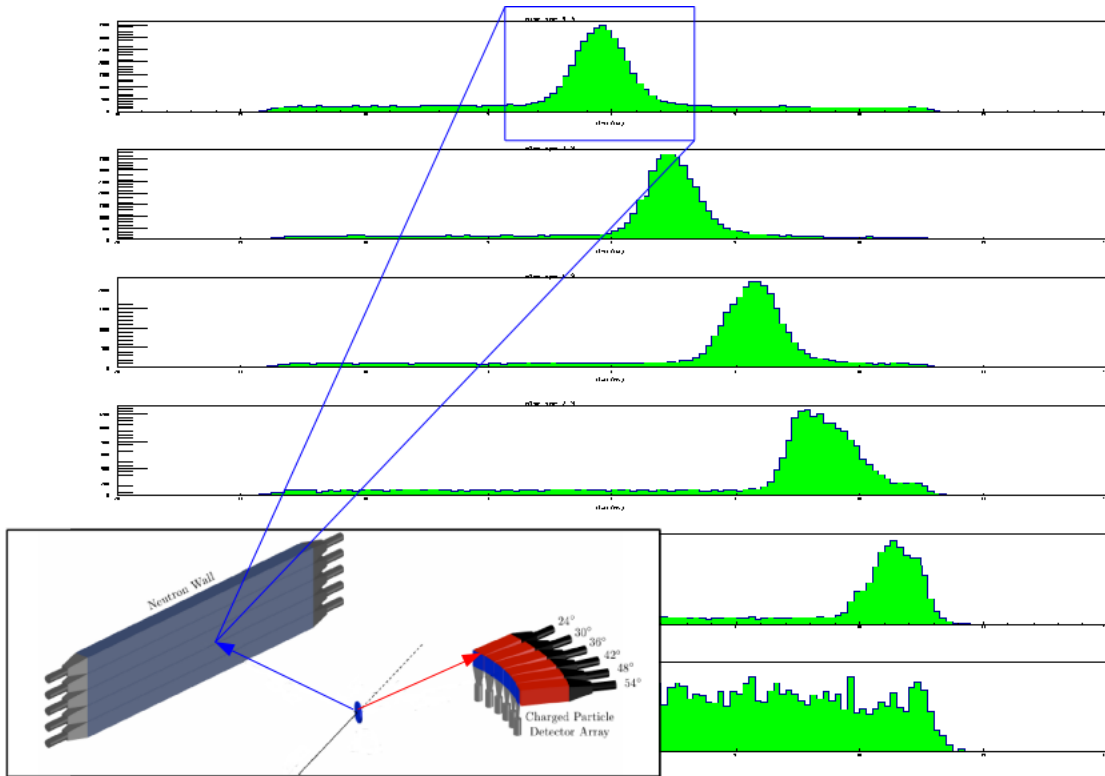
Figure 4.22: The time difference spectrum for a single neutron bar, shown for events which are in coincidence with each proton detector. The top spectrum is for the forward angle proton detector, the second spectrum for the second most forward angle, and so on. By using this coincidence requirement, we are able to select the region around each peak as n-p elastic events. These events are then further analyzed to determine the n-p elastic yield.

Due to this relationship, we expect to see low pulse height ΔE events have high pulse height in the CsI. This is precisely what is shown in **Figure 4.24**. We also expect that higher beam energy events will have a higher CsI ADC value.

We can further constrain which events are analyzed by looking at the time correlation for events in the ΔE and CsI detectors. We know that true events must pass through the plastic only fractions of a nanosecond before interacting in the CsI crystal. In **Figure 4.25**, the time of flight for each detector is plotted in a two-dimensional plot. By making a cut around the central linear section, we can remove events that do not show the proper time correlation. We improve this cut by looking at a second plot that shows $TOF_{CsI} - TOF_{\Delta E}$ for each coincident event. We expect that this plot should be slightly larger than 0, with $\sigma \approx$ 1ns. **Figure 4.26**
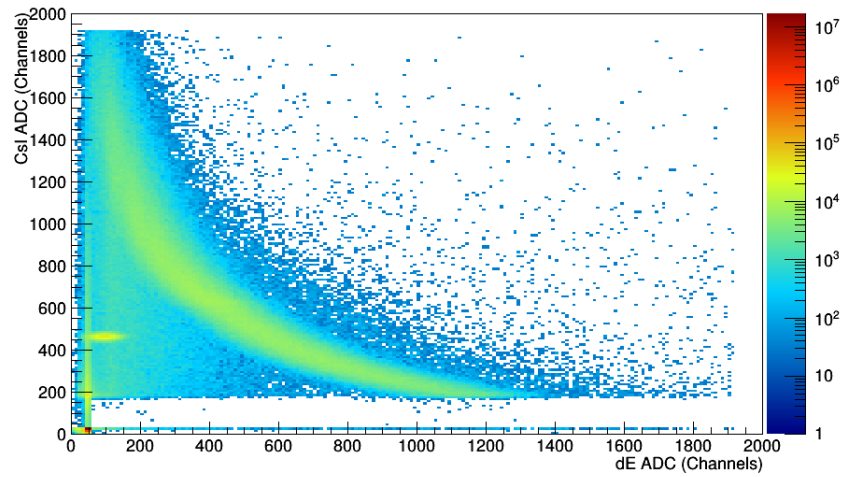
Figure 4.23: CsI versus ΔE ADC spectrum for all events. This plot is semi-log, which allows us to see the underlying band structure. However, this band structure is sitting upon a background that is sitting upon a background of nearly equal size. Note that the z-axis is logarithmic in this plot.
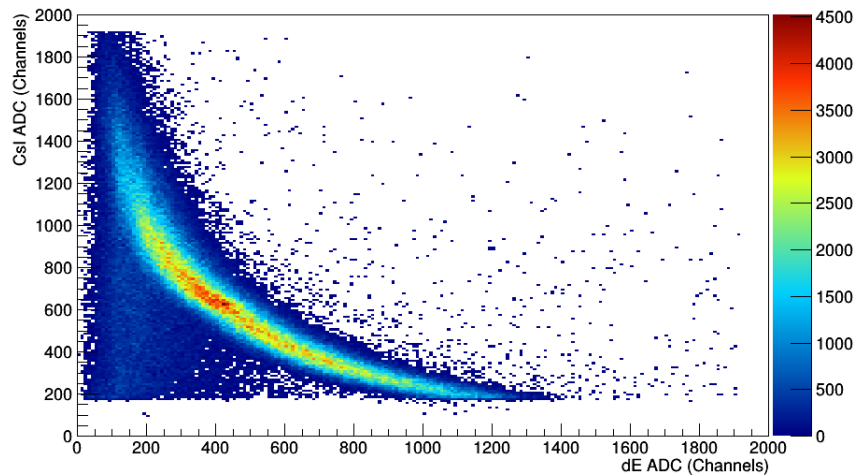
Figure 4.24: CsI versus ΔE ADC spectrum for coincidence events. By selecting elastic events, we isolate the band from the large background and the background to signal ratio is greatly improved in this plot.
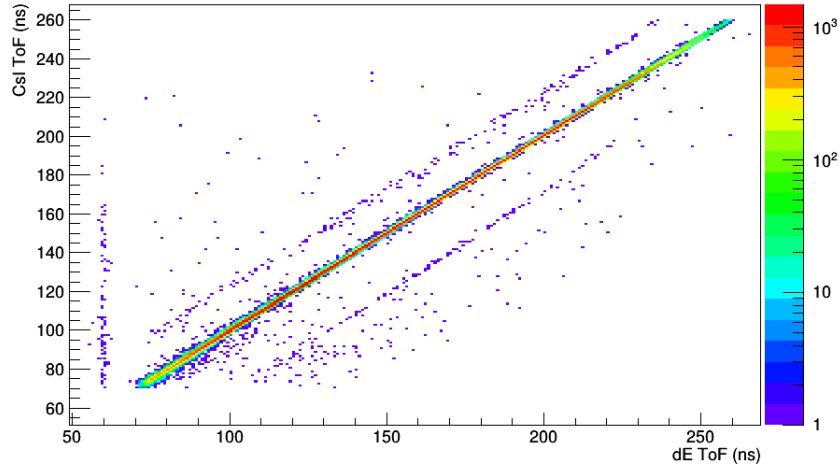
Figure 4.25: The time correlation for elastic proton events. On the x-axis is the time of flight for the ΔE detector, on the y-axis the time of flight for the CsI crystal. The central linear section shows a slope of ~ 1, which is what we expect. The outliers can be removed by making a proper cut.
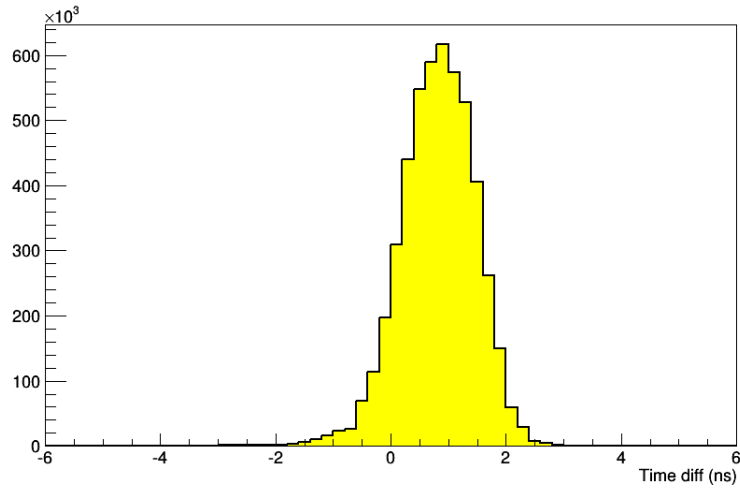
Figure 4.26: The time difference for elastic proton events. The x-axis is $TOF_{CsI} - TOF_{\Delta E}$, which we expect to be slightly larger than 0.

matches this expected result well. By placing cuts on each side of the peak, we further constrain the acceptance to only allow events with perfect correlation.

With these cuts in place, we have a set of events that qualify as elastic events. We cut these events up into 10 MeV beam energy bins to extract yields. Placing energy cuts separates the 'banana' into individual peaks, which we can integrate. An example peak is shown in **Figure 4.27**, with the red box showing the integrated range for the
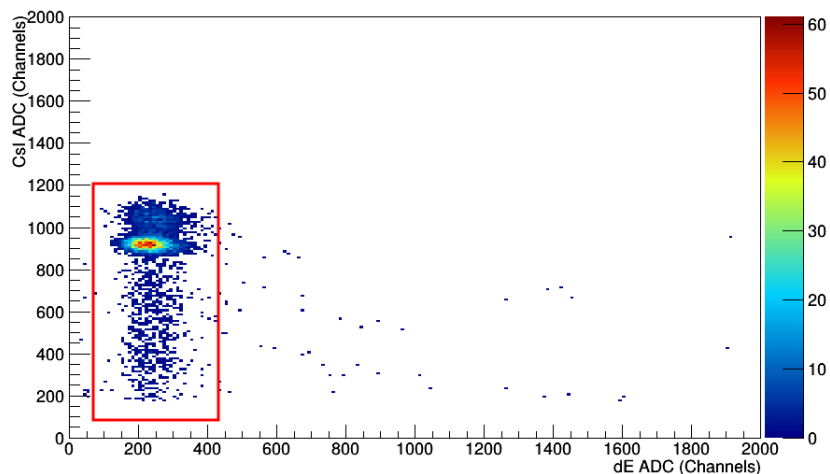
Figure 4.27: ΔE vs CsI ADC spectrum for coincidence events at 130 MeV beam energy. The red box shows the portion of this plot that is integrated to extract the yield.

peak. The peak is clearly visible, however we must also explain the vertical 'band' that surrounds the peak. The lower portion of the band corresponds to events which have partially interacted in a way that doesn't produce light within the CsI crystal. Since our information regarding the pulse height is based entirely on light collection, we do not see any energy deposit that doesn't produce light. The main interactions of this type are nuclear interactions between the incident proton and the CsI nuclei. Inelastic interactions are the main contribution to reducing light production[40] and occur at a roughly 2% rate [41] for protons in CsI. Elastic scattering does contribute to a small reduction in light. However, elastic reactions are generally forward peaked and the proton continues moving through the material after scattering, usually losing less than 2% of its energy [40]. Even with nuclear interactions reducing the light production, these are still valid n-p elastic events and are counted in our yields. Above the peak, the band corresponds to events that produced more light than the rest. These are events that did not lose energy in any way besides ionization, which produces light, and are once again valid events that are counted in the yield.

To integrate the peak for each detector and each energy which all have slightly different peak positions due to gain differences and the correlation between proton

168

energy and beam neutron energy, an algorithm was designed to automate the integration. This algorithm uses ROOT's built in histogram class (TH2)[42] to find the bin with the largest total count. With the applied cuts, this bin is always at the center of the peak of interest. 'x' and 'y' coordinates are determined for the maximal bin. A different value is added to or subtracted from this bin value (for each axis). This value varies with energy and detector. These values are based on analyzing 'by hand' each peak while looking at a small portion of the runs. This determines the limits of the rectangular region to be integrated. Using these limits, the code scans through every bin that falls within the area and uses ROOT's 'GetBinContent()' function to sum the contents of these bins.

At this point, background subtraction also occurs. In order to do this, we use the neutron time difference spectrum. In **Figure 4.22**, we can see that this peak sits on a background of events that are not true elastic events since the recorded angle does not correspond to something that is kinematically possible. These events are likely accidentals due to extra neutrons scattering in the room, cosmic rays, or gamma rays from the beam. Since this background is flat, if we select a region of these events that is outside of the peak and process it like the regular peak, we can find a value that is $\frac{background\ counts}{time\ difference\ bin}$. This value is used to count the number of background events, based on the width of the actual peak selection. This is also an automated process and occurs for each detector and energy during the yield integration. Subtracting this value from the integrated peak yield determines the beam energy dependent yield for each detector. The region from -8 to -12 ns never has an active peak for this data set, and is used to determine the background values.

Another important piece of information is recorded for each set of events, the average energy for the scattered neutron detected in the neutron wall. The efficiency for our neutron detector is energy dependent. The neutron detector is mostly reliant on the n-p scattering cross section in order to create light and this cross section

169
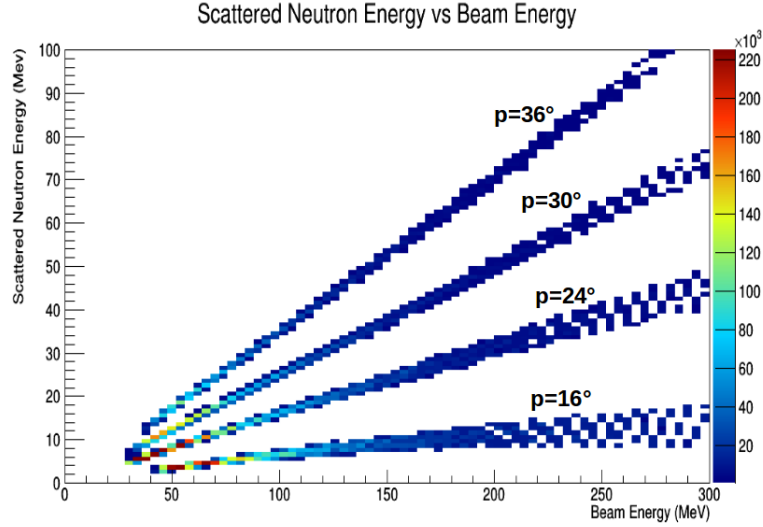
Figure 4.28: Scattered neutron energy versus beam neutron energy. The 4 bands correspond to the 4 proton targets that can have coincident neutrons. Due to the different proton angles, the scattered neutrons have different energies for the same beam energy.

varies from >10 barns to a few hundred millibarns, depending on the energy of the neutron. The n-^{12}C elastic and inelastic cross sections also contribute and similarly vary between barns and millibarns, depending on the energy. **Figure 4.28** shows scattered neutron energy vs beam neutron energy. We see four bands, each one corresponding to one of the proton detectors. The energy of the scattered neutron is both angle and energy dependent, so as the proton angle changes, the scattered neutron angle changes. More discussion of this plot will occur in the final analysis section.

4.2.4   Monte Carlo Simulation

After the analysis to extract both fission yields and n-p elastic yields, we have the majority of the information needed to use **Equation 4.5**. Both yields are determined for the energies of interest, the n-p elastic cross section can be found in various databases (e.g. [43] and [11]), and the fission cross section for the normalization energy can be extracted from the IAEA evaluation. However, the efficiency of our detectors has not been measured in a meaningful way. The fission chamber and

170

charged particle detectors are nearly perfectly efficient[32] and their efficiencies can be neglected. Unfortunately, the neutron detectors have a much smaller efficiency which must be characterized. To address this problem, a model of the neutron wall was constructed using the GEANT4 framework. A thorough description of how the properties of materials are input into GEANT can be found in **Section 3.4.2**.

Each detector was built with BC-408 equivalent scintillation material, BC-800 light guides (made to approximate the half Winston cone, see **Figure 4.29**), and attached to two thin light guide plates which act as the PMTs for each bar. Additionally, four thin plastic scintillators are placed in the proper positions for each proton detector. **Figure 4.30** demonstrates the full setup. One question that must be addressed is the thoroughness of the optical physics package in GEANT. There are four major effects in play during optical photon generation and tracking: scintillation yield, quenching, surface interfaces and bulk attenuation. In the detector generation code, we set the scintillation yield and the Birks' coefficient, which approximates quenching within the material. Both of these values can be found in [16] for our material. This fully determines the optical photon generation. In the detector construction code, we set the bulk attenuation value for our materials (also in [16]). The only other process is the treament of interfaces. GEANT is designed to treat each surface as polished, ground, or some combination of these two set by a user input. Polished surfaces are treated as perfectly smooth interfaces, such that the laws of total internal reflection govern the interaction. GEANT also allows the addition of a material 'wrapped' around a volume. The wrapping can also be assigned optical properties such as reflectivity. Using these inputs, we built an accurate representation of a reflective aluminum foil, which was wrapped around the actual neutron bars.

To calculate accurate results using the Monte Carlo, the input values for interaction cross sections must be accurate. During the initial work to calculate the absolute efficiency for the neutron detectors, the results were non-physical. Upon investiga-

171
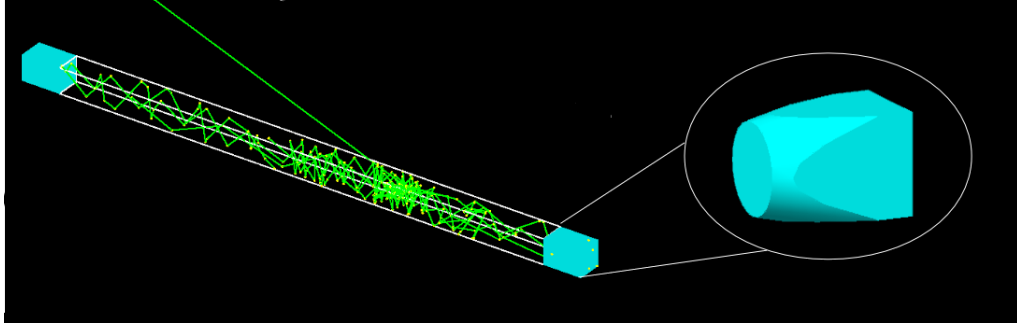
Figure 4.29: A single neutron bar as created in GEANT4 simulation. The lines within the material are example optical photon tracks. The inset is an example of the half Winston cone light guide geometry.
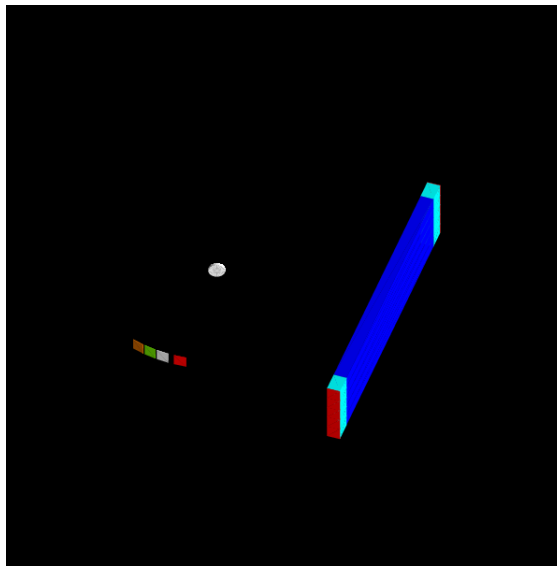
Figure 4.30: Experimental geometry as created in GEANT4 simulation.

tion, we determined that the input cross sections were incorrect. This is discussed in **Appendix A**.

For each event in the Monte Carlo, a neutron-proton conjugate pair is created by randomly selecting a proton energy and direction. These random initial conditions are biased to only select directions that result in the proton passing through a region of solid angle that surrounds the proton detector region. A kinematic calculation is completed based on the proton angle and energy to find the associated neutron energy and angle. A random position is selected within the liquid hydrogen target and then both the neutron and proton are generated at this point with their respective energies

and directions. Events are counted when a proton passes through one of the proton detectors. Every time a proton interacts, we know that the conjugate neutron must pass through the neutron wall. To calculate the efficiency, we count the number of neutrons that are detected and divide that by the number of detected protons. In order to be detected, a neutron must create light in the scintillator, then that light must reach the end of the light guides, where the volumes approximating the PMTs are placed. GEANT4 tracks each optical photon individually. The number of optical photons that reach the PMT plates is a measure of the pulse height spectrum, since the pulse height spectrum is just a measure of current created by light in a PMT. For each PMT, we record time of arrival for the 4th optical photon, which acts as the TDC value. We also record the number of optical photons that arrive for each event, which acts as the ADC value.

In order to calculate a true efficiency, we need to recreate the physical threshold in the GEANT framework. To do this, we use the same method of calibration that we use in the actual experiment. As a calibration point, we throw 4.4 MeV gamma rays into the neutron wall, recording the number of optical photons that arrive at each PMT. We calculate the geometric mean ADC using the PMT pairs, and then look for a Compton edge in the 'number of photons' spectrum. This edge is the same edge we used to calibrate the detectors in the physical experiment, and occurs at 4.159 MeVee. This gives us a method of calibrating $\frac{\text{MeV}}{opticalPhoton}$. Thus, when we do our final efficiency analysis, we only count as a 'hit' those neutrons which produce enough light to overcome the optical photon equivalent of the 4.159 MeVee threshold at each PMT. We completed this analysis for neutrons ranging in energy from 5 MeV to 100s of MeV. This maps the detector efficiency for neutron detection into an energy dependent variable that we can use in our calculation. **Figure 4.31** shows the result of this simulation. The peak at 19 MeV is the result of the 4.159 MeVee threshold. There are two competing phenomena: the creation of light by n-p elastic
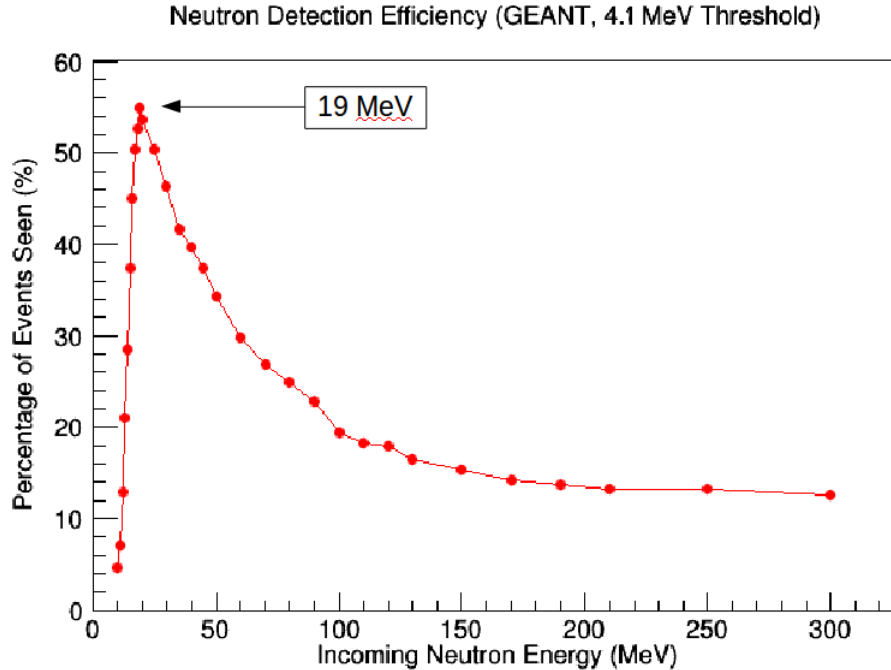
Figure 4.31: Neutron detector efficiency as calculated in GEANT4 Monte Carlo.

scattering and the truncation of event readout by the threshold. The n-p elastic cross section rises as energy decreases, resulting in the upward arc of the efficiency for lower neutron energy. However, at a certain point, not enough light is made per interaction to overcome the threshold and be detected, resulting in the sharp efficiency decline seen at 19 MeV in this plot. The shape of the curve is almost exclusively determined by three cross sections: n-p elastic, n-^{12}C elastic and n-^{12}C inelastic. These are shown in **Appendix A**. The point at 19 MeV looks unnaturally sharp, however this is a 'trick' of the large x-axis range. When zoomed in, the turnover point for the curve is rounded.

Another consideration that can be addressed with the Monte Carlo is the problem of multiple scattering. This is also a question of detector efficiency and should have an energy correlation. To test this, we use the same setup as before, with the full complement of five neutron detectors in the wall. For each event, we look for interaction levels above the threshold in more than one bar. In this type of event,

the neutron interacts in one bar, and then redirects from the proton scattering into another bar where it interacts once again. In order to correct for this, we must know the percentage of events for which this occurs given a neutron energy. We also must find out what portion of these extra scatterings end up inside the cuts that we make on the neutron time difference spectra. We use the same method as described for the efficiency calculation, only with the requirement that two or more bars see an event. This percentage is also calculated from events that interact at least once, so the calculation for this is $\frac{Number\ of\ events\ in\ >1\ bars}{Number\ of\ events\ in\ >=\ 1\ bar}$. This results in **Figure 4.32**. However, since this is measured relative to those events that actually did interact, the percentage of true multiple scattering is actually smaller than this. When the time difference cuts are made, they only account for $\sim 10\%$ of the active region of the bar. Assuming n-p elastic is isotropic (which is not true, but given the complexity of the system, we will use this assumption), the largest possible solid angle of a second detector that is active in the analysis is only 30% of the total solid angle. This assumes an interaction in the adjacent bar which gives a 5 cm radius for the solid angle sphere, 20 cm width for the elastic cut, and the full 10 cm width and 2 m length for the bar. Once scaled by these additional factors, even the 6% value for the multi-scattering becomes a less than 1% effect.

Finally, we used the Monte Carlo to address the corrections for the light attenuation in the bar. Since the optical photon package in GEANT was active, bulk attenuation rates for photons and losses at interfaces are already being handled. To test this, we used a gamma ray source to generate optical photons at specific points within the scintillators. GEANT tracked the optical photons through their lifetimes, and we collected them at the PMT plates. With this data, we could compare the number of photons received at end of the bar with the geometric mean for the data. **Figure 4.33** shows the results. For a single PMT, the position dependence of the result is very strong. For the geometric mean, this dependence is almost entirely
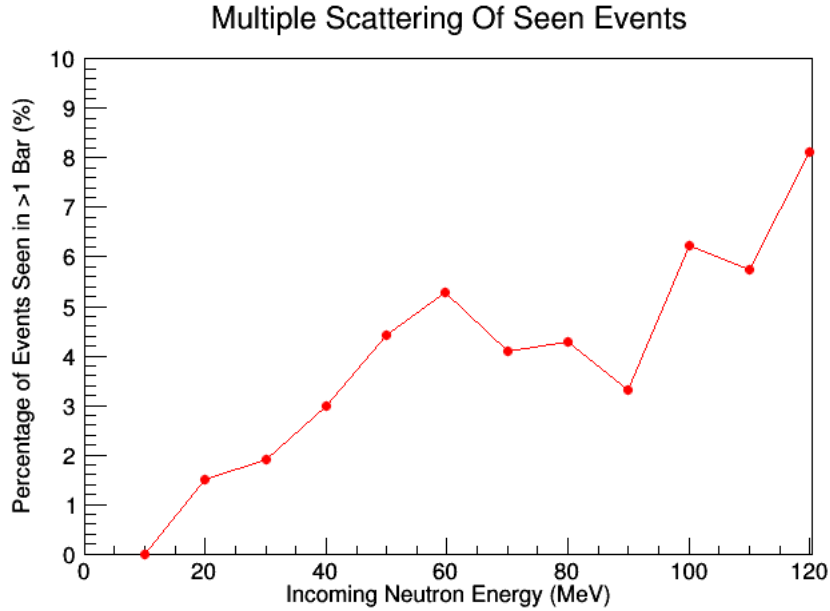
Figure 4.32: Multi-scattering in the neutron bar detectors. This shows $\frac{Number\ of\ events\ in\ >1\ bars}{Number\ of\ events\ in\ >=\ 1\ bar}$.

removed. This Monte Carlo result reproduces the experimental result for these bars, shown in [38]. The position dependence of the geometric mean ADC value can be 'flattened' by applying a correction factor based on this simulation. This is important due to threshold sensitivity of neutron detector efficiency.

4.3 Experimental Results

4.3.1 Details of Cross Section Calculation

As seen in **Equation 4.5**, this analysis only allows us to extrapolate the energy dependence of the cross section based on a normalization energy where the cross section is well known. In this case, it would be ideal to normalize to an energy below 50 MeV where there is a great deal of data. However, the choice of energy is somewhat pre-determined based on the acceptance ranges of the detectors. The limiting factor is finding an energy range where the n-p elastic cross section is well known and we have reliable data to normalize our beam flux. In this case, that limiting factor is determined by the neutron bar efficiency. As seen in **Figure 4.31**,
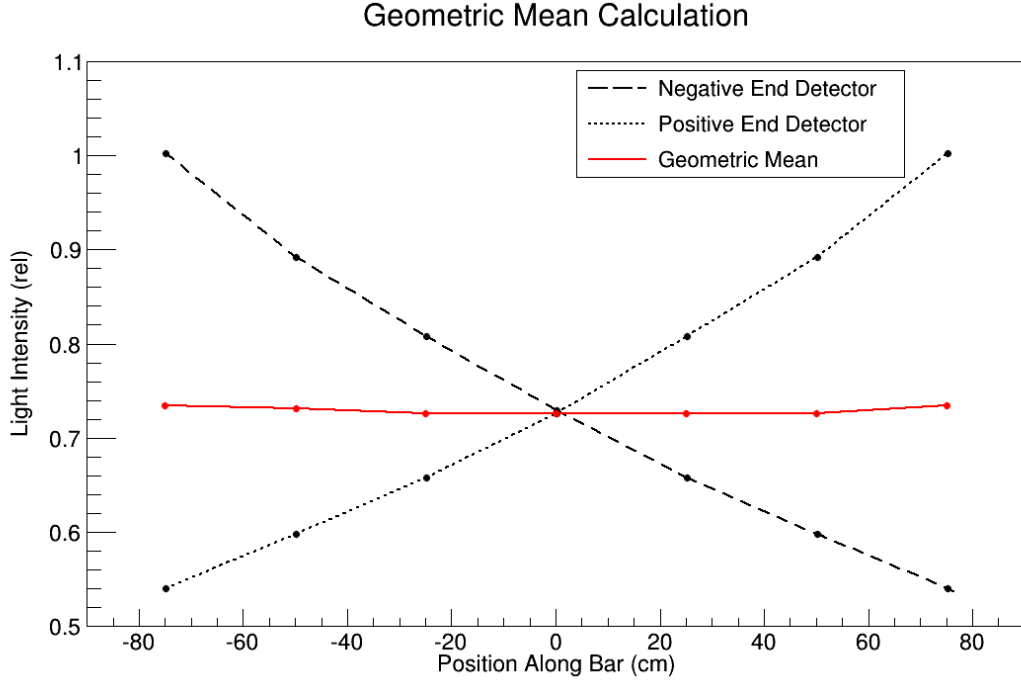
Figure 4.33: A Monte Carlo test of the geometric mean calculation. The middle curve is used to correct the neutron bar ADC values, which are used to set the threshold in the data analysis.

the detector response is not well characterized below 19 MeV due to a threshold effect. Simply put, though the Monte Carlo does have efficiency predictions below that energy, the variation is volatile and not trustworthy. This sets the lower limit on which scattered neutrons will be used in the analysis. **Figure 4.34** shows the scattered neutron energy versus the beam neutron energy plot again, only this time the 19 MeV threshold to the scattered neutron energy is shown. This forces a choice of using only two proton detectors and looking at a lower beam energy or using three detectors and analyzing only above 130 MeV. The two detectors that would be still of use at a lower beam energy are at 30° and 36° and see a much lower counting rate than the forward detectors, especially at higher energies. Due to significantly lowered statistics in the higher energy region if we disregard the 24° detector, we chose to use 130 MeV as our normalization energy and use all three detectors. This sets E^* (in **Equation 4.5**) equal to 130 MeV.

With E^* determined, the only quantity in **Equation 4.5** that is not determined

177
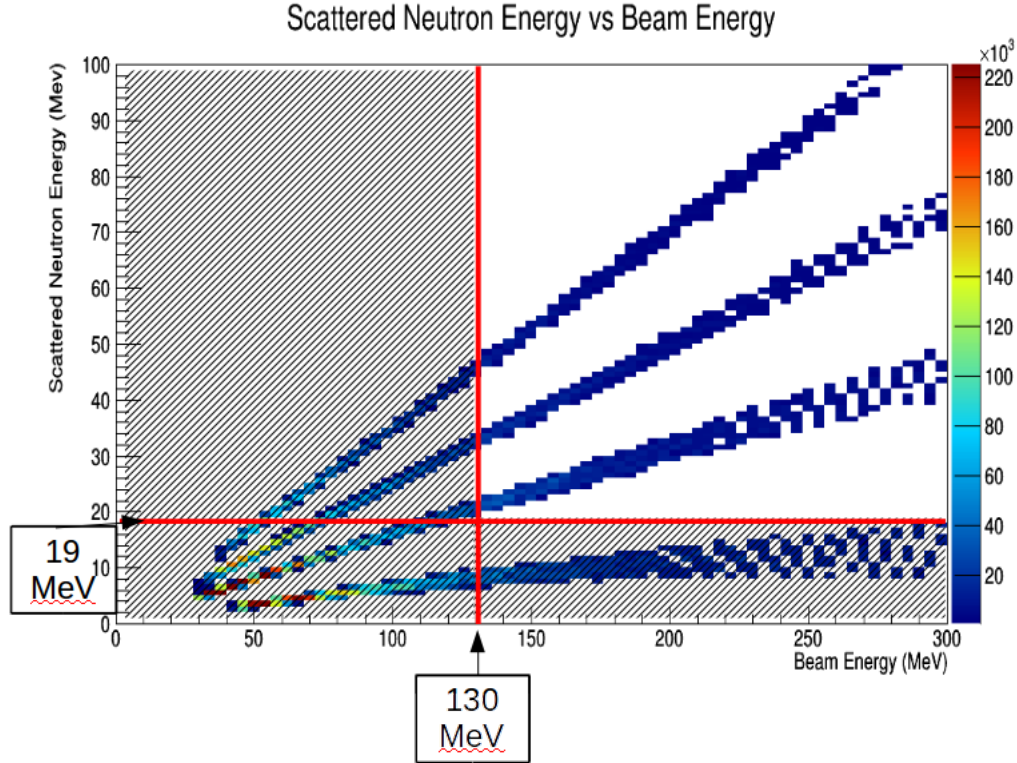
Figure 4.34: Scattered neutron energy versus beam energy, with efficiency threshold shown at 19 MeV. This determines that the lowest energy we can use for normalization is 130 MeV.

is $\frac{d\sigma_e}{d\Omega_e}(E, \theta)$. This is the differential cross section for n-p elastic scattering. This quantity is well-measured and there are various tabulations and evaluation for its value. One of these tabulations is maintained by George Washington University and can be found in the SAID Partial Wave Analysis database[43]. This group uses a quantum decomposition technique to solve scattering problems (i.e. breaking each member of a scattering pair into angular momentum components to solve). The results of these calculations are compared to available data, and for n-p elastic in our energy and angle regions, show excellent agreement. This database gives easy access to the values for the scattering cross section, and the values used for this calculation are shown in **Tables 4.3** through **4.5**.

Table 4.3: n-p elastic cross sections used in this analysis for 24°. This corresponds to a neutron angle of 63.11°. From [43].

θ_p (°)	E_n (MeV)	$\frac{d\sigma}{d\Omega}$ $\left(\frac{mb}{sr}\right)$	E_n (MeV)	$\frac{d\sigma}{d\Omega}$ $\left(\frac{mb}{sr}\right)$
24	130.0	5.155	135.0	5.017
24	140.0	4.890	145.0	4.775
24	150.0	4.668	155.0	4.569
24	160.0	4.477	166.0	4.392
24	170.0	4.311	175.0	4.235
24	180.0	4.163	185.0	4.096
24	190.0	4.031	195.0	3.969
24	200.0	3.910	205.0	3.854
24	210.0	3.800	215.0	3.747
24	220.0	3.697	225.0	3.648
24	230.0	3.601	235.0	3.555
24	240.0	3.511	245.0	3.468
24	250.0	3.426	255.0	3.385
24	260.0	3.345	265.0	3.306
24	270.0	3.268	275.0	3.230
24	280.0	3.194	285.0	3.158
24	290.0	3.122	295.0	3.087
24	300.0	3.052		

4.3.2 Systematic Errors

One of the beauties of this measurement method is that everything except for the normalization is used in a ratio with a similar quantity (see **Equation 4.5**). This is necessary to remove the target information from the calculation, and has the added benefit that it minimizes many of the systematic uncertainties. As an example, if the value for the n-p elastic cross section is systematically low by 1%, this would cancel during the calculation of the cross section due to being divided by the n-p elastic cross section at a different energy that would also be low by 1%. Thus, each source of systematic error will be investigated as a ratio if possible. Since there are several sources of systematic error, each will be discussed briefly below. Some common

Table 4.4: n-p elastic cross sections used in this analysis for 30°. This corresponds to a neutron angle of 57.5°. From [43].

θ_p (°)	E_n (MeV)	$\frac{d\sigma}{d\Omega}$ $\left(\frac{mb}{sr}\right)$	E_n (MeV)	$\frac{d\sigma}{d\Omega}$ $\left(\frac{mb}{sr}\right)$
30	130.0	4.070	135.0	3.939
30	140.0	3.820	145.0	3.713
30	150.0	3.614	155.0	3.524
30	160.0	3.441	165.0	3.364
30	170.0	3.293	175.0	3.226
30	180.0	3.163	185.0	3.104
30	190.0	3.049	195.0	2.996
30	200.0	2.946	205.0	2.898
30	210.0	2.852	215.0	2.808
30	220.0	2.766	225.0	2.726
30	230.0	2.687	235.0	2.649
30	240.0	2.612	245.0	2.576
30	250.0	2.542	255.0	2.508
30	260.0	2.475	265.0	2.443
30	270.0	2.412	275.0	2.381
30	280.0	2.352	285.0	2.322
30	290.0	2.294	295.0	2.265
30	300.0	2.238		

sources of error that do not effect this measurement are also discussed to explain why they are disregarded for this measurement.

Neutron Flux: Due to the white beam used in the experiment, as well as the construction of the ratios to remove all target and flux dependence, this does not contribute.

Detector Solid Angle and Acceptance: The fission chamber foils are both wide enough and homogeneous enough that the beam spot is fully on target. The beam spot has also been measured to a high degree of accuracy and is smaller than the cross-sectional area of the LH$_2$ target, even with errors. For the n-p elastic yield, we are measuring

Table 4.5: n-p elastic cross sections used in this analysis for 36°. This corresponds to a neutron angle of 51.129°. From [43].

θ_p (°)	E_n (MeV)	$\frac{d\sigma}{d\Omega}$ $\left(\frac{mb}{sr}\right)$	E_n (MeV)	$\frac{d\sigma}{d\Omega}$ $\left(\frac{mb}{sr}\right)$
36	130.0	3.243	135.0	3.119
36	140.0	3.009	145.0	2.911
36	150.0	2.822	155.0	2.742
36	160.0	2.669	165.0	2.603
36	170.0	2.542	175.0	2.486
36	180.0	2.435	185.0	2.387
36	190.0	2.342	195.0	2.301
36	200.0	2.261	205.0	2.225
36	210.0	2.190	215.0	2.156
36	220.0	2.125	225.0	2.095
36	230.0	2.066	235.0	2.038
36	240.0	2.011	245.0	1.985
36	250.0	1.960	255.0	1.936
36	260.0	1.912	265.0	1.889
36	270.0	1.867	275.0	1.845
36	280.0	1.824	285.0	1.803
36	290.0	1.783	295.0	1.764
36	300.0	1.744		

all of the data within the same experimental setup, with all energies measured simultaneously. The flight paths are measured to better than a centimeter. These facts, when combined with the ratio of yields, make this error negligible.

Target Information: The measurement method of computing yield ratios removes all target information for LH_2 from our measurement. Uncertainty in this target information is never considered, so it does not contribute. The uranium yields do have a dependence on the thickness and total mass of the uranium target. However, this method only measures the yields in a ratio, so any target dependence is removed, as is its associated error.

Charged Particle Detection: The charged particle array is >99% efficient at detecting charged particles, according to [33], who designed and simulated the array. This fact, combined with the fact we are only measuring a ratio of detected particle yields, makes this uncertainty negligible.

n-p Elastic Cross Section: Data for the n-p elastic cross section is found in the SAID database [43]. This database was also used by [33] and [32]; both report the accuracy of this database as 1%. This claim is confirmed by examining the comparison of the calculation with available data. However, in this measurement, we are using data for three different angles in a simultaneous measurement. Due to this, a generous 3% error is assigned to the n-p elastic cross section ratio under the assumption a 1% systematic shift in the n-p elastic data at each $\theta - n$ would not necessarily cancel.

Neutron Detection Efficiency: To determine the efficiency of the neutron detectors, a Monte Carlo simulation was completed. Neglecting threshold effects, there are essentially four competing effects in this simulation: n-p elastic scattering, ^{12}C-elastic scattering, ^{12}C-inelastic scattering, and scintillation yields. Any uncertainties in the cross sections will cancel due to using a ratio of the efficiencies at different energies. However, the scintillation yields have multiple energy-dependent variations. Quenching of scattered protons is determined by the Birk's equation, and GEANT4 uses the assignment of a Birk's constant to each material to handle quenching. Multiple tests were completed to assure us that quenching is being properly handled within the code. Light production is handled in the code by using a 'photons/MeV' conversion. Uncertainties due to this conversion cancel when considering a ratio of efficiencies at different energies. The threshold effects that arise from setting a software threshold of 4.159 MeVee in the neutron measurements contribute the largest uncertainties. How-

ever, we have avoided this effect by only using events with scattered neutron energy above 19 MeV, which is higher than than region where the efficiency is drastically reduced by the threshold. This is particularly important, as the threshold effects events differently, depending on the scattered neutron energy. A large uncertainty at only the low energies where we are making our normalization would make the measurement impossible. Given all of these competing effects, a 2% uncertainty is assigned to the ratio of efficiencies. In general, all of these effects may cancel, but the complexity of the system and the use of different energies in the ratio makes the assignment of 2% uncertainty necessary.

Yield Summation Method: The method for summing the event yields is a possible source of systematic bias. However, since the same method is used for all summations, the bias will be cancel when evaluated as a ratio. This applies to both the n-p elastic yield summation and the fission yield summation. The yields do have statistical errors which are accounted for, inluding accounting for background subtraction.

Normalization Error, $\sigma_f(E^*)$: Our measurement only directly measures the relative fission cross sections. To compare this with absolute cross section measurements, we must normalize our data to a single point. In this case, we chose to normalize to the IAEA evaluation at 130 MeV[35]. This point has a value of 1.33 ± 0.0548 barns. However, this error is correlated with our overall error, such that an improvement of this error would improve our certainty. Similarly, a change in the value of the tabulation at 130 MeV would appropriately shift our measurement. Because of this unique relationship, when shown this error is combined with the other error bars and plotted as a shaded region.

Detector Timing Resolution: For both the fission chamber and the δE detectors, the

timing resolution for event detection is ~ 1 ns. In our energy region, that translates to about a 2.5% uncertainty in energy. As discussed previously, this comes directly from converting the time difference to energy. However, the bin widths selected for sampling events is much wider than this uncertainty, so this uncertainty is not shown.

Other n-p Scattering: We also considered other scattering types in the normalization yields. Fortunately, n-p elastic is by far the dominant interaction type. Inelastic and quasielastic scatterings have lower cross sections by orders of magnitude. We are also using these yields as a ratio, so these extra contributions, which are already minute, will be at least partially cancelled. As such, contributions by these event types are neglected.

Data Acquisition Dead Time: There are two sources of dead time that must be considered for this experiment. In the DAQ, the fission chamber data were collected via a CAMAC system. Each event in the CAMAC system had ~ 150 μs of processing time. However, the reaction rate in the fission chamber was only ~ 5 Hz, so the associated 'true' dead time where other events might have been lost is significantly less than 1% and is ignored. For the normalization reaction, the dead time can be computed by comparing the number of beam bursts obscured by the FERA system's busy time. The system had a processing time of 80 μs per event. Even at 2 kHz, which is the higher than the highest recorded acquisition rate, only 1.7% of beam bursts would be 'dead' due to the acquisition busy time. Since the yields are being compared in a ratio, and this value is already small, the data acqusition dead time can be safely ignored in both the analysis and the systematic errors.

Our total systematic error is calculated by summing these values in quadrature,

without including the normalization error. This gives a total systematic uncertainty of 3.6%. This is combined with statistical errors to give our overall error in the measurement, which is shown in the error bars in the final result plots. Once combined with statistics, we have a $\sim 5\%$ overall uncertainty.

4.3.3 ^{238}U Neutron-Induced Fission Cross Section Results

A summary of this measurement's result is presented below. As a convention, our results will be presented in blue, filled circles. Note that the error bars shown do not include the error associated with the point of normalization in the IAEA evaluation. Also, though no error bars are shown along the energy axis, a 2.5% error is associated with each energy bin. However, the bin width's are 10 MeV, so this error is 'covered' by the bin width. A table at the end will report each data point and associated errors.

Our data are in good agreement with other available measurements and the expected behavior of the cross section. Other actinides that have also been measured for (n,f) in this energy region (e.g. ^{235}U and ^{239}Pu) show a similar nearly flat, but slightly decreasing, behavior. The data agree with the current IAEA evaluation[35]. Our data are normalized such that the cross section at 130 MeV is artificially made to agree with the IAEA evaluation. All other points are measured relative to this cross section.
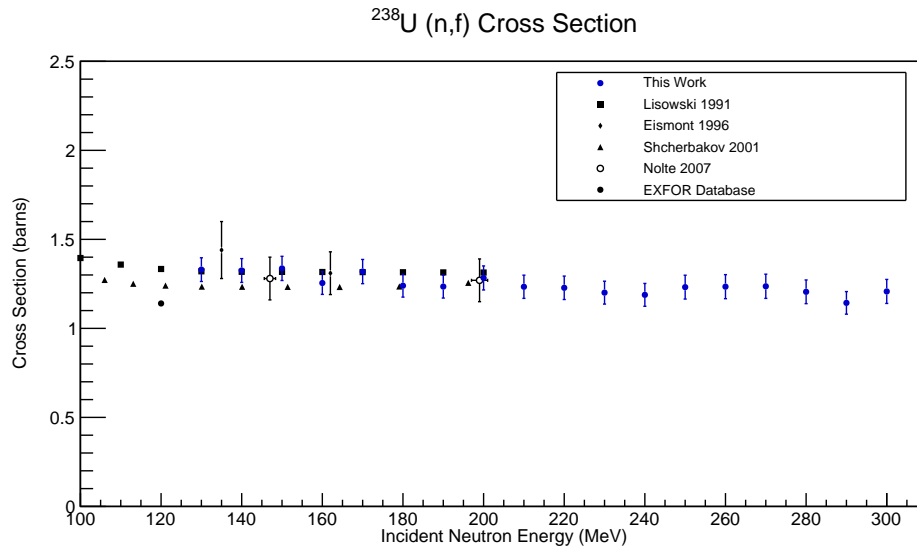
Figure 4.35: ^{238}U neutron-induced fission cross section result for 130-300 MeV. The result is normalized to match the IAEA Standard evaluation at 130 MeV. Error bars have both statistical and systematic effects.
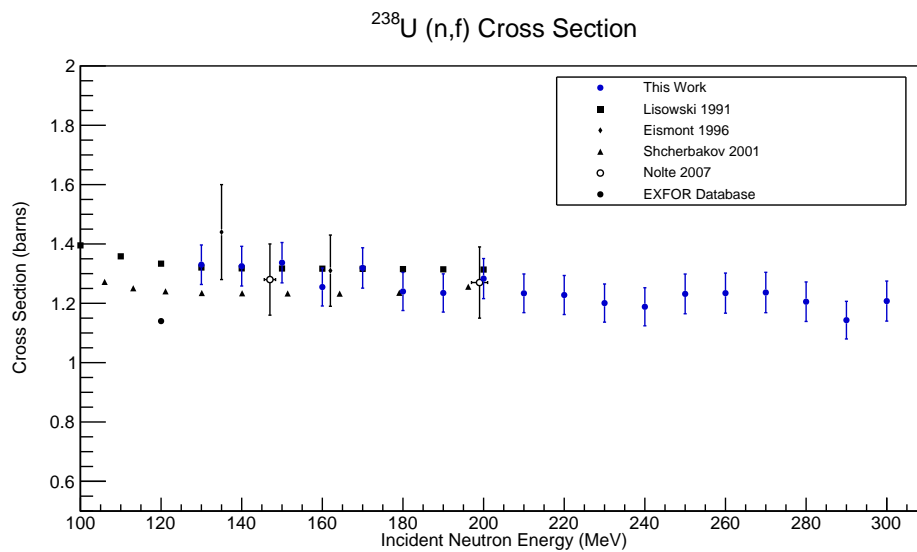
Figure 4.36: Same as **Figure 4.35**, except zoomed in to show overlaps among available data.
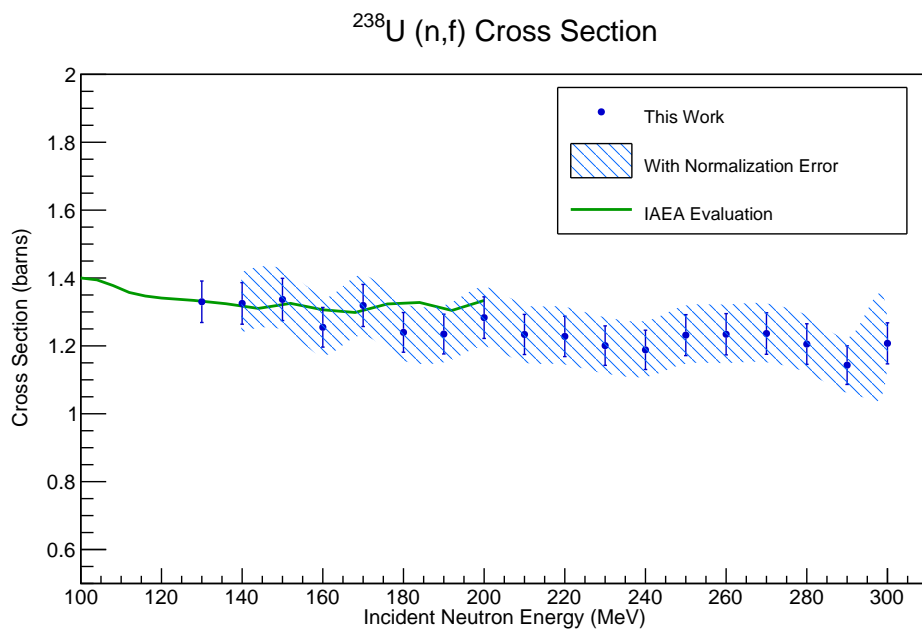
Figure 4.37: ^{238}U neutron-induced fission cross section result for 130-300 MeV. This is compared to the IAEA evaluation which is the standard for ^{238}U neutron-induced fission. The shaded region combines the errors from our measurement and the error associated with the tabulation at the normalization energy of 130 MeV.

Table 4.6: ^{238}U neutron-induced fission cross section results for 130-300 MeV. These errors do not include the error from the normalization point. The data is normalized to agree with the IAEA Evaluation at 130 MeV.

E_n (MeV)	$\sigma_{(n,f)}$ (b)	Error (b)	Error (%)
130	1.3300	0.0666	5.0
140	1.3251	0.0669	5.0
150	1.3369	0.0680	5.0
160	1.2548	0.0639	5.0
170	1.3191	0.0680	5.1
180	1.2399	0.0642	5.1
190	1.2348	0.0644	5.2
200	1.2833	0.0675	5.2
210	1.2337	0.0652	5.2
220	1.2279	0.0658	5.3
230	1.2008	0.0643	5.3
240	1.1883	0.0642	5.4
250	1.2317	0.0669	5.4
260	1.2343	0.0676	5.4
270	1.2364	0.0680	5.5
280	1.2054	0.0666	5.5
290	1.1432	0.0634	5.5
300	1.2075	0.0675	5.5

Chapter 5: Summary and Discussion

The extent of this work can be thought of as two separate but related endeavors. The first project consisted of designing, constructing, and deploying a new type of neutron detector in order to measure the prompt fission neutron energy spectrum for ^{235}U(n,f). The chief success of this project was the demonstration that the measurement is possible with the experimental setup we have designed. The neutron detectors functioned as intended, demonstrating the ability to detect and isolate neutrons from the fission source. In particular, this method has shown the ability to detect neutrons down to 300 keV, which is below the measurement's target energy of 500 keV. Though the statistics were not sufficient to make an absolute measurement of the prompt fission neutron spectrum, the data's agreement with the predicted spectrum shape is great progress. To our knowledge, there have been no measurements of the prompt fission neutron spectrum shape below 1 MeV for beam energies between 1 and 10 MeV. Despite the large error bars, these data are quite encouraging.

The majority of ^{235}U prompt fission neutron spectrum data are reported with arbitrary units. These data, like our data, only measure the shape of the spectrum. The data are generally compared to the predictions set forth in the Los Alamos Model[9] for prompt fission neutron spectra. Though the agreement with theory is quite good in terms of shape, there are almost no absolute measurements for non-thermal beam neutrons. Our measurement method, both in terms of detector type and double time of flight technique, could provide an absolute measurement given adequate statistics. Future attempts at this measurement should be designed with the goal of an absolute measurement of the prompt fission neutron spectrum in as wide an energy range as possible. Data already exist which quantify the neutron multiplicity as a function of laboratory angle, which should make it possible to make

an absolute measurement using the same techniques developed in this work.

Some thought should also be given to the neutron bar design. The layered gamma rejection method, may be an unnecessary complication to the detector design. When this experiment was conceived, the idea of using a two-dimensional plot of mean ADC versus mean time of flight had not been considered. Using only a time of flight cut to select our neutrons, the gamma rejection would have been an invaluable tool to reduce backgrounds and make the measurement feasible. The layered design functioned as intended and matched with rejection efficiency predictions. However, with the two-dimensional cut method, the gamma rejection is less important, as the graphical cut can be tailored to match the neutron distribution precisely, minimizing the background. The layered design should allow for a better measurement of the high energy portion of the spectrum though, as the background gamma ray rejection increases in efficiency for higher energy particles. Previous measurements of the fission neutron spectrum have had difficulties in this energy region due to associated backgrounds and the required time resolution to separate out neutrons in this energy region. The downside of using the thin layered detector design is a diminished time resolution and fewer photoelectrons/MeV. These quantities are both functions of the layer width, as the number of times the light interacts with the surface increases greatly for thin layers. Since each interaction has a probability of losing light, this increase in interactions corresponds to decrease in light collection efficiency. The thin layer geometry may be the limiting factor to measuring below 0.3 MeV and is certainly decreasing the resolution, which introduces an appreciable systematic uncertainty. Further study is necessary to determine whether a single 3 cm thick neutron bar could make this measurement by relying on the two-dimensional cut technique. This could be predicted using a Monte Carlo simulation similar to the one described in **Section 3.4.2**. A Monte Carlo could also predict the number of photoelectrons/MeV. For the current detectors, this value is ~ 26. An increase in this

value would allow the detectors to view lower energy neutrons with higher reliability.

The neutron bar design may also need to be tweaked based on the extreme sensitivity to the threshold. As seen in the efficiency curves calculated in **Chapter 3**, the threshold greatly diminishes the efficiency for low energy neutrons. Since the goal for this design is to measure as low as possible, removing the strong inverse correlation between threshold level and efficiency for low energy events should be a chief concern for future designs. Modifying the design of the detector or the data acquisition electronics may be able to solve this problem.

Overall, this measurement was a step in the right direction. The proof of feasibility, alongside the first results agreeing with well-established theory, shows that this measurement can be made using the techniques we have developed. As a further step, an absolute measurement of the spectrum should be possible. Despite the many failures during the prototyping and calibration measurements, the final results dictate that more work should be dedicated to this measurement due to its feasibility. Recent interactions with a group working on theoretical predictions of fission fragment energy via wave function calculations and calculation of the quantum action[44][45][46], also indicate that there will soon be a more robust, less parameter driven theory than the Los Alamos Model to compare against future data.

The second of the interconnected projects was the measurement of the neutron-induced fission cross section, ^{238}U(n,f). The goal of this measurement was to add to a sparse region of data for the cross section. In the region above 100 MeV there are remarkably few measurements of the neutron-induced fission cross section for ^{238}U. Since the fission cross section for ^{238}U is considered one of the standard neutron interactions (which are meant to be exceedingly well-measured such that they can be used to characterize other neutron reactions), energy regions where the interaction is not well-measured are of particular importance. Perhaps more importantly, nearly all of the reported measurements in this higher energy region are measured relative

to ^{235}U's neutron-induced fission cross section. For evaluators, error correlations are paramount. Since nearly all of the data is measured relative to ^{235}U(n,f), the errors in the ^{235}U cross section are correlated with the ^{238}U cross section errors. Our measurement is made relative to hydrogen (n-p elastic), which means that it has a separate set of correlated errors and can place a tighter constraint on the ^{238}U(n,f) cross section.

Our method for measuring the cross section relied almost exclusively on using input quantities in ratios. By measuring the interaction yields for both ^{238}U(n,f) and n-p elastic at multiple energies, we could look at the yield ratios to determine the rate of reaction at a given energy. We normalized our results to the International Atomic Energy Agency (IAEA) evaluation, showing the energy dependence of the fission cross section in this energy region. The ratio method greatly reduced the associated errors and allowed us to contribute measurements with $\sim 5\%$-level accuracy. These results will be sent to evaluators at the IAEA, who will use them in future evaluations of the cross section data. Since this measurement relied on 'mining' old data, there is no plan for future measurements regarding this quantity within our group. Since this data is measured relative to the hydrogen standard, the contribution to the sparse region of data should help constrain the cross section standard to better than the current $\sim 4.5\%$ accuracy level.

Appendix A: GEANT4 Cross Sections for Plastic Scintillators

For all Monte Carlo simulations completed for this work, we used the pre-made GEANT4 hadronic physics list known as FTFP-BERT-HP. This physics list uses three different models for elastic scattering across the energy region of interest: high precision neutron data (G4NDL) below 20 MeV, the GHEISHA parameterization between 20 MeV and 32.7 MeV, and the high energy elastic scattering model above 32.7 MeV. However, in the initial simulations we were having great difficulty, as we were returning results with discontinuities surrounding the region of 20-32 MeV. After investigation, it was determined that the model GEANT4 was using for n-p elastic cross sections was incorrect in this region. A plot of the elastic np cross section used by FTFP-BERT-HP is shown in **Figure A.1**, compared with ENDF B-VII.1, where all reported energies are laboratory energy. The discontinuity between 20 and 32.7 MeV is due to a flaw in the GHEISHA parameterization. To correct this, a new model called the 'Barashenkov elastic scattering model' [47] is implemented above 20 MeV. This model is pre-built into GEANT4 distributions in the 'G4BGGNucleonElasticXS' class, and is added to the FTFP-BERT-HP model by modifying the elastic physics model directly. **Figures A.2** through **A.4** are of the main cross sections of interest for plastic scintillators, *after* correcting the FTFP-BERT-HP list to use the more physically accurate Barashenkov model.
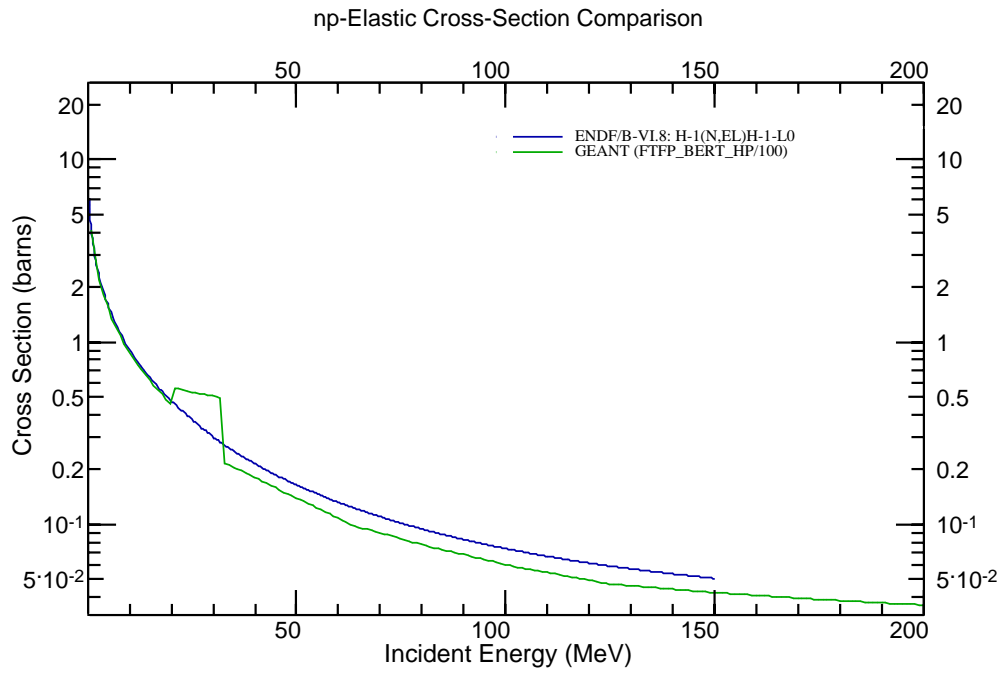
Figure A.1: Comparison of original incorrect GEANT4 (FTFP-BERT-HP) n-p elastic cross section to ENDF.
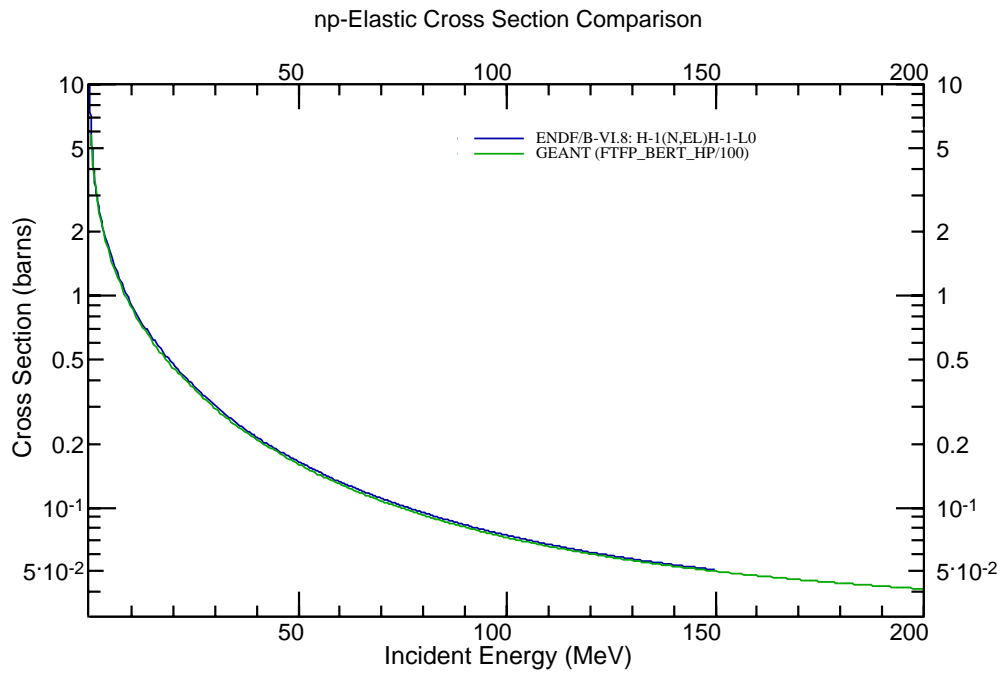
Figure A.2: Comparison of corrected GEANT4 n-p elastic cross section to ENDF.
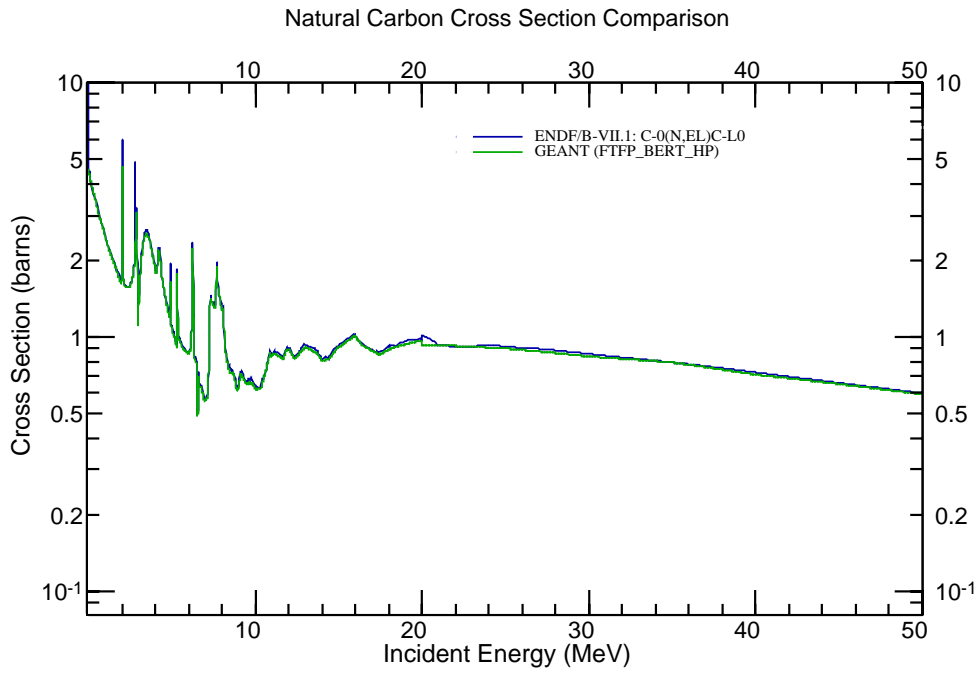
Figure A.3: Comparison of GEANT4 n-^{N}C elastic cross section to ENDF.
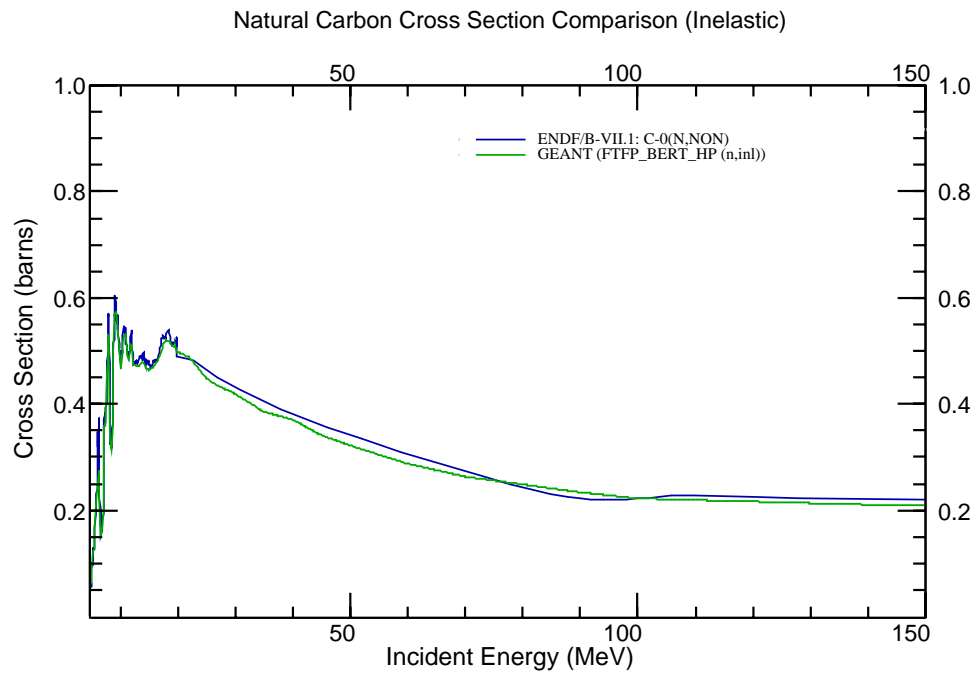
Figure A.4: Comparison of GEANT4 n-^{N}C inelastic cross section to ENDF. ENDF is labeled as 'non-elastic' as that is the comparable interaction type to GEANT's inelastic interaction.

Appendix B: Data Acquisition System

In preparation for the acquisition of the ^{235}U and ^{252}Cf data discussed in **Chapter 3**, we analyzed the beam structure for the experiment. **Figure B.1** demonstrates this structure. One of the key elements is the overall dead time between macro-pulses. These 24 ms blank periods make the overall duty factor of the beam only 2.5%. While the average rate of the beam may be manageable for our detector and data acquisition system, the instantaneous rate is much higher than the system can reasonably handle. This data acquisition system is based on the CAMAC protocol and, for an ADC and TDC combination, has an associated dead time of about 120 μs per event. This dead time is quite limiting when you are only receiving beam 2.5% of the time, and it would limit us to a maximum of 4.8 recorded events per macro-pulse. The system also has an upper limit of 1 kHz, which is acceptable for beam lines with high duty factors, but extremely limiting for the beam line in this experiment. Due to these limitations, a new data acquisition system was constructed for this experiment.
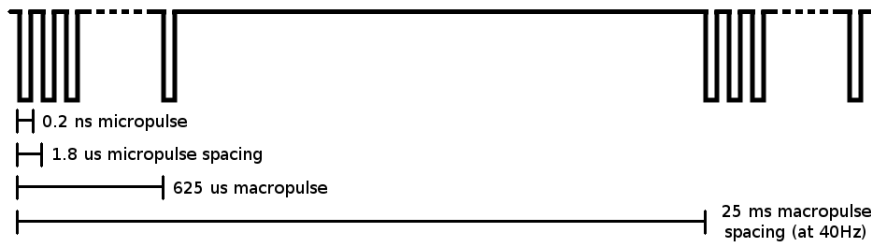
Figure B.1: Beam structure during 2014 prompt fission neutron experiment at WNR.

During the brainstorming phase of this transition, we found that we had a list of requirements for the new system, all of which were mandatory for a data acquisition system (DAQ) to meet our needs.

- Event-based acquisition.

- Low dead time per event.

- Live histogramming (ability to review events in real time during the run).

- ROOT compatible (for easy data analysis).

- User controlled read-out.

- Automated run timer.

- Simple user interface.

Unfortunately, all of the commercially available software either failed when being compared to our checklist or were designed for large laboratories and do not readily scale down to a single machine system. Since these commercial systems were not applicable to our situation, we decided to build a new system.

One of the benefits of building the system from scratch is the ability to choose the hardware that best meets the needs of the experiment. In this case, the desired core mechanic for the hardware was the ability to read events quickly. Though there have been many advancements in digital waveform acquisition, the dead time associated with digitizers is similar to what can be achieved using non-digitizer techniques. Digitizers also produce an overwhelming amount of data that must be stored and processed, as each wave form is converted into 100s of bytes worth of data. For the purposes of all the experiments being run in our lab, digitizers were an unnecessary extra step. Thus, we chose to use a system designed by LeCroy (LRS) known as FERA (Fast Encoding and Readout ADC). This system is based around an ADC

chip which can integrate pulses and store data in ~ 10 μs. If all handshakes between modules are handled in an expedient manner (on the order of nanoseconds), the only dead time for the system will be the time associated with the ADC conversion. This hardware is ideal for our data acquisition needs, as it is event based and has a low dead time. The rest of our 'DAQ requirement list' applies to the software associated with the data acquisition.

The FERA system also has three other modules: a timing module, a memory module, and a system driver. The timing module (TFC) converts time spans into ADC integrable gates which maps time to integrated charge in a linear fashion. This module can be used in tandem with a FERA-ADC to act as a TDC. The memory module stores data in a Last In - First Out (LIFO) manner, such that it is not necessary to read out each event in real time, and you can instead read data in large blocks of many events. The driver module is entirely passive and simply orchestrates data readout by managing the passing of gates and data through various readout lines. It can be thought of as a field commander for the system, as it simply distributes command gates and signals in order to synchronize the active modules. The ADC is known as a LeCroy 4300B, the TFC is a LeCroy 4303, the driver is a LeCroy 4301, and the memory module is a LeCroy 4302.

The FERA system was originally produced in 1986 by LeCroy. However, there have since been significant improvements in many of the chips and functions. One of the largest of these improvements can be achieved by upgrading both the memory and driver modules. When released in 1986, the LRS4302 had a memory that could handle 16,000 data words. If each event has 32 channels of output (16 ADC, 16 TDC), that is a maximum of 500 events in the memory buffer. This, while superior to our memory-less previous system, could be a limiting factor to the system's efficiency. A memory read requires that the DAQ system be made inactive for the duration of the data transfer due to the LIFO method of storage. A company called Cheesecote Mountain

makes a module known as the CMC203 [48], which combines the functionality of the driver and memory into a single module, with a memory of 1,000,000 data words (1 Mword). This module is completely compatible with the 4300B ADC system, and can be used instead of the 4301 and 4302. The CMC203 memory is also First In-First Out (FIFO), which means that it can be read without inhibiting data collection, as new events can be added to the end of the buffer while the buffer is being read. This improves dead time by $\sim 50\%$ compared to the original FERA system, as the only remaining dead time in the system is from the ADC conversion time. Our system uses the CMC203 as the driver and memory, and it reads data from two LRS4300B's: one that is coupled with the TFC to act as a TDC, and one on it's own as an ADC. This gives us 16 channels of ADC and 16 channels of TDC with $\sim 10~\mu$s of dead time per event.

In order to interface a computer with the CAMAC system, one needs a CAMAC controller module. Wiener makes a module called a CCUSB (CAMAC Crate to USB) [49]. This module plugs into the crate controller slots (slots 24 and 25 in a CAMAC crate) and has a two-way USB port. This allows full communication with a DAQ machine. The controller module completes the hardware requirement for the data acquisition system. **Figures B.2** and **B.3** show the hardware for the system as properly connected and a schematic for the connections within the system.

The lack of viable, commercial software has the downside that one must write the software from scratch. However, there are platforms that are designed for this purpose. One such platform is known as KMAX and is produced by Sparrow Corp [50]. This platform is based on Java, but has built-in functionality to interface with CAMAC devices. Simply put, KMAX acts as a driver library and graphical user interface for interacting with CAMAC devices. It also has the ability to separate back-end functionality from the user interface front-end. Thus, it is possible to build a user interface to control data acquisition that requires little-to-no technical knowledge
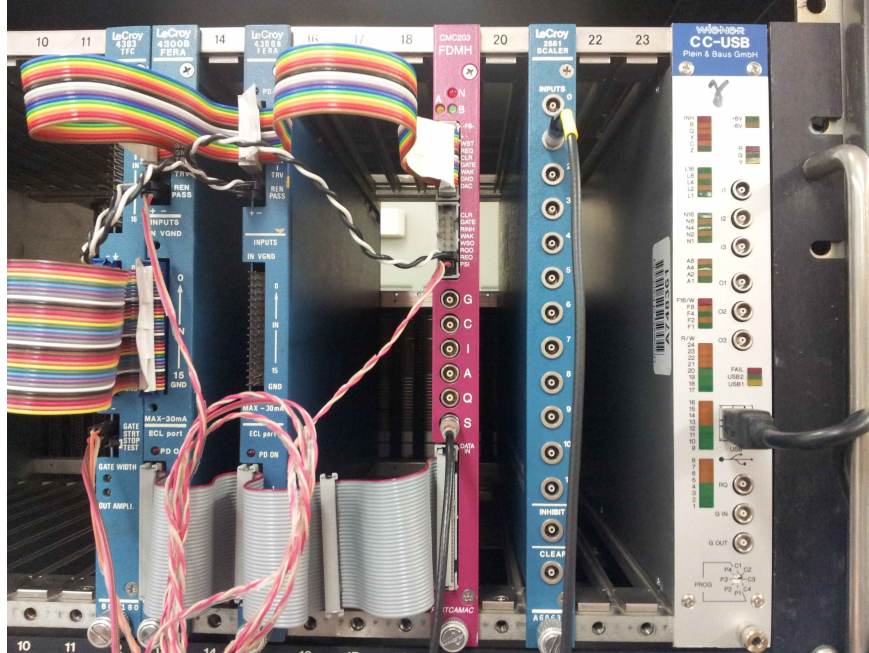
Figure B.2: Photograph of the data acquisition hardware.

from the user. We used this software to design a specialized data acquisition system that has both the front- and back-end functionality desired.

This system has the ability to read in blocks of data as formatted by the CMC203, using the CCUSB as an intermediary. We have written a function that takes this data and converts it into a 'human-readable' form and then stores the data in a text file, creating a log of data for each event. By storing this data in text format, these log files can be read by ROOT and sorted into trees. The system also sorts this data into online histograms during data collection. Since data storage in the CMC203 is automated by the FERA method, the only time the software needs to interface with the CAMAC is during a memory read. Memory reads can occur in three ways in this system:

1. The memory reaches its half-full point and sets a flag to tell the software a read-out is necessary, or

2. A specific time, T (which is set by the user), has elapsed since the last read-out,

To Veto

Busy (S)

Data In (Data Bus, 17 pr)

**CMC203
FERA Driver**

GATE

REO   PSI

Control
Bus (8 pr)

REN

From Analog
Inputs

**Lecroy 4300B
16-Ch ADC
(PD Off)**

Data Out

PASS

REN   PASS

**Lecroy 4300B
16-Ch ADC
(PD On)**

Data Out

In

REO: Read-Enable Output
REN: Read-Enable Input
PASS: Pass Read-Enable
PSI: Pass-Input Return

Out

From Level
Converter

**Lecroy 4303
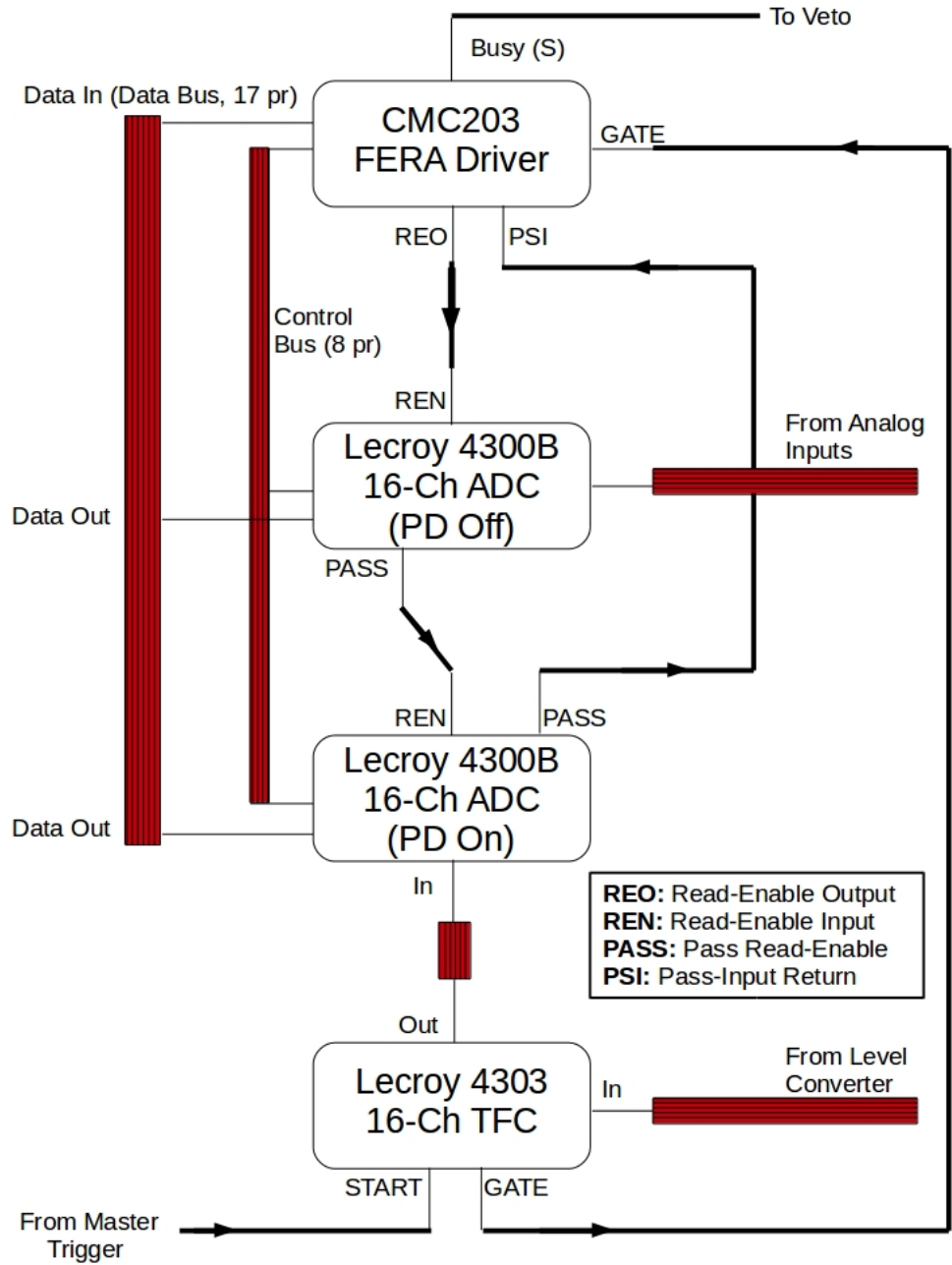16-Ch TFC**

In

START   GATE

From Master
Trigger

Figure B.3: Schematic diagram of CAMAC electronics connections. The thick lines are data buses. Each data bus is made from pairs of wires, so a label of 17 pairs actually connects to 34 pins.
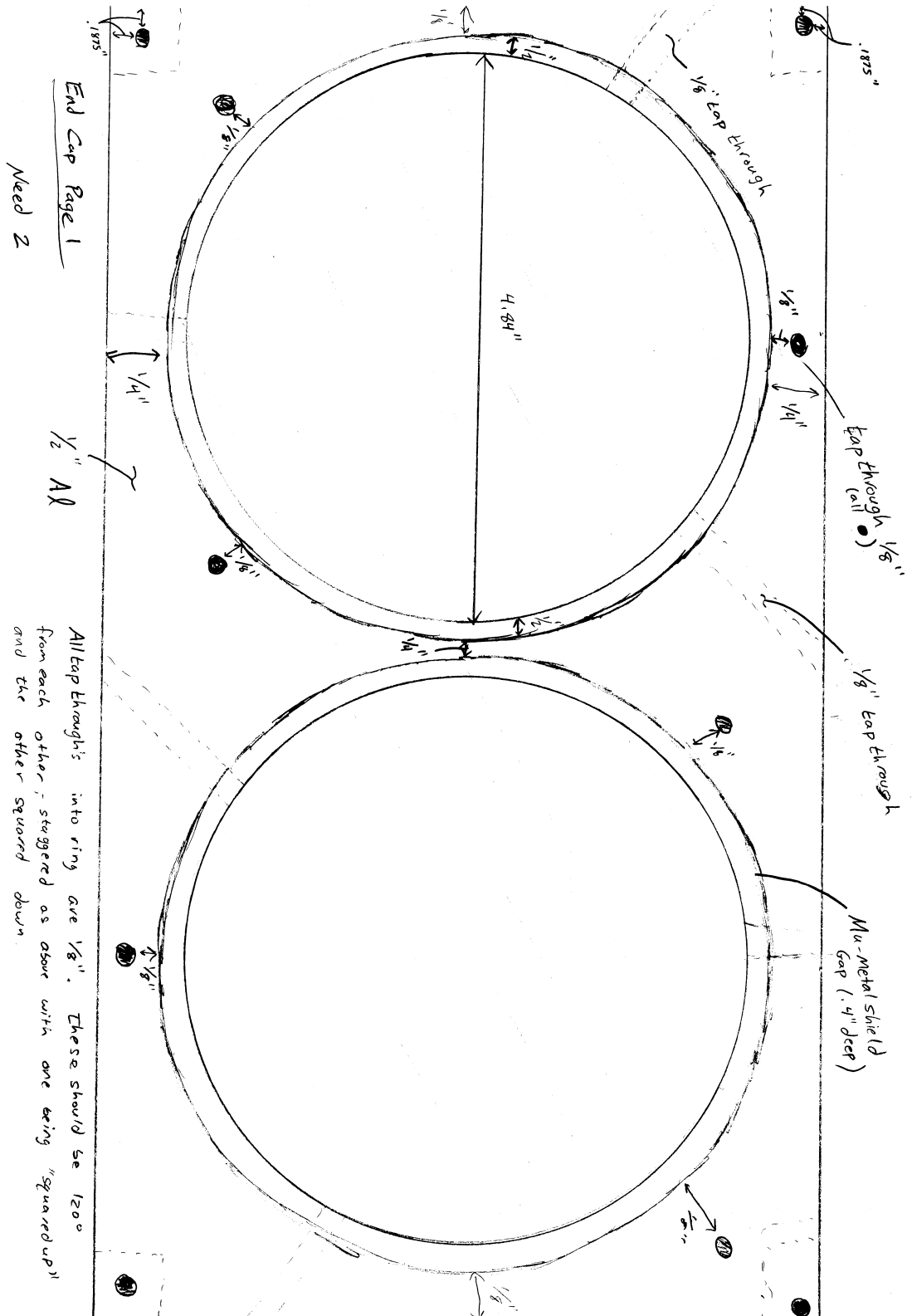
201

or

3. The user has installed an interrupt module in the CAMAC chain and told the software to watch the correct CAMAC channel. Whenever this module receives a gate, it sets a flag to trigger a read-out.

None of these read-out methods require that data taking be stopped, essentially freeing the system from any read-out dead time. The system is also designed to treat all of these read-out triggers equally, so any method of triggering is equally valid.

Though the main function of the system is to read data quickly, store it, and sort it, some secondary functions have also been created. First, there is an automation system in place that allows the user to increment the run every T_R seconds. Second, this system is designed to work with CAMAC (non-FERA) based scaler modules. The scaler data is logged in the data stream for every read-out, marked by a different header in the data stream. Third, the user interface is designed to be entirely point-and-click. Once the system is installed (all of the modules in the correct places and properly connected), the software functions entirely on button presses by the user. The user is not required to do any code alteration. Fourth, online histograms are generated automatically for all 32 input channels. Up to eight 2D histograms are also generated. With these four extra 'functions,' this system fully meets our requirements for a data acquisition system.

Appendix C: Detector Frame Drawings

The following pages show drawings and CAD diagrams of the various pieces that make up both the detector and detector frame. Only some of the pieces have been entered into the CAD program, as they were needed for milling procedures. All documents are included in the initial hand-drawn designs.

End Cap Page 1

Need 2

½" Aℓ

4.84"

.1875"

⅛" tap through

tap through (all ●) ⅛"

⅛" tap through

Mu-metal shield Gap (.4" deep)

⅛"

¼"

¼"

⅛"

⅛"

⅛"

¼"

⅛"

All tap through's into ring are ⅛". These should be 120° from each other, staggered as above with one being "squared up" and the other squared down

Side View:

1/8" tap through

1/2"

3/8"

8/3"

1/4"

8/3"

1/8"

1/8" tap through

Toward center

inset 1/4" deep

3/8"

8/3"

Toward center

12,18"

End Cap Page 2

1" Al

1/4" tap through

10°

.5"

.5

10°

circular Channels cut through
3/16" wide, centered .5" from
center of block
("Gap" just wide enough to
to keep center stable)

"Gap" should be 10° from vertical

1/8"

1/8"

1/8" tap, 3/4" deep

Box Mount Block
need 2

1/8" tap, 3/4" deep

1/8" tap through, counter sunk

.25"

.75"

.75"

.25"

2.5"

1/8" tapthrough, countersunk

1/4" tap, .85" deep

.25"

1" thick Al

2.5"

On Box Mount Rectangle

Need 2
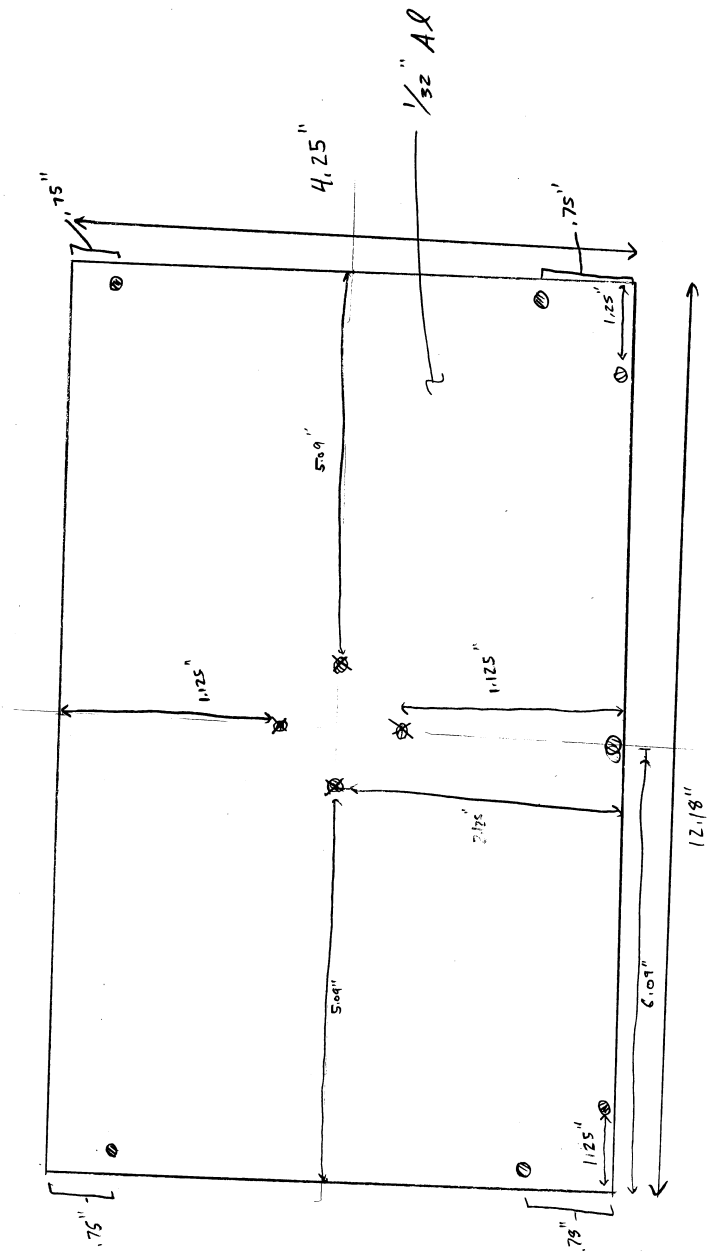
End plate.

All ⊘ are 1/16" tap through   (all .1875" from edge)

__Need 2__

All ⊗ are 1/8" tap through

.75"

4.25"

1/32" Al

.75"

1.25"

6.05"

1.125"

1.125"

2.125"

5.09"

5.09"

12.18"

6.09"

1.25"

1.25"

.75"

.75"

1/8" tap, 1/4" deep

1/16" tap, .1" deep

.5"

1/16" tap, .1" deep

11.68"

5.84"

1/16" tap, .1" deep

.5"

.1"

1/8" tap, 1/4" deep
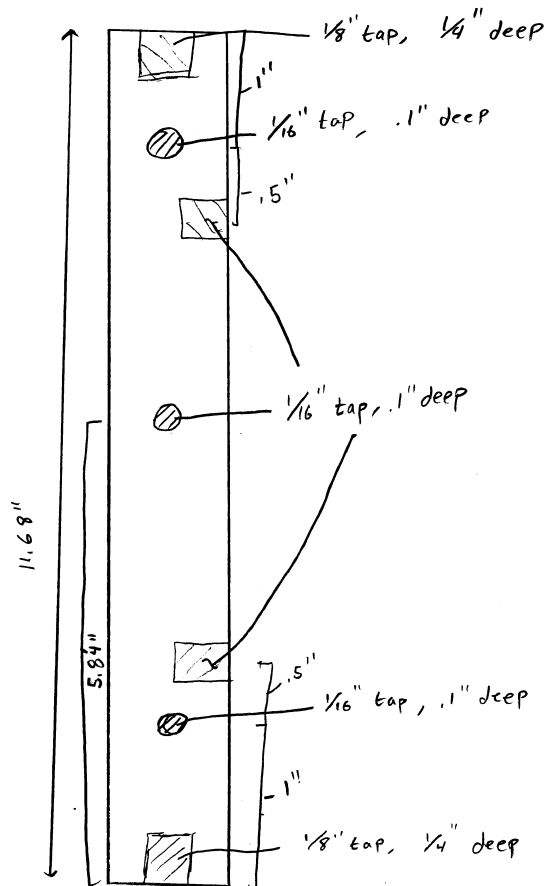
Material: 1/4" square Al

Need 2

Box End Leg (Horizontal)

Rotated View

1/8" tap, 1/2" deep

Counter sunk 1/8" tap through

1/8" tap through Countersink

.1875"

7/16"

11.68"

5.84"

5.84"

1"

1"

3/8" Sq. Al

1/8" tap, 1/2" deep
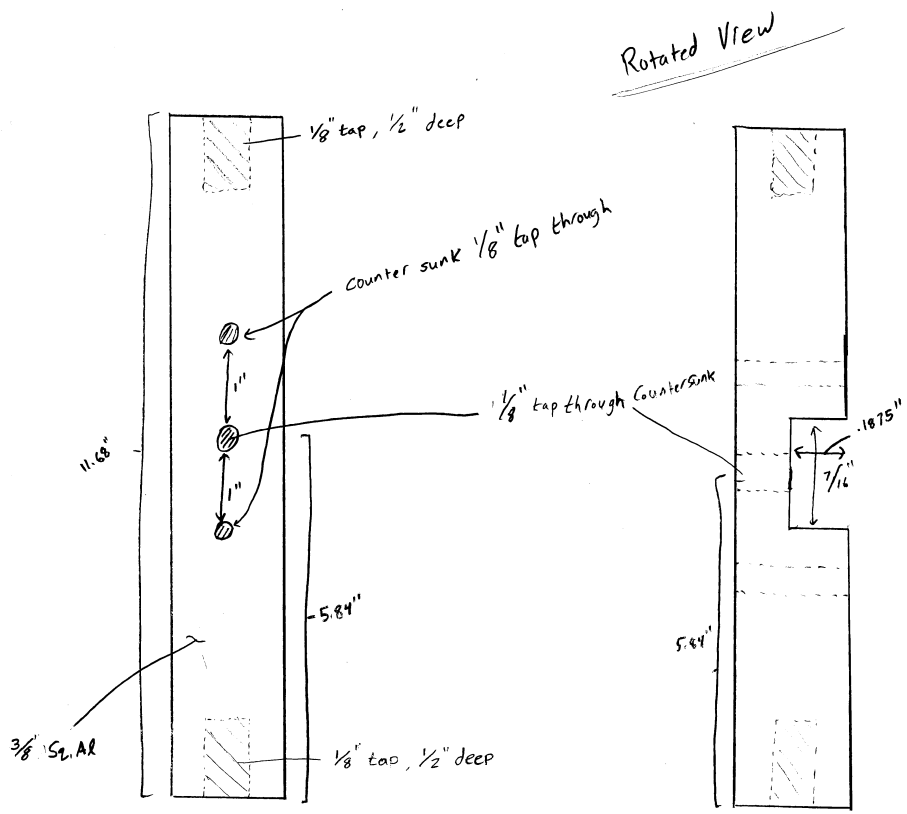
Cross Brace (Horizontal) for Mounting System

Need 2

Rotated View

1/8" tap, 1/2" deep

1/4" tap through

1"

1"

3.75"

1.875"

Counter Sunk

1/8" tap, 1/2" deep

.1875"

7/16"
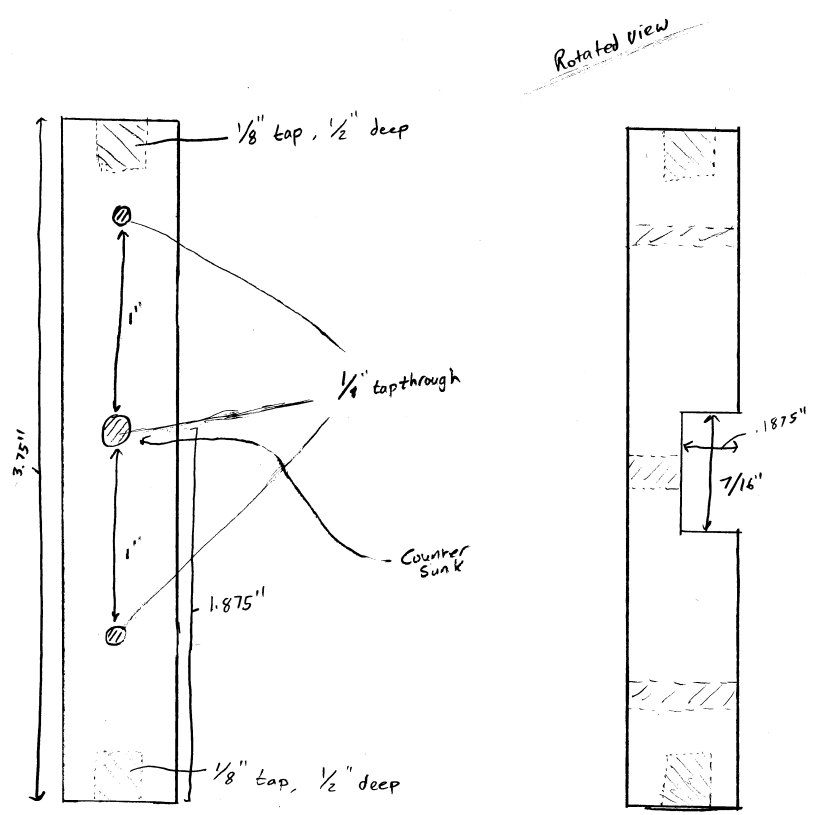
Cross Brace (vertical) for Mounting System

Need 2

1/8" tap, 3/8" deep

1/16" tap through

1/8" tapthrough (counter sink)

1.875"

1/16" tap through

1/8" tap, 3/8" deep

.5"

.25"

3.75"

.25"

.5"
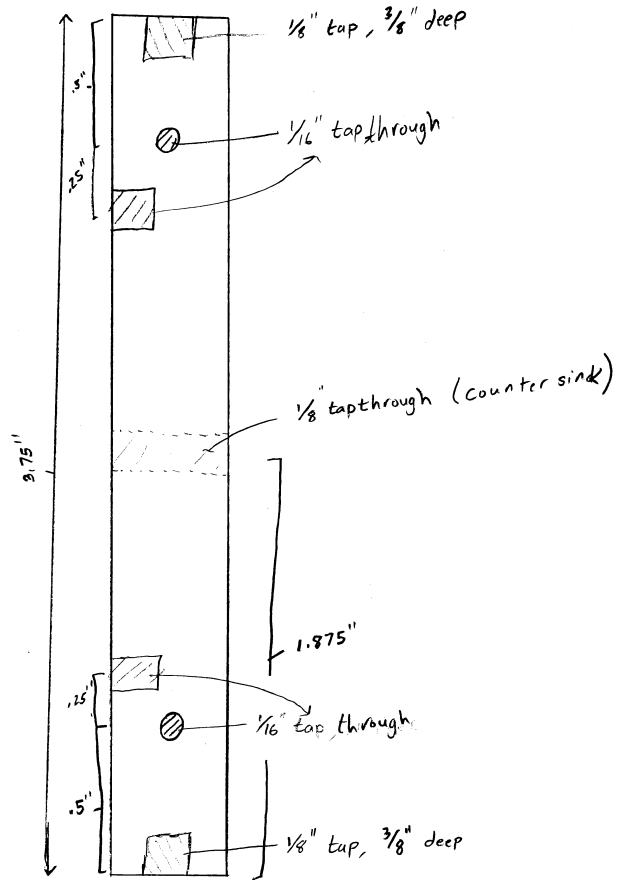
Material : 1/4" square Al
        Need 4

Box   End Leg (vertical)

1/8" tap, 1/2" deep

3.5"

1.75"

1/8" tap, 1/2" deep
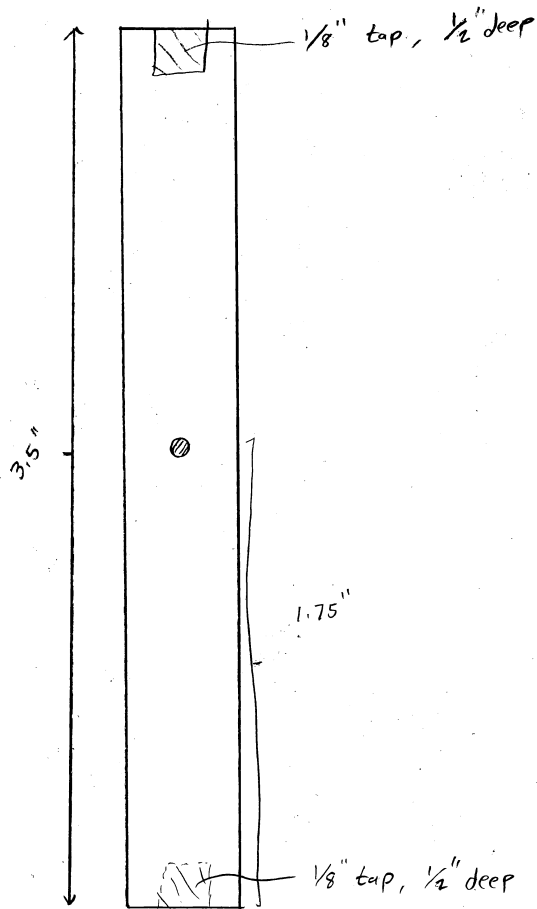
Material: 1/4" square Al

Need 8

Box mid brace
(cross to cross)

.75"

1/32" Aℓ

24.856"

13.956"

1/32" Aℓ

14.184"

2"

18.29"

6.59"

1"

24.856"

14.184"

13.858"

2"

18.29"

6.59"

1"

.5"

.5"

66.08"

4.00"
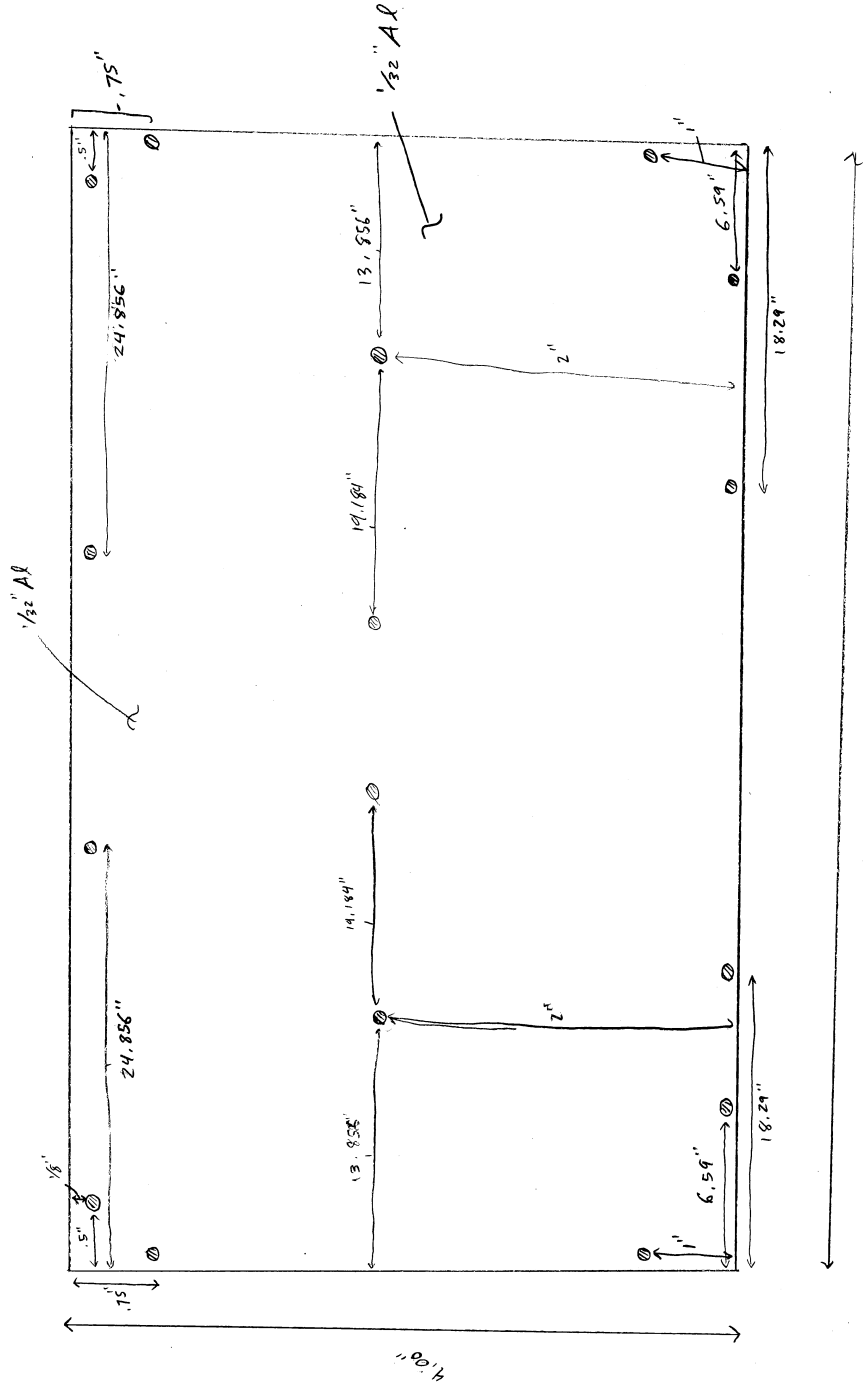
All ⊘ are 1/16" tapped through. All spaced 1/8" from edge

Box Side Plate

Need 2

3/16" drill through from side (see bottom)

1/8"

1/2"

1/8" tap through
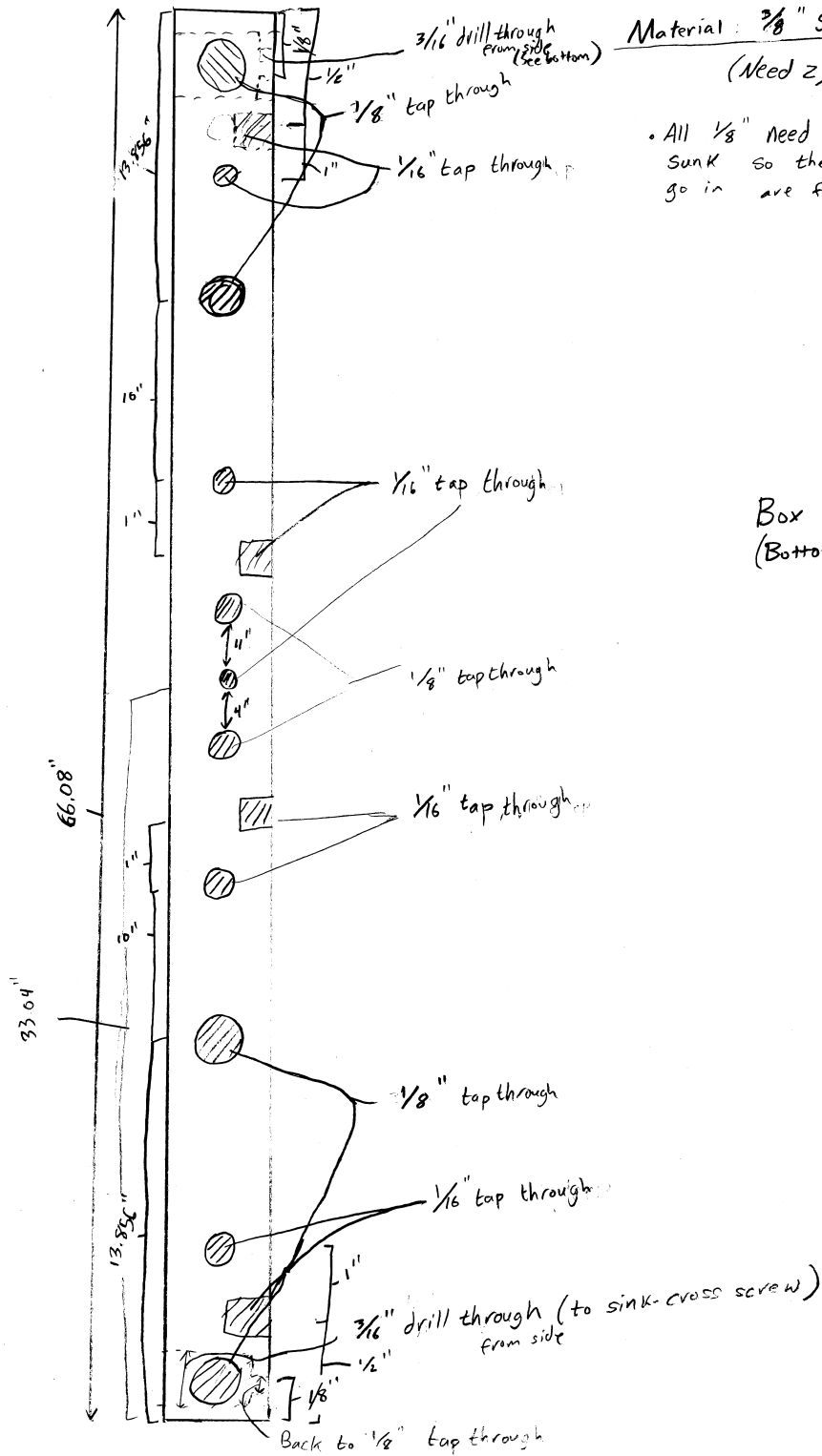
1/16" tap through

Material 3/8" Square Al

(Need 2)

• All 1/8" need to be counter sunk so the screws that go in are flush.

13.856"

16"

1"

1/16" tap through

Box Cross brace
(Bottom)

1/8" tap through

1"

4"

1/16" tap through

66.08"

1"

33.64"

"8"

13.856"

1/8" tap through

1/16" tap through

1"

3/16" drill through (to sink cross screw) from side

1/2"

1/8"

Back to 1/8" tap through
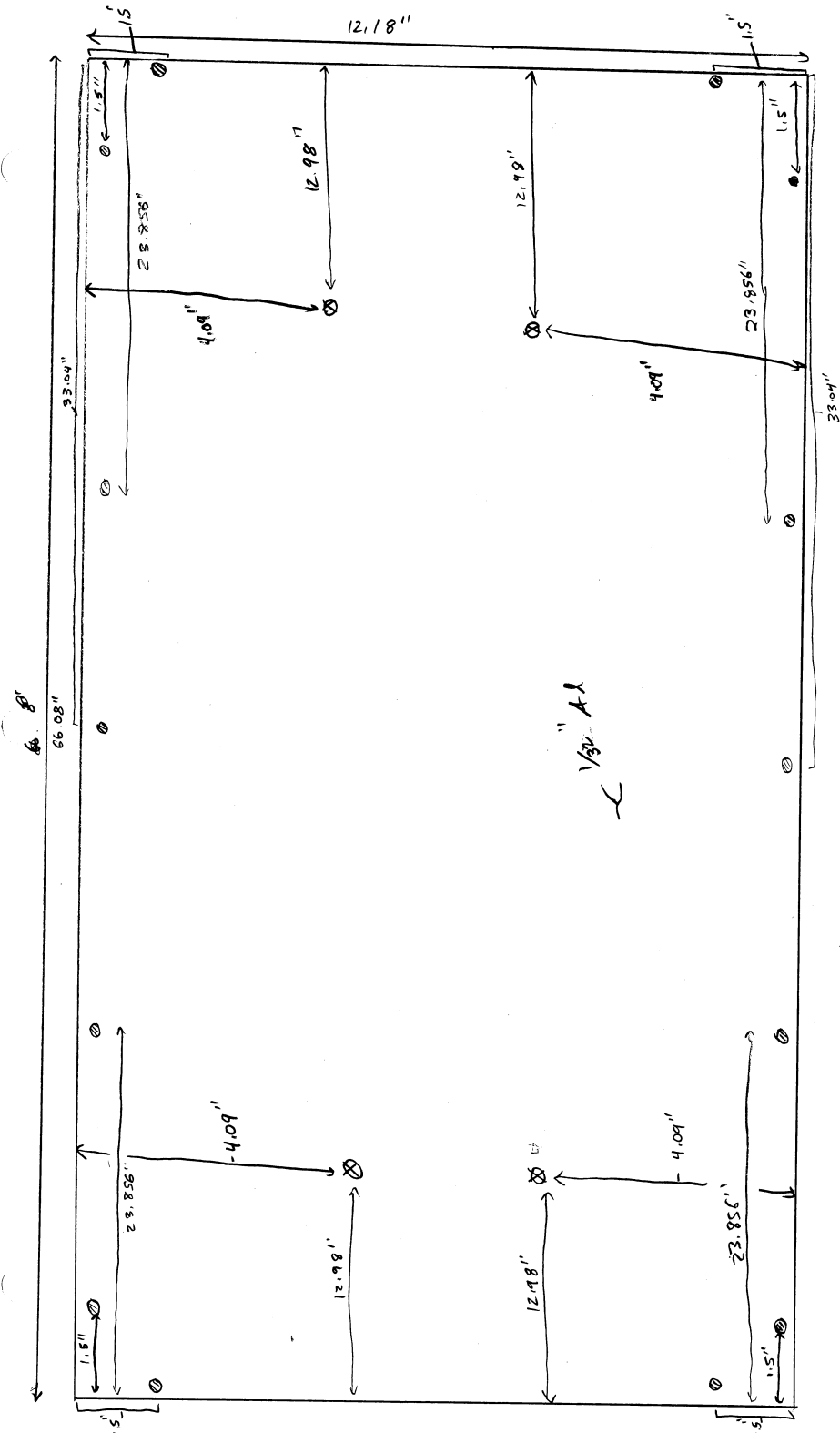
Bottom plate

Need 1

All ⊘ are 1/16" tap through

All ⊗ are 1/8" tap through

All ⊘ are .1875" from edge

12,18"

12.98"

12.99"

23.856"

33.04"

4.09"

4.09"

23.856"

33.04"

66.8"

66.08"

1/32" Al

1.5"

1.5"

1.5"

1.5"

4.09"

23.858"

12.98"

4.09"

12.98"

23.856"

1.5"

1.5"

1.5"

Material: 3/8" Square Al

(Need 2)

1/8"

1.7"

.5"

1/8" tap through

7.766"
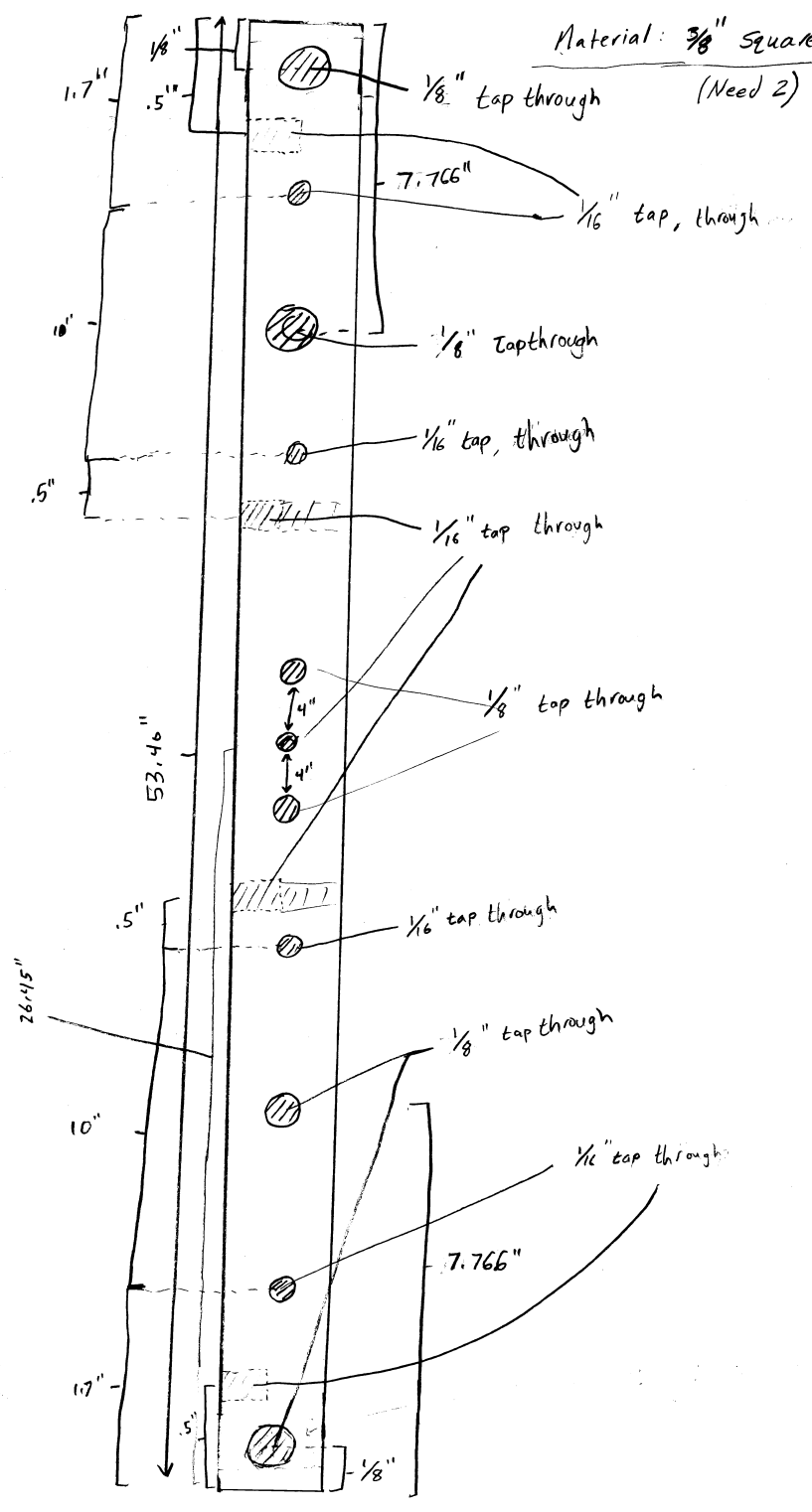
1/16" tap, through

.All 1/8" need to be
counter sunk so that
the screw heads are
flush.
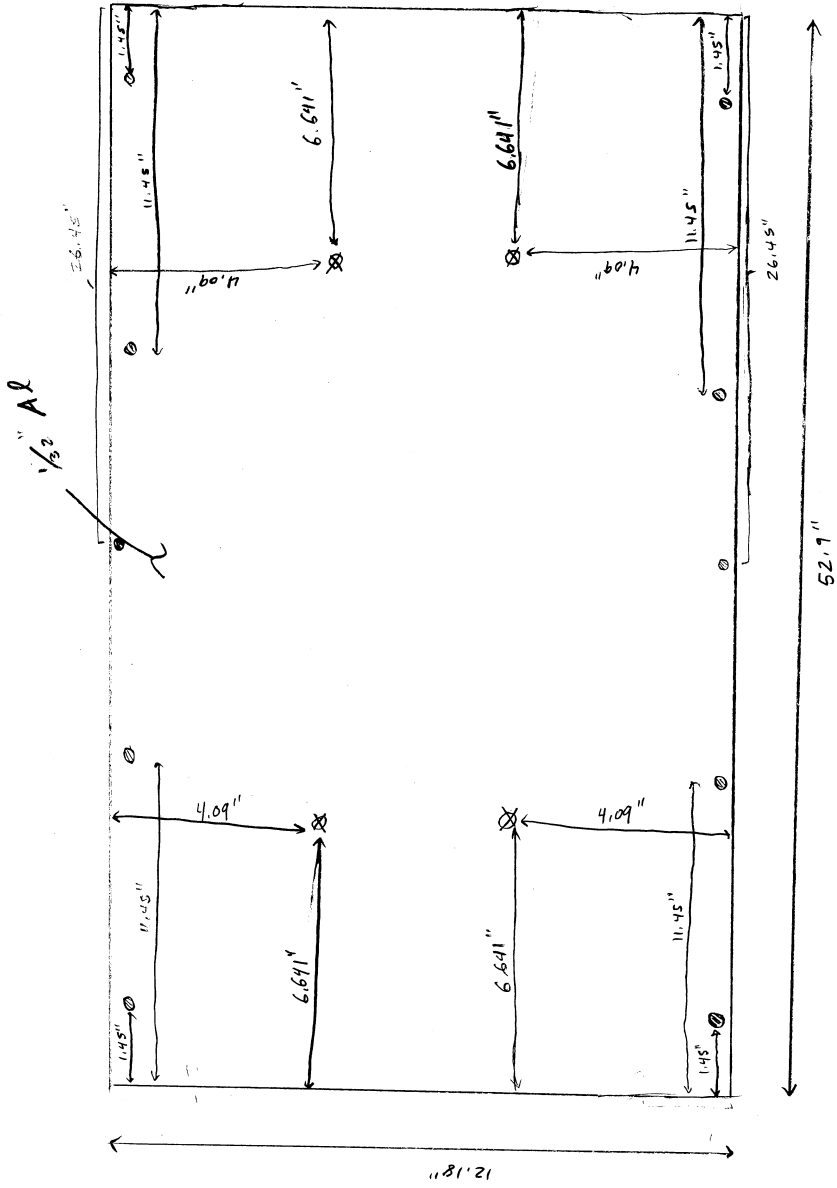
1/8" Tapthrough

10"

1/16" tap, through

.5"

1/16" tap through

Box Cross Brace
(TOP)

1/8" tap through

53.46

4"

4"

.5"

1/16" tap through

26.45"

1/8" tap through

10"

1/16" tap through

7.766"

1.7"

.5"

1/8"

1.45"

6.41"

11.45"

26.45"

4.09"

6.641"

4.09"

6.641"

11.45"

1.45"

1/32" Al

6.641"

11.45"

4.09"

1.45"

6.641"

11.45"

26.45"

1.45"

52.1"

12.18"

Top Plate

Need 1

All ⊘ are 1/16" tapped through. All spaced .1475" from edge.

All ⌀ are 1/8" tap through.

1/8" tap, 1/2" deep

4"

1/8" tap, 1/2" deep
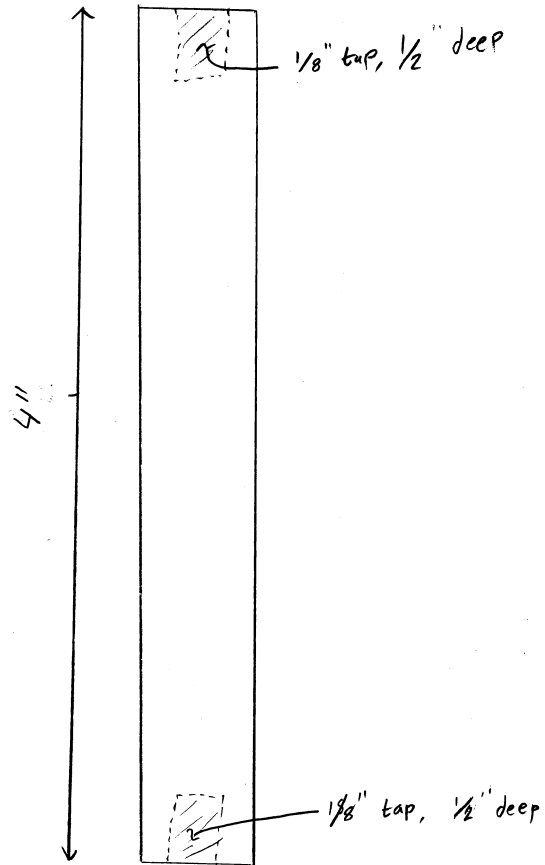
Material: 3/8" square Al:

Need 4

Box mid Brace
(vertical plate to plate)

1/8" deep inset

11/16"

4.84"

1.0375"

.35"

(3 alignment dimples
120° from each other
1/16" diameter, shallow)
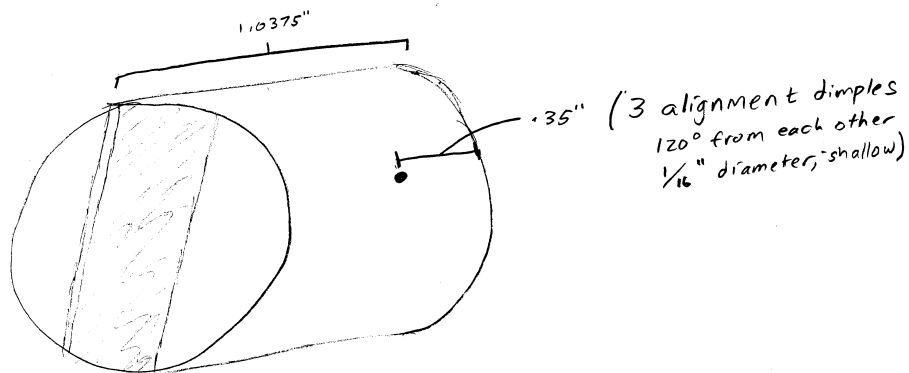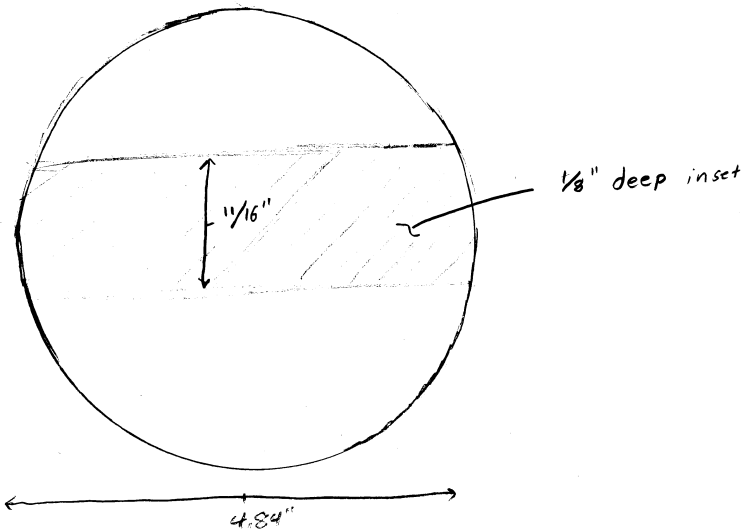
UVT Cylinder ; All sides polished (No oils)

Need 4

Lightguide to PMT

4.25"

11.69"

12.18"

6.34"

AR plate for PMT holding

Center of Plate if drawn Properly

5/8"

5/8"

2.125"

2.33"

24°

Light guide Arc

1 13/16"

1 13/16"

3.17"

3.17"

-7.606"

6.766"

Light guide slant

Z.W. Miller

1/32 Chamfer

.13

1.50

1.04

Ø4.84
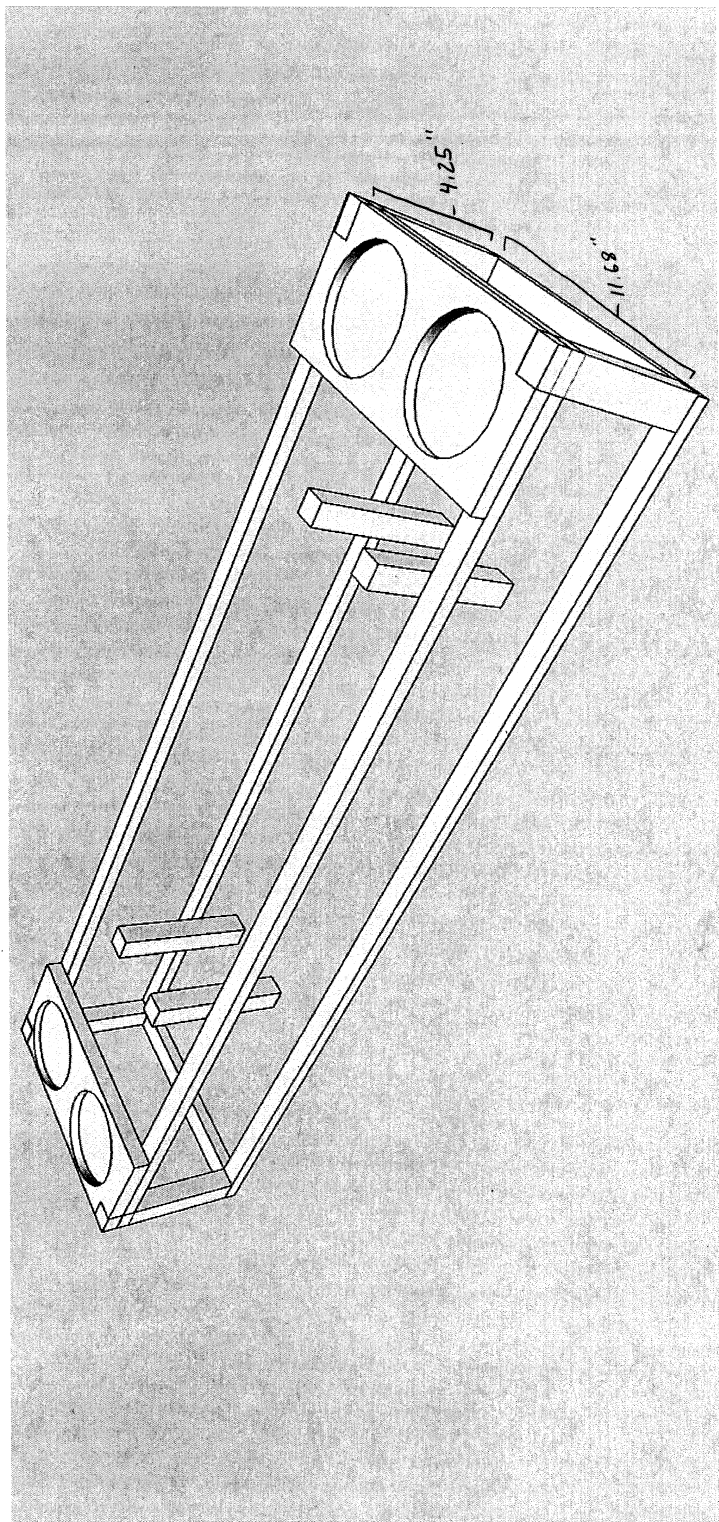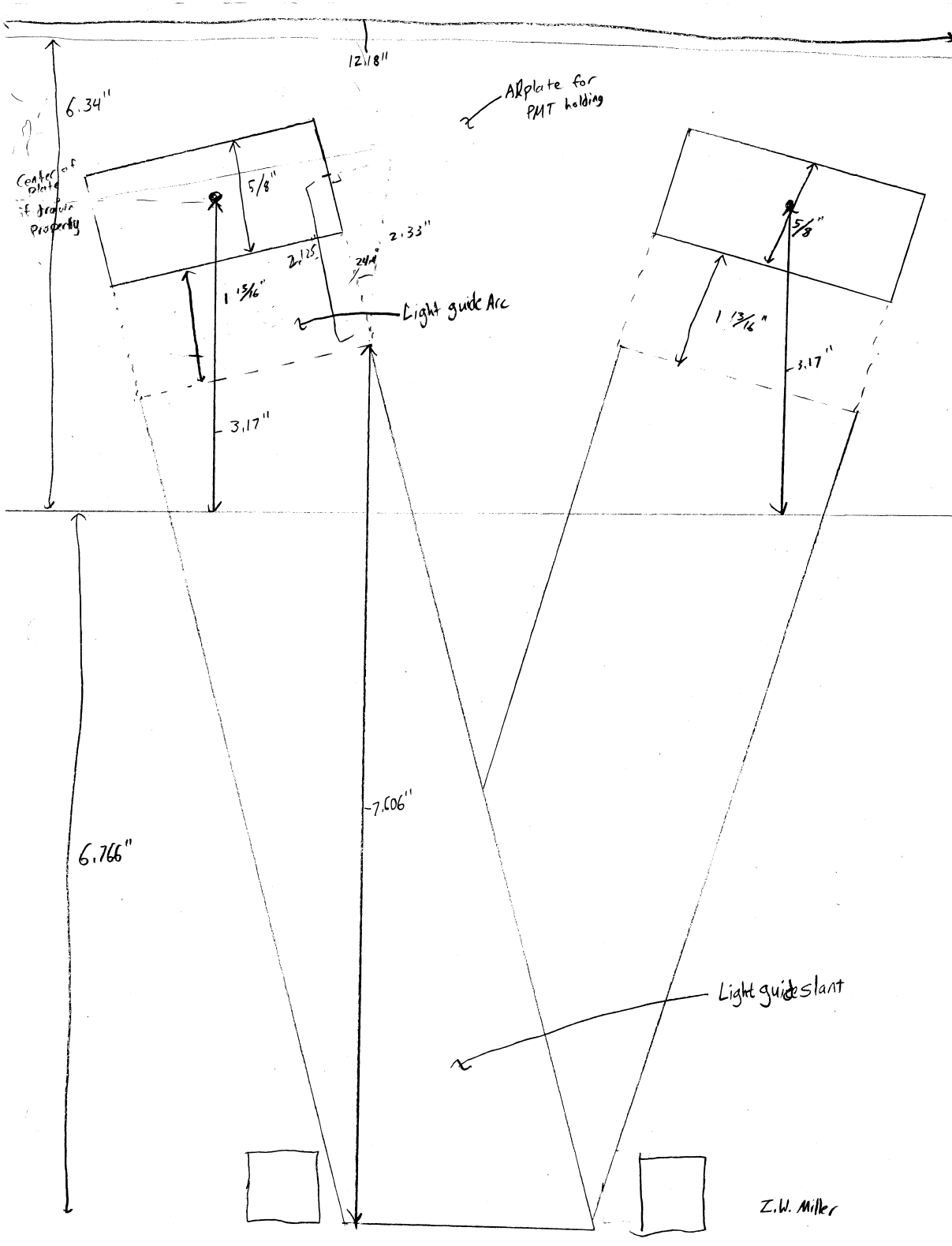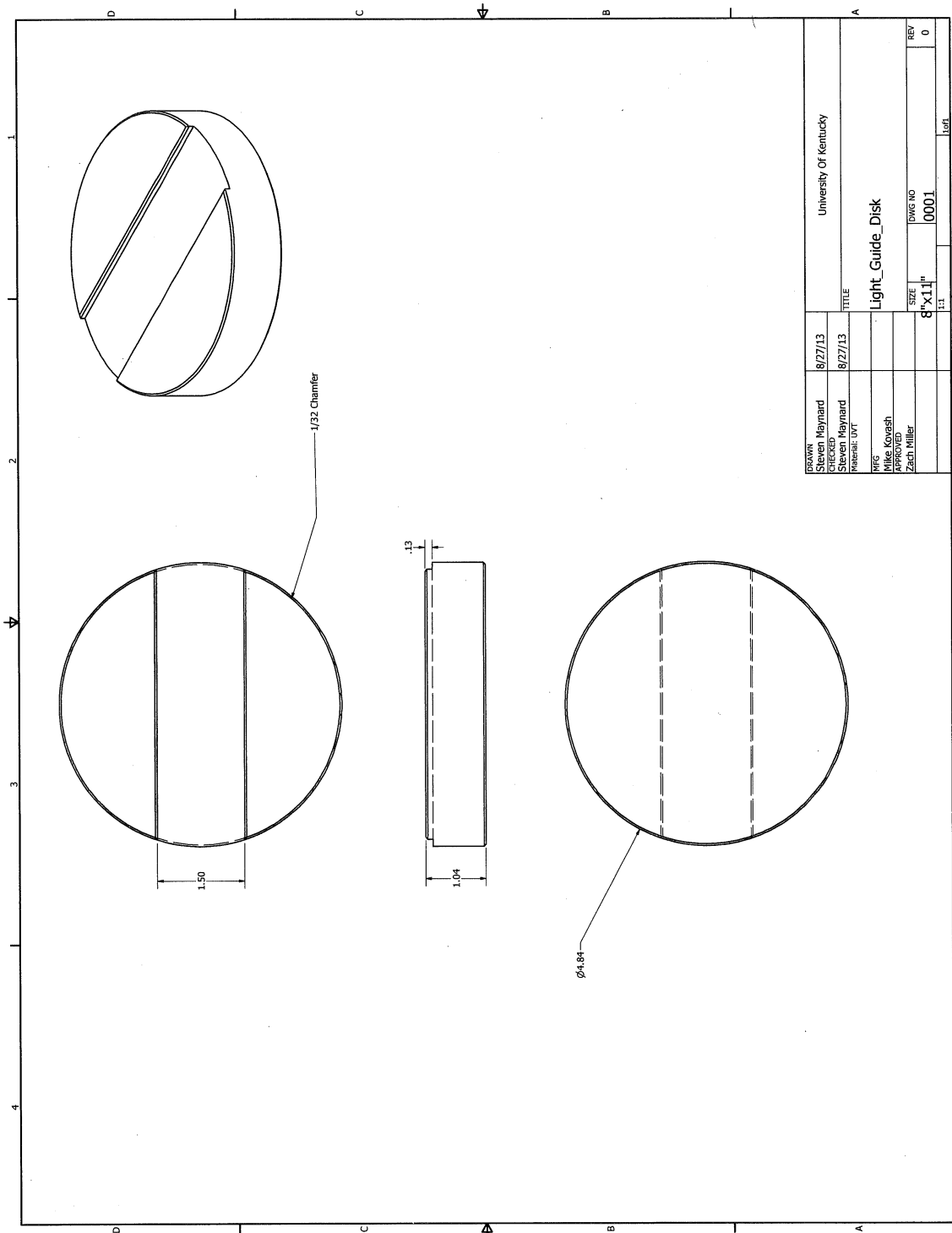
DRAWN	Steven Maynard	8/27/13		University Of Kentucky	
CHECKED	Steven Maynard	8/27/13			
Material: UVT			TITLE	Light_Guide_Disk	
MFG	Mike Kovash				
APPROVED	Zach Miller		SIZE 8"x11"	DWG NO 0001	REV 0
			1:1	1 of 1	

Notes:

* All Surfaces are to be fine polished (No Scratches)
* Slots Can have a 1/32" Radius In Corners.

1.50

R2.25

R3.75

.12

.75

.16

.12

4.33

3.75

DRAWN	Steven Maynard	8/29/13		
CHECKED	Steven Maynard	8/29/13		University Of Kentucky
QA			TITLE	
MFG	Dr. Mike Kovash			Light_Guide_Adapter
APPROVED	Zach Miller			
		SIZE 8.5"x11"	DWG NO 0005	REV 0
		2	1 Of 1	1

CLR for 6/32 thur
Counterbore 1/4 .150 deep

6/32 tapped thur

6/32 tapped thur

CLR FOR 6/32 SCREW
Counterbore 1/4 .150 deep

6/32 tapped thur

6/32 tapped thur Centered .1875 from both ends

1.70
7.77
10.00
22.70
26.70

22.70
7.77
10.00
1.70

.38
.38

DRAWN	Steven Maynard	8/29/13		University Of Kentucky
CHECKED	Steven Maynard	8/29/13		
Material: 6061 AL			TITLE	
MFG	Dr. Mike Kovash			Box_Cross_Brace_Top
APPROVED	Zach Miller			
			SIZE 8.5"x11"	DWG NO 0006	REV 0
			SCALE	1 Of 1

All Holes are CLR holes to pass screws into top rail.

Also these holes are to be placed on the right hand side of plate as well. (Mirror Image)

52.90

.03

11.45
6.64
11.99
8.09
4.06
.19
1.15
12.18

University Of Kentucky

DRAWN Steven Maynard	9/9/13				
CHECKED Steven Maynard	9/9/13	TITLE			
Material: 6061 AL			Light_Guide_Frame_Top		
MFG Dr. Mike Kovash					
APPROVED Zach Miller		SIZE 8.5"x11"	DWG NO 0007		REV 0
		SCALE			1 of 1

.38

.38

.50

4.00

6/32 tapped hole 2x's

DRAWN	Steven Maynard	9/9/13	University Of Kentucky			
CHECKED	Steven Maynard	9/9/13				
Material: 6061 Al			TITLE			
MFG	Dr. Mike Kovash		Box_Mid_Brace4			
APPROVED	Zach Miller					
			SIZE 8.5"x11"	DWG NO 0008	REV 0	
				1 Of 1		

4.63

1.08

.38

.19

.19

Ø.19

5.09

7.09

6/32 Tapped Hole
4x's

11.43

12.18

11.99

.190 CLR Hole 2x's

.19

3.17

8/32 Tapped Holes
2x's

.38

DRAWN	Steven Maynard	9/9/13
CHECKED	Steven Maynard	9/9/13
Material: 6061 AL		
MFG	Dr. Mike Kovash	
APPROVED	Zach Miller	

TITLE
End_Plate

University Of Kentucky

SIZE
8.5"x11"

DWG NO
0010

REV
1

SCALE

1 OF 1
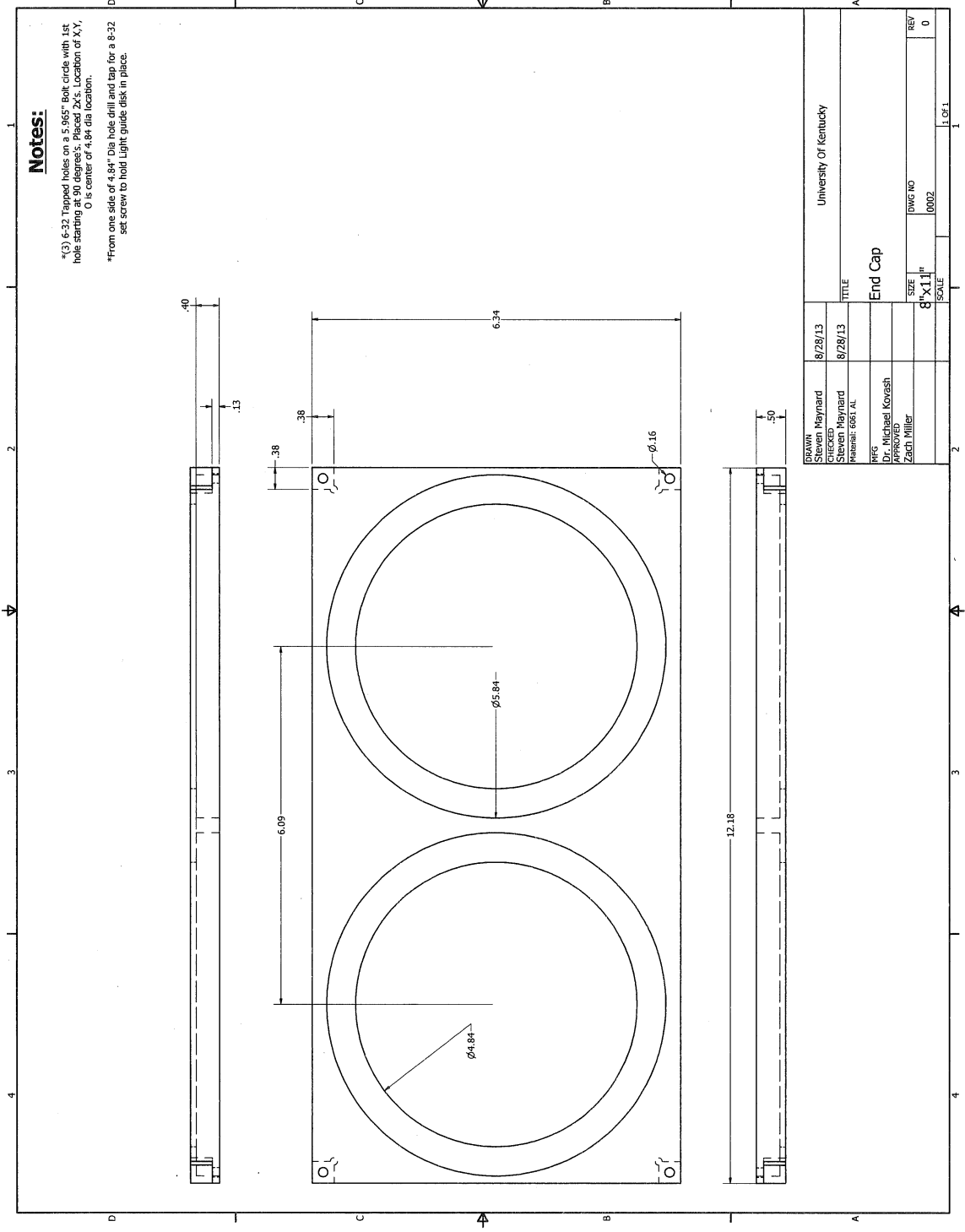
Notes:

*(3) 6-32 Tapped holes on a 5.965" Bolt circle with 1st hole starting at 90 degree's. Placed 2x's. Location of X,Y, O is center of 4.84 dia location.

*From one side of 4.84" Dia hole drill and tap for a 8-32 set screw to hold Light guide disk in place.

.40

.13

.38

.38

6.34

Ø.16

Ø5.84

6.09

Ø4.84

12.18

.50

DRAWN	Steven Maynard	8/28/13		University Of Kentucky
CHECKED	Steven Maynard	8/28/13		
Material: 6061 AL			TITLE	
MFG	Dr. Michael Kovash		End Cap	
APPROVED	Zach Miller			
			SIZE 8"x11"	DWG NO 0002	REV 0
			SCALE		1 Of 1

R.41

Ø.25 — Clearance for a bolt.

2.50

.22   .14

R.59

2.50

2.25

1.00

8-32 Threaded .750" Deep 2x's

DRAWN	Steven Maynard	8/28/13		University Of Kentucky
CHECKED	Steven Maynard	8/28/13		
Material: 6061 AL			TITLE	
MFG	Dr. Michael Kovash			Box_Mount_Block
APPROVED	Zach Miller			
			SIZE 8"x11"	DWG NO 0003	REV 0
				1 Of 1

Bibliography

[1] K. Krane, *Introductory Nuclear Physics.* John Wiley and Sons, New York, third ed., 1987.

[2] F. Shiraishi and M. Hosoe, "Mass distribution of fission fragments from ^{235}U(n$_{th}$, f) by simultaneous measurements of velocity and energy," *Nuclear Instruments and Methods*, vol. 107, no. 3, pp. 493 – 500, 1973.

[3] N. Bohr and J. A. Wheeler, "The mechanism of nuclear fission," *Phys. Rev.*, vol. 56, pp. 426–450, Sep 1939.

[4] R. Vandenbosch and J. R. Huizenga, *Nuclear Fission.* Academic Press, New York and London, 1973.

[5] Author Unknown. `http://astro1.panet.utoledo.edu/~ljc/liquid_drop.jpg`, Accessed 13 March 2015.

[6] W. Loveland, "Chapter 11: Fission," *Oregon State University*, p. 43, Accessed 27 March, 2015.

[7] B. C. Diven, H. C. Martin, R. F. Taschek, and J. Terrell, "Multiplicities of fission neutrons," *Phys. Rev.*, vol. 101, no. 3, pp. 1012–1015, 1956.

[8] J. S. Fraser, "The angular distribution of prompt neutrons emitted in fission," *Phys. Rev.*, vol. 88, no. 3, pp. 536–541, 1952.

[9] D. G. Madland and J. R. Nix, "Calculation of prompt fission neutron spectra," in *International Conference on Nuclear Cross Sections for Technology, Knoxville, TN*, p. 788, NBS Special Publication 594, Washington D.C., 22-26 October, 1979.

[10] P. Staples, J. Egan, G. Kegel, A. Mittler, and M. Woodring, "Prompt fission neutron energy spectra induced by fast neutrons," *Nuclear Physics A*, vol. 591, no. 1, pp. 41 – 60, 1995.

[11] Brookhaven National Laboratory, "Evaluated Nuclear Data Files." `http://www.nndc.bnl.gov/endf`, Accessed 2014.

[12] W. Crookes, "On radiation," *Journal of the Franklin Intitute*, vol. 108, no. 5, p. 305, 1879.

[13] J. B. Birks, *The Theory and Practice of Scintillation Counting.* Pergamon Press Ltd., 1964.

[14] B. H. Daub, V. Henzl, M. A. Kovash, J. L. Matthews, Z. W. Miller, K. Shoniyozov, and H.Yang, "Measurements of the neutron-proton and neutron-carbon total cross-sections from 150 to 800 kev," *Physical Review C*, vol. 87, no. 014005, 25 January 2013.

[15] Brookhaven National Laboratory, "Evaluated Nuclear Data Files." `http://www.nndc.bnl.gov/endf`, Accessed 7 January, 2015.

[16] G. F. Knoll, *Radiation Detection and Measurement.* John Wiley and Sons Publishing, fourth ed., 2010.

[17] Saint-Gobain Crystals, *Organic Scintillation Materials Brochure*, 2014.

[18] R. L. Craun and D. L. Smith, "Analysis of response data for several organic scintillators," *Nuclear Instruments and Methods*, vol. 80, p. 239, 1970.

[19] National Institute of Standards and Technology, "ESTAR Database." `http://www.nist.gov/pml/data/star/`, Accessed 23 January 2015.

[20] K. Shoniyozov, "Gamma-neutron detector design." University of Kentucky Poster Session, Personal Correspondence, 2009.

[21] T. Massam, "Light guide design for timing measurements in large counters," *Nuclear Instruments and Methods*, vol. 141, no. 2, p. 251, 1 March 1977.

[22] Hamamatsu Company, "Hamamatsu R1250 Specifications." `http://www.hamamatsu.com/us/en/R1250.html`, Accessed 15 January 2015.

[23] S. Noda, R. C. Haight, R. O. Nelson, M. Devlin, J. M. O'Donnell, A. Chatillon, T. Granier, G. Bélier, J. Taieb, T. Kawano, and P. Talou, "Prompt fission neutron spectra from fission induced by 1 to 8 mev neutrons on ^{235}U and ^{239}Pu using the double time-of-flight technique," *Phys. Rev. C*, vol. 83, p. 034604, Mar 2011.

[24] R. C. Haight, S. Noda, and J. M. ODonnell, "Los alamos analysis of an experiment to measure fission neutron output spectra from neutron-induced fission of 235u and 239pu," *LA-UR-08-2585*, 2008.

[25] C. Y. Wu, R. Henderson, J. Gostic, R. C. Haight, and H. Y. Lee, "Low-mass fission detector for the fission neutron spectrum measurement," *LLNL-TR-461044*, 2010.

[26] C. Y. Wu, R. Henderson, and J. Gostic, "Parallel plate avalanche counter," *LLNL-JRNL-661405*, 2014.

[27] C. Y. Wu and R. C. Haight. Personal Correspondance, Measured 28 August 2014.

[28] Los Alamos National Laboratory, "Weapons neutron research facility website." `http://wnr.lanl.gov/_assets/flight_paths/flight_paths.php`, Accessed 9 February 2015.

[29] H. Bethe and J. Ashkin, *Experimental Nuclear Physics.* John Wiley, New York, e. segre ed., 1953.

[30] T. Taddeucci, "Modelling of Our Present Experiments." `https://www.oecd-nea.org/science/meetings/pnd22/presentations/1-HAIGHT.pdf`, 2014.

[31] E. Ertan, T. Akdogan, M. B. Chtangeev, W. A. Franklin, P. A. M. Gram, M. A. Kovash, J. L. Matthews, and M.Yuly, "Cross sections of neutron-deuteron elastic scattering in the energy range 135-250 mev," *Physical Review C*, vol. 87, no. 0340003, 2013.

[32] M. Chtangeev, "Neutron-deuteron elastic scattering and the three-nucleon force," *M.S. Thesis, Massachussettes Institute of Technology*, 2005.

[33] T. Akdogan, "Pion production in the neutron-proton interaction," *Ph.D. Thesis, Massachussettes Institute of Technology*, 2003.

[34] Brookhaven National Laboratory, National Nuclear Data Center, "Experimental nuclear reaction data (exfor)." `http://www.nndc.bnl.gov/exfor/exfor.htm`, Accessed 1 March 2014.

[35] S. Badikov, C. Zhenpeng, and A.D. Carlson et al., *International Evaluation of Neutron Cross Section Standards.* International Atomic Energy Association (IAEA), 2007.

[36] P. Lisowski, "The ^{238}U(n,f) Cross Section," in *Proc. International Conference on Nuclear Data for Science and Technology*, p. p. 97, 30 May - 3 June, 1988.

[37] S. A. Wender, S. Balestrinit, A. Brown, R. Haight, C. Laymon, P. Lisowski, W. McCorkle, R. O. Nelson, and W. Parke, "A fission ionization detector for neutron flux measurements at a spallation source," *Nuclear Instruments and Methods A*, vol. 336, p. 226, 1993.

[38] C. Jiang, "A precision measurement of neutron-neutron scattering length a_{nn} via $\pi^- d \to \gamma\, n\, n$," *Ph.D. Thesis, University of Kentucky*, 2005.

[39] R. Hagedorn and J. D. Jackson, *Relativistic Kinematics: A Guide to the Kinematic Problems of High Energy Physics*. W. A. Benjamin Inc., New York, 1963.

[40] D. Measday and C. Richard-Serre, "The loss of protons by nuclear inelastic interactions in various materials," *Nuclear Instruments and Methods*, vol. 76, no. 1, pp. 45 – 54, 1969.

[41] A. Sourkes, M. de Jong, C. Goulding, W. van Oers, E. Ginkel, R. Carlson, A. Cox, and D. Margaziotis, "Proton loss by nuclear inelastic interactions in CsI, NaI, NE102, {NE213} and stilbene," *Nuclear Instruments and Methods*, vol. 143, no. 3, pp. 589 – 594, 1977.

[42] CERN, "ROOT Data Analysis Framework." `https://root.cern.ch/drupal/`, Accessed 13 March 2015.

[43] Center for Nuclear Studies, George Washington University, "SAID Partial Wave Analysis." `http://gwdac.phys.gwu.edu/`, Accessed 4 January 2015.

[44] J. Sadhukhan, J. Dobaczewski, W. Nazarewicz, J. A. Sheikh, and A. Baran, "Pairing-induced speedup of nuclear spontaneous fission," *Phys. Rev. C*, vol. 90, p. 061304, Dec 2014.

[45] J. D. McDonnell, W. Nazarewicz, and J. A. Sheikh, "Third minima in thorium and uranium isotopes in a self-consistent theory," *Phys. Rev. C*, vol. 87, p. 054327, May 2013.

[46] Y. Zhu and J. C. Pei, "Microscopic description of neutron emission rates in compound nuclei," *Phys. Rev. C*, vol. 90, p. 054316, Nov 2014.

[47] V. S. Barashenkov, "Elastic interactions of high energy particles," *Fortschritte der Physik*, vol. 10, no. 5, 1962.

[48] Cheesecote Mountain CAMAC, *CMC203 Manual*, 2007.

[49] Wiener, Plein, and Baus Elektronik, *CCUSB Module and Manual*, 2012.

[50] Sparrow Corp., "Kmax software for data acquisition environments." `http://www.sparrowcorp.com/products/software`, 2014.

[51] A. Khadjavi, "Calculation of solid angle subtended by rectangular apertures," *J. Opt. Soc. Am.*, vol. 58, pp. 1417–1418, 1968.

Vita

<div align="center">

Zachariah W. Miller

</div>

Education:

      University of Kentucky

      Lexington, KY

      M.S., Physics

      September 2012

      Eastern Kentucky University

      Richmond, KY

      B.S., Physics

      May 2009

Professional Positions:

      University of Kentucky

      Research Assistant

      June 2010 - Present

      University of Kentucky

      Teaching Assistant

      August 2009 - June 2012

      Eastern Kentucky University

      Adjunct Professor

      July 2011 - January 2012

Publications:

Response of BC-418 Plastic Scintillator to Low-Energy Protons, B.H. Daub, V. Henzl, M.A. Kovash, J.L. Matthews, Z.W. Miller, K. Shoniyozov, H. Yang, Nuclear Instruments and Methods in Physics Research Section A: Accelerators, Spectrometers, Detectors and Associated Equipment, Volume 701, 11 February 2013, Pages 171-175, ISSN 0168-9002, `http://dx.doi.org/10.1016/j.nima.2012.11.025`

Measurements of the Neutron-Proton and Neutron-Carbon Total cross sections from 150 to 800 keV, B. H. Daub, V. Henzl, M. A. Kovash, J. L. Matthews, Z. W. Miller, K. Shoniyozov, and H. Yang, PHYSICAL REVIEW C 87, 014005 (2013), 25 January 2013, `http://link.aps.org/doi/10.1103/PhysRevC.87.014005`